Transport Coefficients in Dense Active Brownian Particle Systems

Inaugural Dissertation

zur Erlangung des Doktorgrades

der Mathematisch-Naturwissenschaftlichen Fakultät

der Heinrich-Heine Universität Düsseldorf

vorgelegt von

Julian Reichert

aus Saarbrücken

Köln, November 2020

aus dem Institut für Theoretische Physik II weicher Materie
der Heinrich-Heine-Universität Düsseldorf

Gedruckt mit der Genehmigung der
Mathematisch-Naturwissenschaftlichen Fakultät
der Heinrich-Heine-Universität Düsseldorf

Berichterstatter:

1. Prof. Dr. Thomas Voigtmann

2. Prof. Dr. Hartmut Löwen

Tag der mündlichen Prüfung:

17.12.2020

Für meine Eltern Nicole und Dietmar

Abstract

The investigation of transport phenomena in crowded active matter is of substantial interest to obtain a fundamental understanding of many biophysical processes, such as the dynamics of cells and the associated mechanisms of morphogenesis. Despite their great relevance, the underlying physical principles are insufficiently understood in lack of appropriate theories for dense systems far from equilibrium. One out of the few theoretical approaches that are capable to address the regime of high densities under non-equilibrium conditions is given by a recent formulation of the mode-coupling theory of the glass transition to describe the collective dynamics of active Brownian particles. By suitably extending this mode-coupling approach, this work aims to investigate non-equilibrium transport coefficients in dense suspensions of active particles in two dimensions.

Starting from a microscopic description, the central quantity of this work is given by the transient correlation function of two angle-resolved microscopic densities in mixtures of active and passive particles, the approximation of which within the framework of the mode-coupling theory constitutes the first goal. Based on the resulting equations, further mode-coupling approaches are derived to predict the transient dynamics and the mean-squared displacement of active or passive tagged particles in both active and passive dense host environments. Moreover, the mode-coupling approximated dynamical correlation functions are exploited to approximate Green-Kubo-type expressions for further transport coefficients such as the viscosity and the effective swimming velocity that can be derived within the framework of the integration-through-transients formalism.

A central constituent of the present work comprises a test of the mode-coupling theory for active Brownian particles against results from a simulation of event-driven active Brownian hard-disks. Both methods deliver largely qualitative, and in some cases near quantitatively consistent results. This provides an important contribution to assess the applicability of the theory and the general quality of its used approximations. Moreover, the use of two independent methods leads to a deeper understanding of the universal properties of active transport at high densities that have been barely addressed so far. A governing principle arises in the presence of competing length scales, represented by the cageing length of volume exclusion and the persistence length of active locomotion. This principle has played a subordinate role for most previous approaches for model systems of active particles, which mainly referred to diluted systems or systems of moderate densities, but is of decisive importance at high densities.

The methods of this work are further employed to assess current experimental results from a setup with diffusiophoretic active Janus particle in a binary colloidal mixture close to the glass transition point. In a final part of this work, mixing effects in monodisperse systems of active and passive particles are discussed with respect to the influences of the composition and the strength of the activity of the components on the dynamics and the glass transition. The results reveal the possibility to influence the viscosity of samples by targeted doping with active particles.

Kurzzusammenfassung

Die Untersuchung von Transportphänomenen in dicht gefüllter aktiver Materie ist von erheblichem Interesse, um ein grundlegendes Verständnis vieler biophysikalischer Prozesse zu erhalten, wie beispielsweise der Dynamik von Zellen und den damit verbundenen Mechanismen der Morphogenese. Trotz ihrer großen Relevanz sind die zugrundeliegenden physikalischen Prinzipien unzureichend verstanden, da es an geeigneten Theorien für Systeme bei hohen Dichten fernab des Gleichgewichts mangelt. Einer der wenigen theoretischen Ansätze, die in der Lage sind, den Bereich hoher Dichten unter Nichtgleichgewichtsbedingungen zu beschreiben, ist eine kürzlich entwickelte Formulierung der Modenkopplungstheorie des Glasübergangs zur Beschreibung der kollektiven Dynamik aktiver Brownscher Teilchen. Durch eine geeignete Erweiterung dieses Modenkopplungsansatzes zielt diese Arbeit darauf ab, Nichtgleichgewichts-Transportkoeffizienten in dichten Suspensionen aktiver Teilchen in zwei Dimensionen zu untersuchen.

Ausgehend von einer mikroskopischen Beschreibung ist die zentrale Größe dieser Arbeit durch die transiente Korrelationsfunktion zweier winkelaufgelöster mikroskopischer Dichten in Mischungen aktiver und passiver Teilchen gegeben, deren Approximation im Rahmen der Modenkopplungstheorie das erste Ziel darstellt. Basierend auf den resultierenden Gleichungen werden weitere Modenkopplungsansätze zur Vorhersage der transienten Dynamik und der mittleren quadratischen Verschiebung aktiver oder passiver Tracerteilchen sowohl in aktiven als auch in passiven dichten Umgebungen hergeleitet. Darüber hinaus werden die mit der Modenkopplungstheorie genäherten dynamischen Korrelationsfunktionen zur Approximation von Green-Kubo-artigen Ausdrücken weiterer Transportkoeffizienten, wie der Viskosität und der effektive Schwimmgeschwindigkeit, welche sich im Rahmen des „integration-through-transients“ Formalismus herleiten lassen, ausgenutzt.

Ein zentraler Bestandteil der vorliegenden Arbeit ist ein Test der Modenkopplungstheorie für aktive Brownsche Teilchen gegenüber Ergebnissen aus einer eventgetriebenen Simulation aktiver Brownscher Scheiben. Die Ergebnisse beider Methoden zeigen weitgehend qualitative, und in einigen Fällen nahezu quantitativ konsistente Ergebnisse. Dies liefert einen wichtigen Beitrag zur Beurteilung der Anwendbarkeit der Theorie und der allgemeinen Qualität der verwendeten Näherungen. Darüber hinaus führt die Verwendung zweier unabhängigen Methoden zu einem tieferen Verständnis der universellen Eigenschaften des aktiven Transports bei hohen Dichten, die bisher kaum untersucht wurden. Ein grundlegendes Prinzip ergibt sich hierbei aus dem Vorliegen konkurrierender Längenskalen, die durch die Käfiglänge des Volumenausschlusses und die Persistenzlänge der aktiven Fortbewegung gegeben sind. Dieses Prinzip hat bei den meisten bisherigen Ansätzen für Modellsysteme aktiver Teilchen eine untergeordnete Rolle gespielt, da diese sich hauptsächlich auf verdünnte Systeme oder Systeme mittlerer Dichten bezogen, ist aber bei hohen Dichten von entscheidender Bedeutung.

Die Methoden dieser Arbeit werden weiterhin eingesetzt, um aktuelle experimentelle Ergebnisse aus einem Aufbau mit diffusiophoretischen aktiven Janus-Teilchen in einer binären kolloidalen Mischung nahe dem Glasübergangspunkt zu bewerten. In einem letzten Teil dieser Arbeit werden Mischeffekte in monodispersen Systemen aus aktiven und passiven Teilchen im Hinblick auf die Einflüsse der Zusammensetzung und der Stärke der Aktivität der Komponenten auf die Dynamik und den Glasübergang diskutiert. Die Ergebnisse weisen die Möglichkeit auf, die Viskosität von Proben durch Dotierung mit aktiven Teilchen gezielt zu beeinflussen.

List of Publications

The following publications are based on the results of this work:

- J. Reichert, L. F. Granz, Th. Voigtmann · Transport Coefficients in Dense Active Brownian Particle Systems: Mode-Coupling Theory and Simulation Results
  under review for European Physical Journal E
- J. Reichert, Th. Voigtmann · Tracer Dynamics in Crowded Active-Particle Suspensions
  Preprint: arXiv:2010.13769
- J. Reichert, Th. Voigtmann · Mode-Coupling Theory for Tagged-Particle Motion of Active Brownian Particles
  Preprint: arXiv:2010.13763

List of Acronyms

MCT Mode-coupling theory

ABP Active Brownian particle

FDT Fluctuation-dissipation theorem

ITT Integration-through-transients

MIPS Motility-induced phase separation

ISF Intermediate scattering function $S^{\alpha,\beta}_{l,l'}(\vec{q},t)$

SISF Self-intermediate scattering function $S^{s}_{l,l'}(\vec{q})$

MSD Mean-squared displacement $\delta r^2(t)$

BD Brownian dynamics

Contents

1. Introduction

Today's studies estimate the number of microbial species on earth to be about one trillion, of which only a very tiny fraction have been discovered at all [1]. Arguably, one of the key achievements that have contributed to the development of such rich biodiversity is the fact that first microorganisms were able to develop forms of directional locomotion, sophisticated navigation strategies and organize themselves collectively into swarms. These processes greatly enhanced their survival and replication capabilities and can be regarded as game-changers in the development of complex life and evolution. Conceptually, such microorganisms fall into the general class of so-called active matter, which refers to (not necessarily living) systems that dissipate energy to perform complex tasks. The research on active matter constitutes a fascinating field which has received increasing interest in recent year and has created a growing interdisciplinary research community with many bridges between various scientific disciplines such as biology, engineering, chemistry, medicine, biophysics, and others.

With regards to microscopic scales, the investigation of active matter has, in particular, experienced keen interest in the research of living or artificial systems, that exploit a self-propulsion mechanism to move through a liquid, so-called microswimmers [2]. These usually evolve in the hydrodynamic regime of low Reynolds numbers, where viscous forces are predominant over inertia. For such systems, the underlying physical laws of the swimming behaviour are governed by the Stokes equation, which implies the celebrated Scallop Theorem [3,4]. It states that an effective swimming motion is only achieved for such mechanisms, which are distinguishable under time reversal. Microswimmers like bacteria, algae or sperm achieve motility by breaking this time reversibility through non-reciprocal flagellated motion [5, 6], mostly associated with purposeful exploitations of the hydrodynamic interactions with their environment that is mediated by the surrounding fluid [7–9].

Inspired by the research on microswimmers in recent decades, it has been achieved with great success to craft micron-sized objects which exploit artificially stimulated swimming mechanisms by dissipating externally supplied energy, e.g. in form of heat absorption through laser light or by the consumption of "fuel" provided by the surrounding medium. The most common examples include diffusiophoretic colloidal Janus particles in a water-lutidine mixture [10], chemically active particles [11, 12], thermophoretic swimmers [13] or magnetically active particles [14] among many others [15]. Artificial systems of microswimmers make it feasible to externally control the

self-propulsion mechanism which makes them greatly advantageous for experimental investigations of active particles. Moreover, the design of artificial microswimmers can be inspired by their natural counterparts. Chlamydomonas algae couple their swimming behaviour to lighting conditions to optimize photosynthesis [16] and a similar mechanism is found for sperms that reach the egg cell by adapting their swimming behaviour to follow messenger elements [17]. Such guided motions towards chemical gradients (chemotaxis [18]), light (phototaxis [19]), or gravitational fields (gravitaxis [20]) are only a few examples which emphasize the rich phenomenology of active transport. Studying and adapting such strategies to artificially designed microswimmers provides novel access to optimize transport strategies in complex environments with a vast application spectrum in biology or medicine: Today, micro-robotic devices are already being designed to perform complex tasks such as drug delivery [21] or artificial fertilization [22].

From the point of view of theoretical physics active particles represent ideal showcases of systems that are intrinsically out of equilibrium. The implying non-equilibrium features (like the lack of detailed balance) interplay with novel types of interactions. This has revealed anomalous phenomena and intriguing collective behaviours in active particle systems that would have been impossible for systems in thermodynamic equilibrium. Examples include the clustering behaviour of purely repulsively interacting self-propelled particles at intermediate densities, referred to as motility-induced phase separation (MIPS) [23–27] or the presence of active pressures in systems of active anisotropic particles that lack an equation of state and depend on the microscopic details of the interaction with the container [27, 28]. Studying such phenomena on a theoretical level requires the adoption of coarse-grained models that greatly reduce the enormous number of degrees of freedom that are present in many-body systems of active particles. Simultaneously these models must include the paradigmatic features of persistent locomotion and the interactions both between particles and the solvent. A fundamental model that is capable to do so is that of the active Brownian particle (ABP), which combines the features of translational and rotational Brownian motion with a body-fixed self-propulsion force (but neglects hydrodynamic interactions). The ABP model can additionally be supplemented with two-body-type interactions such as a hard-core potential, but also by phenomenologically inspired many-particle-types of interactions that describe aligning effects [29] or quorum sensing [30]. Even such minimalistic models are capable to reproduce generic features of active particles seen in in experiments, which is why the ABP model has become popular to theoretically investigate active matter in recent years.

Although the ABP model has been extensively studied on the single-particle level as well in the regime of low and moderate densities, theoretical approaches and investigations that address the regime of high densities are still rare. Filling this gap is most desirable to obtain a better fundamental understanding of the physical mechanisms that are present in crowded active matter and that are highly relevant for many biological systems, be it the dynamics of the cytoskeleton or that of cell migration, whose understanding is of great importance in the context of morphogenesis, including the underlying mechanisms of tumour development. [31–36]. These examples of crowded active matter have in common to reveal signs of dynamical arrest which means that they have relaxation times that can exceed typical microscopical time scales

by several orders of magnitude. This is similarly known for glass-forming systems that appear both on atomistic scales in the context of supercooled liquids as well as on micron scales in dense colloidal suspensions.

A well-established theoretical approach that is capable to make predictions for the slow dynamics associated with the glass formation is the mode-coupling theory of the glass transition (MCT) [37]. MCT predicts an idealized fluid-glass transition singularity point from the equilibrium static structure factor and has been successfully applied in various contexts, including colloidal mixtures [38], granular matter [39], particles in porous media [40], confined fluids [41] or colloids in external flows [42]. The underlying physical principle that describes the glass formation can be understood in a simple picture of particle cages that form at high densities and are also present in dense active particle systems. This has established the concept of active glasses [43] and has encouraged to develop different mode-coupling approaches for model systems of active particles [44–47]. These theories have provided a better understanding of the interplay of dynamical arrest and activity and have revealed that glasses are indeed sustainable under active forces that act on the individual particle level. This was debated in the first place because colloids which are collectively driven by external flows are known not to be able to form glasses, as any arbitrary small global stress contribution is able to break the cage structure in finite time.

The following work focuses on the MCT approach developed by Liluashvili et al. [47] to describe dynamical density correlation functions of hard-core repulsive spherical ABPs in 2D at high densities (ABP-MCT in the following), which has been successfully applied to predict the shift of the glass transition point to higher densities that is associated with an activity. Still, there remain further promising application fields of the theory: It is a major strength of MCT, that it bases on a microscopic description of the system, thus it provides access to describe microscopic phenomena, such as the self-diffusion of tracer particles. On the other hand, the so-called integration-through-transients (ITT) formalism [48] constitutes the theoretical framework to relate the microscopic transient dynamics predicted by the ABP-MCT to non-equilibrium transport coefficients by applying a projection operator technique that allows deriving MCT-approximated Green-Kubo-type expressions. Therewith the first goal of this work is described, that is to provide the theoretical framework to describe non-equilibrium transport phenomena in crowded active particle suspensions within the ABP-MCT. To do so, this work will restrict to a 2D model of ABPs, which allows to considerably simplify the calculations while still preserving the qualitative outcomes of a 3D model, since the predictions of MCT are known to be insensitive on the spacial dimension. Besides that, many experimental studies of active particles, including those referred to in this work, refer to systems whose motion is limited in one dimension, e.g. caused by sedimentation or by the dimensions of the sample cell, and can therefore be considered as quasi-2D.

With respect to the classical MCT for non-active particles, a large number of contributions exist which confirm its (semi-)quantitative predictive power both in form of comparisons with simulations [49–52] and experiments [53–55]. So far, it it unknown if this predictability similarly holds for the ABP-MCT since the correlation functions it provides are of transient-type. This means that they describe the quenched dynamics from an equilibrated state after switching on

activity, that is obtained by performing statistical averages taken in the equilibrium ensemble while evolving with the full non-equilibrium dynamics. Most simulations or experiments of active particles, however, relate to steady-state-type statistics that are far easier to sample and it is not clear if there arise strong qualitative towards a transient-type of statistics. This constitutes a further main objective of this work to test the ABP-MCT predictions in terms of an in-depth comparative study with the results from an event-driven simulation of active Brownian hard-disks. Moreover, this allows exploring the characteristic properties of active transport phenomena at high densities by two independent methods.

The present work consists of seven chapters whose outline is given as follows. Chapter 2 presents the model system of ABPs and introduces further required theoretical concepts from statistical physics, including that of transient correlation functions that form the cornerstone of the ABP-MCT. Chapter 3 starts with a phenomenological description of the glass transition and summarizes the achievements of previous MCTs. Subsequently, a special perspective on approaches for systems far from equilibrium will be given and the major result of the ABP-MCT so far will be summarized. This will be followed by a generalization of the ABP-MCT to arbitrary mixtures of active and passive particles. The resulting equations are further exploited to describe the tagged particle motions of active and passive particles in both active and passive crowded environments. The resulting mode-coupling equations are subsequently analyzed in the hydrodynamic limit to obtain an equation of motion for the mean-squared displacement (MSD). The ABP-MCT approximated correlation functions are further employed for the calculation of the shear viscosity and the effective swimming velocity. Chapter 4 will introduce the methodology of an event-driven simulation of active Brownian hard-disks and the simulation results will subsequently be compared with the predictions from the ABP-MCT for the self-intermediate scattering function and further transport coefficients of active and passive tracer particles both in active and passive environments. Chapter 5 will refer to some recent experimental results of active Janus particles in passive colloidal suspension close to dynamical arrest. In chapter 6 the predictions of the ABP-MCT are discussed with respect to the composition change in monodisperse mixtures of active and passive particles. Finally chapter 7 summarizes the major achievements of this work and points out further perspectives of the theory.

2. Active Brownian Particles

2.1 Model Description

Active Brownian particles (ABPs) provide a fundamental description of persistent locomotion motion under the neglection of hydrodynamic interactions. Besides undergoing overdamped Brownian diffusion described by the translational diffusion coefficient D_t, ABPs experience a constant self-propulsion force that translates into a constant self-propulsion velocity v_0 along a body-fixed orientation vector $\vec{o}_i(\theta_i)$. This vector underlies diffusive rotational dynamics with a rotational diffusion coefficient D_r. In terms of an overdamped Langevin equation in 2D the equations of motion of the position $\vec{r}_i$ and orientation θ_i of the i-th particles, where $i = 1, ...N$, read

$$\begin{aligned} d\vec{r}_i &= \mu\vec{F}_i dt + \sqrt{2D_t}d\vec{W}_i + v_0\vec{o}_i(\theta_i)dt, \\ d\theta_i &= \sqrt{2D_r}dW_{\theta_i}, \end{aligned} \tag{2.1.1}$$

where $\vec{W}_i$ and W_{θ_i} each denote independent realisations of a Wiener process with white noise properties. It is further assumed that there is no zero surface friction or any interaction that acts on the rotational degrees of freedom, e.g., aligning interactions often observed for microswimmers, which means that the orientation vector $\vec{o}_i(\theta_i) = (\cos\theta_i, \sin\theta_i)^T$ is purely evolving through rotational diffusion. To model volume exclusion between the particles, a hard-core interaction potential is assumed given by

$$u_{i,j}(|\vec{r}_i - \vec{r}_j|) = \begin{cases} \infty, & \text{if} \quad |\vec{r}_i - \vec{r}_j| < \sigma, \\ 0, & \text{else}, \end{cases} \tag{2.1.2}$$

with the particle diameter σ and $\vec{F}_i = -\vec{\nabla}_i \sum_{j\neq i} u_{i,j}$ denoting the force acting on particle i. Since microswimmers evolve in a low-Reynolds number regime where viscous damping is predominant over inertia effects, an overdamped dynamics is a reasonable assumption and the interaction force $\vec{F}_i$ leads to an instantaneous drift velocity proportional to the mobility μ that obeys the fluctuation-dissipation theorem (FDT) $\mu = D_t\beta$ with $\beta = 1/(k_bT)$. Note that according to the FDT D_r and D_t do not represent independent parameters. In 3D the FDT predicts $D_r = 3D_t/\sigma^2$, while finding a similar relation in 2D is in general not possible since D_t becomes unbounded due to hydrodynamic tails in the velocity-autocorrelation function [56]. On the

other hand, for many microswimmers, the rotational dynamics is governed by mechanisms that are not dominated by thermal fluctuations, like for E.coli bacteria, who erratically change their orientation by rotating flagella bundles which leads to a run-and-tumble like motion [57]. This motivates to treat D_r as an independent parameter that accounts for an inverse time scale of a persistent locomotion.

Despite the simplicity of the ABP model, it is capable to explain many generic features of self-propelled particles, like tendencies to wall accumulations [58] or the formation of clusters in repulsively interacting collections of active particles [59]. The feasibility of reproducing such effects is demonstrated in figure 2.1.2 where snapshots from a simulation of purely repulsively interacting ABPs are presented. The particles are confined in the x-direction by a soft wall-potential and there apply periodic boundary conditions in the y-direction. With increasing activity, there emerges both a strong accumulation of particles at the two enclosing walls and the formation of clusters between the walls. Both phenomena are typical features seen in interacting self-propelled particles, which have already been reported in different experimental setups and are successfully reproduced by a simple model of interacting ABPs.

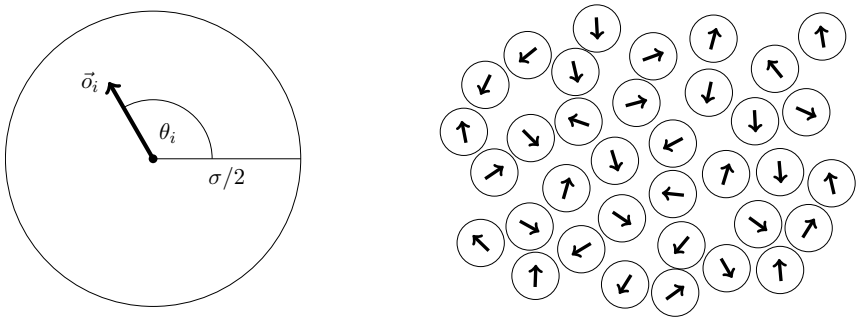

Figure 2.1.1.: *Schematic sketch of the ABP model. The left figure shows a single ABP with diameter σ and an orientation vector $\vec{o}_i(\theta_i)$. The right figure shows a collection of active Brownian hard-disks.*

It is convenient to choose fundamental basic units for lengths and times, which is sufficient to express all remaining model parameters in terms of these basic units. Therefore lengths will be expressed in units of the hard-core diameter σ and times in units of the translational diffusive time scale $t_0 = \sigma^2/D_t$ in the following. The resulting model parameters for experimental realizations of microswimmers shall be emphasized for some specific examples: Despite the enormous diversity of living organisms, the universality of the physical laws that govern their motion leads to the observation that 1-10 body lengths per second provide a reasonable estimate for the maximum speed of any organism regardless of its size [60]. Assuming a microswimmer with a dimension of about 1 µm and a diffusion time scale in an aqueous solution of 1 s means that $v_0\sigma/D_t \sim 1-10$, that is the parameter regime primarily addressed in this work. The diffusive time scale simultaneously provides an estimate for the rotational diffusion coefficient of $D_r\sigma^2/D_t \sim 1$ by exploiting the connection between D_t and D_r. These estimates might, however, differ significantly for artificial microswimmers, as for laser-driven Janus particles the self-propulsion velocity can reach magnitudes in the order of $v_0\,\sigma/D_t \sim 100$ [15].

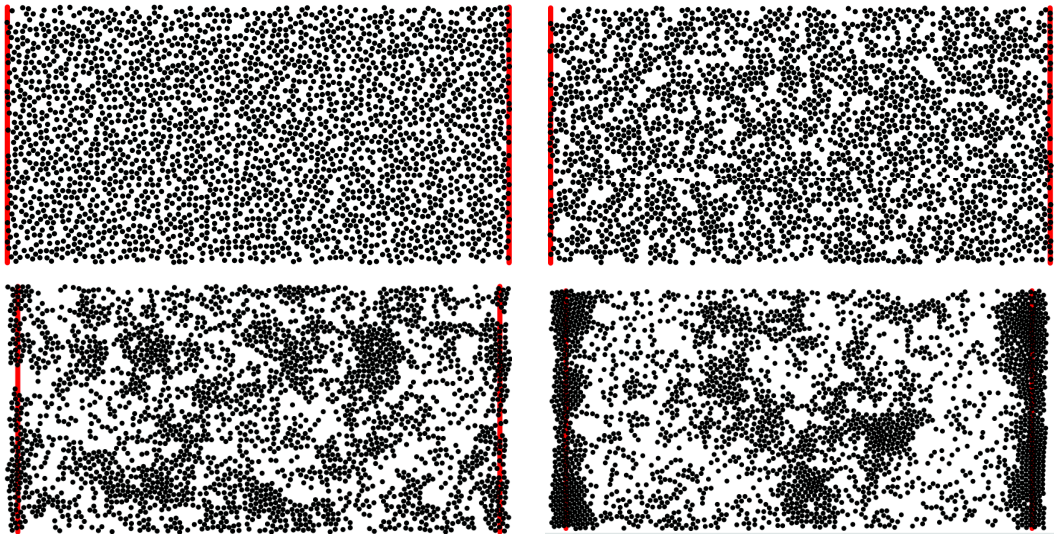

Figure 2.1.2.: *Simulation snapshots at equal times of ABPs interacting via a repulsive Weeks-Chandler-Andersen potential for varying activites (increasing form top left to bottom right). The particles are confined by a soft wall-potential in the x-direction (indicated in red) and periodic boundary conditions apply in the y-direction [61].*

Besides ABPs, there exist numerous further computational models to study active matter. Pionering work in that context has been carried out by Wiczek in the development of the Vicsek Model that has, as one of the first computational models for active matter, successfully reproduced the swarm behaviour of living systems and explained flocking phenomena [62]. An ABP related model is that of the run-and-tumble particle, with a rotational dynamics that changes unsteadily in tumble events instead of continuous diffusion. Differences and analogies between both models have already been widely discussed [63]. Rather than describing activity with an orientation vector that undergoes Brownian diffusion, so-called active Ornstein-Uhlenbeck particles enter activity through a Gaussian-noise term with a finite persistence time described by an Ornstein-Uhlenbeck process [64]. Beyond these rather simple models, there exists an enormous number of further theoretical and computational models [69] that are suitable for the description of complex active systems and greatly reduce the enormous number of their degrees of freedom. These models find wide application in the field of biophysics and particularly include descriptions of active gels and filaments [65], molecular motors [66], cell dynamics [67] and tissue growth [68] among many others [69].

2.2 Exact Solutions

Equation (2.1.1) is a stochastic differential equation which describes the evolution of trajectories under single realisations of the white noise terms. Following the theory of Ito-calculus [70] it can be translated into an equivalent equation of motion for the noise-averaged conditional probability distribution $p(\Gamma, t|\Gamma_0, t_0)$ of the combined N-particle phase space $\Gamma = (\Gamma_{\vec{r}}, \Gamma_\theta)$ at time t under the condition that the system was prepared in the phase space configuration $\Gamma_0 = (\Gamma_{\vec{r}_0}, \Gamma_{\theta_0})$ at $t = t_0$. The time evolution of $p(\Gamma, t|\Gamma_0, t_0)$ is governed by the so called

Smoluchowski equation

$$\partial_t p(\Gamma, t|\Gamma_0, t_0) = \mathbf{\Omega}(\Gamma) p(\Gamma, t|\Gamma_0, t_0), \tag{2.2.1}$$

$$\mathbf{\Omega}(\Gamma) = \sum_{i=1}^{N} D_t \vec{\nabla}_i \left(\vec{\nabla}_i - \beta \vec{F}_i \right) + D_r \partial_{\theta_i}^2 - v_0 \vec{\nabla}_i \cdot \vec{o}_i, \tag{2.2.2}$$

with the initial condition $p(\Gamma, t_0|\Gamma_0, t_0) = \delta(\Gamma - \Gamma_0)$ and the Smoluchowski operator $\mathbf{\Omega}$, which consists of an equilibrium part describing Brownian diffusion and the particle-particle interactions, and a non-equilibrium part that accounts for activity, thus it is convenient to write $\mathbf{\Omega} = \mathbf{\Omega}_{\text{eq}} + \delta\mathbf{\Omega}$ with $\delta\mathbf{\Omega} = -\sum_i v_0 \vec{\nabla}_i \cdot \vec{o}_i$. Defining the translational and rotational probability currents $\vec{j}_{t,i} := D_t \left(\vec{\nabla}_i - \beta \vec{F}_i \right) - v_0 \vec{o}_i$ and $j_{r,i} = D_r \partial_{\theta_i}$, the differential equation for $p(\Gamma, t|\Gamma_0, t_0)$ can be expressed equivalently as a continuity equation:

$$\partial_t p(\Gamma, t|\Gamma_0, t_0) = \sum_i (\vec{\nabla}_i \vec{j}_{t,i} + \partial_{\theta_i} j_{r,i}) p(\Gamma, t|\Gamma_0, t_0). \tag{2.2.3}$$

Integrating out the translational degrees of freedom and dropping the surface terms of the translational probability current, the conditional distribution of the orientations $p(\Gamma_\theta, t|\Gamma_{\theta_0}, t_0) = \int d\Gamma_{\vec{r}}\, d\Gamma_{\vec{r}_0} p(\Gamma, t|\Gamma_0, t_0)$ fulfills the differential equation

$$\partial_t p(\Gamma_\theta, t|\Gamma_{\theta_0}, t_0) = D_r \sum_i \partial_{\theta_i}^2 \, p(\Gamma_\theta, t|\Gamma_{\theta_0}, t_0). \tag{2.2.4}$$

This is nothing but a diffusion equation which can be factorized into the independent solution for the rotational degrees of freedom of each particle, meaning that the solution can be developed on a single-particle level. The resulting probability distribution of the orientation θ of single particle is given by the well-known solution of a Wiener process

$$p(\theta, t|\theta_0, t_0) = \frac{1}{\sqrt{4\pi D_r (t - t_0)}} \exp\left(-\frac{(\theta - \theta_0)^2}{4 D_r (t - t_0)} \right). \tag{2.2.5}$$

One further defines the joint-probability distribution $p(\theta, t, \theta_0, t_0) = (2\pi)^{-1} p(\theta, t|\theta_0, t_0)$ of having the orientation angle evolved from θ_0 at t_0 to θ at t by following the assumption of equally distributed inital orientations. This allows to perform an exact calculation of the autocorrelation-function of the orientation vector of a spherical ABP defined as

$$\langle \vec{o}(\theta(t)) \cdot \vec{o}(\theta_0(t_0)) \rangle := \int d\theta \int d\theta_0 \, p(\theta, t, \theta_0, t_0) \, \vec{o}(\theta(t)) \cdot \vec{o}(\theta_0(t_0)) = e^{-D_r \Delta t}. \tag{2.2.6}$$

As one expects from a Markovian-process, the dependence is only on the time difference $\Delta t = t - t_0$ and the result yields a characteristic correlation time, often denoted as the so-called persistence time $\tau_r := D_r^{-1}$, which indicates a typical time scale it takes to randomize the orientation vector from an initial configuration. It translates into an associated length scale, the persistence length $l_p := v_0 \tau_r$, that indicates the distance which the particle covers balistically during this time scale on average.

2.2.1 Free Particle

For non-interacting systems, the noise- and ensemble averaged motion of a single ABP can be characterized even more precisely. For brevity let $t_0 = 0$ and $\vec{r}_i(0) = 0$ in the following. The calculation of the mean displacements proceeds by integrating the equation of motion for $\vec{r}_i(t)$ (2.1.1) in time and exploiting $\langle d\vec{W}_i \rangle = 0$ which yields

$$\langle \vec{r}(t) \rangle = v_0 \int d\theta \int d\theta_0 \int_0^t dt' p(\theta, t', \theta_0, 0) \vec{o}\,(\theta(t')) = 0, \tag{2.2.7}$$

which is an expected result since there is no favorable orientation of the ABP. In a similar fashion, the mean-squared displacement can be written as [71]

$$\begin{aligned} \langle \vec{r}^{\,2}(t) \rangle = 2D_t \int_0^t dt' \int_0^t dt'' \Big\langle d\vec{W}(t') d\vec{W}(t'') \Big\rangle \\ + v_0^2 \int_0^t dt_1 \int_0^{t_1} dt_2 \int d\theta_0 \int d\theta_1 \int d\theta_2\, \vec{o}\,(\theta_1(t_1)) \cdot \vec{o}\,(\theta_2(t_2))\, p(\theta_1, t_1, \theta_2, t_2) \\ + v_0^2 \int_0^t dt_1 \int_{t_1}^t dt_2 \int d\theta_0 \int d\theta_1 \int d\theta_2\, \vec{o}\,(\theta_1(t_1)) \cdot \vec{o}\,(\theta_2(t_2))\, p(\theta_2, t_2, \theta_1, t_1). \end{aligned} \tag{2.2.8}$$

Rewriting the joint-probability $p(\theta_2, t_2, \theta_1, t_1)$ as

$$p(\theta_2, t_2, \theta_1, t_1) = \frac{1}{2\pi}\, p(\theta_2, t_2 | \theta_1, t_1)\, p(\theta_1, t_1 | \theta_0, 0), \quad t_2 > t_1 \tag{2.2.9}$$

allows to derive the following expression after carrying out the integration

$$\langle \vec{r}^{\,2}(t) \rangle := \delta r^2(t) = 4D_t t \left[1 + Pe \left(1 + \frac{e^{-D_r t} - 1}{D_r t} \right) \right], \tag{2.2.10}$$

where the Péclet number was introduced as $Pe := v_0^2/(2D_r D_t)$. When considering this exact solution for $\delta r^2(t)$ in the different temporal regimes $t \ll \tau_r$ and $t \gg \tau_r$, the different states of motion of the free ABP can be analyzed more precisely by using a Taylor expansion up to the second-order. This yields crossover times for the characteristic stages of motion that are given by

$$\tau_\nu := \frac{2}{D_r Pe}, \qquad l_\nu = \sqrt{\delta r^2(\tau_\nu)/4} = \frac{2D_t}{v_0}, \tag{2.2.11}$$

$$\tau_l := \frac{2}{D_r} \left(1 + \frac{1}{Pe} \right), \qquad l_l := \sqrt{\delta r^2(\tau_l)/4} = \frac{2D_t}{v_0} + \frac{v_0}{D_r} = l_\nu + l_p, \tag{2.2.12}$$

where the crossover times have been associated to corresponding length scales. Figure 2.2.1 depicts a schematic representation of $\delta r^2(t)$ as well as the derived crossover length- and time scales. For $t \ll \tau_\nu$, the MSD of the free ABP shows the same Brownian short-time diffusion as seen for a passive particle until the crossover length scale l_ν before switching to a ballistic regime for $\tau_\nu \ll t \ll \tau_l$ on length scales $l_\nu \ll l \ll l_l$. Finally the MSD is characterized by an enhanced long-time diffusive behaviour at times $t \gg \tau_l$ with an effective diffusion coefficient $D_{\text{eff}} = D_t\,(1 + Pe)$. Knowing these transition points between the different states of motion is

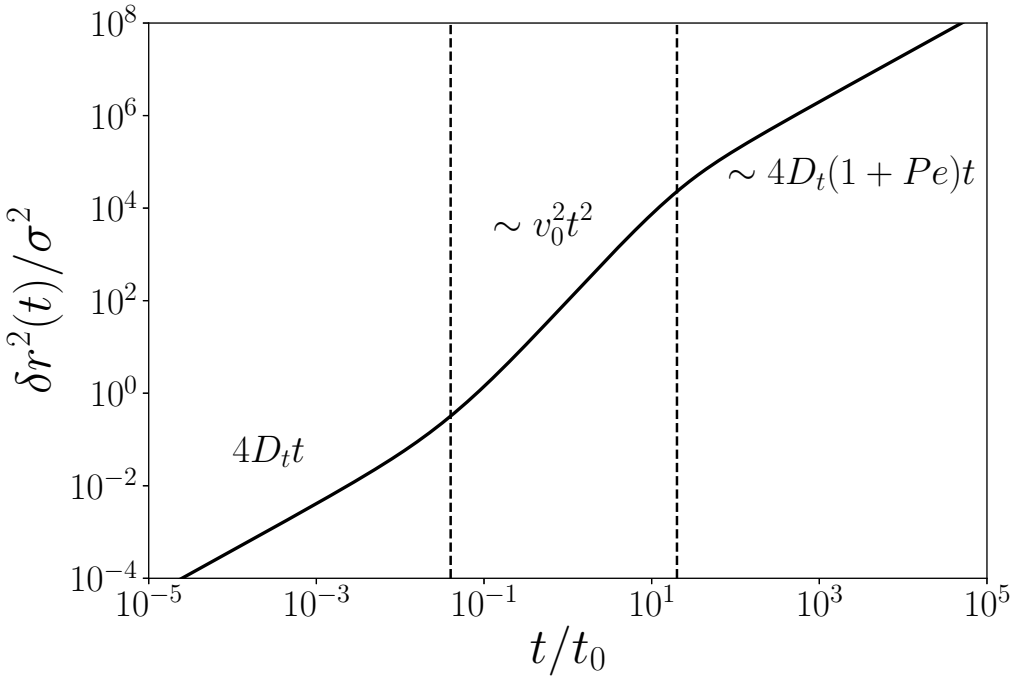

Figure 2.2.1.: *Schematic sketch of the mean-squared displacement $\delta r^2(t)$ of a free ABP. The dashed lines represent the crossover time scales τ_ν and τ_l.*

of fundamental importance to understand active motion in the case when additional competing length scales emerge. If these length scales are large compared to l_l, it constitutes a promising strategy to map the ABP to a passive Brownian particle with an effective diffusion constant. The reliability of this approach can be verified experimentally in low-density systems of ABPs, e.g. in systems with sedimenting active Janus particles [72]. If the sedimentation length of the particles becomes much larger then their persistence length, the height distribution is well described by a Boltzmann distribution $\rho(h) \sim e^{-mg\,h/k_bT_{\text{eff}}}$ with an effective temperature $k_bT_{\text{eff}} = D_{\text{eff}}/\mu$. On the other hand, such a distribution profile is not observed if the persistence length exceeds the sedimentation length. When describing active transport phenomena in combination with volume exclusion effects, an additional length in the form of the cageing length emerges, which is easily exceeded by typical persistence lengths of microswimmers. This makes the simple-minded approach of an effective diffusion highly unreliable at high densities as will be seen later.

Despite its simplicity, the model of non-interacting ABPs still remains subject to current publications. Very recently interesting connections between equilibrium polymer models and the ABP model have been shown. Notably, the probability distribution for the end-to-end distribution of the worm-like-chain model of semi-flexible polymers, which has been investigated back in 1952 [73] long before the ABP model, obeys the same Smoluchowski equation as the free ABP under the absence of thermal noise. Shee et al. have demonstrated in [74] that it is possible to construct a polymer model that yields an exact mapping to an ABP with thermal noise and have exploited that mapping to derive exact expressions of all moments of the ABP in arbitrary dimensions.

2.3 Transient Correlation Functions

In the following, an observable $A(\Gamma)$ for a given phase-space configuration Γ at time t is considered. Before switching on activity for $t > 0$, the system is prepared in an equilibrium state Γ_0 at $t_0 = 0$ according to the equilibrium Boltzmann distribution $p_{\mathrm{eq}}(\Gamma_0) \sim e^{-\beta U(\Gamma_0)}$ which implies the joint-probability distribution of the full phase space to obey $p(\Gamma, t, \Gamma_0, 0) = p(\Gamma, t|\Gamma_0, 0)\, p_{\mathrm{eq}}(\Gamma_0)$. According to (2.2.1) a formal solution for $p(\Gamma, t, \Gamma_0, 0)$ is then given by

$$p(\Gamma, t, \Gamma_0, 0) = e^{\mathbf{\Omega} t}\delta(\Gamma - \Gamma_0)\, p_{\mathrm{eq}}(\Gamma_0). \tag{2.3.1}$$

Now one defines the transient ensemble average of $\langle A\rangle^{v_0}(t)$ as follows

$$\langle A(t)\rangle^{v_0} := \int d\Gamma \int d\Gamma_0\, A(\Gamma) p(\Gamma, t, \Gamma_0, 0) = \int d\Gamma p_{\mathrm{eq}}(\Gamma) e^{\mathbf{\Omega}^\dagger t} A(\Gamma) = \langle e^{\mathbf{\Omega}^\dagger t} A(\Gamma)\rangle, \tag{2.3.2}$$

with $\langle ...\rangle$ denoting the equilibrium weighted scalar product. Further, the adjoint Smoluchwoski operator $\mathbf{\Omega}^\dagger$ was introduced, which definition follows from the unweighted scalarproduct of the phase space integration. Given two observables O and O' there holds $\int d\Gamma O \mathbf{\Omega} O' = \int d\Gamma O' \mathbf{\Omega}^\dagger O$. In the case of the ABP Smoluchowski operator, $\mathbf{\Omega}^\dagger$ can be derived by integrating by parts twice resulting in

$$\mathbf{\Omega}^\dagger(\Gamma) = \sum_{i=1}^{N} D_t \left(\vec{\nabla}_i + \beta \vec{F}_i\right) \vec{\nabla}_i + D_r \partial_{\theta_i}^2 + v_0 \vec{o}_i \cdot \vec{\nabla}_i. \tag{2.3.3}$$

The transient ensemble average describes the quenched dynamics from an equilibrated state when activity is suddenly switched on. Since the evolution of the probability distribution is uniquely fixed by the initial equilibrium distribution and the governing time evolution operator $e^{\mathbf{\Omega}^\dagger t}$, the expression for $\langle A(t)\rangle^{v_0}$ translates into an equilibrium ensemble average. One notes further the analogy to quantum mechanics in the alternation between the Schrödinger and Heisenberg picture as the time evolution has been shifted from the observable to a time evolution operator. An alternate expression for $\langle A(t)\rangle^{v_0}$ results from the operator identity $e^{\mathbf{\Omega} t} = 1 + \int_0^t dt' e^{\mathbf{\Omega} t'} \mathbf{\Omega}$ by writing

$$p(\Gamma, t, \Gamma_0, 0) = e^{\mathbf{\Omega} t}\delta(\Gamma - \Gamma_0)\, p_{\mathrm{eq}}(\Gamma_0) = \left(1 + \int_0^t dt' e^{\mathbf{\Omega} t'} \mathbf{\Omega}\right) \delta(\Gamma - \Gamma_0)\, p_{\mathrm{eq}}(\Gamma_0). \tag{2.3.4}$$

This means that the transient average of A obeys

$$\langle A(t)\rangle^{v_0} = \int d\Gamma_0 \int d\Gamma\ A(\Gamma, t) p(\Gamma, t, \Gamma_0, 0) = \int d\Gamma\, p_{\mathrm{eq}}(\Gamma) A(\Gamma) + \int d\Gamma \int_0^t dt' A(\Gamma) e^{\mathbf{\Omega} t'} \mathbf{\Omega}\, p_{\mathrm{eq}}(\Gamma). \tag{2.3.5}$$

The second term can now be simplified by noting that in equilibrium $\mathbf{\Omega}_{\mathrm{eq}} p_{\mathrm{eq}} = 0$, i.e.,

$$\int d\Gamma \int_0^t dt' A(\Gamma) e^{\mathbf{\Omega} t'} \delta\mathbf{\Omega}\, p_{\mathrm{eq}} = \int d\Gamma \int_0^t dt' (\delta\mathbf{\Omega} p_{\mathrm{eq}}) e^{\mathbf{\Omega}^\dagger t'} A(\Gamma) = \int_0^t dt' \Big\langle \frac{\delta\mathbf{\Omega} p_{\mathrm{eq}}}{p_{\mathrm{eq}}} e^{\mathbf{\Omega}^\dagger t'} A \Big\rangle. \tag{2.3.6}$$

This identity reveals the integration-through-transients (ITT) formula, first proposed by Cates and Fuchs [42] in the context of shear-driven glasses

$$\langle A(t)\rangle^{v_0} = \langle A\rangle + \int_0^t dt' \Big\langle \frac{\delta\mathbf{\Omega} p_{\mathrm{eq}}}{p_{\mathrm{eq}}} e^{\mathbf{\Omega}^\dagger t'} A \Big\rangle. \tag{2.3.7}$$

Its generalization for arbitrary time-dependent pertubations follows straightforwardly by introducing time-ordered exponentials in the formal solution of the Smoluchowski equation, e.g. carried out for colloidal system exposed to time-dependent flows in [75].

The ITT formalism constitutes a powerful tool to account for the change of an observable caused by the modification of the probability distribution due to some perturbation that acts on the system. It remains exact for arbitrary strong drivings and delivers generalized Green-Kubo-type expressions for non-equilibrium transport coefficients. However, it needs to be pointed out that it poses a hopeless endeavour in almost any many-body system to find exact solutions for the correlation function that is involved, i.e., computational schemes become inevitable. Whereas in principle, the correlation function given in the integrand could be sampled from simulations, such an approach usually turns out to be too laborious since the averages that are involved must exclusively be taken over the initially equilibrated state due to the transient nature of the correlation function. In simulations, it is, therefore, more common to use linear-response-approximated ITT expressions by neglecting the perturbation in the time evolution operator $e^{\mathbf{\Omega}^\dagger t'}$ which allows evaluating (2.3.7) from equilibrium simulations. This has proven to deliver satisfactory results for transport coefficients such as the effective swimming velocity [76] or the mobility [77] of ABPs in a regime of for small self-propulsion velocities in low-density systems.

To address parameter regimes that do not fit in the scope of linear response, it is therefore desirable to develop theories that deliver approximate expressions for transient correlation functions. Developing such a theory requires a more generalized formulation of equation (2.3.2). Following the calculations carried out before, the transient correlation function $\langle A(t)B(0)\rangle^{v_0}$ between the equilibrium realization of an observable B at $t = 0$ and that of A at later time t with respect to the time evolution according to the Smoluchowski equation can be expressed as

$$\langle B(0)A(t)\rangle^{v_0} := \int d\Gamma \int d\Gamma_0\, A(\Gamma, t)\, p(\Gamma, t, \Gamma_0, 0) B(\Gamma_0) = \langle B\, e^{\mathbf{\Omega}^\dagger t} A\rangle. \tag{2.3.8}$$

In the next chapter, the mode-coupling theory for active Brownian particles (ABP-MCT) will be presented as a suitable approximation for a specific type of transient correlations between two microscopic densities. With these correlation functions at hand, ITT formulas can be suitably approximated by using a projection operator technique. This combined MCT-ITT approach will result in constitutive equations of non-equilibrium transport coefficients in terms of correlation function that are based on a purely microscopic theory.

3. Mode-Coupling Equations

The mode-coupling theory of the idealized glass transition [37] constitutes a well-established approach to predict the slow structural dynamics in dense glass-forming liquids. Hereby, the term glass comprises amorphous solids which form, e.g., if colloidal suspensions are sufficiently densified under a simultaneous suppression of any thermodynamic phase transitions like crystallization, which is most efficiently achieved by an appropriately chosen size disparity of the constituents. Just as liquids, glassy materials lack a long-range spacial order with the consequence that both materials cannot be distinguished solely from single configurations of each system. However, there exists a transition point that drastically differentiates a glass from a fluid. This so-called glass transition marks the emergence of a dynamical arrested state and small deviations from this (idealized) sharp transition point imply dramatic changes in the structural relaxation time and related macroscopic transport coefficients such as the viscosity or long-time diffusion coefficients. A physical intuitive explanation of the implicated spontaneous arrest at the glass transition is represented by the picture of a particle trapped in a cage, that is formed by immediate neighbouring particles at high densities. Such cages can barely be overcome within the present thermal fluctuations. This means that the system will remain in a non-ergodic state in a period of time that exceeds diffusive time scales by several orders of magnitude. The resulting slow dynamics of glass-forming systems at high densities that is predicted by MCT is experimentally accessible by measuring the dynamical scattering function Φ. This is achieved in dynamical light scattering experiments for colloidal glass-formers or in dynamical neutron-scattering experiments of supercooled liquids, which represent another class of glass-forming systems. Both have in common to reveal the typical two step-behaviour of Φ in the vicinity to the transition point, that is schematically sketched in figure 3.0.1. After a microscopic time scale, the correlation function evolves very close to a plateau value within the so-called β-regime. On the fluid side of the transition, there emerges another relaxation regime describing the ultimate decay of the correlation function on time scales much larger than the typical diffusive time scale which is empirically well-described by the stretched exponential decay of a Kohlrausch-law. This so-called α-regime is not observed on the glass side of the transition where the correlation function remains on the plateau for infinite times. An outstanding achievement of MCT in that context is the quantitative prediction of universal scaling laws for the dynamic correlation functions for these distinctive relaxation regimes close to the glass transition point where asymptotic expansions of the MCT equation provide power-law predictions that are valid on clearly defined time-windows and become increasingly large in the vicinity of

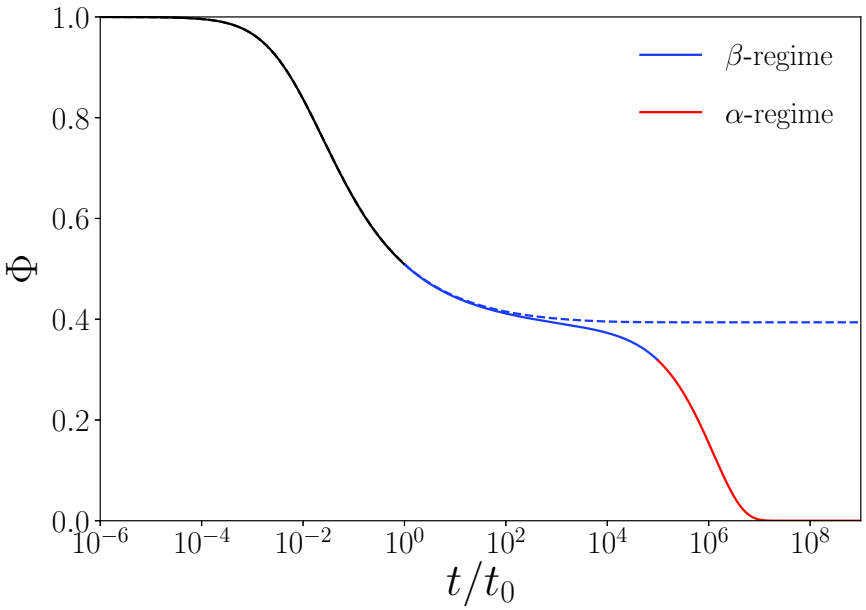

Figure 3.0.1.: *Schematic sketch of the two-step decay of the dynamical scattering function* Φ *close to the glass transition point. The solid line describes the dynamics closely below, the dashed line closely above the MCT glass transition point. The blue colour indicates the regime of the* β*-relaxation process, the red colour that of the* α*-relaxation process.*

the glass transition point [78,79]. These predictions have also been well-confirmed in a variety of experimental setups [53–55] and computer simulations [49, 51].

The fundamental concepts and phenomenological assumptions of dynamical arrest like the caging effect that are incorporated by MCT can in turn also be applied to systems that are far from equilibrium. In these systems, structural relaxation does not mainly stem from thermal fluctuations but is also affected by both external or intrinsic driving forces or energy dissipation. Approaches that fit into that context are, e.g., that by the pioneering work from Fuchs et al. who developed an MCT for systems in a steady flow [48] or that for driven granular systems by Kranz et. al in which energy dissipation caused by inelastic collisions has been considered and successfully adapted to systems with shear-flows. [39, 80].

The increasing interest in active matter in recent years has given rise to attempts to develop MCTs for active particles to investigate the effects of active forces on the structural relaxation and the dynamics close to the glass transition point. A first approach has been worked out by Brader et al. in the framework of an effective diffusion mapping [44]. The outcome of an enhanced structural relaxation concomitant with activity has been predicted by computer simulations before [81], but is expected from an effective diffusion approach as it accounts activity by an effectively enhanced temperature. Moreover, the fundamental assumption of such an approach is conflicting to be applied in an MCT as typical length scales close to the glass transition point are in the order of the caging length l_c for which the Lindemann criterion for melting [82] provides a reasonable estimation through $l_c \sim 0.1\sigma$. This is easily exceeded by typical persistence lengths of microswimmers in experimental setups or simulations as mentioned before.

Szamel et al. have worked out an MCT for athermal active Ornstein-Uhlenbeck particles where translational thermal noise is neglected [45, 46]. Their approach follows the assumption of a separation of time scales for the structural relaxation and the relaxation of the rotational degrees of freedom, allowing to derive an effective time evolution operator. Additionally to the static structure, correlation functions between particle velocities are required as an additional input to the theory which have first to be acquired by computer simulations. The theory of Szamel et al. has revealed a non-monotonic dependence of the relaxation time on the strength of active driving such that depending on the rotational correlation time active forces have shown to be capable to slow down the dynamics. Such a behaviour is not observed in the MCT that will be discussed in this work and might be related to the absence of thermal noise in the approach by Szamel et al.. A further ABP related MCT approach comprises force-driven probe particles in dense suspensions [83]. This theory has revealed that there exists a force threshold which needs to overcome to delocalize driven tracer particle that is immersed in glassy environments. Such a model of a constant force driven tracer particle bears some analogy to the ABP model with vanishing rotational diffusion coefficients, that will be discussed later on.

The theory that this work aims to extend is the ABP-MCT by Liluashvili et al. [47, 84], whose main achievements shall be briefly outlined in the following. The cornerstone of this approach is that it starts from a complete microscopic description of all degrees of freedom of the system, in particular including those of the rotational dynamics that are considered exactly as given by the time evolution of the Smoluchowski equation without any prior assumptions of an effective time evolution operator or effective diffusion preliminaries. This means that the emerging length- and time scales resulting from the persistent motion are taken properly into account which turns out to be of fundamental importance to explain the qualitative outcomes of the theory. ABP-MCT has been successfully applied to predict a fluid-glass transition surface in the three-dimensional parameter space spanned by(ϕ, v_0, D_r), where ϕ denotes the packing fraction of the system. The critical glass transition packing fraction ϕ_c has been found to increase monotonically with the persistence length, that has been reasoned with an enhanced cage breaking ability with increasing persistent driving. However, the glass transition revealed to explicitly depend on both the Péclet number Pe and the persistence length l_p, in contrast to transition diagrams that have been reported for the motility-induced phase separation (MIPS) that occurs in active particle systems with intermediate-densities. This can be explained by the emergence of an additional length scale in systems with high densities represented by the localization length due to cageing. Moreover, the transition diagram determined by Liluashvili et al. has shown strong qualitative similarities with that for the jamming transition of a self-propelled Voronoi model [67], a model to describe the slow dynamics of cell motility in dense tissues.

The present chapter provides a generalization of the ABP-MCT approach to describe the slow dynamics in mixtures of active and passive particles. Hence the structure of the equations and the technical steps to derive the theory are of similar spirit as in [47], but besides some straightforward generalization, various new aspects and extensions will be presented that will provide the theoretical framework for the calculation of non-equilibrium transport coefficients later on.

3.1 ABP-MCT for Mixtures

A r-component mixtures with N_α ABP constituents of type α, where $\alpha = 1...r$, is considered where the concentration of species α shall be denoted as $x_\alpha = N_\alpha/N$ with $\sum_\alpha N_\alpha = N$, and $\{D_t^\alpha, D_r^\alpha, v_0^\alpha\}$ defining the ABP parameter space. Assuming an overdamped dynamics the phase space is completely described by the positions of all particles and a time evolution according to the Smoluchowski equation applies. Within the formalism introduced in the last chapter, the evolution of the phase space distribution is governed by the Smoluchowski operator

$$\mathbf{\Omega} = \sum_{(i,\alpha)} D_t^\alpha \vec{\nabla}_i^\alpha \left(\vec{\nabla}_i^\alpha - \beta \vec{F}_i^\alpha\right) + D_r^\alpha \left(\partial_{\theta_i}^\alpha\right)^2 - v_0^\alpha \vec{\nabla}_i^\alpha \cdot \vec{o}_i^\alpha. \tag{3.1.1}$$

As the time evolution of the rotational degrees of freedom is decoupled from those of translational motion, it will further prove to be convenient to account for this in terms of the splitting $\mathbf{\Omega}(\{D_t^\alpha, D_r^\alpha, v_0^\alpha\}) = \mathbf{\Omega}_T(\{D_t^\alpha, v_0^\alpha\}) + \mathbf{\Omega}_R(\{D_r^\alpha\})$. Starting point of the ABP-MCT is the introduction of a microscopic density $\rho^\alpha(\vec{r}, \theta) = \sum_{j=1}^{N_\alpha} \delta(\vec{r} - \vec{r}_j^\alpha)\delta(\theta - \theta_j^\alpha)$ for both spacial- and rotational coordinates of the N_α-particle phase space of type α. Of central inerest are the angular resolved density fluctuations, defined as the spherical-harmonics expanded Fourier-transformation of such microscopic densities. They read

$$\rho_l^\alpha(\vec{q}) = \frac{1}{\sqrt{N}} \sum_{j=1}^{N_\alpha} e^{i\vec{q}\cdot\vec{r}_j^\alpha} e^{il\theta_j^\alpha}, \quad l = -\Lambda_L ... \Lambda_L, \tag{3.1.2}$$

where the wavevector $\vec{q}$ and the discrete rotational indices l have been introduced with Λ_L denoting some cutoff of the expansion. Ideally, there applies $\Lambda_L \to \infty$, but as for the continuous wavenumber q such a cutoff will be inevitable for numerical considerations. The main objective of the ABP-MCT is the development of an approximate expression for the intermediate scattering function (ISF), defined as the transient correlation function of two angular resolved density fluctuation according to the ITT-based expression of equation (2.3.8). Respectively, the ISF is defined as

$$S_{l,l'}^{\alpha,\beta}(\vec{q}, t) := \left\langle \rho_l^\alpha(\vec{q})^* e^{\Omega^\dagger t} \rho_{l'}^\beta(\vec{q}) \right\rangle. \tag{3.1.3}$$

With $\mathbb{K} = \mathbb{C}^{(2\Lambda_L+1)\times(2\Lambda_L+1)}$, the ISF is a $\mathbb{K}^{r\times r}$ dimensional matrix whose elements provide information both about correlations between translational and rotational degrees of freedom between different species. At $t = 0$ the ISF coincides with the (angle-resolved) equilibrium static structure factor and the matrix elements can be exactly calculated by applying the definition of the equilibrium average, leading to

$$S_{l,l'}^{\alpha,\beta}(q) = \frac{1}{N} \sum_{j=1}^{N_\alpha} \sum_{k=1}^{N_\beta} \int d\Gamma_{\vec{r}}\, p_{\mathrm{eq}} \mathrm{e}^{-i\vec{q}\cdot\left(\vec{r}_j^\alpha - \vec{r}_k^\beta\right)} \int d\Gamma_\theta\, \mathrm{e}^{-i\left(l\theta_j^\alpha - l'\theta_k^\beta\right)} \tag{3.1.4}$$

$$= \delta_{l,0}\delta_{l',0}\left(S^{\alpha\beta}(q) - x_\alpha\delta_{\alpha,\beta}\right) + x_\alpha\delta_{l,l'}\delta_{\alpha,\beta}, \tag{3.1.5}$$

where $S^{\alpha\beta}(q)$ denotes the usual isotropic passive hard-disk structure factor matrix that is linked to the direct correlation functions $c^{\alpha,\beta}(q)$ and the density $\rho = N/V$ via a generalized Ornstein-Zernike equation that reads

$$\left(S^{-1}\right)^{\alpha,\beta}_{l,l'}(q) = \frac{\delta_{l,l'}\delta_{\alpha,\beta}}{x_\alpha} - \rho c^{\alpha,\beta}(q)\delta_{l,0}\delta_{l',0}, \tag{3.1.6}$$

and fulfills $\sum_{l_1,\gamma} S^{\alpha,\gamma}_{l,l_1}(q)\cdot\left(S^{-1}\right)^{\gamma,\beta}_{l_1,l'}(q) = \delta_{l,l'}\delta_{\alpha,\beta}$. Note that contrary to the static structure factor and systems with rotational symmetries the correlation functions that have been introduced here are not invariant under rotations of the wavevector $\vec{q}$. This is because introducing self-propulsion vectors breaks the rotational symmetry even for spherical particles. Nevertheless there holds a straightforward transformation rule that results from the simple behaviour of the system under global rotations. It follows by noting that a rotation of the wavevector by an angle $\delta\varphi$, represented in polar coordinates $\vec{q} = (q, \varphi_q)$, can be expressed equivalently by a global rotation of the system by $\delta\varphi$. This yields the following unitary transformation law for the ISF:

$$S^{\alpha,\beta}_{l,l'}\Big((q, \varphi_q + \delta\varphi), t\Big) = e^{-i(l-l')\delta\varphi} S^{\alpha,\beta}_{l,l'}\Big((q, \varphi_q), t\Big). \tag{3.1.7}$$

This transformation law is advantageous since it reduces the dimensionality of the correlation function parameter space. On the other hand, it reveals a relation between real- and imaginary parts by choosing $\delta\varphi = \pi$ which implies

$$\left(S^{\alpha,\beta}_{l,l'}\right)^*(\vec{q}, t) = (-1)^{(l-l')} S^{\alpha,\beta}_{-l,-l'}(\vec{q}, t). \tag{3.1.8}$$

In particular, this means that $S^{\alpha,\beta}_{0,0}(\vec{q}, t)$ remains real which is no longer trivial in view of the underlying non-equilibrium time evolution, see for example the related correlation function of a constant force driven tracer particle which possesses a non-vanishing imaginary part as a consequence of the fixed direction of pulling [83]. The ABP correlation function remains reals because the active force acts isotropically on all particles. Furthermore, it is explicitly highlighted that the correlation functions defined here are in general not symmetric both under exchanging species and rotational indices as they are their passive counterparts. This immediately follows from the observation that the self-adjointness of the Smoluchowski operator with respect to the Boltzmann-weighted scalar product is no longer fulfilled owing to the active perturbation, which in turn breaks the time-reversal symmetries of the underlying time evolution operator.

A further useful symmetry property of the ISF results from checking, that the global variable transformation $\{r^\gamma_{i,x}, r^\gamma_{i,y}, \theta^\gamma_i\} \to \{r^\gamma_{i,x}, -r^\gamma_{i,y}, -\theta^\gamma_i\}$ keeps both p_{eq} and $\mathbf{\Omega}^\dagger$ unchanged. Choosing $\vec{q} = qe_x$, this implies according to equation (3.1.3) that $S^{\alpha,\beta}_{l,l'}(q\vec{e}_x, t) = S^{\alpha,\beta}_{-l,-l'}(q\vec{e}_x, t)$ and combining this with equation (3.1.8) reveals that $S^{\alpha,\beta}_{l,l'}(q\vec{e}_x, t)$ has a vanishing imaginary- or real part if $|l - l'|$ is chosen either even or odd. This can be generalized to arbitrary φ_q by using the transformation law for rotations of the wavevector, meaning that

$$e^{i(l-l')\varphi_q} S^{\alpha,\beta}_{l,l'}(\vec{q}, t) = e^{-i(l-l')\varphi_q} S^{\alpha,\beta}_{-l,-l'}(\vec{q}, t). \tag{3.1.9}$$

3.1.1 Mori-Zwanzig Formalism

The projection operator formalism developed by Zwanzig and Mori [85] constitutes a standard scheme to obtain an exact equation of motion for the ISF. It follows the idea to express observables in a basis of density functions. Therefore one introduces the projection operator

$$\boldsymbol{\mathcal{P}} = \sum_{\substack{l,l',\vec{q} \\ \alpha\beta}} |\rho_l^\alpha(\vec{q})\rangle \left(S^{-1}\right)_{l,l'}^{\alpha,\beta}(q)\langle\rho_{l'}^\beta(\vec{q})^*|, \qquad \boldsymbol{\mathcal{Q}} = \mathbb{1} - \boldsymbol{\mathcal{P}}, \tag{3.1.10}$$

where the factor $(S^{-1})_{l_1,l_2}^{\alpha,\beta}(q)$ accounts for the projector property of $\boldsymbol{\mathcal{P}}^2 = \boldsymbol{\mathcal{P}}$. Furthermore, a bra-ket notation $\langle A|B\rangle = \langle A\,B\rangle$ for the equilibrium weighted scalar product is introduced. One further introduces the orthogonal projector $\boldsymbol{\mathcal{Q}} := \mathbb{1} - \boldsymbol{\mathcal{P}}$ which trivially fulfills $\boldsymbol{\mathcal{Q}}\boldsymbol{\mathcal{P}} = \boldsymbol{\mathcal{P}}\boldsymbol{\mathcal{Q}} = 0$ and $\boldsymbol{\mathcal{Q}}\rho_l^\alpha(\vec{q})\rangle = 0$. Now one writes

$$\partial_t e^{\boldsymbol{\Omega}^\dagger t} = \boldsymbol{\Omega}^\dagger e^{\boldsymbol{\Omega}^\dagger t} = \boldsymbol{\Omega}^\dagger(\boldsymbol{\mathcal{P}} + \boldsymbol{\mathcal{Q}})e^{\boldsymbol{\Omega}^\dagger(\boldsymbol{\mathcal{P}}+\boldsymbol{\mathcal{Q}})t}, \tag{3.1.11}$$

and Dyson-decomposition formula for propagators is exploited further on. It states [85]

$$e^{\boldsymbol{\Omega}^\dagger(\boldsymbol{\mathcal{P}}+\boldsymbol{\mathcal{Q}})t} = e^{\boldsymbol{\Omega}^\dagger\boldsymbol{\mathcal{Q}}t} + \int_0^t dt' e^{\boldsymbol{\Omega}^\dagger\boldsymbol{\mathcal{Q}}(t-t')}\boldsymbol{\Omega}^\dagger\boldsymbol{\mathcal{P}}e^{\boldsymbol{\Omega}^\dagger t'}. \tag{3.1.12}$$

Inserting this relation into (3.1.11) and multiplying with $|\rho_{l'}^\beta(\vec{q})\rangle$ from the right and $\langle\rho_l^\alpha(\vec{q})^*|$ from the left yields an exact evolution equation for the ISF, denoted as Mori-Zwanzig equation of motion. It can be expressed in a compact matrix notation as

$$\partial_t \boldsymbol{S}(\vec{q},t) = -\boldsymbol{\omega}(\vec{q})\boldsymbol{S}^{-1}(q)\boldsymbol{S}(\vec{q},t) + \int_0^t dt' \boldsymbol{K}(\vec{q},t-t')\boldsymbol{S}^{-1}(q)\boldsymbol{S}(\vec{q},t'). \tag{3.1.13}$$

Here the frequency matrix $\boldsymbol{\omega}(\vec{q})$ was introduced whose entries are defined as the matrix elements of $\boldsymbol{\Omega}^\dagger$. A straightforward calculation yields

$$\omega_{l,l'}^{\alpha,\beta}(\vec{q}) = -\left\langle\rho_l^\alpha(\vec{q})^*\,\boldsymbol{\Omega}^\dagger\rho_{l'}^\beta(\vec{q})\right\rangle = \left(D_r^\alpha l^2 + D_t^\alpha q^2\right)x_\alpha\delta_{l,l'}\delta_{\alpha,\beta} - \frac{iv_0^\beta q}{2}e^{-i(l-l')\varphi_q}S_{l,l}^{\alpha,\beta}(q)\delta_{|l-l'|,1}. \tag{3.1.14}$$

It will be further crucial to distinguish translational- and rotational parts of $\boldsymbol{\omega}(\vec{q})$ such that one writes $\boldsymbol{\omega}(\vec{q}) = \boldsymbol{\omega}_T(\vec{q}) + \boldsymbol{\omega}_R$ with $\boldsymbol{\omega}_R = D_r l^2\,\mathbb{1}$. The quantity appearing in the convolution is denoted as diffusion kernel and is determined by

$$K_{l_1,l_2}^{\alpha,\beta}(\vec{q},t) = \left\langle\rho_{l_1}^\alpha(\vec{q})^*\,\boldsymbol{\Omega}^\dagger\boldsymbol{\mathcal{Q}}\mathrm{e}^{\boldsymbol{\Omega}^\dagger t}\boldsymbol{\mathcal{Q}}\boldsymbol{\Omega}^\dagger\rho_{l_2}^\beta(\vec{q})\right\rangle. \tag{3.1.15}$$

There holds $\boldsymbol{K}(\vec{q},t) = 0$ if the interaction between the particles becomes negligible. This immediately follows from the fact that for a free particle the action of the fluctuating force $\boldsymbol{\mathcal{Q}}\boldsymbol{\Omega}^\dagger$ on a density vanishes since

$$\boldsymbol{\mathcal{Q}}\boldsymbol{\Omega}^\dagger\rho_l^\alpha(\vec{q}) = -(D_t^\alpha q^2 + D_r^\alpha l^2 + iv_0^\alpha\vec{o}_j^\alpha\cdot\vec{q})\boldsymbol{\mathcal{Q}}\rho_l^\alpha(\vec{q}) = 0. \tag{3.1.16}$$

Following similar arguments implies that there arise no contributions to $\boldsymbol{K}(\vec{q},t)$ when inserting the rotational parts of $\boldsymbol{\Omega}^\dagger$ on the left- and right-hand side of the time evolution in the definition of $\boldsymbol{K}(\vec{q},t)$, even in interacting systems. For the right-hand side, this is trivially seen with the same arguments given for the free particle. For the left-hand side, the same argument applies which follows from the observation that $\boldsymbol{\Omega}_R$ is self-adjoint regarding the equilibrium weighted scalar product as it is not affected by activity.

3.1.2 Free Particle Solution

Before extending the theory to interacting systems, the solution of the Mori-Zwanzig equation in the case of a vanishing memory-kernel, describing the motion of a free ABP, shall be investigated in more detail in the following. This case allows to drop indices accounting for particle-types in the following and the structure factor becomes $S_{l,l'}(q) = \delta_{l,l'}$. The formal solution to equation (3.1.13) is then given by the matrix exponential

$$\boldsymbol{S}(\vec{q},t) = e^{-\boldsymbol{\omega}(\vec{q})t}. \tag{3.1.17}$$

The following calculations aim to show that this is indeed an alternative representation of the more commonly known exact solution of the single-ABP ISF that has been presented by Kurzthaler et al. before [86]. Without loss of generality the restriction $\vec{q} = q\vec{e}_x$, shall be assumed further on. The known procedure to solve a matrix exponential equation is to find a diagonalization in terms of a transformation matrix $\boldsymbol{\mathcal{T}}$ and a diagonal matrix $\boldsymbol{\mathcal{D}}$ which fulfil

$$\boldsymbol{\omega} = \boldsymbol{\mathcal{T}}\,\boldsymbol{\mathcal{D}}\,\boldsymbol{\mathcal{T}}^{-1}. \tag{3.1.18}$$

The transformation matrix $\boldsymbol{\mathcal{T}}$ can be determined by following the solution strategy for $S_{0,0}(\vec{q},t)$ by Kurzthaler et al. with a straightforward generalization to matrix elements that involve rotational degrees of freedom. According to equation 2.3.8, the ISF can be expressed as

$$\begin{aligned} S_{l,l'}(\vec{q},t) &= \int d\theta\, d\theta_0\, d\vec{r}\, d\vec{r}_0\, e^{il'\theta} e^{-il\theta_0} e^{i\vec{q}\cdot(\vec{r}-\vec{r}_0)} p(\vec{r},\theta,t,\theta_0,\vec{r}_0) \\ &= \frac{1}{2\pi}\int d\theta\, d\theta_0\, d\vec{r}\, e^{il'\theta} e^{-il\theta_0} e^{i\vec{q}\cdot\vec{r}} p(\vec{r},\theta,t|\theta_0) = \frac{1}{2\pi}\int d\theta\, d\theta_0 e^{il'\theta} e^{-il\theta_0} \tilde{p}(\vec{q},\theta,t|\theta_0), \end{aligned} \tag{3.1.19}$$

where the initial position $\vec{r}_0$ has been integrated out by exploiting the translational invariance of the joint-probability distribution. The remaining translational degrees of freedom have been expressed in terms of the Fourier-transformed conditional probablity density $\tilde{p}(\vec{q},\theta,t|\theta_0) := \int d\vec{r}\, p(\vec{r},\theta,t|\theta_0) e^{i\vec{q}\cdot\vec{r}}$. A differential equation for $\tilde{p}$ is derived as follows

$$\begin{aligned} \partial_t \tilde{p}(\vec{q},\theta,t|\theta_0) &= \int d\vec{r}\, \partial_t p(\vec{r},\theta,t|\theta_0) e^{i\vec{q}\cdot\vec{r}} = \int d\vec{r}\, \boldsymbol{\Omega}\, p(\vec{r},\theta,t|\theta_0) e^{i\vec{q}\cdot\vec{r}} \\ &= \int d\vec{r}\, p(\vec{r},\theta,t|\theta_0) \boldsymbol{\Omega}^\dagger\, e^{i\vec{q}\cdot\vec{r}} = \tilde{\boldsymbol{\Omega}}\, \tilde{p}(\vec{q},\theta,t|\theta_0), \end{aligned} \tag{3.1.20}$$

with an operator

$$\tilde{\boldsymbol{\Omega}} = iv_0\, \vec{o}\cdot\vec{q} + D_r\partial_\theta^2 - D_t q^2. \tag{3.1.21}$$

Alike for the time-independent Schrödinger equation, the solution can be developed by determining the eigenfunctions of the operator $\tilde{\mathbf{\Omega}}$, where the non-trivial angular part of this eigenvalue problem is described by the differential equation

$$\Big(\frac{d^2}{dx^2} - 2k\cos(2x)\Big)f(x) = \lambda f(x), \tag{3.1.22}$$

where the substitution $x = \theta/2$ was used and the imaginary deformation parameter $k = -2il_p$ was introduced. The solution of this eigenvalue equation is given by the π-periodic even and odd Mathieu functions $\mathrm{ce}_{2n}(k,x)$ and $\mathrm{se}_{2n+1}(k,x)$ with respective eigenvalues $a_{2n}(k)$ and $b_{2n+1}(k)$ [87]. They form a complete basis of orthogonal functions with $\int_0^{2\pi} dx \mathrm{ce}_{2n'}(x)\mathrm{ce}_{2n}(x) = \pi\delta_{n,n'}$ and same for se_{2n+1} and can be expressed in Fourier-series of sine and cosines by

$$\mathrm{ce}_{2n}(k,x) = \sum_{m=0}^{\infty} A_{2m}^{2n}(k)\cos(2mx), \qquad \mathrm{se}_{2n+1}(k,x) = \sum_{m=0}^{\infty} B_{2m}^{2n+1}(k)\sin((2m+2)x). \tag{3.1.23}$$

The completeness relations for the basis of even and odd Mathieu function imply the following conditions for the coefficients of the Fourier-expansions:

$$\sum_n A_{2m}^{2n}A_{2m'}^{2n} = \delta_{m,m'} - \frac{1}{2}\delta_{m,0}\delta_{m',0}, \qquad \sum_n B_{2m}^{2n+1}B_{2m'}^{2n+1} = \delta_{m,m'}. \tag{3.1.24}$$

$\tilde{p}(\vec{q},\theta,t|\theta_0)$ is now expanded in the Mathieu functions' basis. Making use of the initial condition $\tilde{p}(\vec{q},\theta,t=0|\theta_0) = \delta(\theta-\theta_0)$ delivers [86]

$$\begin{aligned}\tilde{p}(\vec{q},\theta,t|\theta_0) = \frac{e^{-q^2D_t t}}{\pi}\sum_{n=0}^{\infty}\Big\{&\mathrm{ce}_{2n}(k,\theta_0/2)\mathrm{ce}_{2n}(k,\theta/2)e^{-D_r a_{2n}(k)t/4} \\ &+ \mathrm{se}_{2n+1}(k,\theta_0/2)\mathrm{se}_{2n+1}(k,\theta/2)e^{-D_r b_{2n+1}(k)t/4}\Big\}.\end{aligned} \tag{3.1.25}$$

Inserting back into (3.1.19) the ISF finally reads

$$\begin{aligned}S_{l,l'}(\vec{q},t) = e^{-q^2D_t t}\sum_{n=0}^{\infty}2\cdot\Bigg\{&\Big[\int_0^{2\pi}\frac{d\theta}{2\pi}\mathrm{ce}_{2n}(k,\theta/2)e^{il'\theta}\Big]\Big[\int_0^{2\pi}\frac{d\theta}{2\pi}\mathrm{ce}_{2n}(k,\theta/2)e^{-il\theta}\Big]e^{-D_r a_{2n}(k)t/4} \\ &+\Big[\int_0^{2\pi}\frac{d\theta}{2\pi}\mathrm{se}_{2n+1}(k,\theta/2)e^{il'\theta}\Big]\Big[\int_0^{2\pi}\frac{d\theta}{2\pi}\mathrm{se}_{2n+1}(k,\theta/2)e^{-il\theta}\Big]e^{-D_r b_{2n+1}(k)t/4}\Bigg\}.\end{aligned} \tag{3.1.26}$$

The θ-integration can be connected to the contributing Fourier-coefficients by using

$$\int_0^{2\pi}\frac{d\theta}{2\pi}\mathrm{ce}_{2n}(k,\theta/2)e^{\pm il\theta} = \frac{1}{2}\Big(A_{|2l|}^{2n} + A_0^{2n}\delta_{l,0}\Big), \tag{3.1.27}$$

$$\int_0^{2\pi}\frac{d\theta}{2\pi}\mathrm{se}_{2n+1}(k,\theta/2)e^{\pm il\theta} = \pm\,\mathrm{sign}(l)\frac{i}{2}B_{|2l|-2}^{2n+1}. \tag{3.1.28}$$

This allows to identify the transformation matrix $\boldsymbol{\mathcal{T}}$ and the diagonal matrix $\boldsymbol{\mathcal{D}}$ as one can argue that if equation (3.1.26) is another representation of (3.1.17), there must hold

$$\mathcal{T}_{l,l_1} = \begin{cases} \frac{1}{2\sqrt{2}}\Big(A^{2n}_{|2l|} + A^{2n}_0\delta_{l,0} + A^0_{|2l|}\delta_{n,0} + A^0_0\delta_{l,0}\delta_{n,0}\Big), & |l_1| = 2n \\ -\operatorname{sign}(l)\frac{i}{2\sqrt{2}}\Big(B^{2n+1}_{|2l|-2} + B^1_{|2l|-2}\delta_{n,0}\Big), & |l_1| = 2n+1 \end{cases} \tag{3.1.29}$$

$$\mathcal{T}^{-1}_{l_1,l'} = \begin{cases} \frac{1}{2\sqrt{2}}\Big(A^{2n}_{|2l'|} + A^{2n}_0\delta_{l,0} + A^0_{|2l'|}\delta_{n,0} + A^0_0\delta_{l',0}\delta_{n,0}\Big), & |l_1| = 2n \\ \operatorname{sign}(l')\frac{i}{2\sqrt{2}}\Big(B^{2n+1}_{|2l'|-2} + B^1_{|2l'|-2}\delta_{n,0}\Big), & |l_1| = 2n+1 \end{cases} \tag{3.1.30}$$

$$\mathcal{D}_{l_1,l_1} = \begin{cases} D_t q^2 + \frac{D_r}{4}a_{2n}(k), & |l_1| = 2n \\ D_t q^2 + \frac{D_r}{4}b_{2n+1}(k), & |l_1| = 2n+1 \end{cases} \tag{3.1.31}$$

where $\sum_{l_1}\mathcal{T}_{l,l_1}\mathcal{T}^{-1}_{l_1,l'} = \delta_{l,l'}$ is easily seen by making use of the relations in (3.1.24). It needs further to be proven that $\boldsymbol{\mathcal{T}}\boldsymbol{\mathcal{D}}\boldsymbol{\mathcal{T}}^{-1} = \boldsymbol{\omega}$ as defined in equation (3.1.14). This requires to exploit the following recurence relations for the eigenvalues a_{2n} and b_{2n+1}, that are obtained by inserting the expansions of the Mathieu functions into the differential equation for $\tilde{p}(\vec{q},\theta,t)$ (3.1.22):

$$a_{2n}A^{2n}_{2m} = m^2A^{2n}_{2m} + k(1+\delta_{m,1})A^{2n}_{2m-2} + kA^{2n}_{2m+2}, \tag{3.1.32}$$

$$b_{2n+1}B^{2n+1}_{2m} = (m+1)^2B^{2n+1}_{2m} + kB^{2n+1}_{2m-2} + kB^{2n+1}_{2m+2}, \tag{3.1.33}$$

with the convention $A^{2n}_{2m} = B^{2n+1}_{2m} = 0$ for $m < 0$. With these relations at hand, a straightforward calculation reveals indeed that

$$\sum_{l_1=-\infty}^{\infty}\mathcal{T}_{l,l_1}\mathcal{D}_{l_1,l_1}\mathcal{T}^{-1}_{l_1,l'} = \Big(D_t q^2 + D_r l^2\Big)\delta_{l,l'} - \frac{iv_0 q}{2}\delta_{|l-l'|,1}, \tag{3.1.34}$$

which is equation (3.1.14) for $\vec{q} = q\vec{e}_x$.

From using a numerical scheme to solve the matrix exponential in equation (3.1.17), solutions for different matrix elements of the free particle ISF are presented in figure 3.1.1 for characteristic wavenumbers. These wavenumbers have been associated with the crossover length scales of the free active particle derived in the last chapter via $l_q = 2\pi/q$. It can be seen that the $S_{0,0}(q,t)$ component presented in subfigure (a) reveals the characteristic regimes of diffusive and ballistic motion. As expected, the representing modes of short-time diffusive motion that fulfill $2\pi/q \ll l_\nu$ decay like those of a passive particles as $S_{0,0}(q,t) = e^{-D_t q^2 t}$. On the other hand when considering length scales that fulfil $2\pi/q \gg l_l$ the respective relaxation modes are dominated by the effective long-time diffusion of the particle and are revealing a decay according to[1] $S_{0,0}(q,t) = e^{-D_{\text{eff}}\,q^2 t}$. The non-monotonic oscillatory behaviour that is observed in the intermediate wavenumber regime both for $S_{0,0}(q,t)$ and for the non-diagonal elements $S_{1,0}(\vec{q},t)$ and $S_{0,1}(\vec{q},t)$ in (b) captures the ballistic regime and is a clear fingerprint of the present non-equilibrium dynamics, as this would be an impossible property in any equilibrium system where one can be shown that any equilibrium time evolution implies that there must exist a repre-

[1] This follows from the low-q expansion $S_{0,0}(q,t) \approx 1 - (q^2/4)\delta r^2(t)$ after inserting equation (2.2.10). The low-q expansion will be discussed in more detail in section 3.4.

sentation of the ISF in terms of a superposition of purely relaxing exponentials [88]. Subfigure (b) additionally depicts the $S_{1,1}(\vec{q},t)$ correlation functions for the same wavenumbers as for $S_{0,0}(\vec{q},t)$, revealing an additional modulation with $e^{-D_r t}$ that is the dominating contribution on the long-time diffusion at low wavenumbers.

The presented free particle solutions for the $(0,0)$ component of the ISF have also been experimentally confirmed by using a differential dynamic microscopy technique in a diluted mixture of catalytic Janus particles immersed in hydrogen peroxide [86]. Measuring the free particle ISF has shown to be a useful tool to probe the relevant length scales and the model parameters to describe diluted systems of microswimmers, since the characteristic behaviour of the free active motion can be directly linked to the behaviour of the ISF in a distinctive wavenumber regime.

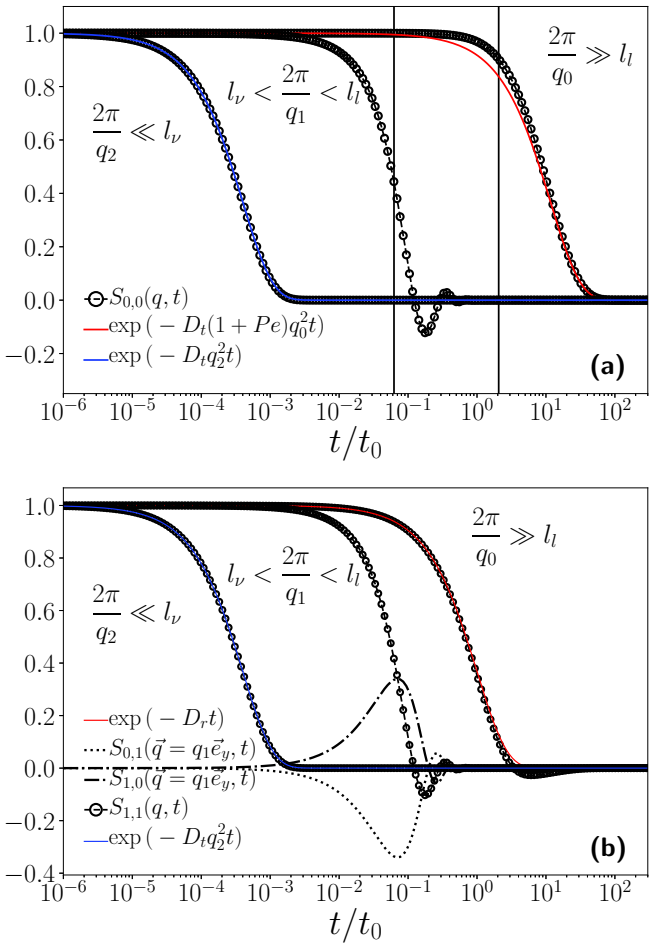

.

Figure 3.1.1.: *ISF of a free ABP at different wavenumbers q. Numerical solutions are drawn in black, blue and red lines are respective approximations of the short- and long-time diffusive regime. The parameters are $l_\nu = 0.25\sigma$, $l_l = 8.25\sigma$, $q_0\sigma = 0.05$, $q_1\sigma = 2.5$, $q_2\sigma = 60$* ***(a)*** *shows solutions for $S_{0,0}(q,t)$ that represent the same distinct length- and time scales as in figure 2.2.1.* ***(b)*** *shows further matrix elements where $S_{1,1}(q,t)$ is presented for the same wavenumbers as in (a).*

3.1.3 Mori-Zwanzig Equation with Friction Kernel

Addressing back to the case of interacting systems, the convolution integral in the Mori-Zwanzig equation must be accounted for and the diffusion-kernel $\boldsymbol{K}(\vec{q},t)$ requires to be suitably approximated due to its complexity. MCT provides the appropriate framework for this endeavour. It is, however, a common procedure not to directly approximate the diffusion-kernel $\boldsymbol{K}(\vec{q},t)$, but first to derive a more robust variant of the Mori-Zwanzig equation which involves a so-called friction kernel, that is more suitable to describe the dynamics close or above the glass transition point. This transition is characterized by the observation that certain density-correlations in the system persist for infinite times, formally described by non-vanishing long-time values of the ISF, that are denoted as the non-ergodicity parameters

$$f_{l,l'}^{\alpha,\beta}(\vec{q}) := \lim_{t\to\infty} S_{l,l'}^{\alpha,\beta}(\vec{q},t). \tag{3.1.35}$$

In order to investigate the long-time behaviour of the ISF, it is instructive to introduce the Laplace-transformation $LT[f(t)](z)$ defined as

$$LT[f(t)](z) := f(z) := \int_0^\infty dt\ e^{-zt} f(t), \tag{3.1.36}$$

since the convolution term of the Mori-Zwanzig equation conveniently factorizes in the Laplace-space. Further, the non-ergodicity of an observable $A(t)$ in time-space can be attributed to a $1/z$ for the respective Laplace-transformed quantity $A(z)$ by making use of the final-value theorem $\lim_{t\to\infty} A(t) = \lim_{z\to 0} z\cdot A(z)$. This means that non-ergodic matrix elements of the ISF are required to possess a $1/z$ pole. For these elements, the Laplace-transform of equation (3.1.13) implies the memory-kernel to behave like $\lim_{z\to 0} M_{l,l'}^{\alpha,\beta}(\vec{q},z) = \omega_{l,l'}^{\alpha,\beta}(\vec{q})$ above the glass transition which is a strong criterion that is hardly fulfilled by any approximation for $\boldsymbol{M}(\vec{q},t)$ and one therefore seeks for another type of memory-function that is subject to more robust criteria. The derivation of such a memory-kernel is achieved technically by performing a further projection step. Within this projection step, the present relaxation channels of translational and rotational motion must be separately taken into account. In the particular case of spherical ABP, the rotational degrees of freedom are solely driven by diffusive rotational dynamics, meaning that they can never underly dynamical arrest. A projection operator that preserves this feature is anticipated by choosing

$$\boldsymbol{\mathcal{P}'} = -\sum_{\substack{l_1,l_2,\vec{q}\\ \alpha\beta}} \left|\rho_{l_1}^{\alpha}(\vec{q})\right\rangle \left(\omega_T^{-1}\right)_{l_1,l_2}^{\alpha,\beta}(\vec{q}) \left\langle \rho_{l_2}^{\beta}(\vec{q})^*\, \boldsymbol{\Omega}_T^\dagger\right|, \quad \boldsymbol{\mathcal{Q}'} = \mathbb{1} - \boldsymbol{\mathcal{P}'}. \tag{3.1.37}$$

After inserting another unity operator in the time evolution operator appearing in (3.1.15) by writing $\boldsymbol{\Omega}^\dagger = \boldsymbol{\mathcal{Q}'}\boldsymbol{\Omega}^\dagger + \boldsymbol{\mathcal{P}'}\boldsymbol{\Omega}^\dagger$ and exploiting the Dyson decomposition once more leads to an equation of motion given by

$$\boldsymbol{K}(\vec{q},t) = \boldsymbol{m}(\vec{q},t) - \int_0^t dt'\ \boldsymbol{K}(\vec{q},t-t')\boldsymbol{\omega}_T^{-1}(\vec{q})\boldsymbol{m}(\vec{q},t'), \tag{3.1.38}$$

that involves a so-called friction kernel $\boldsymbol{m}(\vec{q},t)$ which reads

$$m_{l,l'}^{\alpha,\beta}\left(\vec{q},t\right)=\left\langle \rho_{l}^{\alpha}\left(\vec{q}\right)^{*}\boldsymbol{\Omega}_{T}^{\dagger}\boldsymbol{\mathcal{Q}}\mathrm{e}^{\boldsymbol{\Omega}_{\mathrm{irr}}^{\dagger}t}\boldsymbol{\mathcal{Q}}\boldsymbol{\Omega}_{T}^{\dagger}\rho_{l'}^{\beta}\left(\vec{q}\right)\right\rangle . \tag{3.1.39}$$

with the so-called irreducible Smoluchowski operator $\boldsymbol{\Omega}_{\mathrm{irr}}^{\dagger}:=\boldsymbol{\Omega}^{\dagger}\boldsymbol{\mathcal{Q}'}$. Calculating the Laplace-transform of equations (3.1.38) subsequently reveals the relation

$$\boldsymbol{K}(\vec{q},z)=\left(\boldsymbol{m}^{-1}(\vec{q},z)+\boldsymbol{\omega}_{T}^{-1}(\vec{q})\right)^{-1}, \tag{3.1.40}$$

which is then inserted in the Laplace-transformed version of equation (3.1.13) to eliminate the diffusion kernel. The simplicity of an individual relaxation channel allows for an analytical back-transform to the time domain. This yields an equation of motion for the ISF that only depends on the friction kernel. It reads

$$\partial_{t}\boldsymbol{S}(\vec{q},t)=-\boldsymbol{\omega}(\vec{q})\boldsymbol{S}^{-1}(q)\boldsymbol{S}(\vec{q},t)-\int_{0}^{t}dt'\boldsymbol{m}(\vec{q},t-t')\boldsymbol{\omega}_{T}^{-1}(\vec{q})\Big[\partial_{t'}\boldsymbol{S}(\vec{q},t')+\boldsymbol{\omega}_{R}\boldsymbol{S}^{-1}(q)\boldsymbol{S}(\vec{q},t')\Big]. \tag{3.1.41}$$

This is the central equation of this work, where $\boldsymbol{m}(\vec{q},t)$ will be subject to the mode-coupling approximation in a further step. The necessity of a separate treatment of the present relaxation channels in terms of an appropriately chosen projection operator has also proven to be crucial in other variants of MCT as for the case of liquids confined in narrow channels. There the relaxation of modes perpendicular and parallel to the enclosing wall must be accounted for within separate irreducible projectors which results in distinct friction kernel contributions for each relaxation channel and coupling terms between them [41, 89]. Within the ABP-MCT, memory-kernel contributions of rotational motion do not exist and the coupling of rotational and translational degrees of freedom is expressed in the special structure of equation (3.1.41) within the so-called hopping term $\boldsymbol{\omega}_{R}\boldsymbol{S}^{-1}(q)\boldsymbol{S}(\vec{q},t)$. This term accounts for the fact that certain density correlation in the system will remain ergodic even if the translational motion simultaneously experiences dynamical arrest.

Indeed, a further analysis of equation (3.1.41) in the Laplace-domain [84] reveals the condition $\boldsymbol{\omega}_{R}\boldsymbol{S}^{-1}(q)\boldsymbol{f}(\vec{q})=0$, which requires $f_{l,l'}^{\alpha,\beta}(\vec{q})=0$ for $l\neq0$ whereas all $f_{0,l'}^{\alpha,\beta}(\vec{q})\neq0$ for $\phi>\phi_{c}$. This non-symmetric behaviour is a further manifestation of the present non-equilibrium time evolution and can be rationalized by the observation that translational degrees of freedom are influenced by rotational degrees of freedom, but not the other way arround. In other words, the slow dynamics of a density fluctuation $|\rho_{l'}^{\beta}(\vec{q},t)^{*}\rangle$ will always be superimposed by the decay of the rotational correlations for $t\gg\tau_{r}$ if projected on the $\langle\rho_{l}^{\alpha}(\vec{q})|$ subspace if $l\neq0$ and $\alpha=\beta$ and will vanish if $l\neq0$ and $\alpha\neq\beta$, whereas the projection on $\langle\rho_{0}^{\alpha}(\vec{q})|$ displays the influence of the rotational degrees of freedom of type β on the strucural relaxation of type α that is, if β denotes an active particle type, detectable just up to the structural relaxation time of the system and persists for infinite times above the glass transition point.

It further needs to be pointed out that equation (3.1.41) requires the knowledge of the inverse of the translational part of the frequency matrix, $\boldsymbol{\omega}_{T}^{-1}(\vec{q})$, that is necessary to be taken on a

infinite dimensional matrix algebra. In general, it is not possible to find an analytic solution for this problem and numerical considerations that can only involve a finite number of rotational modes must carefully take into account that matrix inversion and performing a cutoff are not expected to commute. One could think of applying the transformations introduced for the exact diagonalization of the frequency matrix given by equation (3.1.18) in the free particle solution which would in principle allow for a trivial inversion, but the determination of the expansion coefficients for the Mathieu functions can be reduced to a similar eigenvalue problem on an infinite matrix algebra [87]. A possible remedy is to start with an inversion of $\boldsymbol{\omega}_T(\vec{q})$ for a large matrix and perform the desired cutoff afterwards. The degree of accuracy for this approximation will become clearer later when the tagged particle dynamics is discussed where the translational part of the frequency matrix can be inverted analytically for arbitrary cutoffs due to a simplified structure.

A well-known observation from classical MCT is that its predictions become insensitive on the discretization of the wavenumber integration if the upper cutoff for $\vec{q}$ is chosen sufficiently high. For the ABP-MCT a similar question arises on how important the inclusion of higher rotational modes is for the qualitative predictions of the theory. The results that will be presented later indicate that a first-order consideration, which only includes the modes linked with $\Lambda_L = 1$, is already able to provide quantitatively consistent results with simulations. This is supported by the observation that explicit couplings that arise in ABP-MCT predicted equations for central quantities as the MSD or the effective swimming velocity are only for $\Lambda_L = 1$.

3.1.4 Mode-Coupling Approximation

The following steps will sketch the derivation of the memory-kernel in the MCT approximation. It starts by noting that dynamical arrest close to the glass transition point is triggered by the cageing effect of particles, suggesting a phenomenological approach to reduce the dynamics to the space of product states of density pairs. One defines the two-point projector

$$\boldsymbol{\mathcal{P}}_2 := \sum_{1,2,3,4} |\rho_1\rho_2\rangle g_{1,2,3,4} \langle\rho_3^*\rho_4^*|, \tag{3.1.42}$$

where the convenient short hand writing with triples $i := (\vec{q}_i, l_i, \gamma_i)$ has been introduced with the notation $\sum_i := \sum_{l_i,\vec{q}_i.\gamma_i}$ and $\delta_{i,j} = \delta_{\vec{q}_i,\vec{q}_j}\delta_{l_i,l_j}\delta_{\gamma_i,\gamma_j}$. Moreover the normalization coefficient $g_{1,2,3,4}$ has to be chosen such that $\boldsymbol{\mathcal{P}}_2$ fulfills projector properties. The first crucial step towards an approximate expression for the memory-kernel is achieved by inserting two-point projectors before and after the propagator in equation (3.1.39), resulting in

$$m_{l,l'}^{\alpha,\beta}(\vec{q},t) \approx \left\langle \rho_l^\alpha(\vec{q})^* \, \boldsymbol{\Omega}_T^\dagger \boldsymbol{\mathcal{Q}}\boldsymbol{\mathcal{P}}_2 \mathrm{e}^{\boldsymbol{\Omega}_{\mathrm{irr}}^\dagger t} \boldsymbol{\mathcal{P}}_2 \boldsymbol{\mathcal{Q}}\boldsymbol{\Omega}_T^\dagger \rho_{l'}^\beta(\vec{q}) \right\rangle. \tag{3.1.43}$$

The cornerstone of the mode-coupling approximation is the factorization of 4-point correlation function into products of 2-point correlation functions [37,90] by writing

$$\left\langle \rho_3^*\rho_4^* \mathrm{e}^{\boldsymbol{\Omega}_{\mathrm{irr}}^\dagger t} \rho_{1'}\rho_{2'} \right\rangle \approx S_{3,1'}(t) \, S_{4,2'}(t) + S_{3,2'}(t) \, S_{4,1'}(t) \, . \tag{3.1.44}$$

This further allows to identify the normalization factor $g_{1,2,3,4}$ by exploiting the idempotency criterion for $\boldsymbol{\mathcal{P}}_2$ which reveals

$$g_{1,2,3,4} \approx \frac{1}{2} S^{-1}_{1,3} S^{-1}_{2,4}. \tag{3.1.45}$$

Moreover, averages involving three densities are approximated in terms of the convolution approximation by neglecting static triplet correlation functions, meaning that [91,92]

$$\left\langle \rho^*_1 \rho^*_2 \rho_3 \right\rangle \approx \frac{1}{\sqrt{N}} \sum_{\epsilon} \frac{1}{x^2_\epsilon} S^{\gamma_1,\epsilon}_{l_1,l_1}(q_1) S^{\gamma_2,\epsilon}_{l_2,l_2}(q_2) S^{\gamma_3,\epsilon}_{l_3,l_3}(q_3) \delta_{\vec{q}_1+\vec{q}_2,\vec{q}_3} \delta_{l_1+l_2,l_3}. \tag{3.1.46}$$

This allows to evaluate the static expressions $\left\langle \rho^\alpha_l(\vec{q})^* \boldsymbol{\Omega}^\dagger_T \boldsymbol{\mathcal{Q}} \rho_1 \rho_2 \right\rangle$ and $\left\langle \rho^*_{3'} \rho^*_{4'} \boldsymbol{\mathcal{Q}} \boldsymbol{\Omega}^\dagger_T \rho^\beta_{l'}(\vec{q}) \right\rangle$ and combining the result with the mode-coupling approximation of the propagator results in the following equation for the memory-kernel, as presented in detail in appendix A.1:

$$m^{\alpha,\beta}_{l,l'}(\vec{q}) \approx \frac{\rho}{2} \int \frac{d^2p}{(2\pi)^2} \sum_{\substack{l_1 \dots l_4 \\ \gamma_1 \dots \gamma_4}} \mathcal{W}^{\alpha,\gamma_1,\gamma_2}_{l,l_1,l_2}(\vec{q},\vec{q}-\vec{p},\vec{p}) S^{\gamma_1,\gamma_3}_{l_1,l_3}(\vec{q}-\vec{p},t) S^{\gamma_2,\gamma_4}_{l_2,l_4}(\vec{p},t) \mathcal{V}^{\beta,\gamma_3,\gamma_4}_{l',l_3,l_4}(\vec{q},\vec{q}-\vec{p},\vec{p}), \tag{3.1.47}$$

$$\mathcal{V}^{\beta,\gamma_3,\gamma_4}_{l',l_3,l_4}(\vec{q},\vec{k},\vec{p}) := D^\beta_t \Big[(\vec{q}\cdot\vec{k}) c^{\gamma_3,\beta}(k) \delta_{l_3,0} \delta_{\gamma_4,\beta} + (\vec{q}\cdot\vec{p}) c^{\gamma_4,\beta}(p) \delta_{l_4,0} \delta_{\gamma_3,\beta} \Big] \delta_{l_3+l_4,l'}, \tag{3.1.48}$$

$$\begin{aligned}
\mathcal{W}^{\alpha,\gamma_1,\gamma_2}_{l,l_1,l_2}(\vec{q},\vec{k},\vec{p}) := {} & D^\alpha_t \Big[(\vec{q}\cdot\vec{k}) c^{\gamma_1,\alpha}(k) \delta_{l_1,0} \delta_{\gamma_2,\alpha} + (\vec{q}\cdot\vec{p}) c^{\gamma_2,\alpha}(p) \delta_{l_2,0} \delta_{\gamma_1,\alpha} \Big] \delta_{l_1+l_2,l} \\
& + \sum_\epsilon \frac{1}{x^2_{\gamma_2}} \frac{i v^\epsilon_0}{2\rho} k e^{i(l_1+l_2-l)\varphi_k} S^{\alpha,\gamma_2}_{l,l}(q) S^{\gamma_2,\epsilon}_{l-l_2,l-l_2}(k) \left(S^{-1}\right)^{\epsilon,\gamma_1}_{l_1,l_1}(k) \delta_{|l-l_1-l_2|,1} \\
& + \sum_\epsilon \frac{1}{x^2_{\gamma_1}} \frac{i v^\epsilon_0}{2\rho} p e^{i(l_1+l_2-l)\varphi_p} S^{\alpha,\gamma_1}_{l,l}(q) S^{\gamma_1,\epsilon}_{l-l_1,l-l_1}(p) \left(S^{-1}\right)^{\epsilon,\gamma_2}_{l_2,l_2}(p) \delta_{|l-l_1-l_2|,1} \\
& - \frac{1}{x^2_{\gamma_1}} \frac{i v^{\gamma_1}_0}{2\rho} q e^{i(l_1+l_2-l)\varphi_q} S^{\alpha,\gamma_1}_{l,l}(q) \delta_{\gamma_1,\gamma_2} \delta_{|l-l_1-l_2|,1}.
\end{aligned} \tag{3.1.49}$$

Here the static vertex functions $\boldsymbol{\mathcal{W}}(\vec{q},\vec{k},\vec{p})$ and $\boldsymbol{\mathcal{V}}(\vec{q},\vec{k},\vec{p})$ have been introduced. They are only entered by the equilibrium static structure factors and the self-propulsion velocities, i.e., consistently with equation (3.1.39), the dependence on the rotational diffusion coefficients is only implicitly entered in the memory-kernel through the time evolution of the Smoluchowski operator, but not in the vertex functions. For a single-component active system, the presented MCT equations are also fully consistent with those found in [47].

The memory-kernel in the mode-coupling approximation is given as a functional of the ISF which establishes a self-consistent system of equations, that uniquely determines the time evolution of the ISF according to the Mori-Zwanzig equation (3.1.41) by fixing the initial condition with the short-time solution of free diffusion. The only inputs that need to be provided to solve the dynamics are numerical values or appropriate theoretical predictions for the equilibrium static structure factor of the passive hard-sphere system for which numerous theories already exist (see [93–95] for 2D hard-disks). This constitutes a remarkable achievement that only by entering such equilibrium theories the ABP-MCT is feasible to gain insights into non-equilibrium dynamical features beyond the limitations of perturbative theories like linear response, however at the price, that the correlation functions are of transient-type.

It is further noted, that the memory-kernel obeys the same unitary transformation law from equation (3.1.7) for rotations of the wavevector $\vec{q} = (q, \varphi_q)$. This implies that the ISF maintains this transformation law even under the time evolution of the MCT approximated memory-kernel. This is straightforwardly checked by considering a transformation $\varphi_q \to \varphi_q + \delta\varphi$ of the memory-kernel. By using the substitution $\varphi_p \to \varphi_p + \delta\varphi$ in the wavevector integration of the memory-kernel implies $\varphi_k \to \varphi_k + \delta\varphi$. With these replacements and by exploiting the transformation rules of the initial short time ISFs, the demanded phase factor $e^{-i(l-l')\delta\varphi}$ is recovered. Obviously, the frequency matrix given by equation (3.1.14) obeys the same transformation behaviour as the ISF and the memory-kernel. This immediately implies that the time evolution of the Mori-Zwanzig equation conserves the transformation rule of the ISF even after the application of the mode-coupling approximation.

3.2 Asymptotic Equations

The glass transition is formally characterized by a bifurcation scenario of the non-ergodicity parameter $\boldsymbol{f}(\vec{q})$. Usually the determination of $\boldsymbol{f}(\vec{q})$ is not carried out by explicitly calculating the ISF on very large time scales, but by using a time-independent iterative algebraic equation, which is derived from the Laplace-transformation of the Mori-Zwanzig equation under the assumption of vanishing derivatives of the correlation functions close to the plateau value. Following this assumption an equation for $\boldsymbol{f}(\vec{q})$ reads

$$\boldsymbol{f}(\vec{q}) + \boldsymbol{S}(q)\,\boldsymbol{\omega}^{-1}(\vec{q})\boldsymbol{m}[\boldsymbol{f}(\vec{q}), \boldsymbol{f}(\vec{q})]\boldsymbol{\omega}_T^{-1}(\vec{q})\big(\bar{\boldsymbol{f}}(\vec{q}) - \boldsymbol{S}(q)\big) = 0, \tag{3.2.1}$$

where $\bar{\boldsymbol{f}}(\vec{q}) := \boldsymbol{f}(\vec{q}) + \boldsymbol{\omega_R} \int_0^\infty dt\, \boldsymbol{S}^{-1}(q)\boldsymbol{S}(\vec{q}, t)$. Here the memory-kernel was expressed in terms of the mode-coupling functional as a bilinear form of two correlation functions with $\boldsymbol{m}[\boldsymbol{f}(\vec{q}), \boldsymbol{f}(\vec{q})]$ denoting an evaluation of the memory-kernel where the involved ISFs have been replaced by $\boldsymbol{f}(\vec{q})$. The appearance of the term $\bar{\boldsymbol{f}}(\vec{q})$ is due to the hopping term and leads to the fact that equation (3.2.1) is no longer self-consistent because $\bar{\boldsymbol{f}}(\vec{q})$ is required to be explicitly evaluated in the time-domain by integration of the ISF at least on time-scales of the persistence time, because $\boldsymbol{\omega_R}\boldsymbol{S}^{-1}(q)\boldsymbol{S}(\vec{q}, t)$ will always reveal a decay at least after τ_r. This observation is manifested in a crossover behaviour of the ISF that has not been observed in previous MCTs and is exemplified for the one-component theory in [47]: At times $t \approx \tau_r$, there emerges a transition between two different pleateau values. This transition marks the crossover of a glass with an infinite persistence time τ_r, where $\bar{\boldsymbol{f}}(\vec{q}) = \boldsymbol{f}(\vec{q})$ and a glass with finite τ_r with $\bar{\boldsymbol{f}}(\vec{q}) \neq \boldsymbol{f}(\vec{q})$.

Expressing the non-ergodicity parameter in terms of the mode-coupling functional constitutes the starting point for the glass transition asymptotics for the ISF. However, the requirement of equation (3.2.1) to evaluate dynamical quantities bears some problems in this case because a reliable asymptotic expansion requires a very precise determination of the glass transition point, which is not possible due to the necessity of very many numerical evaluations of the hopping integral close to the bifurcation. It is therefore instructive first to investigate the case $D_r = 0$ in more detail. In this case, the hopping term vanishes and equation (3.2.1) results in the

usual algebraic equation known from passive MCT which implies the ISF to reveal the known asymptotic regimes depicted in figure 3.0.1. Even though the limits $D_r \to 0$ and $t \to \infty$ are not necessarily expected to commute and different scaling laws are expected to emerge for $D_r \neq 0$, studying the case $D_r = 0$ can serve as an interesting first starting point to investigate the non-trivial influence of activity on the details of the glass transition asymptotics. One might further expect some similarities between the cases $D_r = 0$ and $D_r \neq 0$ for systems below the glass transition whose structural relaxation time is still exceeded by the persistence time τ_r, meaning that the crossover behaviour for $t \gg \tau_r$ is cancelled. Moreover, the case $D_r = 0$ can serve as a simplified model to study active systems with arrested rotational degrees of freedom, be it dense suspensions of self-propelled elongated particles or spherical active particles with rough surfaces that experience strong contact friction forces at high densities.

Asymptotic expansions of MCT equations have been worked out in great detail for passive mixtures [38] and first results have already been presented for the monodisperse ABP-MCT with $D_r = 0$ [96]. In the latter case, the calculations can be conducted exactly as same as for the theory of passive mixtures and do not provide any new insights. The following steps therefore only aim to sketch the readily known standard MCT-asymptotics and are focused to summarize the necessary quantities to predict the divergence behaviour of the α-relaxation process. This is in particular interest in the context of this work as this allows to characterize transport coefficients close to dynamical arrest. For a more rigorous derivation of the MCT-asymptotics with additional higher-order expansions, the reader is referred to [38, 78].

Let therefore be $D_r^\alpha = 0$ for all α in the following. The starting point of an asymptotic description close to the glass transition point is to note, that the ISF evolves very close to the non-ergodicity parameter where $\partial_t \boldsymbol{S}(\vec{q}, t) = 0$. This leads to a preliminary assumption of a power series at the critical point where the difference to the plateau value is regarded as a small quantity, i.e.,

$$\boldsymbol{S}(\vec{q}, t) - \boldsymbol{f}^c(\vec{q}) \sim \boldsymbol{h}(\vec{q})(t/t_0)^{-a} + \mathcal{O}(t/t_0)^{-2a}), \quad t \gg t_0, \tag{3.2.2}$$

where t_0 denotes a typical time scale of the short-time relexation and a denotes an unknown exponent for now. Exploiting the identity $\partial_t \int_0^t dt'\, f(t-t')g(t') = \int_0^t dt'\, f(t-t')\partial_{t'} g(t') + f(t)g(0)$, the Mori-Zwanzig equation can written as

$$\boldsymbol{S}(\vec{q}, t) = \boldsymbol{S}(q)\boldsymbol{M}(\vec{q}, t)\boldsymbol{S}(q) - \boldsymbol{S}(q)\partial_t \int_0^t dt'\, \boldsymbol{M}(\vec{q}, t - t')\boldsymbol{S}(\vec{q}, t'), \tag{3.2.3}$$

where the abbrevation $\boldsymbol{M}(\vec{q}, t) := \boldsymbol{\omega}^{-1}(\vec{q})\boldsymbol{m}(\vec{q}, t)\boldsymbol{\omega}^{-1}(\vec{q})$ has been introduced. Inserting the expansion for $\boldsymbol{S}(\vec{q}, t)$ in the EOM and exploiting the identity

$$\partial_t \int_0^t dt'\, (t - t')^{-x} t'^{-y} = \frac{\Gamma(1-x)\Gamma(1-y)}{\Gamma(1-x-y)} t^{-x-y} \tag{3.2.4}$$

allows counting powers in t which yields self-consistent equations for $\boldsymbol{f}^c(\vec{q})$ and the so-called critical amplitude $\boldsymbol{h}(\vec{q})$. Counting terms of order t^0 and dropping the $\vec{q}$-dependence for brevity reveals

$$\boldsymbol{f}^c + \boldsymbol{S}^c\, \boldsymbol{M}[\boldsymbol{f}^c, \boldsymbol{f}^c](\boldsymbol{f}^c - \boldsymbol{S}^c) = 0, \tag{3.2.5}$$

with the superscript c denoting critical quantities at the transition point. This is nothing but equation (3.2.1) evaluated at the critical point for vanishing rotational diffusion coefficients. Collecting terms in t^{-a} shows

$$\boldsymbol{h} = 2(\boldsymbol{S}^c - \boldsymbol{f}^c)\boldsymbol{M}[\boldsymbol{f}^c, \boldsymbol{h}](\boldsymbol{S}^c - \boldsymbol{f}^c) := \boldsymbol{C}\,[\boldsymbol{h}], \tag{3.2.6}$$

which has been expressed in terms of an eigenvalue equation for the left eigenvector $\boldsymbol{h}$ induced by the linear map $\boldsymbol{C}[\boldsymbol{h}]$. Correspondingly there exists a right eigenvector $\hat{\boldsymbol{h}}$ of $\boldsymbol{C}$ which fulfils $\hat{\boldsymbol{h}}\boldsymbol{C} = \hat{\boldsymbol{h}}$. Both left and right eigenvectors are uniquely determined up to two normalization coefficients, where it will prove to be convenient to fix the following conditions to simplify later occuring terms:

$$\hat{\boldsymbol{h}}^\dagger : \boldsymbol{h} = 1, \tag{3.2.7}$$

$$\hat{\boldsymbol{h}}^\dagger : \boldsymbol{h}(\boldsymbol{S}^c - \boldsymbol{f}^c)^{-1}\boldsymbol{h} = 1. \tag{3.2.8}$$

Here the contraction operator : was defined as

$$\boldsymbol{A} : \boldsymbol{B} := \sum_{\substack{\vec{q},\, l_1, l_2 \\ \gamma_1, \gamma_2}} A^{\gamma_1,\gamma_2}_{l_1,l_2}(\vec{q}) B^{\gamma_2,\gamma_1}_{l_2,l_1}(\vec{q}). \tag{3.2.9}$$

The introduced quantities are sufficient to calculate the exponent a which describes the initial decay towards the plateau value. This exponent is linked to the so-called exponent parameter λ for which the following relationship can be derived by extending the expansion to the next higher order [38]:

$$\lambda := \frac{\Gamma(1-a)^2}{\Gamma(1-2a)} = \hat{\boldsymbol{h}}^\dagger : (\boldsymbol{S}^c - \boldsymbol{f}^c)\boldsymbol{M}[\boldsymbol{h}, \boldsymbol{h}](\boldsymbol{S}^c - \boldsymbol{f}^c). \tag{3.2.10}$$

For times that exceed typical microscopic time scales of the system, MCT states that all correlation functions will evolve close to the plateau value according to the same power-law with exponent a on a certain time window t_σ. It can be shown that this time scale grows like $t_\sigma \sim |\sigma|^{-1/2a}$, where σ is in first-order linear in the separation parameter $\epsilon = (\phi - \phi_c)/\phi_c$ that defines the distance to the glass transition point. If $\epsilon < 0$ another time-window $t_\sigma^{'}$ emerges for $t \gg t_\sigma$ that describes the transition towards the final α-relaxation regime. A nontrivial statement of MCT ist that the scaling laws for the ISF towards the α-regime can be obtained by the replacement $a \to -b$ in the previous expansion, which reveals the well-known von-Schweidler law with an exponent b that fulfils

$$\lambda = \frac{\Gamma(1+b)^2}{\Gamma(1+2b)}. \tag{3.2.11}$$

A further statement that can be derived within the MCT expansion is that the implying time-window of the α-relaxation process diverges like $t'_\sigma \sim |\sigma|^{-\gamma}$, with the non-universal exponent

$$\gamma := \frac{1}{2a} + \frac{1}{2b}. \tag{3.2.12}$$

The resulting divergence behaviour simultaneously holds for the ISFs of all wavenumbers, which is one of the central cornerstones of MCT. This is of particular interest in the context of this work since transport coefficients predicted from MCT are nothing but functionals of the

ISF, meaning that they are well-specified with the knowledge of the α-relaxation time. Consequently, transport coefficients close to the critical point predicted from MCT follow the same power-law with exponent γ that can be derived by calculating the exponent parameter λ.

3.3 Tagged Particle Dynamics

The ABP-MCT for mixtures includes the specific case in which a single tracer particle is immersed in a surrounding bath. This scenario is of particular interest in the context of experiments and simulations where the statistics of single-particle quantities is far easier accessible rather than those of collective quantities. It further allows to study different interesting scenarios, like the motion of an active tracer particle in a host of passive hard-disks or the response of a passive particle to an active bath. Last but not least, studying the tagged particle dynamics in the limit of low wavenumbers gives rises to equations of motion for the MSD as seen later.

The tagged particle shall be charaterized by the coordinates $\Gamma_s = (\vec{r}_s, \theta_s)$ and ABP parameters (D_t^s, D_r^s, v_0^s) furtheron. This means that the evolution of the probability density of the combined phase space $\Gamma = \Gamma_s \times \Gamma_b$ of bath- and tracer particles is determined by the total Smoluchowski operator given by $\mathbf{\Omega} = \mathbf{\Omega}_s + \mathbf{\Omega}_b$ with

$$\mathbf{\Omega}_s = \vec{\nabla}_s \left(\vec{\nabla}_s - \beta \vec{F}_s \right) + D_r^s \partial_{\theta_s}^2 - v_0^s \vec{\nabla} \cdot \vec{o}_s. \tag{3.3.1}$$

In the following, it will be convenient to introduce the concentration resolved fluctuating density which results in a concentration rescaled ISF as follows:

$$\tilde{\rho}_l^\alpha(\vec{q}) := \frac{1}{\sqrt{x_\alpha}} \rho_l^\alpha(\vec{q}), \qquad \tilde{\boldsymbol{S}}^{\alpha,\beta}(\vec{q},t) := \frac{1}{\sqrt{x_\alpha x_\beta}} \boldsymbol{S}^{\alpha,\beta}(\vec{q},t). \tag{3.3.2}$$

The quantity of interest that characterizes the dynamics of the tracer particle in the bath is the self-intermediate scattering function (SISF) defined as

$$\tilde{S}_{l,l'}^{s,s}(\vec{q},t) := S_{l,l'}^s(\vec{q},t) = \left\langle \tilde{\rho}_l^s(\vec{q})^* e^{\mathbf{\Omega}^\dagger t} \tilde{\rho}_{l'}^s(\vec{q}) \right\rangle, \tag{3.3.3}$$

where the introduction of a rescaled density has ensured $\boldsymbol{S}^s(\vec{q},t) \sim \mathcal{O}(1)$ as desired. An equation of motion for $\boldsymbol{S}^s(\vec{q},t)$ can be derived from equation (3.1.41) by considering a $(r+1)$ component mixture in the limit of a dilute tracer density $x_s \to 0$. The time evolution of the concentration resolved ISF reads

$$\partial_t \tilde{\boldsymbol{S}}(\vec{q},t) + \tilde{\boldsymbol{\omega}}(\vec{q}) \tilde{\boldsymbol{S}}^{-1}(q) \tilde{\boldsymbol{S}}(\vec{q},t) + \int_0^t dt' \; \tilde{\boldsymbol{m}}(\vec{q},t-t') \tilde{\boldsymbol{\omega}}_T^{-1}(\vec{q}) (\partial_t \tilde{\boldsymbol{S}}(\vec{q},t') + \tilde{\boldsymbol{\omega}}_R \tilde{\boldsymbol{S}}^{-1}(q) \tilde{\boldsymbol{S}}(\vec{q},t')) = 0, \tag{3.3.4}$$

where the tilted quantities are defined as in (3.3.2). It is further instructive to consider a schematic representation, where tagged- and collective contributions are split into different

blocks. Following equation (3.1.6) one finds in leading order of x_s that

$$\tilde{\boldsymbol{S}}^{-1}(\vec{q}) = \begin{pmatrix} \mathbb{1}_{2\Lambda_L+1} & -\rho \boldsymbol{c}^{b,s}\sqrt{x_s} \\ -\rho \boldsymbol{c}^{s,b}\sqrt{x_s} & (\tilde{\boldsymbol{S}}^{-1})^{b,b} \end{pmatrix}, \tag{3.3.5}$$

where the first row and first column accounts for tagged particle variables. An inversion of this matrix can be performed by exploiting a matrix-inversion formula for block matrixes. Let $\mathbb{K} = \mathbb{C}^{(2\Lambda_L+1)\times(2\Lambda_L+1)}$ and let $\boldsymbol{A} \in \mathbb{K}^{1\times 1}$, $\boldsymbol{D} \in \mathbb{K}^{r\times r}$ be square matrices with $\boldsymbol{A}$ invertible, $\boldsymbol{B} \in \mathbb{K}^{1\times r}$ and $\boldsymbol{C} \in \mathbb{K}^{r\times 1}$ matrices with $\boldsymbol{D}-\boldsymbol{C}\boldsymbol{A}^{-1}\boldsymbol{B}$ invertible then there holds

$$\begin{pmatrix} \boldsymbol{A} & \boldsymbol{B} \\ \boldsymbol{C} & \boldsymbol{D} \end{pmatrix}^{-1} = \begin{pmatrix} \boldsymbol{A}^{-1} + \boldsymbol{A}^{-1}\boldsymbol{B}(\boldsymbol{D}-\boldsymbol{C}\boldsymbol{A}^{-1}\boldsymbol{B})^{-1}\boldsymbol{C}\boldsymbol{A} & -\boldsymbol{A}^{-1}\boldsymbol{B}(\boldsymbol{D}-\boldsymbol{C}\boldsymbol{A}^{-1}\boldsymbol{B})^{-1} \\ -(\boldsymbol{D}-\boldsymbol{C}\boldsymbol{A}^{-1}\boldsymbol{B})^{-1}\boldsymbol{C}\boldsymbol{A}^{-1} & (\boldsymbol{D}-\boldsymbol{C}\boldsymbol{A}^{-1}\boldsymbol{B})^{-1} \end{pmatrix}. \tag{3.3.6}$$

Applying this formula to (3.3.5) reveals

$$\tilde{\boldsymbol{S}}(q) = \begin{pmatrix} \mathbb{1}_{2\Lambda_L+1} & -\rho \tilde{\boldsymbol{S}}^{b,b}\cdot \boldsymbol{c}^{b,s}\sqrt{x_s} \\ -\rho \boldsymbol{c}^{s,b}\cdot\tilde{\boldsymbol{S}}^{b,b}\sqrt{x_s} & \tilde{\boldsymbol{S}}^{b,b} \end{pmatrix} + \boldsymbol{\mathcal{O}}(x_s). \tag{3.3.7}$$

This implies that a schematic representation of the frequency-matrix reads

$$\tilde{\boldsymbol{\omega}}(\vec{q}) = \begin{pmatrix} \boldsymbol{\omega}^s(\vec{q}) & \boldsymbol{\mathcal{O}}(\sqrt{x_s}) \\ \boldsymbol{\mathcal{O}}(\sqrt{x_s}) & \tilde{\boldsymbol{\omega}}^{b,b} \end{pmatrix} + \boldsymbol{\mathcal{O}}(x_s), \tag{3.3.8}$$

with the tagged particle frequency matrix $\boldsymbol{\omega}^s(\vec{q}) := -\langle \tilde{\rho}^s_l(\vec{q})^* \boldsymbol{\Omega}^\dagger \rho^s_{l'}(\vec{q})\rangle = \boldsymbol{\omega}^s_T(\vec{q}) + \boldsymbol{\omega}_R$ where the matrix elements are

$$\omega^s_{T,l,l'}(\vec{q}) = D^s_t q^2 - i\frac{v^s_0 q}{2} e^{-i(l-l')\varphi_q}\delta_{|l-l'|,1}, \qquad \omega_{R,l,l'} = D^s_r l^2 \delta_{l,l'}. \tag{3.3.9}$$

The inversion of $\tilde{\boldsymbol{\omega}}_T(\vec{q})$ directly follows from (3.3.6) and reads schematically

$$\tilde{\boldsymbol{\omega}}_T^{-1}(\vec{q}) = \begin{pmatrix} \boldsymbol{\omega}_T^{s^{-1}} & \boldsymbol{\mathcal{O}}(\sqrt{x_s}) \\ \boldsymbol{\mathcal{O}}(\sqrt{x_s}) & (\tilde{\boldsymbol{\omega}}_T^{b,b})^{-1} \end{pmatrix} + \boldsymbol{\mathcal{O}}(x_s). \tag{3.3.10}$$

By knowing the scaling behaviour of the structure factor with the tracer density, a tedious inspection of all terms in equation (3.1.47) that is not elaborated here shows that $\tilde{\boldsymbol{m}}^{\alpha,\beta}$ takes a similar form and can be written as

$$\tilde{\boldsymbol{m}}(\vec{q},t) = \begin{pmatrix} \boldsymbol{m}^s & \boldsymbol{\mathcal{O}}(\sqrt{x_s}) \\ \boldsymbol{\mathcal{O}}(\sqrt{x_s}) & \tilde{\boldsymbol{m}}^{b,b} \end{pmatrix} + \boldsymbol{\mathcal{O}}(x_s), \tag{3.3.11}$$

with the tracer memory-kernel $\boldsymbol{m}^s(\vec{q},t) := \tilde{\boldsymbol{m}}^{s,s}(\vec{q},t) \sim \mathcal{O}(1)$. One can also show that all couplings to tracer variables vanish in the limit $x_s \to 0$ in $\tilde{\boldsymbol{m}}^{b,b}$. This expected since a vanishing small concentration of tracer particles will not be detectable in the dynamics of the bath in the thermodynamic limit. Extraction of the (s,s) component from equation (3.3.4) in leading order of x_s

subsequently allows to derive an equation of motion for the SISF:

$$\partial_t \boldsymbol{S}^s(\vec{q},t) = -\boldsymbol{\omega}^s(\vec{q})\boldsymbol{S}^s(\vec{q},t) - \int_0^t dt' \boldsymbol{m}^s(\vec{q},t-t')\boldsymbol{\omega}_T^{s^{-1}}(\vec{q})\Big[\partial_{t'}\boldsymbol{S}^s(\vec{q},t') + \boldsymbol{\omega}_R^s \boldsymbol{S}^s(\vec{q},t')\Big]. \quad (3.3.12)$$

One further makes the same observation as in passive MCT that $\boldsymbol{m}^s(\vec{q},t)$ does not couple to mixed correlation functions between tracer and bath variables in leading order of x_s. As derived in detail in appendix A.2 the contributing parts of the tracer memory-kernel can then be written as

$$m^s_{l,l'}(\vec{q},t) \approx \rho \int \frac{d^2p}{(2\pi)^2} \sum_{\substack{l_1,l_2 \\ \gamma_1\neq s,\gamma_2\neq s}} \mathcal{V}^{s,\gamma_1,\gamma_2}_{l,l_1,l_2}(\vec{q},\vec{q}-\vec{p})\; S^s_{l_2,l'}(\vec{p},t)\; S^{\gamma_1,\gamma_2}_{l_1,0}(\vec{q}-\vec{p},t), \quad (3.3.13)$$

with a static vertex function $\boldsymbol{\mathcal{V}}^s(\vec{q},\vec{k}) = \boldsymbol{\mathcal{V}}_{\mathrm{eq}}(\vec{q},\vec{k}) + \delta\boldsymbol{\mathcal{V}}(\vec{q},\vec{k})$ that combines an equilibrium part exactly given as from passive MCT and an active contribution explicity entered by the activities of both bath and tracer particles. The vertex functions are

$$\begin{aligned}
(\mathcal{V}_{\mathrm{eq}})^{s,\gamma_1,\gamma_2}_{l,l_1,l_2}(\vec{q},\vec{k}) &= (D^s_t)^2 c^{\gamma_1,s}(k)c^{\gamma_2,s}(k)(\vec{q}\cdot\vec{k})^2\delta_{l,l_2}\delta_{l_1,0},\\
\delta\mathcal{V}^{s,\gamma_1,\gamma_2}_{l,l_1,l_2}(\vec{q},\vec{k}) &= iD^s_t\frac{\vec{q}\cdot\vec{k}}{2}ke^{-i(l-l_1-l_2)\varphi_k}\sum_{\epsilon\neq s}c^{\epsilon,s}(k)c^{\gamma_2,s}(k)\Big(v_0^{\gamma_1}\frac{S^{\epsilon,\gamma_1}(k)}{x_{\gamma_1}}\delta_{l,l_2} - v_0^s\delta_{\gamma_1,\epsilon}\delta_{l_1,0}\Big)\delta_{|l-l_1-l_2|,1},
\end{aligned} \quad (3.3.14)$$

where the interaction between tracer and bath is entered through the tracer-bath direct correlation functions $c^{\alpha,s}(k)$. An alternate derivation of these equations in a monodisperse system has already been carried out in [84] by following the strategy to use a mixed density projection operator given by

$$\boldsymbol{\mathcal{P}}^s_2 := \sum_{1,2,3,4} |\rho^s_1\rho_2\rangle g^s_{1,2,3,4}\langle\rho^{s^*}_3\rho^*_4| \quad (3.3.15)$$

to derive the mode-coupling approximation for the tracer memory-kernel. This ansatz incorporates the interaction between bath and tracer particles through product states of respective densities. The result is fully consistent with that through the theory of mixtures presented here which offers a generalization to arbitrary tracer environments.

In analogy to equation (3.2.5) there follows an algebraic equation for non-ergodicity parameter $\boldsymbol{f}^s(\vec{q})$ of the tracer particle in the case $D^s_r = 0$ given by

$$\boldsymbol{f}^s(\vec{q}) + \boldsymbol{\omega}^{s^{-1}}(\vec{q})\boldsymbol{m}^s[\boldsymbol{f},\boldsymbol{f}^s]\boldsymbol{\omega}^{s^{-1}}(\vec{q})\big(\boldsymbol{f}^s(\vec{q}) - \mathbb{1}\big) = 0, \quad (3.3.16)$$

where $\boldsymbol{m}^s[\boldsymbol{f},\boldsymbol{f}^s]$ denotes an evaluation of $\boldsymbol{m}^s$ where the correlation functions have been replaced by $\boldsymbol{f}(\vec{q})$ and $\boldsymbol{f}^s(\vec{q})$.

3.3.1 Exact Inversion

Due to the simplified structure of the tagged particle frequency matrix, it is possible to obtain an exact inversion formula for its translational part $\omega^s_{T_{l,l'}}(\vec{q})$ for arbitrary values of the rotational

cutoff-number Λ_L. This can be achieved by closing a recurrence relation for the inverse of tridiagonal matrices [97] in the special case of Toeplitz matrices as it is $\boldsymbol{\omega}_T^s(\vec{q})$. A cumbersome calculation that is skipped here reveals in the limit $\Lambda_L \to \infty$

$$\omega^{s\,-1}_{T_{l,l'}}(\vec{q}) = e^{-i(l-l')\varphi_q} \frac{(iv_0^s q)^{|l-l'|}}{\Delta\left(D_t^s q^2 + \Delta\right)^{|l-l'|}}, \qquad \Delta := \sqrt{(D_t^s q^2)^2 + (v_0^s q)^2}. \tag{3.3.17}$$

This expression is straightforwardly verified by showing that $\boldsymbol{\omega}_T^s(\vec{q}) \cdot \boldsymbol{\omega}_T^{s\,-1}(\vec{q}) = \mathbb{1}$ is fulfilled for arbitrary Λ_L. It displays a peculiar behaviour for varying v_0^s, that provides some insightful interpretations. In figure 3.3.1, $\omega^{s\,-1}_{T_{0,0}}(q)$ is plotted against q in a double logarithmic representation, with v_0^s varying by several orders of magnitude. There emerges a crossover from a $1/q^2$ behaviour, equally found for a passive tracer, to a $1/q$ behaviour at $q \approx v_0^s/D_t^s$. This crossover can be rationalized by the motion of a free ABP, as the ballistic regime is only resolved on length scales $l \gg l_\nu = 2D_t^s/v_0^s$ that is accounted for by $\omega^{s\,-1}_{T_{0,0}}(q)$ if $2\pi/q \gg l_\nu$ while the regime $2\pi/q \ll l_\nu$ displays the features of passive Brownian diffusion. A further curious behaviour is seen when

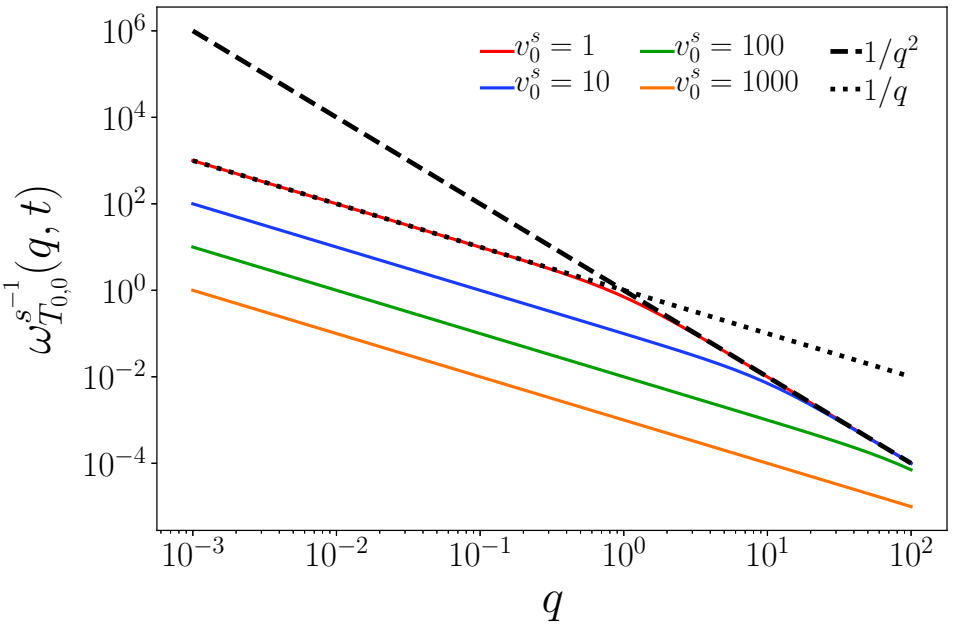

Figure 3.3.1.: *Analytical solution for* $\omega^{s\,-1}_{T_{0,0}}$ *according to equation* (3.3.17) *for different* v_0^s. *Black lines are* $1/q$ *and* $1/q^2$ *asymptotes as indicated.*

comparing numerical solutions for $\omega^{s\,-1}_{T_{0,0}}(q)$ at finite cutoffs Λ_L with the predictions from the analytic expression, as presented in figure 3.3.2 (a)-(d). The solutions for finite Λ_L reveal clear deviations from the presented analytical expression below a certain crossover wavenumber, that marks the emergence of different low-q asymptotes, depending on whether Λ_L is chosen even or odd. These discrepancies arise because for fixed Λ_L the numerical inversion of the low-q asymptote is considering the regime of small $q \cdot \Lambda_L$, whereas the true low-q asymptote that is relevant for physical application is only correct in the limit $q \cdot \Lambda_L \to \infty$ and this is always fulfilled for the presented analytical expression. One further notes that to correctly resolve the behaviour

of $\omega^{s\,-1}_{T_{0,0}}(q)$, the cutoff Λ_L must be chosen larger with increasing v_0^s. To correctly resolve the behaviour in a regime of relevant wavenumbers for the integration of the memory-kernel, the required Λ_L quickly approaches regimes that are far beyond the MCT numerics, which complexity rapidly increases with Λ_L. This observation provides a hint for the instabilities that occur at high self-propulsion velocities in the numerical routines that will be used later to solve the ABP-MCT dynamics since the non-commutative behaviour of inversion and cutoff formation presumably also occurs for the ISF in the numerical scheme and becomes most striking at large v_0.

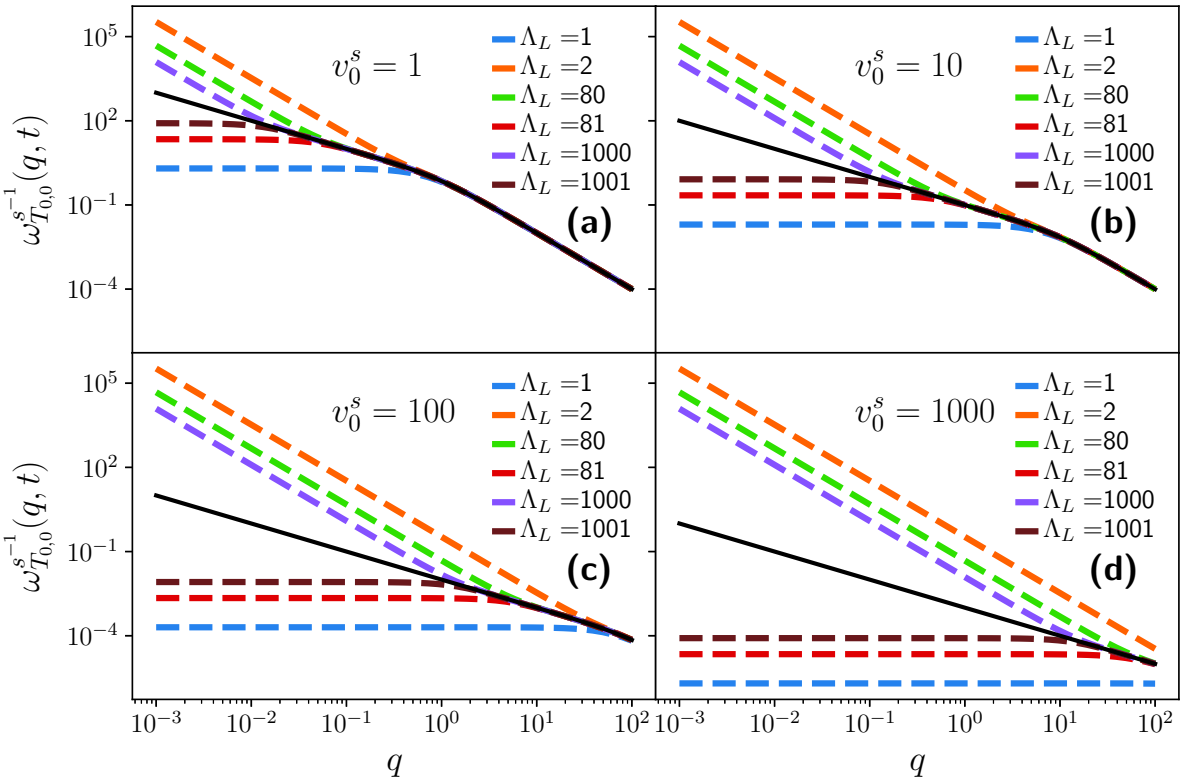

Figure 3.3.2.: ***(a)-(d)*** *Comparison between numerical solutions of* $\omega^{s\,-1}_{T_{0,0}}$ *at finite* Λ_L *(dashed coloured lines) with predictions from equation* (3.3.17) *(black solid lines) for different* v_0^s *and* Λ_L.

3.4 Hydrodynamic Limit and MSD

The dynamics of a tagged particle provides the theoretical basis to derive an equation of motion for the MSD of tracer particles in host environments. A fundamental relation between the SISF and the MSD is seen by considering the limit of low-q in equation (3.3.3), which reveals

$$\delta r^2(t) = 1 - \lim_{q\to 0}\left(\frac{4}{q^2}S^s_{0,0}(q,t)\right). \tag{3.4.1}$$

By extracting $S^s_{0,0}(q,t)$ from equation (3.3.12) and inserting this relation yields an equivalent set of coupled equations for $\delta r^2(t)$ of the tagged particle, reading

$$\partial_t \delta r^2(t) + \lim_{\vec{q}\to 0}\int_0^t dt' \sum_l m^s_{0,l}(\vec{q},t-t')\omega^{s^{-1}}_{T_{l,0}}(\vec{q})\partial_{t'}\delta r^2(t') = 4D^s_t + \lim_{\vec{q}\to 0}\frac{4}{q^2}\sum_{\pm}\omega^s_{0,\pm 1}S^s_{\pm 1,0}(\vec{q},t)$$
$$+ \lim_{\vec{q}\to 0}\int_0^t dt' \frac{4}{q^2}\sum_{\substack{l\\ l'\neq 0}} m^s_{0,l}(\vec{q},t-t')\omega^{s^{-1}}_{T_{l,l'}}(\vec{q})\left[\partial_{t'}S^s_{l',0}(\vec{q},t') + l'^2 D^s_r S^s_{l',0}(\vec{q},t')\right]. \tag{3.4.2}$$

The structure of this equation exceeds the complexity of its passive version through additional couplings to low-q $S_{l,0}(\vec{q},t)$ correlation functions. It is pointed out that the equation for the MSD is invariant under the rotation of the wavevector $\vec{q}$ according to the transformation law given by equation (3.1.7), as it is expected since it results from the isotropic $(0,0)$ component. Nevertheless, it still needs to be checked that all $q\to 0$ terms are well-defined by inspecting the low-q behaviour of all quantities that are involved. One first step to do so is to note that $S^{\alpha,\beta}_{l,l'}(\vec{q},t)$ is of order $q^{|l-l'|}$. This follows by observing that there only arise non-vanishing contribution from the time evolution operator that result from a $|l-l'|$-fold action of $\delta\mathbf{\Omega}^\dagger$ on $\rho^\beta_{l'}(\vec{q})$ which generates terms that are at least of order $q^{|l-l'|}$.

This is sufficient to perform a first consistency check of the equation of motion for the MSD by validating that it indeed reproduces the well-known analytic expression of the MSD for a free ABP from equation (2.2.10). To do so it is convenient to introduce the q-independent isotropic correlation function

$$\hat{\phi}^s_{\pm 1,0}(t) := \lim_{\vec{q}\to 0}\frac{1}{q}e^{\pm i\varphi_q}S^s_{\pm 1,0}(\vec{q},t). \tag{3.4.3}$$

For a free particle, the memory-integrals in equation (3.4.2) can be dropped which leads to the following equation of motion for the MSD

$$\partial_t \delta r^2 = 4D^s_t - \sum_{\pm} 2iv^s_0\hat{\phi}^s_{\pm 1,0}(t). \tag{3.4.4}$$

For $v^s_0 = 0$, the trivial solution of a passive particle $\partial_t\delta r^2 = 4D^s_t$ results. If $v^s_0 \neq 0$ there appear couplings that fulfill

$$\partial_t S_{\pm 1,0}(\vec{q},t) + \sum_{l'}\omega^s_{\pm 1,l'}S^s_{l',0}(\vec{q},t) =$$
$$\partial_t S_{\pm 1,0}(\vec{q},t) + \omega^s_{\pm 1,0}(\vec{q})S^s_{0,0}(q,t) + \omega^s_{\pm 1,\pm 1}(q)S^s_{\pm 1,0}(\vec{q},t) + \omega^s_{\pm 1,\pm 2}(\vec{q})S^s_{\pm 2,0}(\vec{q},t) = 0. \tag{3.4.5}$$

Checking the individual terms in the second line reveals that the first three are of order $\mathcal{O}(q)$ while the last one is of order $\mathcal{O}(q^3)$. Thus by multiplying both sides with $(1/q)e^{\pm i\varphi_q}$ and taking $q\to 0$ yields

$$\partial_t\hat{\phi}^s_{\pm 1,0}(t) = \frac{iv^s_0}{2} - D^s_r\hat{\phi}^s_{\pm 1,0}(t), \quad \Rightarrow \quad \hat{\phi}^s_{\pm 1,0}(t) = \frac{iv^s_0}{2D^s_r}(1-e^{-D^s_r t}), \tag{3.4.6}$$

where the initial condition $S^s_{\pm1,0}(0) = 0$ was used. Inserting this solution back into (3.4.4) and performing an integration while using the initial condition $\delta r^2(0) = 0$ finally results in equation (2.2.10).

To solve the equation of motion for the MSD in the general case of interacting particles requires to determine the hydrodynamic limits of the matrix elements of the memory-kernel and the inverse of the translational part of the frequency matrix. The latter results for the trivial case $v_0^s = 0$ of a passive tracer in $\omega^{s\,-1}_{T_{l,l'}}(\vec{q}) = 1/q^2\delta_{l,l'}$. For $v_0^s \neq 0$ a Taylor-expansion of (3.3.17) shows the following expression in leading order of q:

$$\omega^{s\,-1}_{T_{l,l'}}(\vec{q}) = e^{-i(l-l')\varphi_q} i^{|l-l'|}\left[\frac{1}{v_0^s q} - \frac{|l-l'|D_t^s}{(v_0^s)^2}\right] + \mathcal{O}(q). \tag{3.4.7}$$

This means that the limits $\vec{q} \to 0$ and $v_0^s \to 0$ do not commute as the low-q asymptote changes discontinuously from $\mathcal{O}(q^{-2})$ to $\mathcal{O}(q^{-1})$ when switching on the activity of the tracer particle. This means that any small activity is detectable in the system if only the length scale that is observed is chosen sufficiently large. It will also lead to entirely different equations of motion for the MSD in the respective cases of passive and active tracers as seen below.

The low-q expansion of the tracer memory-kernel is presented in the following by starting with an expansion of the vertex functions $\boldsymbol{\mathcal{V}}_{\rm eq}(\vec{q},\vec{k})$ and $\delta\boldsymbol{\mathcal{V}}(\vec{q},\vec{k})$ given by the equations in (3.3.14). Setting $\vec{k} = \vec{q} - \vec{p}$ and writing $(\vec{q}\cdot\vec{k})k = (q^2 - \vec{q}\cdot\vec{p})\,k$, one can exploit the Taylor-expansion for a function of a scalar variable $f(k) = f(p) - f'(p)\vec{q}\cdot\vec{p}/p + \mathcal{O}(q^2)$. Making further use $e^{\pm i\alpha_k} = -e^{\pm i\alpha_p} + \mathcal{O}(\vec{q}\cdot\vec{e}_{\varphi_p})$ the Taylor expansion of the both equilibrium and non-equilibrium in equation (3.3.14) read in leading order of q

$$(\mathcal{V}_{\rm eq})^{s,\gamma_1,\gamma_2}_{l,l_1,l_2}(\vec{q},\vec{k}\,) = (D_t^s)^2 c^{\gamma_1,s}(p)c^{\gamma_2,s}(p)\,(\vec{q}\cdot\vec{p}\,)^2\,\delta_{l,l_2}\delta_{l_1,0} + \mathcal{O}(q^3), \tag{3.4.8}$$

$$\begin{aligned}\delta\mathcal{V}^{s,\gamma_1,\gamma_2}_{l,l_1,l_2}(\vec{q},\vec{k}) = i\frac{D_t^s}{2}e^{-i(l-l_1-l_2)\varphi_p}\delta_{|l-l_1-l_2|}\Bigg\{&\Big((\vec{q}\cdot\vec{p}\,)p - \frac{(\vec{q}\cdot\vec{p}\,)^2}{p} - q^2p\Big)\\ &\times\sum_{\epsilon\neq s}c^{\epsilon,s}(p)c^{\gamma_2,s}(p)\Big(v_0^{\gamma_1}\frac{S^{\epsilon,\gamma_1}(p)}{x_{\gamma_1}}\delta_{l,l_2} - v_0^s c^{\gamma_1,s}(p)\delta_{l_1,0}\delta_{\gamma_1,\epsilon}\Big)\\ -(\vec{q}\cdot\vec{p}\,)^2\partial_p\Big[\sum_{\epsilon\neq s}&c^{\epsilon,s}(p)c^{\gamma_2,s}(p)\Big(v_0^{\gamma_1}\frac{S^{\epsilon,\gamma_1}(p)}{x_{\gamma_1}}\delta_{l,l_2} - v_0^s c^{\gamma_1,s}(p)\delta_{l_1,0}\delta_{\gamma_1,\epsilon}\Big)\Big]\\ &+\mathcal{O}\Big((\vec{q}\cdot\vec{p}\,)(\vec{q}\cdot\vec{e}_{\varphi_p})\Big)\Bigg\} + \mathcal{O}(q^3).\end{aligned} \tag{3.4.9}$$

It is convenient to introduces isotropized correlation functions as $\hat{S}^{\alpha,\beta}_{l,l'}(p,t) := e^{i(l-l')\varphi_p}S^{\alpha,\beta}_{l,l'}(\vec{p},t)$ which allows to express the correlation functions that appear in the $\vec{p}$ integration of equation

(3.3.13) in terms of

$$\begin{aligned} S^s_{l_2,l'}(\vec{p},t) &= e^{-i(l_2-l')\varphi_p}\hat{S}^s_{l_2,l'}(p,t), \\ S^{\gamma_1,\gamma_2}_{l_1,0}(\vec{k},t) &= e^{-il_1(\varphi_p+\pi)}\Big(1-\frac{\vec{q}\cdot\vec{p}}{p}\partial_p+\mathcal{O}(\vec{q}\cdot\vec{e}_{\varphi_p})\Big)\hat{S}^{\gamma_1,\gamma_2}_{l_1,0}(p,t)+\mathcal{O}(q^2). \end{aligned} \tag{3.4.10}$$

After inserting the expansions (3.4.8), (3.4.9) and (3.4.10) into equation (3.3.13), the $\vec{p}$ integration is performed in polar coordinates, where the φ_p integration can be done analytically. The resulting matrix elements of the tracer memory-kernel that will be relevant for the latter calculation of the MSD are given in leading order in q as follows:

$$(m_{\mathrm{eq}})^s_{0,0}(\vec{q},t) = (D^s_t q)^2\frac{\rho}{4\pi}\int_0^\infty dp\sum_{\gamma_1\neq s,\gamma_2\neq s} p^3 c^{\gamma_1,s}(p)c^{\gamma_2,s}(p)\hat{S}^s_{0,0}(p,t)\hat{S}^{\gamma_1,\gamma_2}_{0,0}(p,t)+\mathcal{O}(q^3), \tag{3.4.11}$$

$$\begin{aligned} \delta m^s_{0,0}(\vec{q},t) = iD^s_t q^2\frac{\rho}{8\pi}\int_0^\infty dp\sum_{\substack{\epsilon\neq s\\ \gamma_1\neq s,\gamma_2\neq s}}\Bigg\{ & v_0^{\gamma_1}\partial_p\Big[p^3c^{\epsilon,s}(p)c^{\gamma_2,s}(p)\frac{S^{\epsilon,\gamma_1}(p)}{x_{\gamma_1}}\sum_\pm \hat{S}^{\gamma_1,\gamma_2}_{\pm1,0}(p,t)\Big]\hat{S}^s_{0,0}(p,t) \\ & + v_0^s\partial_p\Big[p^3c^{\epsilon,s}(p)c^{\gamma_2,s}(p)\delta_{\epsilon,\gamma_1}\hat{S}^{\gamma_1,\gamma_2}_{0,0}(p,t)\Big]\sum_\pm\hat{S}^s_{\pm1,0}(p,t)\Bigg\}+\mathcal{O}(q^3), \end{aligned} \tag{3.4.12}$$

$$\begin{aligned} \delta m^s_{0,l}(\vec{q},t) = -i\delta_{|l|,1}e^{il\varphi_q}D^s_t q\frac{\rho}{8\pi}\int_0^\infty dp\sum_{\substack{\epsilon\neq s\\ \gamma_1\neq s,\gamma_2\neq s}} p^3c^{\epsilon,s}(p)c^{\gamma_2,s}(p)\Bigg\{ & v_0^{\gamma_1}\frac{S^{\epsilon,\gamma_1}(p)}{x_{\gamma_1}}\hat{S}^s_{0,l}(p,t)\sum_\pm\hat{S}^{\gamma_1,\gamma_2}_{\pm1,0}(p,t) \\ & + v_0^s\delta_{\epsilon,\gamma_1}\sum_\pm\hat{S}^s_{l,\pm1}(p,t)\hat{S}^{\gamma_1,\gamma_2}_{0,0}(p,t)\Bigg\}+\mathcal{O}(q^2), \end{aligned} \tag{3.4.13}$$

$$\begin{aligned} \delta m^s_{l,0}(\vec{q},t) = -i\delta_{|l|,1}e^{-il\varphi_q}D^s_t q\frac{\rho}{8\pi}\int_0^\infty dp\sum_{\substack{\epsilon\neq s\\ \gamma_1\neq s,\gamma_2\neq s}} p^3c^{\epsilon,s}(p)c^{\gamma_2,s}(p)\Bigg\{ & v_0^{\gamma_1}\frac{S^{\epsilon,\gamma_1}(p)}{x_{\gamma_1}}\sum_\pm\hat{S}^s_{l,0}(p,t)\hat{S}^{\gamma_1,\gamma_2}_{\pm1,0}(p,t) \\ & + v_0^s\delta_{\epsilon,\gamma_1}\sum_\pm\hat{S}^s_{l\pm1,0}(p,t)\hat{S}^{\gamma_1,\gamma_2}_{0,0}(p,t)\Bigg\}+\mathcal{O}(q^2), \end{aligned} \tag{3.4.14}$$

where any other $m^s_{l,l'}(\vec{q},t)$ shows to be of order $\mathcal{O}(q)$ for $|l-l'|=1$ and of order $\mathcal{O}(q^2)$ else. Having determined the low-q behaviour of all quantities, the resulting equations of motion for $\delta r^2(t)$ after performing the limits in equation (3.4.2) are given in the following by distinguishing the scenarios of active and passive tracer particles. This is necessary because there arise different equation of motion as one notes that the components of the memory-kernel that couple in leading order to $\delta r^2(t)$ change in the respective scenarios. As derived in detail in appendix A.3.1 the

equation of motion for a passive tracer reads

$$\begin{aligned}\partial_t \delta r^2(t) + D_t^s \int_0^t dt' \hat{m}^s(t-t')\delta r^2(t') &= 4D_t^s, \\ \hat{m}^s(t) := \lim_{q\to 0} \frac{1}{(D_t^s q)^2}\Big((m_{\mathrm{eq}})^s_{0,0}(\vec{q},t) + \delta m^s_{0,0}(\vec{q},t)\Big).\end{aligned} \tag{3.4.15}$$

This is the same equation that is already known from passive MCT, but with an extra memory-kernel $\delta m^s_{0,0}(\vec{q},t)$. The activity of the host particles is being entered in two different ways. On the one hand, there arises an implicit contribution through a faster relaxation of the $S_{0,0}(\vec{q},t)$ correlation function within $(m_{\mathrm{eq}})^s_{0,0}(\vec{q},t)$ when increasing activity. This can be seen as a renormalization of the density as activity shifts the glass transition density. On the other hand, there emerges an explicit activity-induced term $\delta m^s_{0,0}(\vec{q},t)$ that translates typical features of active motion like superdiffusive behaviour to the passive particle through couplings to $S^{\alpha,\beta}_{\pm 1,0}(\vec{q},t)$ correlation functions of the active bath.

The equation of motion for $\delta r^2(t)$ in the case of an active tracer particle becomes more complicated because additional couplings to low-q $S_{l,0}(q,t)$ correlation functions are involved, that are governed by a separate equation of motion. Using the expansions for the memory-kernels and equation (3.4.7), the same structure as for the free particle is observed that only $\hat{\phi}^s_{\pm 1,0}(t)$ correlators surive in leading order of q. As derived in detail in appendix A.3.2 the equation of motion for $\delta r^2(t)$ is given by

$$\begin{aligned}\partial_t \delta r^2(t) + \frac{i}{v_0^s}\int_0^t dt' \sum_{\pm} \hat{m}^s_{0,\pm 1}(t-t')\partial_{t'}\delta r^2(t') &= 4D_t^s - \sum_{\pm} 2iv_0^s \hat{\phi}^s_{\pm 1,0}(t) \\ + \frac{4i}{v_0^s}\int_0^t dt' \hat{m}^s_{0,0}(t-t') \sum_{\pm}\left[\partial_{t'}\hat{\phi}^s_{\pm 1,0}(t') + D_r^s \hat{\phi}^s_{\pm 1,0}(t')\right], \\ + \frac{4D_t^s}{(v_0^s)^2}\int_0^t dt' \sum_{\pm} \hat{m}^s_{0,\pm 1}(t-t') \sum_{\pm}\left[\partial_{t'}\hat{\phi}^s_{\pm 1,0}(t') + D_r^s \hat{\phi}^s_{\pm 1,0}(t')\right],\end{aligned} \tag{3.4.16}$$

$$\partial_t \hat{\phi}^s_{\pm 1,0}(t) = \frac{iv_0^s}{2} - D_r^s \hat{\phi}^s_{\pm 1,0}(t) - \frac{i}{v_0^s}\int_0^t dt' \hat{m}^s_{\pm 1,0}(t-t') \sum_{\pm}\left[\partial_{t'}\hat{\phi}^s_{\pm 1,0}(t') + D_r^s \hat{\phi}^s_{\pm 1,0}(t')\right]. \tag{3.4.17}$$

Where the isotropized and q-independent memory-kernels are defined as

$$\hat{m}^s_{l,l'}(t) = \lim_{\vec{q}\to 0} \frac{q^{|l-l'|}}{q^2} e^{i(l-l')\varphi_q} m^s_{l,l'}(\vec{q},t). \tag{3.4.18}$$

If the system experiences dynamical arrest, the tracer particle remains in a localized state for infinite times, meaning that $\lim_{t\to\infty}\delta r^2(t)$ approaches a constant, while becoming unbounded in the fluid state. In the first case, the plateau value of the MSD indicates the localization length of the tracer via the relation $4l_c^2 = \lim_{t\to\infty}\delta r^2(t)$ which can be calculated from the long-time behaviour of the memory-kernels. This is achieved by dropping $\partial_t \delta r^2(t)$ at long times wherein the case of a passive tracer, both equations in (3.4.15) reveal

$$l_c = 1/\sqrt{\lim_{t\to\infty} \hat{m}^s(t)}. \tag{3.4.19}$$

It is therefore possible to immediately calculate the localization length from the non-ergodicity parameters $\boldsymbol{f}(\vec{q})$ and $\boldsymbol{f}^s(\vec{q})$ by replacing the correlation functions in $\hat{m}^s(t)$ with them. In the specific case of $D_r = 0$, this constitutes an efficient way to calculate l_c by using the self-consistent iterative equations for $\boldsymbol{f}(\vec{q})$ and $\boldsymbol{f}^s(\vec{q})$.

In the case of an active tracer, the equation for the localization length changes entirely and can be obtained for $D_r^s = 0$ by

$$\lim_{t\to\infty} \delta r^2(t) = \lim_{t\to\infty} \frac{v_0^s}{\sum_\pm i\hat{m}^s_{0,\pm1}(t)} \Big[4D_t^s - \sum_\pm \hat{f}^s_{\pm1,0}\Big(2iv_0^s - \frac{4i}{v_0^s}\hat{m}^s_{0,0}(t) - \frac{4D_t^s}{(v_0^s)^2}\sum_\pm \hat{m}^s_{0,\pm1}(t)\Big)\Big], \tag{3.4.20}$$

where the $\hat{f}_{\pm1,0} := \lim_{t\to\infty}\hat{\phi}_{\pm1,0}(t)$ are obtained by

$$\sum_\pm \hat{f}^s_{\pm1,0} = \frac{(v_0^s)^2}{\lim_{t\to\infty}\sum_\pm \hat{m}^s_{\pm1,0}(t)}. \tag{3.4.21}$$

3.5 ITT Effective Swimming Velocity

A transport coefficient that is specific for ABPs is given by the effective swimming velocity which underlying definition stems from the projection of the velocity vector in the direction of orientation. Both vectors are in general not expected to be equally aligned in an interacting system as for a free self-propelled particle. The effective swimming velocity, therefore, accounts for the reduction of motility through interactions with the host environment. An expression for v^α results from the overdamped Langevin-equation for $\dot{\vec{r}}_i^\alpha$ by projecting on $\vec{o}_i^\alpha$ and taking the transient ensemble average. This yields

$$v^\alpha = v_0^\alpha + \frac{D_t^\alpha\beta}{N_\alpha}\sum_{i=1}^{N_\alpha}\Big\langle \vec{F}_i^\alpha\cdot\vec{o}_i^\alpha\Big\rangle^{v_0}. \tag{3.5.1}$$

After applying the ITT formula (2.3.7) the effective swimming velocity is expressed as a Green-Kubo integral by using $\delta\boldsymbol{\Omega}p_{\mathrm{eq}} = -\beta\sum_{(j,\gamma)}v_0^\gamma\vec{F}_j^\gamma\cdot\vec{o}_j^\gamma p_{\mathrm{eq}}$. This results in

$$\frac{D_t^\alpha\beta}{N_\alpha}\sum_{i=1}^{N_\alpha}\Big\langle\vec{F}_i^\alpha\cdot\vec{o}_i^\alpha\Big\rangle^{v_0} = -\frac{D_t^\alpha\beta^2}{N_\alpha}\sum_{i=1}^{N_\alpha}\sum_{(j,\gamma)}v_0^\gamma\int_0^\infty dt\Big\langle\vec{F}_j^\gamma\cdot\vec{o}_j^\gamma\, e^{\boldsymbol{\Omega}^\dagger t}\,\vec{F}_i^\alpha\cdot\vec{o}_i^\alpha\Big\rangle = -\frac{D_t^\alpha\beta^2}{N_\alpha}\lim_{z\to0}\sum_\gamma v_0^\gamma C^{\gamma,\alpha}(z), \tag{3.5.2}$$

where the integral has been expressed in terms of the correlation function $C^{\gamma,\alpha}(z)$ in Laplace space that reads

$$C^{\gamma,\alpha}(z) := \sum_{i=1}^{N_\alpha}\sum_{j=1}^{N_\gamma}\Big\langle\vec{F}_j^\gamma\cdot\vec{o}_j^\gamma\,(z-\boldsymbol{\Omega}^\dagger)^{-1}\,\vec{F}_i^\alpha\cdot\vec{o}_i^\alpha\Big\rangle. \tag{3.5.3}$$

This is a straightforward generalization of the Green-Kubo expression that has already been derived and approximated in the framework of the linear-response theory [76] as well as in the MCT-ITT approach [84] for a single-component active system. Before this MCT-ITT approach can be extended to the theory of mixtures, the derived ITT expression demands some further

treatment because the force-force correlation function that is involved obeys the same characteristics as the diffusion memory-kernel in equation (3.1.15) close to the glass transition point, meaning that it would easily violate $v^\alpha < 0$. Following the same technical steps as when rewriting the diffusion kernel in terms of a friction kernel the force-force correlator can be rewritten in terms of an irreducible Smoluchowski operator by defining

$$\mathbf{\Omega}^\dagger_{\mathrm{irr}} := \mathbf{\Omega}^\dagger - \frac{D_t^\alpha \beta^2}{N_\alpha} \sum_{i=1}^{N_\alpha} \sum_{j=1}^{N_\gamma} \left| \vec{F}_i^\alpha \cdot \vec{o}_i^\alpha \right\rangle \left\langle \vec{F}_j^\gamma \cdot \vec{o}_j^\gamma \right| . \tag{3.5.4}$$

Inserting this expression into $C^{\gamma,\alpha}(z)$ and making use of the Dyson decomposition written in Laplace space,

$$(z - \boldsymbol{A} + \boldsymbol{B})^{-1} = (z - \boldsymbol{A})^{-1} + (z - \boldsymbol{A} + \boldsymbol{B})^{-1} \boldsymbol{B} (z - \boldsymbol{A})^{-1}, \tag{3.5.5}$$

reveals a connection between $C^{\gamma,\alpha}(z)$ and $C^{\gamma,\alpha}_{\mathrm{irr}}(z)$, where the latter is defined by replacing $\mathbf{\Omega}^\dagger$ with $\mathbf{\Omega}^\dagger_{\mathrm{irr}}$ in equation (3.5.3). One finds

$$C^{\gamma,\alpha}(z) = \frac{C^{\gamma,\alpha}_{\mathrm{irr}}(z)}{1 + (D_t^\alpha \beta^2 / N_\alpha) C^{\gamma,\alpha}_{\mathrm{irr}}(z)}. \tag{3.5.6}$$

Taking the limits $z \to 0$ on both sides and transforming back to the time domain results in

$$\int_0^\infty dt\, C^{\gamma,\alpha}(t) = \frac{\int_0^\infty dt C^{\gamma,\alpha}_{\mathrm{irr}}(z)}{1 + (D_t^\alpha \beta^2 / N_\alpha) \int_0^\infty dt\, C^{\gamma,\alpha}_{\mathrm{irr}}(t)}. \tag{3.5.7}$$

The irreducible correlator $C^{\gamma,\alpha}_{\mathrm{irr}}(t)$ is suitable to be subject of the mode-coupling approximation by inserting two-point projectors, viz.

$$C^{\gamma,\alpha}_{\mathrm{irr}}(t) \approx \sum_{i=1}^{N_\alpha} \sum_{j=1}^{N_\gamma} \left\langle \vec{F}_j^\gamma \cdot \vec{o}_j^\gamma \boldsymbol{\mathcal{P}}_2 e^{\mathbf{\Omega}^\dagger_{\mathrm{irr}} t} \boldsymbol{\mathcal{P}}_2 \vec{F}_i^\alpha \cdot \vec{o}_i^\alpha \right\rangle. \tag{3.5.8}$$

The calculation of the static vertex functions is presented in detail in appendix A.4 where it is shown that the irreducible correlator that determines v^α can be written after performing the MCT approximation as

$$\begin{aligned} \frac{D_t^\alpha \beta^2}{N_\alpha} C^{\gamma,\alpha}_{\mathrm{irr}}(t) \approx \frac{D_t^\alpha \rho}{8\pi x_\alpha} \sum_{\substack{\gamma_1..\gamma_4 \\ l=\pm1, l'=\pm1}} \int_0^\infty dp\, p^3 c^{\gamma_1,\gamma_2}(p) c^{\gamma_3,\gamma_4}(p) \delta_{\gamma,\gamma_2} \\ \times \left(\hat{S}^{\gamma_1,\gamma_3}_{0,0}(p,t) \hat{S}^{\gamma_2,\gamma_4}_{l,l'}(p,t) \delta_{\alpha,\gamma_4} + \hat{S}^{\gamma_1,\gamma_3}_{0,l}(p,t) \hat{S}^{\gamma_2,\gamma_4}_{l',0}(p,t) \delta_{\alpha,\gamma_3} \right). \end{aligned} \tag{3.5.9}$$

Restricting to the effective swimming velocity v of a single component active system, this expression yields

$$v = \frac{v_0}{1 + (D_t \beta^2 / N) \int_0^\infty dt\, C_{\mathrm{irr}}(t)}, \tag{3.5.10}$$

with $C_{\mathrm{irr}}(t)$ as given as in (3.5.9) by dropping all species indices and already derived in [84]. In this case, the mean effective swimming velocity exhibits an interesting connection with the motility-induced phase separation: Although the ABP-MCT assumes the system to be homo-

geneous and does not consider this phenomenon from first principle, the effective swimming velocity can be exploited to construct an effective free energy functional, that yields a stability criterion for a spinodal decomposition to occur in a homogeneous system [98]. This criterion has been invoked in [84] to construct a MIPS transition diagram that has revealed qualitative agreements with those reported from simulations.

A further implying special case of equation (3.5.9), that will be in the focus of interest in the numerical analysis of the MCT equations later on is the effective swimming velocity v^s of an active tagged particle in a passive hard-disk environment. In this case the derived MCT-ITT expression yields by taking the limit $x_s \to 0$

$$v^s = \frac{v_0^s}{1 + D_t^s \beta^2 \int_0^\infty dt C_{\mathrm{irr}}^s(t)}, \tag{3.5.11}$$

with an irreducible correlator given by

$$D_t^s \beta^2 C_{\mathrm{irr}}^s(t) \approx \frac{D_t^s \rho}{8\pi} \sum_{\substack{\gamma_1 \neq s, \gamma_2 \neq s \\ l=\pm 1, l'=\pm 1}} \int_0^\infty dp\, p^3 c^{\gamma_1,s}(p) c^{\gamma_2,s}(p) \hat{S}_{l,l'}^s(p,t) \hat{S}_{0,0}^{\gamma_1,\gamma_2}(p,t). \tag{3.5.12}$$

Moreover one checks for the disappearance of an effective swimming velocity of a passive particle type α in an active bath from equation (3.5.9) as an expected physical result. This is seen by noting that there can only arise contributions for $C^{\gamma,\alpha}(t)$ correlators with $\gamma \neq \alpha$ denoting active particle types. But these correlators vanish as they are entered by $\hat{S}_{l,l'}^{\gamma,\alpha}(p,t)$ and $\hat{S}_{0,l}^{\gamma_1,\alpha}(p,t)$ that both disappear for $l, l' \neq 0$.

3.6 ITT Zero-Shear Viscosity

A transport coefficient that quantifies the stress contributions arising in dense suspension close to dynamical arrest is the zero-shear viscosity, denoted as η in the following. An approximate expression for η can be derived by following the MCT-ITT approach by considering a system that is subject to a constant shear-flow in one direction. In this case, the trajectories are governed by the following overdamped Langevin-equation

$$\begin{aligned} d\vec{r}_i^{\,\alpha} &= \beta D_t^\alpha \vec{F}_i^\alpha dt + \sqrt{2D_t^\alpha} d\vec{W}_i^{\,\alpha} + v_0^\alpha \vec{o}_i^{\,\alpha}(\theta_i^\alpha) dt + \boldsymbol{\kappa} \cdot \vec{r}_i^{\,\alpha} dt, \\ d\theta_i^\alpha &= \sqrt{2D_r^\alpha} dW_{\theta_i}^\alpha. \end{aligned} \tag{3.6.1}$$

Here $\boldsymbol{\kappa}$ denotes the flow tensor, which in the case of a a linear shear flow in x-direction with a constant shear rate $\dot{\gamma}$ is given by $\kappa_{x,y} = \dot{\gamma}\, \delta_{a,x} \delta_{b,y}$, fulfilling the incompressibility condition $\mathrm{tr}(\boldsymbol{\kappa}) = 0$ with tr denoting the trace operator. Note that any flow gradient induces a constant torque on all particles, that would have to be considered when discussing the dynamics of ABPs. This term is neglected however as it vanishes in the case $\dot{\gamma} \to 0$ that will be the only of interest later on for the calculation of the zero-shear viscosity. The presented equations of motion can be translated into an equivalent time evolution equation for the probability density that is driven

by the Smoluchowski operator

$$\mathbf{\Omega} = \sum_{(i,\alpha)} D_t^\alpha \vec{\nabla}_i^\alpha \left(\vec{\nabla}_i^\alpha - \beta \vec{F}_i^\alpha \right) + D_r^\alpha \partial_{\theta_i^\alpha}^2 - v_0^\alpha \vec{\nabla}_i^\alpha \cdot \vec{o}_i^\alpha - \vec{\nabla}_i^\alpha \boldsymbol{\kappa} \cdot \vec{r}_i^\alpha, \tag{3.6.2}$$

where an additional non-equilibrium pertubation in form of the shear flow emerges. To disciminate the two types of non-equilibrium contributions, one splits $\delta\mathbf{\Omega} = \delta\mathbf{\Omega}^{v_0} + \delta\mathbf{\Omega}^{\dot\gamma}$. A macroscopic variable that characerizes the stress contributions in the system is the (transient) shear stress $\sigma^{x,y}$, defined as the transient average of the microscopic stress tensor $\hat\sigma^{x,y} := -V^{-1}\sum_{(i,\alpha)} F_{i,x}^\alpha r_{i,y}^\beta$ as

$$\sigma^{x,y} := \left\langle \hat\sigma^{x,y} \right\rangle^{v_0,\dot\gamma} = -\frac{1}{V} \sum_{(i,\alpha)} \left\langle F_{i,x}^\alpha \, r_{i,y}^\alpha \right\rangle^{v_0,\dot\gamma}. \tag{3.6.3}$$

Applying the ITT formula requires to calculate the action of $\delta\mathbf{\Omega}$ on the Boltzmann-distribution. This results in

$$\delta\mathbf{\Omega}\, p_{\mathrm{eq}} = -\sum_{(i,\alpha)} (v_0^\alpha \vec{\nabla}_i^\alpha \vec{o}_i^\alpha + \vec{\nabla}_i{}^\alpha \boldsymbol{\kappa} \cdot \vec{r}_i^\alpha) p_{\mathrm{eq}} = -\sum_{(i,\alpha)} v_0^\alpha \beta \vec{F}_i^\alpha \vec{o}_i^\alpha p_{\mathrm{eq}} + \dot\gamma \beta V \hat\sigma^{x,y} p_{\mathrm{eq}}, \tag{3.6.4}$$

and reveals a Green-Kubo type expression for the shear stress as given as follows

$$\begin{aligned} \sigma^{x,y} &= -\sum_{(i,\alpha)} v_0^\alpha \int_0^\infty dt \left\langle \beta \vec{F}_i^\alpha \vec{o}_i^\alpha e^{\mathbf{\Omega}^\dagger t} \hat\sigma^{x,y} \right\rangle + \dot\gamma \beta V \int_0^\infty dt \left\langle \hat\sigma^{x,y} e^{\mathbf{\Omega}^\dagger t} \hat\sigma^{x,y} \right\rangle \\ &= \left\langle \hat\sigma_{x,y} \right\rangle^{v_0} + \left\langle \hat\sigma_{x,y} \right\rangle^{\dot\gamma}, \end{aligned} \tag{3.6.5}$$

where $\langle \hat\sigma^{x,y} \rangle = 0$ was exploited in equilibrium. It is further noted that the associated structure of the Smoluchowski operator violates the translational invariance of the system due to the shear flow term. This means that at finite shear rates, transient correlation functions must account for this effect by including time-dependent advection of the wavevectors [48]. However, these considerations can also be dispensed in the limit $\dot\gamma \to 0$ performed later on.

In a similar fashion as in the last section, the equilibrium averages in the definition of the shear stress are approximated by inserting the two-point projectors given by equation (3.1.42) which allows the MCT approximation to be applied once more, thus

$$\sigma^{x,y} \approx -\sum_{(i,\alpha)} v_0^\alpha \int_0^\infty dt \left\langle \vec{o}_i^\alpha \beta \vec{F}_i^\alpha \boldsymbol{\mathcal{P}}_2 e^{\mathbf{\Omega}^\dagger t} \boldsymbol{\mathcal{P}}_2 \hat\sigma^{x,y} \right\rangle + \dot\gamma \beta V \int_0^\infty dt \left\langle \hat\sigma^{x,y} \boldsymbol{\mathcal{P}}_2 e^{\mathbf{\Omega}^\dagger t} \boldsymbol{\mathcal{P}}_2 \hat\sigma^{x,y} \right\rangle. \tag{3.6.6}$$

The calculation of the static vertex functions is shifted to appendix A.5, revealing that the first term, the explicit active contribution to the stress, vanishes[1]. The contributing term to the zero-shear viscosity in the MCT-ITT approximation is

$$\eta = \lim_{\dot\gamma \to 0} \frac{\sigma^{x,y}}{\dot\gamma} \approx \frac{\rho^2}{32\pi\beta} \int_0^\infty dt \int_0^\infty dq\, q^3 \ \mathrm{tr}\left[\left(\boldsymbol{S}_{0,0}(q,t) \partial_q \boldsymbol{c}(q) \right)^2 \right]. \tag{3.6.7}$$

[1] This should already hold from equation (3.6.5) before applying the MCT approximation by calculating powers of $\mathbf{\Omega}^\dagger$ and calculating the equilibrium average, but is not easily seen.

This means that the influence of activity is only implicitly entered in terms of its influence on the $\boldsymbol{S}_{0,0}(q,t)$ correlation functions. The shear viscosity in the limit of small shear rates is also denoted as yield-viscosity and indicates the minimum work, that is required to break the global cage structure of the system and restore the ergodicity in the system. It is therefore closely related to the relaxation time which becomes clear for systems close to the glass transition point where the integrand is dominated by the long-time contributions of the correlation functions. In this case, η is well approximated by replacing the correlation functions with their plateau value and the time integral is approximated by the relaxation time,

$$\eta \approx \frac{\rho^2}{32\pi\beta} \int_0^\infty dq\, q^3\, \tau_\alpha(q)\, \mathrm{tr}\left[\left(\boldsymbol{f}_{0,0}(q)\partial_q \boldsymbol{c}(q)\right)^2\right]. \tag{3.6.8}$$

This means that the decisive variable to characterize the stress contributions near the glass transition point is the exponent parameter γ that describes the divergence of the $\tau_\alpha(q)$. It is therefore of great interest to investigate the non-trivial effect of activity on this divergence behaviour by using the asymptotic expansion of the MCT equations presented in section 3.2. Further, it is noted that by following the spirit of the ITT formalism only allows calculating relative viscosity contributions, that stem from the perturbation of the hard-disk interaction, meaning that both contributions of the solvent and single-particle contributions are entirely left out. This yields a good approximation at medium and high densities since the solvent's contribution to the viscosity is in first-order in the density by noting the well-known Einstein correction. But on the other hand, the lack to describe single-particle contributions inhibits the investigation of diluted active particle systems for which intriguing viscosity contributions on a single particle level have been reported which are designated to lead to a highly-debated superfluid-like behaviour of active particles [99–101].

4. Comparison with Simulations

As a central part of this work, this chapter is dedicated to a quantitative comparative study between the predictions of the ABP-MCT and results from an event-driven Brownian dynamics simulation with active Brownian hard-disks in two dimensions (BD in the following). The ABP-MCT predictions for the collective dynamics of a monodisperse active system have already been discussed in [47] and [84] focusing on the influence of the ABP parameters on the relaxation time and the shape of the glass transition diagram. In this chapter, the different scenarios which arise from the active and passive tagged particle dynamics in a monodisperse passive or active environment shall be targeted. These scenarios are (*i*) an active tracer particle in a passive environment, (*ii*) a passive tracer particle in an active environment, and (*iii*) and active tracer particle in an identical active environment. Before presenting and discussing the results, a few remarks about the simulation method and the numerical procedure to solve the mode-coupling equations will be given, as well as the general methodology of how the results from both methods can be quantitatively compared.

4.1 Event-Driven Active Brownian Dynamics Simulation

Event-driven Brownian dynamics is a well-established method to simulate a system of strictly non-overlapping hard-disks. The idea of the algorithm is to combine the standard simulation method of Brownian dynamics with an event-driven algorithm for a deterministic system of hard-disks as proposed in [102]. The method has been validated to reproduce the correct 2-particle displacement distribution according to the Smoluchowski equation in a system of passive hard-disks [103] and can be straightforwardly adapted to systems of active particles [104]. The procedure of the algorithm is to assign pseudo-velocities to both translational and rotational degrees of freedom according to the Langevin equation of free Brownian motion after so-called Brownian-events, and an additional drift velocity that accounts for an active self-propulsion. The assignment of pseudo-velocities takes place after a fixed time unit, the Brownian-timestep $\Delta\tau_b$. Subsequently, all particles are propagated according to laws of ballistic motion in terms of an event-driven algorithm by predicting and performing collision events over a variety of collisions during $\Delta\tau_b$, whereby the collision rules are chosen to fulfil both energy and momentum conservation.

For the case that two particles i and j with radii R_i and R_j and masses m_i and m_j and separated by $\vec{r}_{i,j} = \vec{r}_i - \vec{r}_j$ will collide in the future, the collision will occur after [105]

$$\Delta t = \frac{-(\vec{v}_{i,j} \cdot \vec{r}_{i,j}) - \sqrt{(\vec{v}_{i,j} \cdot \vec{r}_{i,j})^2 - v_{i,j}^2 (r_{i,j}^2 - (R_i + R_j)^2)}}{v_{i,j}^2}, \tag{4.1.1}$$

where the relative velocity $\vec{v}_{i,j} = \dot{\vec{r}}_{i,j}$ was introduced. The velocities after the collision $\vec{v}_i'$ and $\vec{v}_j'$ according to the laws of energy and momentum conservation are

$$\vec{v}_i' = \vec{v}_i - \frac{2(\vec{v}_{i,j} \cdot \vec{r}_{i,j})\vec{r}_{i,j}}{(R_i + R_j)^2(1 + m_i/m_j)}, \qquad \vec{v}_j' = \vec{v}_j + \frac{2(\vec{v}_{i,j} \cdot \vec{r}_{i,j})\vec{r}_{i,j}}{(R_i + R_j)^2(1 + m_j/m_i)}. \tag{4.1.2}$$

Moreover, the particle masses must be chosen pursuant to $m = \Delta\tau_b/(2\beta D_t)$ to meet the requirements of the FDT. This follows from the fictive velocity distribution of Brownian diffusion to match the Maxwell-Boltzmann distribution [103]. This requires the masses to obey $m_i R_j = m_j R_i$ to account for the Stokes-Einstein relation for the translational diffusion coefficients.

All simulations were carried out in a box with periodic boundary conditions and packing fractions ranging from $\phi_{BD} = 0.5 - 0.80$ with a constant number of particles $N = 625$, i.e., the different densities have been achieved by varying the simulation box size. Mimicking the behaviour of an infinite system with a system with periodic boundary condition inevitably leads to finite-size effects and additional care must also be taken to eliminate possible drifts both of rotational and translational diffusion after assigning the pseudo-velocities through subtracting the respective average velocities. Otherwise, this would lead to undesired artefacts that are especially dangerous in the rotational degrees of freedom as there a drift would lead to effectively enhanced rotational diffusion coefficients that would attenuate the long-time diffusion.

As a monodisperse system of hard-disks would start to crystalize at $\phi_{BD} \approx 0.69$ and this crystallization transition is not described by MCT, it has to be suppressed in the simulations. This is known to be efficiently achieved by the introduction of a small size polydispersity, for example in terms of a continuous particle diameter distribution, that was chosen according to a Gaussian distribution with a standard deviation of 20% of the mean diameter. Such polydispersity was observed to lead to a suppression of MIPS for the investigated parameter regime and only homogeneous systems are considered in the present study, desirable in so far as MIPS is also not accounted for by the ABP-MCT. Polydispersity is also a present feature in almost all experimental colloidal systems and is inevitable for the experimental investigation of glass-forming systems as seen later. Note that both crystallization and MIPS could just as well have been prevented by using a binary mixture with properly chosen composition and size ratio. However, polydispersity achieved in terms of a symmetrical diameter distribution can be better approximated with a monodisperse system with a mean diameter which makes it more feasible to compare the BD results to the monodisperse MCT outcomes.

On the other hand, the generation of well-equilibrated start configurations for systems with a continuous diameter distribution is itself challenging regarding the considered density regime,

as it already constitutes a non-trivial task to generate a non-overlapping arrangement of such a system, since disposing the particles on a simple cubic lattice most probably creates forbidden configurations for the high densities considered here. A method to generate an allowed polydisperse arrangement is described by the Lubachevsky–Stillinger algorithm [106] which proposes to slowly increase the particle diameters of an initially monodisperse system. In addition to the particle collisions, swelling events according to a swelling rate are implemented in which particles are inflated with the restriction that they remaining non-overlapping. These swelling events are performed until all particles are very close to the desired target diameter. Subsequently, the system needs to be equilibrated by ensuring a sufficient structural rearrangement that becomes increasingly difficult at high densities due to the strong presence of the cageing effect in that regime. Achieving equilibrated start configurations has proven to be most efficiently be achieved by evolving the systems purely by Newtonian-dynamics through switching off the Brownian-events during that procedure since this ensures a quicker structural decorrelation of the system.

Simulation results were obtained in terms of both transient averages over the initially equilibrated state and stationary averages over all possible time-shifts between stationary states with different obtained equilibrated start configurations for both the MSD and the SISF for a variety of wavenumbers. To sufficiently sample the single-particle statistics and the heterogeneous cage structures, 200 simulations were carried out for each set of parameters if the tagged particle type has differed from the bath particle type, whereas 20 simulations have shown to be sufficient to sample the statistics of a system with only one single active component. Unless otherwise stated, all simulation results that will be shown in the following will refer to the stationary type of averaging.

4.2 Density Mapping between MCT and BD

Solving MCT equations requires first and foremost an input for the static structure factors. While previous investigations of the ABP-MCT carried out in [47] have been obtained by using the hard-disk structure factors predicted by the theory of Baus and Colot [94], the hard-disk structure factors used here were obtained from a density functional theory approach proposed by Thorneywork et. al [95]. The latter theory additionally provides the tracer bath direct correlation function for different size ratios of the tracer compared to the bath particle and allow to calculate structure factors for arbitrary compositions. With this theory as an input, the mode-coupling equations were solved with a time-decimation algorithm that is specially adapted to the present structure of the Mori-Zwanzig equation with a hopping term and provides solutions for the ISF and SISF over many decades in time. Details of the algorithm are presented in the appendix of [47] and are not repeated here. Having successively determined both the ISF and SISF, the low-q limits of the tagged particle memory-kernel can be computed and a similar time-decimation scheme can be used to solve the equation of motion for $\delta r^2(t)$. All results presented in this chapter were obtained on a uniform wavevector-grid with $q_{\min} = 2.5$ and $q_{\max} = 40$ with $N_q = 128$ grid points, were the wavevector integration has been carried out with a higher-order open Newton-Cotes formula to account for the divergence at $q \to 0$ that occurs in the

wavenumber integration in 2D. Moreover, the rotational cutoff was chosen as $\Lambda_L = 1$. This set of parameters has provided numerically stable solution for self-propulsion velocities up to $v_0 \sim 8D_t/\sigma$.

By using a bisection method that searches for the root of $f_{0,0}(q)$ as a function of ϕ in the passive system, where $f_{0,0}(q)$ is determined through iteratively solving the algebraic equation (3.2.1) for $D_r = 0$, the passive glass transition point was found at $\phi_c \approx 0.6986$, which is close to that reported by Bayer et. for the same 2D system under usage of a structure factor taken from a hypernetted chain approximation, bringing $\phi_c \approx 0.6968$ [107]. Besides the difference in the structure factor, the deviation can also be attributed to the varying discretization scheme for the wavenumber grid and different integration schemes. Either way, a very precise determination of the transition point is not required in a comparative study with simulations since an equal density mapping is not expected in the first place for several reasons. First of all, it is well-known from former simulations in 2D [107] and 3D [50] that structure factors found in simulations generally differ from those predicted by approximate theories. Most theories are capable to reproduce the right peak position that stems from the hard-core volume exclusion and consistently reveals an increasing local ordering in the form of sharper peaks when increasing the density. Correctly, these peaks are also shifted to higher q values when increasing the density, but the effect of local ordering shows to be overestimated resulting in a lower second peak as observed in simulations. This peak height influences the outcome of the wavevector integration carried out in the MCT calculations and results in an overestimation of the glass-formation tendency in MCT compared to what is observed in simulations [51]. But even when incorporating the structure factors obtained from the BD simulation as input for the MCT calculation as it was carried out in [51], this still leads to discrepancies owing to the approximate nature of MCT whose degree of quality is hard to quantify such that a parameter-free comparison is not possible even in that case and requires a density-mapping between both methods. For this work, the deviations from such a density-mapping should be minimized for an optimal investigation of activity effects. To achieve such an optimal mapping, least-square fits of the SISFs from the passive BD at fixed wavenumber $q = 7.5$ to the SISFs from the passive MCT have been carried out for several densities. Results from these fits for different ϕ_{BD} are depicted in figure 4.2.1 (a) and show a very good agreement in the whole range of fitted densities. The fit reveals a linear relation between the densities from MCT and BD given by $\phi_{BD} = 1.651 \cdot \phi_{MCT} - 0.376$, which is additionally presented in the inset of figure 4.2.1 (a). With higher densities though, it becomes apparent that the MCT underestimates the SISFs in an intermediate time window after the short-time diffusion. This effect has also been reported for the ISF in a similar comparative study between BD and MCT in 2D [52] and reveals the general weak point of MCT in the description of the intermediate time regime. Still, the quantitative description of the final α-relaxation phase and the resulting structural relaxation time whose prediction is the major strength of MCT, is throughout satisfactory over the whole range of presented densities. Going beyond this density range reveals a breakdown of the linear density-mapping is found, which can be attributed to ergodicity-restoring effects in the simulations that are not captured by the MCT. These effects stem from various origins and are reflected in deviations of the generalized Stokes-Einstein relation in terms of a decoupling of self-diffusion and structural relaxation caused by

cage-hopping effects [108] or dynamical heterogeneities [109]. To that reason, the investigations of this thesis are largely limited to the density range where a linear mapping was still possible, offering a good compromise between manageable simulation times and the emergence of a slow structural dynamics.

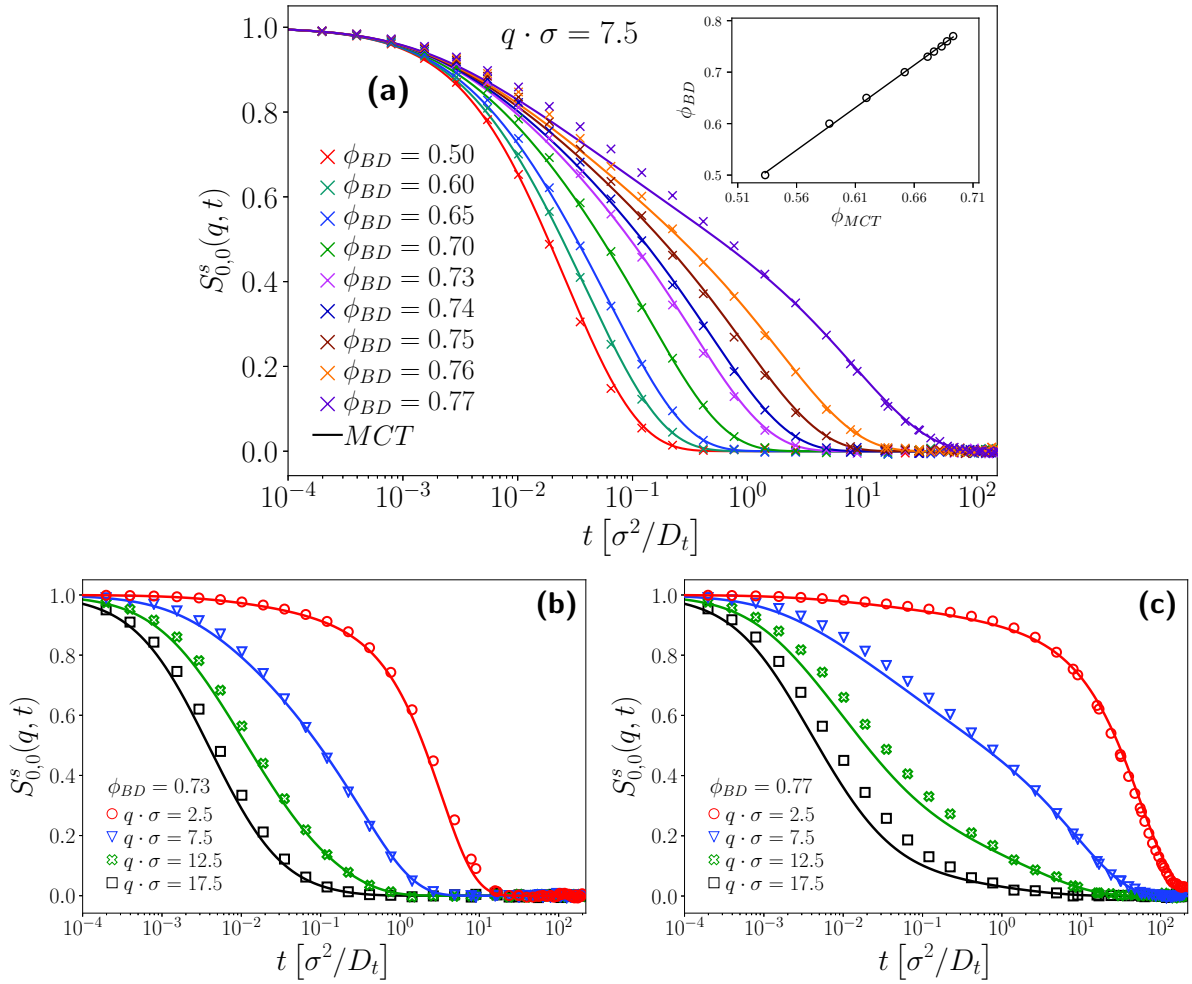

Figure 4.2.1.: ***(a)*** *$S^s_{0,0}(\vec{q},t)$ of a passive tracer particle in the passive hard-disk system for a fixed wavenumber $q = 7.5$ and different packing fractions ϕ_{BD} as indicated. Crosses show BD simulation results, lines are least-square fits to the MCT predictions with resulting optimal ϕ_{MCT} described by the linear fit $\phi_{BD} = 1.651\phi_{MCT} - 0.376$, shown as black line in the inset.* ***(b)-(c)*** *$S^s_{0,0}(\vec{q},t)$ as in the main figure, but for fixed densities $\phi_{BD} = 0.73$ and $\phi_{BD} = 0.77$ each for varying q.*

To estimate the quality of the density mapping for the description of the SISF in a full range of wavenumbers, additional correlation functions are shown in the figures 4.2.1 (b) and (c). These correspond to the different maxima of the structure factor at $q = 7.5$, $q = 12.5$, $q = 17.5$ and the lowest accessible wavenumber $q = 2.5$ for MCT, each for the densities $\phi_{BD} = 0.73$ and $\phi_{BD} = 0.77$ in the respective figures. For the density, $\phi_{BD} = 0.77$ the deviations in the intermediate time range become visible again and do increase with higher wavenumbers, which can be attributed to the erroneous treatment of the short-time collision regime of MCT.

The performed MCT fits for the SISF could additionally be used as a basis for a comparison between the MSDs. Although the fit for the SISF to the lowest wavenumber is well matched between BD and MCT, systematic deviations in the limiting case $q \to 0$, that is necesarry to resolve the MSD, are to be expected, as documented in detail in [50] and [51]. Since this work primarily aims for an investigation of the influence of the activity, it is important to minimize these systematic deviations for an optimal comparison of the respective active systems. A separate density adjustment for the comparison of MSDs between BD and MCT was therefore performed, as shown in figure 4.2.2, that forms the basis for later comparisons of MSDs of active particles. This comparison reveals a quantitatively satisfactory agreement over the entire density range.

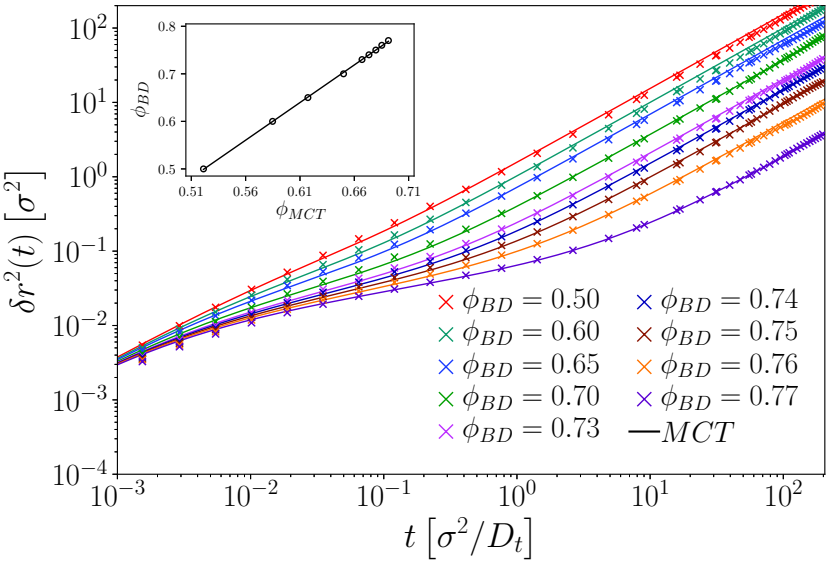

Figure 4.2.2.: *MSD of a passive tracer particle in the passive hard-disk system for different packing fractions ϕ_{BD} as indicated. Crosses show BD simulation results, lines are MCT fits with resulting optimal ϕ_{MCT} described by the linear fit $\Phi_{BD} = 1.661\phi_{MCT} - 0.337$, shown as black line in the inset.*

4.3 Active Tracer in the Passive Bath

Having adjusted the densities from MCT and BD in an error-minimizing way, the results from both methods shall now be compared in an active system. The discussion starts with the scenario of an active tagged particle in a host system of passive hard-disks. In the simulations, the diameter of the active tracer was chosen as the mean diameter of the passive bath particles. All ABP parameters were identically chosen in both BD and MCT, and except for the density no further parameters were adjusted.

4.3.1 Self-Intermediate Scattering Function

Before addressing the regime of high densities, it is worth to check if the BD simulations are capable to confirm the theoretical prediction of the free particle SISFs developed in 3.1.2. The

agreement can be very well confirmed as demonstrated in figure 4.3.1 where numerical solutions of equation 3.1.17 are compared with the simulation results. Both results exhibit the oscillatory behaviour of $S_{0,0}(q,t)$ and $S_{0,1}(q \cdot \vec{e}_y, t)$ in the intermediate wavenumber regime and the simulations confirm the long-time diffusive decay for $S_{0,0}(q,t)$. The comparison to the simulation results also allows assessing the influence of the rotational cutoff number Λ_L on the numerical solutions of the Mori-Zwanzig equation. As demonstrated in figure 4.3.1, both solutions only become quantitatively according if the matrix exponential to determine the SISFs is taken for $\Lambda_L = 10$, which is far beyond the limitations of the MCT numerics. Nevertheless, even $\Lambda_L = 1$ as will be used to determine the SISFs in the mode-coupling approximation later on delivers satisfactory results here.

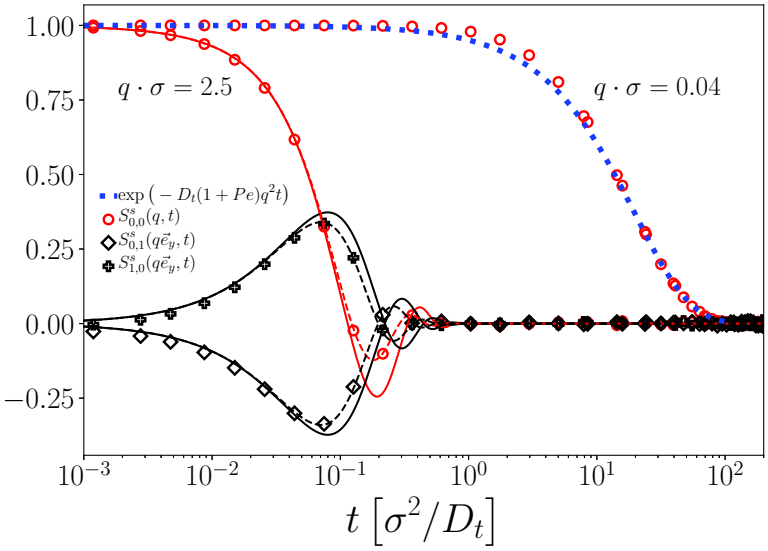

Figure 4.3.1.: *SISFs of an active tracer particle in a diluted system of passive hard-disks at fixed $v_0^s = 8$ and $D_r^s = 1$. Symbols show BD simulation results, solid lines are numerical solutions of equation 3.1.17 for $\Lambda_L = 1$, dashed lines for $\Lambda_L = 10$. The blue dotted lines shows the low-q prediction for $q = 0.04$ according to the long-time diffusion constant of a free ABP.*

To test the ABP-MCT predictions for the tagged particle dynamics, SISFs at fixed density $\phi_{BD} = 0.77$ are presented the figures 4.3.2 (a)-(d) and 4.3.4 (a)-(d) for different self-propulsion velocities each for $D_r^s = 1$ and $D_r^s = 0.05$ and compared to the corresponding simulation results. It can be observed that the correlation functions are only weakly coupled to the activity of the tracer and reveal a similar shape to those found for the corresponding passive tracer particle in figure 4.2.1 (c). This observation can be reasoned by the weak influence of the tracer's activity on the surrounding cage structure in the presented parameter regime. A stronger variation can therefore only be observed for small wavenumbers when resolving the behaviour of the tracer particle on large length scales. This is best seen by investigating the α-relaxation times $\tau_\alpha^s(q)$, defined as $S_{0,0}^s(\tau_\alpha, q) = 0.1$ as a function of the wavenumber as presented in the figures 4.3.3 and 4.3.5, where the trend of a stronger variation at low wavenumbers is confirmed in both MCT and BD results for several densities, though the MCT results reveal a non-monotonic trend for $\tau_\alpha^s(q)$ when increasing v_0^s at fixed $D_r^s = 1$ and $\phi_{BD} = 0.77$ that cannot be confirmed from the BD results.

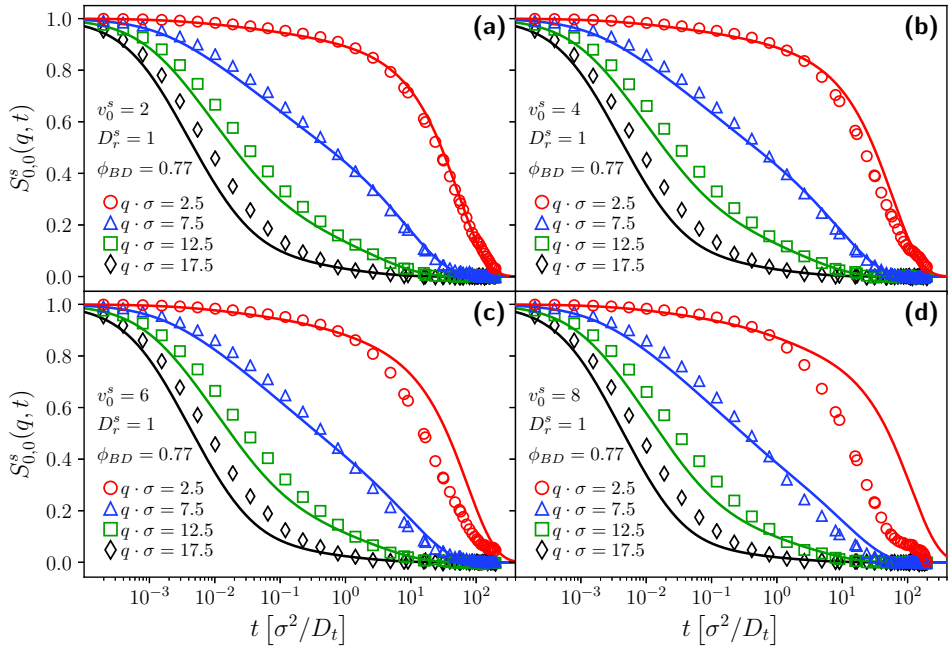

Figure 4.3.2.: *(a)-(d)* $S^s_{0,0}(\vec{q},t)$ *of an active tracer particle in the passive hard-disk system for different wavenumbers* q *and self-propulsion velocities* v_0^s *at fixed* $\phi_{BD} = 0.77$ *and fixed* $D_r^s = 1$. *Symbols show BD simulation results, lines are MCT fits with adjusted* ϕ_{MCT}.

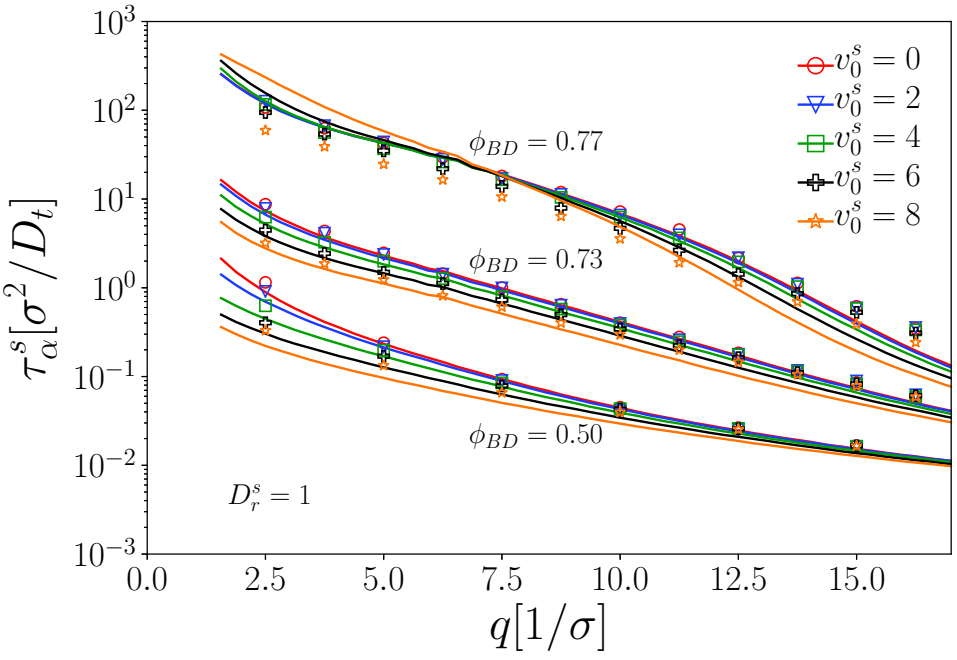

Figure 4.3.3.: *Relaxation times* $\tau^s_\alpha(q)$ *as a function of the wavenumber* q *for an active tracer particle in the passive hard-disk system for different self-propulsion velocities* v_0^s *and densities* ϕ_{BD} *at fixed* $D_r = 1$. *Symbols are simulation results, lines are MCT fits with adjusted* ϕ_{MCT}.

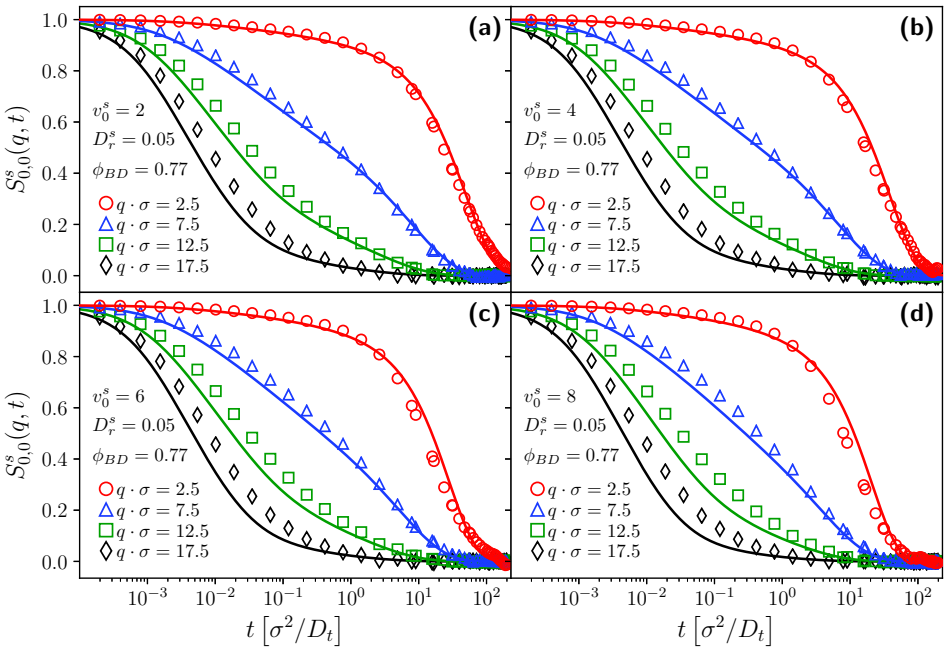

Figure 4.3.4.: ***(a)-(d)*** *$S^s_{0,0}(\vec{q},t)$ of an active tracer particle in the passive hard-disk system for different wavenumbers q and self-propulsion velocities v_0^s at fixed $\phi_{BD} = 0.77$ and fixed $D_r^s = 0.05$. Symbols show BD simulation results, lines are MCT fits with adjusted ϕ_{MCT}.*

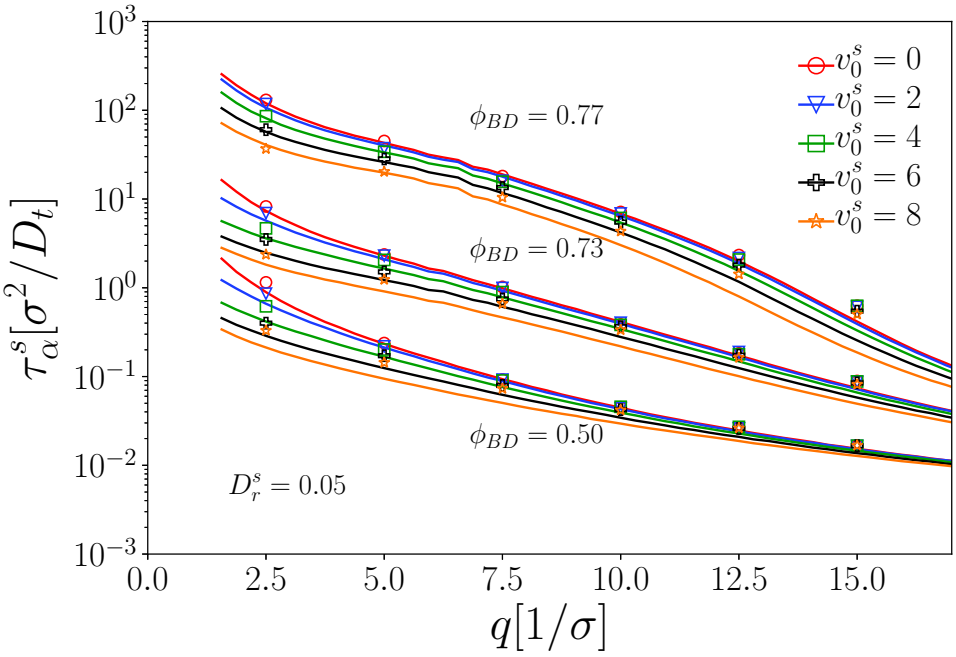

Figure 4.3.5.: *Relaxation times $\tau_\alpha^s(q)$ as a function of the wavenumber q for an active tracer particle in the passive hard-disk system for different self-propulsion velocities v_0^s and densities ϕ_{BD} at fixed $D_r = 0.05$. Symbols are simulation results, lines are MCT fits with adjusted ϕ_{MCT}.*

To address a parameter regime that goes beyond the stability range of the time-decimation algorithm, further simulation results with larger v_0^s were carried out. The results are depicted in the figures 4.3.6 (a)-(d) and reveal a notable influence on the structural dynamics if the activity of the tracer is chosen sufficiently high. One can observe a significant influence on the correlation functions in the entire wavenumber regime. From $v_0 = 64$ on, the relaxation time is of similar order as for the corresponding correlation functions of the free particle and exhibits the typical undershoots that is an indication of a pronounced ballistic motion.

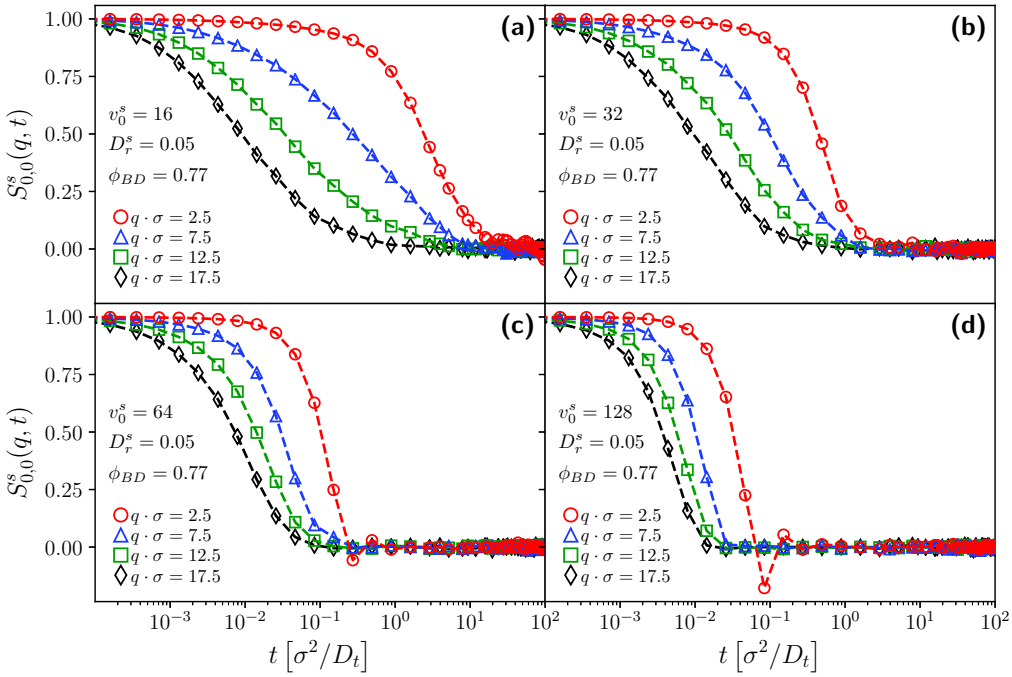

Figure 4.3.6.: ***(a)-(d)*** *$S^s_{0,0}(\vec{q},t)$ of an active tracer particle in the passive hard-disk system for different wavenumbers q and self-propulsion velocities v_0^s at fixed $\phi_{BD} = 0.77$. Symbols show BD simulation results, dashed lines are eye guides.*

4.3.2 Mean-Squared Displacement

Results for the MSD that were obtained from both simulations and from the MCT predictions by solving the equations (3.4.16) and (3.4.17) are shown in the figures 4.3.7 (a) and 4.3.8 (a) each for different rotational diffusion coefficients $D_r^s = 1$ and $D_r^s = 0.05$ and various ϕ_{BD} as well as the same v_0^s as discussed for the SISFs. The presented MSDs show a much stronger variation both with v_0^s and D_r^s as the presented SISFs. This is expected as the MSD resolves the tagged particle correlator for $q \to 0$. Both ABP-MCT predictions and simulation results exhibit the characteristic phases of anomalous diffusion in terms of a sub- and superdiffusive behaviour. Like in the passive system, a short-time diffusive motion is seen with a subsequent transition to a subdiffusive regime through the presence of the cageing effect. Whereas this subdiffusive phase always arises, the subsequent superdiffusive behaviour as an already known feature of the free active particle is not observed in all cases. Its emergence hinges on the interplay between structural relaxation and the simultaneous decorrelation of the rotational degrees of freedom. If

the structural relaxation within the subdiffusive regime proceeds faster than the decorrelation of the rotational degrees of freedom, a superdiffusive regime follows from the plateau until the same crossover time τ_l towards the long time diffusion regime that has been derived for a free active particle in equation (2.2.11). On the other hand, if the relaxation time exceeds τ_l, superdiffusion is suppressed over the entire time-window as exemplarily demonstrated for the MSDs with $\phi = 0.77$ and $D_r^s = 1$. The free particle time scales also allow reasoning the lack of superdiffusive behaviour before the plateau in the presented parameter regime from the crossover time scale τ_ν that indicates the transition from the short-time diffusive to the ballistic regime because the associated length scale l_ν always exceeds the localization length $l_c \approx 0.1\sigma$ of the tracer particle, meaning that collisions arise which hinder the subsequent superdiffusive behaviour through the cageing effect. As expected, the ultimate stage of the MSDs follows a long-time diffusive behaviour according to an effective diffusion constant that increases both with the self-propulsion velocity and the persistence time, but is far weaker than in the free ABP system. For the parameter regime that lacks superdiffusive behaviour ($D_r^s = 1, \phi_{BD} = 0.77$) the influence of the activitiy of the tracer can be assessed with a mapping to the motion of a passive tracer with a reduced effective density ϕ_{eff}^{BD} as depicted as black dotted lines in figure 4.3.7.

The different stages of anomalous diffusion are best seen in time-dependent local diffusion exponents $\alpha(t)$ that were additionally extracted from the MSDs for MCT and BD results. Writing the MSD in terms of $\delta r^2(t) \sim t^\alpha$, these local diffusion exponents are determined with the logarithmic derivative as

$$\alpha(t) = t\frac{d}{dt}\ln \delta r^2(t). \tag{4.3.1}$$

This allows for a precise identification of the transitions between subdiffusive ($\alpha < 1$) to diffusive ($\alpha = 1$) and superdiffusive ($\alpha > 1$) behaviour. The resulting $\alpha(t)$ for the presented MSDs are additionally depicted in the figures 4.3.7 **(b)**-**(e)** and 4.3.8 **(b)**-**(e)** each for fixed self-propulsion velocities and all densities. As an additional reference, the exponents of the free particle as well as its transition times determined from equation (2.2.12) and (2.2.11) are shown. These exponents consistently reveal the occurrence of cageing in form of pronounced minima and the enhancement of superdiffusion with increasing persistence lenghts. Furtheron they confirm that superdiffusive behaviour can be supressed in the entire time window which is the case for $\phi_{BD} = 0.77$ and $D_r^s = 1$.

The physical effects which have been reasoned to explain the emergence of sub- and superdiffusive behaviour are consistently described by both the ABP-MCT predictions and simulation results. The agreement is even of quantitative nature in some parts which is notable in view of several sources of errors that hamper the comparison between both methods, as the influence of polydispersity in the simulations or finite size effects. On the other hand, the general approximate nature of the MCT results is not quantifiable. A further striking observation is the overall agreement despite different kinds of averaging in terms of transient MCT results and stationary BD results which suggests that these differences do not seem to be relevant for the qualitative outcomes in the parameter regimes that were addressed here.

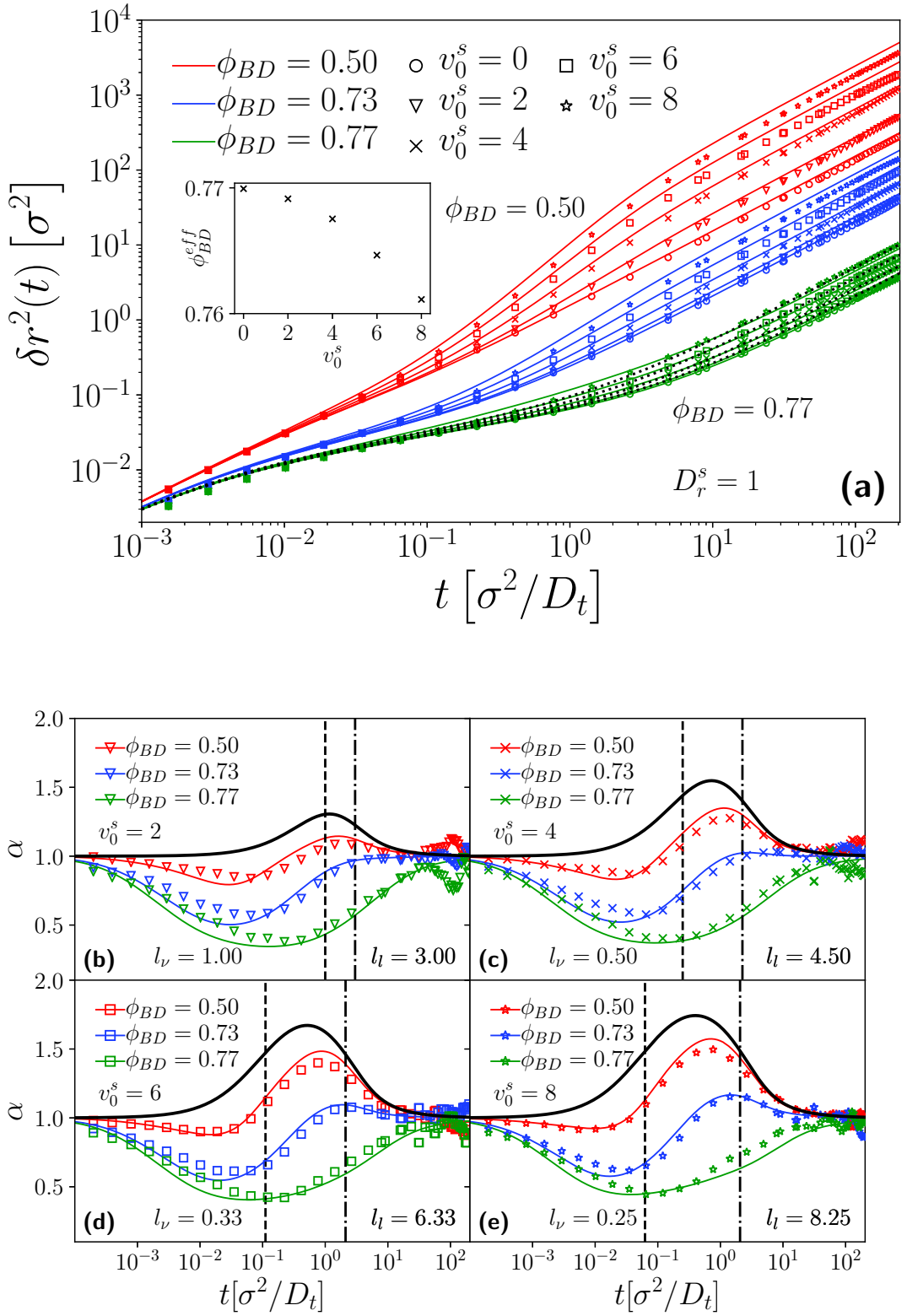

Figure 4.3.7.: *(a) MSD of an active tracer in a passive hard-disk environment for different self-propulsion velocites v_0^s and packing fractions ϕ_{BD} at fixed rotational diffusion coefficient $D_r^s = 1$. Symbols are simulation results, lines are MCT results with adjusted densities ϕ_{MCT}. Black dotted lines are fits to a passive system with an effective density, with ϕ_{BD}^{eff} indicated in the inset. (b)-(e) Local diffusion exponents $\alpha(t)$. The black solid line shows the analytical solution according to the free particle MSD. The dashed line represents τ_ν, the dashed dotted line τ_l.*

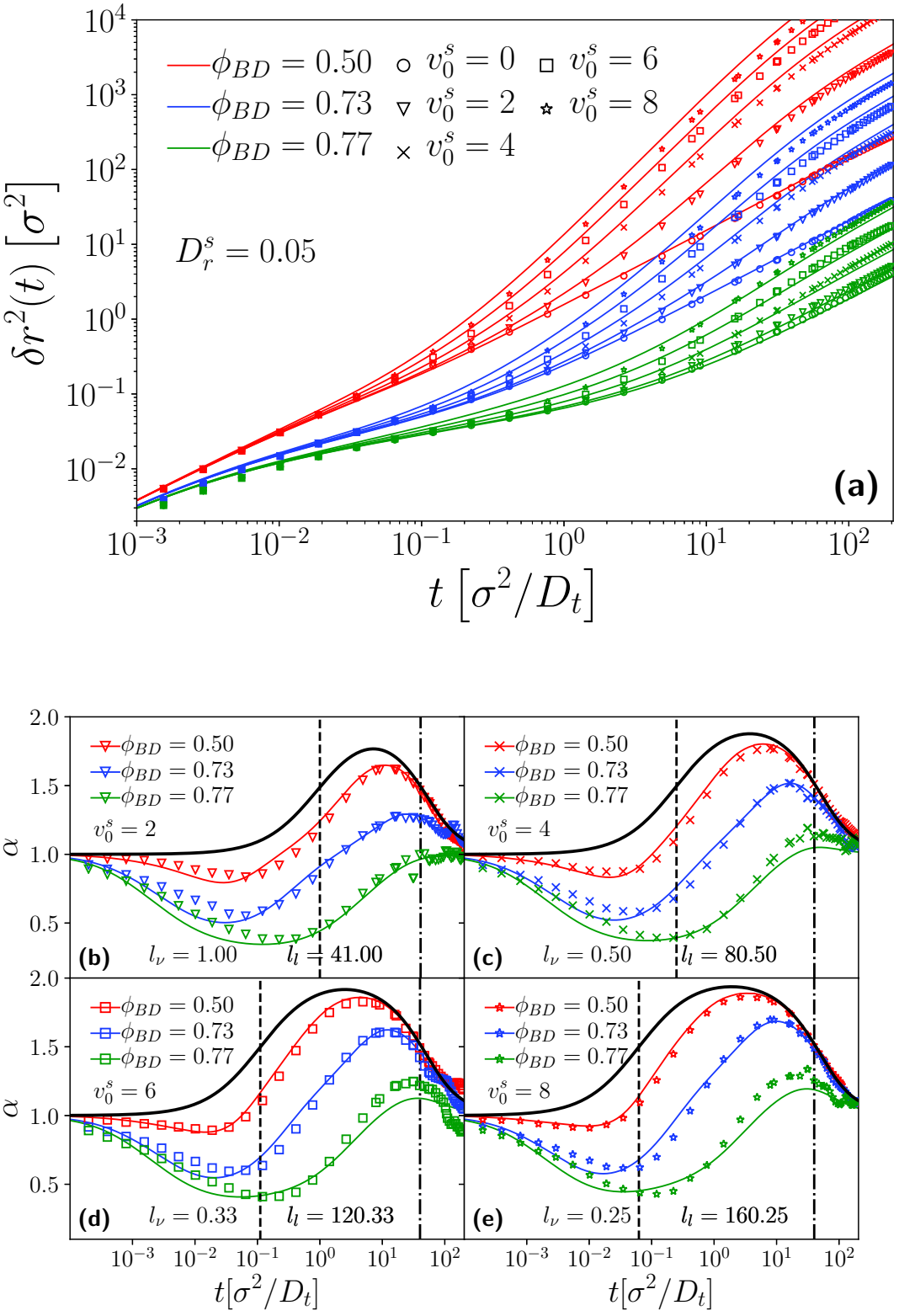

Figure 4.3.8.: *(a) MSD of an active tracer in a passive hard-disk environment for different self-propulsion velocites v_0^s and packing fractions ϕ_{BD} at fixed rotational diffusion coefficient $D_r^s = 0.05$. Symbols are simulation results, lines are MCT results with adjusted densities ϕ_{MCT}. **(b)-(e)** Local diffusion exponents $\alpha(t)$. The black solid line shows the analytical solution according to the free particle MSD. The dashed line represents τ_ν, the dashed dotted line τ_l.*

The results for the MSD confirm the observation made for the tagged particle dynamics that activity of the tracer does only lead to a slight reduction of the structural relaxation time, seen by the fact that increasing v_0^s does not lead to a faster emergence of superdiffusive behaviour. This is the main reason that explains the good agreement of the ABP-MCT predictions with the simulation results without the necessity of fitting any parameters except for the density because the motion of the particle is well characterized by the knowledge of the free particle time scales and the structural relaxation time. Both time scales are well-matched since the former is an intrinsic parameter of the ABP and the latter is adjusted through the density mapping between the passive MSDs from BD and MCT. Still, it needs to be stressed out that the reliable predictions of MSDs by the ABP-MCT is through its feasibility to correctly include the competition between both time scales as a central part of the theory.

Alike as for the tagged particle dynamics, figure 4.3.9 addresses MSDs obtained from simulations that go beyond the self-propulsion velocities of the stability range of the time-decimation algorithm and correspond to the SISFs depicted in figure 4.3.6 (a)-(d). The presented MSDs confirm the conjecture of a significantly enhanced structural relaxation at very high activities of the tracer particle. This behaviour is reflected in an attenuated plateau phase leading to a relaxation time that is roughly decreased by one decade if v_0^s is doubled, consistently seen for the corresponding SISFs in figure 4.3.4 (a)-(d). Interestingly, the motion of the active tracer shares the features of a free ABP if v_0^s is chosen sufficiently high. As seen for $v_0^s = 128$ the MSD of the tracer can be mapped to that of a free particle with an effectively reduced self-propulsion velocity $v_{0_{eff}}^s = 16$ over a large time window, additionally depicted in the figure as a black line. This is consistently seen for the SISF that exhibits the typical undershoots of the free particle solution.

A condition for the emergence of superdiffusive behaviour before the plateau region can be written as $l_\nu < l_{\mathrm{loc}}$ where l_{loc} denotes a typical localization length of the active tracer in the passive hard-disk environment. This length scale is indicated by the plateau height of the MSD and the critical localization length at the glass transition point $l_c \approx 0.1\sigma$ represents an estimate for a lower bound for l_{loc}. Figure 4.3.10 (a) and (b) show the MSDs and respective diffusion exponents resulting from BD and MCT for parameters in the sense of $l_\nu < l_{\mathrm{loc}}$ at constant Péclet number $Pe = 16$. Both methods confirm the emergence of a superdiffusive behaviour in the short-time regime, but only the simulations resolve an expected subdiffusive plateau regime, while the MCT solutions suggest an immediate transition to a long-time diffusive behaviour that is reflected in a quick decay of the memory-kernel after the short-time dynamics. This failure of MCT points to issues that are related to the approximation of the memory-kernel in the present parameter regime and illustrate the general difficulties to achieve the regime of high self-propulsion velocities, even if the persistence time is kept small.

The simulation results reveal that the MSDs collapse in the long-time diffusive regime according to an effective diffusion constant as seen for the solution for the MSD of the free particle at constant Péclet number. This observation gives rises to an attempt to circumvent the numerical issues related to the mode-coupling equations in the spirit of an effective diffusion mapping approach of the memory-kernel by following the idea of replacing $D_t^s \rightarrow D_t^s(1 + Pe^s)$ in the equation of motion (3.4.15) for the MSD of a passive tracer in a passive hard-disk environment.

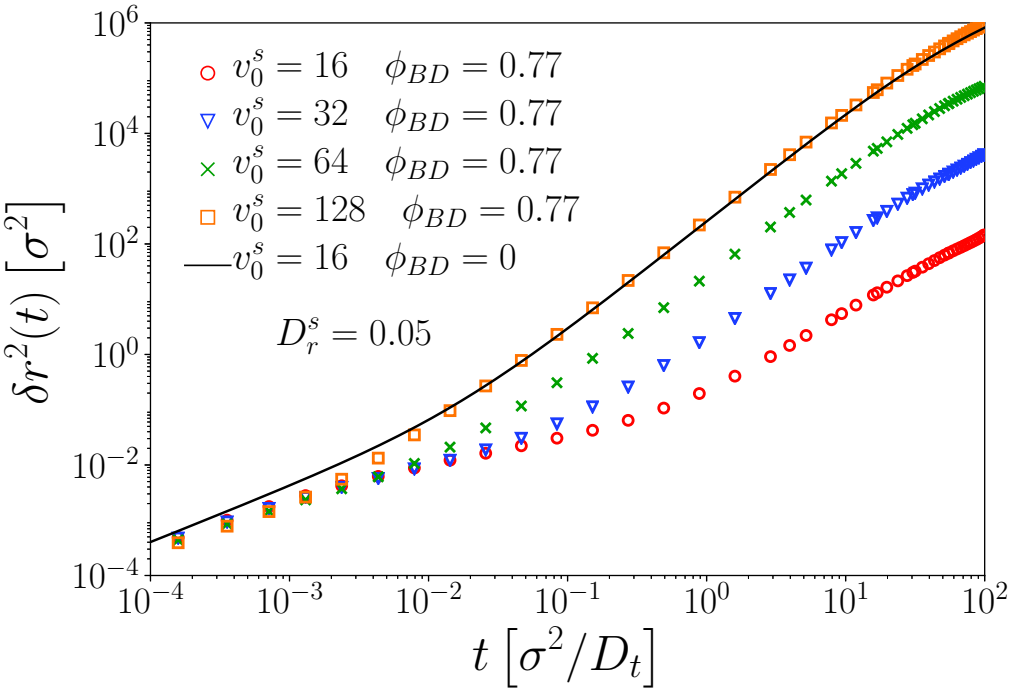

Figure 4.3.9.: *Simulation results for the MSD of an active tracer particle in a passive hard-disk environment for the same ABP parameters as in figure 4.3.6 (a)-(d). The black line shows the analytical solution of a free active particle for* $v_0^s = 16$ *and* $D_r^s = 0.05$.

This solution is shown as black dashed line in 4.3.10 (a), but also fails to describe the long-time diffusive regime consistently with the simulation results and demonstrates that such mappings on a single Péclet number that are well established in the case of diluted systems need be treated with caution when addressing the regime of high densities.

The further discussion is dedicated to a more detailed analysis of the long-time diffusive constants extracted through $4D_t^L = \delta r^2(t_{\max})/t_{\max}$ from both the ABP-MCT predictions and the simulation results. The influence of the packing fraction on the long-time diffusion coefficients at a constant rotational diffusion coefficient $D_r^s = 1$ and several v_0^s is depicted in figure 4.3.11. Here the MCT results predict the expected characteristic power-law behaviour according to

$$D_t^L(\phi) \sim (\phi_c - \phi)^\gamma \tag{4.3.2}$$

when approaching the glass transition. This power-law can also be verified by corresponding fits that are represented as black dotted lines for densities close to the glass transition. These fits do predict identical ϕ_c for the respective v_0^s as well as exponent parameters γ for all presented curves. The idealized power-law is not reproduced in the simulations, where the diffusion constants show an inflexion point near the divergent density predicted from the MCT fits instead. This is an expected observation, that can be reasoned by the emergence of ergodicity restoring effects not considered by MCT and have already been mentioned in the previous section. As it was already evident for the presented MSDs, the enhancement of the long-time diffusion both with increasing self-propulsion velocity and decreasing density is qualitatively well-confirmed by both methods while the agreement becomes quantitatively satisfying for high densities, which are

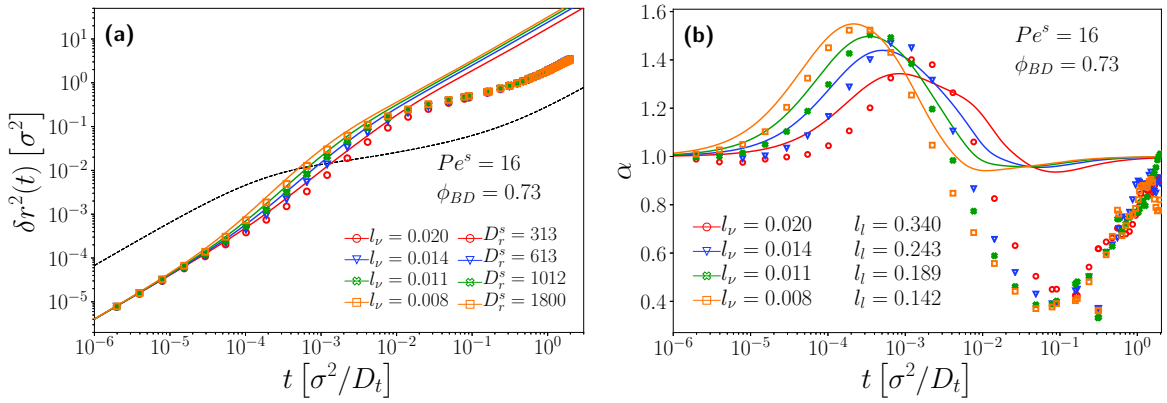

Figure 4.3.10.: ***(a)*** *MSD of an active tracer in the passive hard-disk system for a fixed tracer Péclet number* $Pe^s = 16$ *and fixed* $\phi_{BD} = 0.73$ *for different* l_ν *and* l_l*. Symbols are simulation results, lines are ABP-MCT predictions with adjusted densities* ϕ_{MCT} ***(b)*** *Local diffusion exponents* $\alpha(t)$*.*

still not too close to the divergence point of MCT. Major deviations are particularly reflected in a stronger amplification of the long-time diffusive behaviour by increasing the self-propulsion velocities in the regime of the lowest presented densities and these effects amplify with increasing v_0^s.

Figure 4.3.12 depicts the long-time diffusion constants as a function of the tracer's Péclet number Pe^s for both MCT and BD predictions at different densities and rotational diffusion coefficients. Upon reaching a certain threshold value of the Péclet number, both MCT and BD predict a strong amplification of the long-time diffusion constant, which indicates the emergence of superdiffusive behaviour. On the other hand, if superdiffusion is suppressed, the increase of the Péclet number barely influences the long-time diffusion only through the slightly stronger cage breaking ability of the tracer particle. The comparison between MCT and BD results reveals largely quantitative agreements in the entire parameter range and underlines the reliable prediction of transport coefficients by the presented ABP-MCT.

It is further instructive to check in more detail how the long-time diffusion coefficient scales with the Péclet number by validating an approach in the spirit of an effective-diffusion mapping

$$D_t^L = D_t^L(\phi, Pe^s \to 0)(1 + Pe^{\text{eff}}), \tag{4.3.3}$$

with $D_t^L(\phi, Pe^s \to 0)$ denoting the long-time diffusion of the passive tracer and some parameter-dependent effective Péclet number Pe^{eff}. As this expression becomes exact for $\phi \to 0$ and $Pe^{\text{eff}} = Pe$, one can check if a simple approach in terms of a rescaling $Pe^{\text{eff}} = \alpha Pe$ with $0 \leq \alpha \leq$ is capable to match the results for $D_t^L(\phi)$. Whereas a simple-minded approach for $\alpha = 1$ fails (black dotted line), one can find ϕ- and D_r^s- dependent α that convincingly describes the dependence of D_t^L in the whole range of Péclet numbers. This means that the long-time diffusive behaviour of the tracer particle can be equivalently described as the motion of a free particle with a renormalized Péclet number.

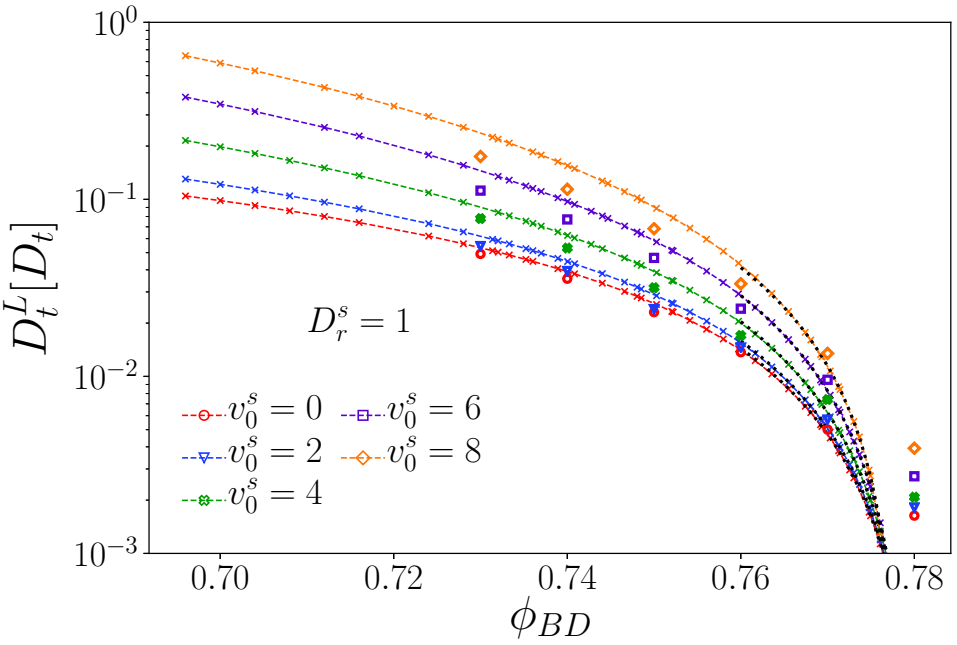

Figure 4.3.11.: *Long-time diffusion constants D_t^L of an active tracer in the passive hard-disk environment as a function of the packing fraction ϕ_{BD} at fixed rotational diffusion coefficient $D_r^s = 1$ for different self-propulson velocites v_0^s. Symbols are simulation results, dashed coloured lines with small crosses are MCT results with adjusted densities ϕ_{MCT}. The dotted black lines are power-law fits according to equation* (4.3.2).

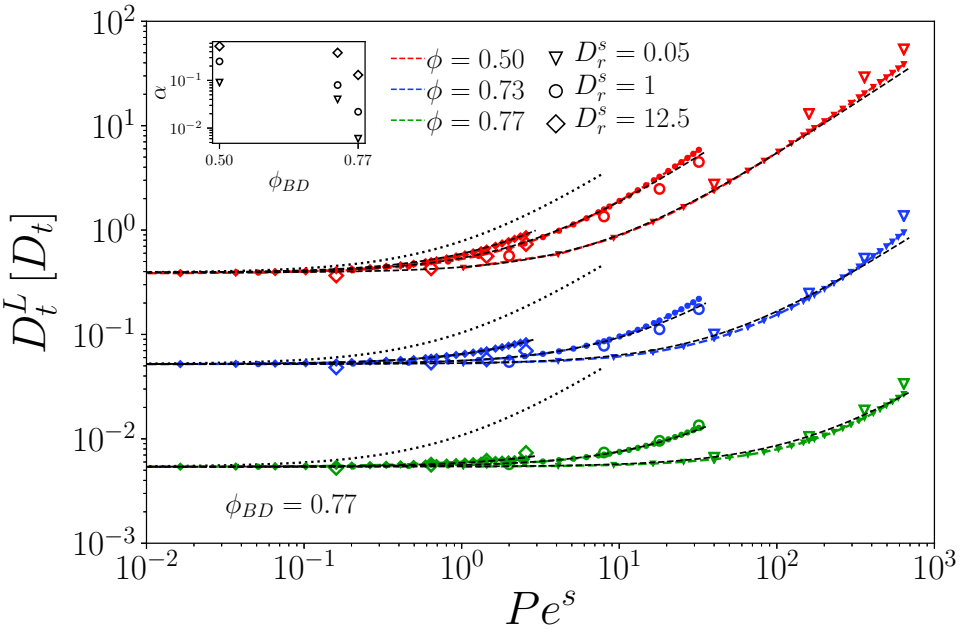

Figure 4.3.12.: *Long-time diffusion constants D_t^L of an active tracer in the passive hard-disk system as a function of the Péclet number Pe^s for different densities and rotational diffusion coefficients D_r^s. Symbols are simulation results, dashed coloured lines with small symbols are MCT results with adjusted densities ϕ_{MCT}. The black dotted line describes a behaviour according to equation* (4.3.3) *for $\alpha = 1$ for each density. Black dashed lines are for ϕ and D_r^s adjusted α, with the fitted α shown in the inset.*

4.3.3 Effective Tracer Swimming Velocity

This section aims for a test of the MCT-ITT approach for the effective swimming velocity v^s of an active tracer in the passive hard-disk system as derived in equation (3.5.11) by comparing with BD results. In the first place, the way of determining the effective swimming velocity v^s from a simulation of strictly hard-core interacting particles in the sense of an average over the projected force as in equation (3.5.1) is not obvious, since the particles are non-overlapping at any time, which begs the question how to properly define the force. Previous investigations on the effective swimming velocity have been restricted to soft particle-type of interactions like the Weeks-Chandler-Andersen potential that would allow a clean definition at this point. Nevertheless a simple approach that can be conducted within the event-driven simulation to determine the swimming velocity is to associate the displacement $\Delta\vec{r}^s(i\cdot\Delta\tau_b) = \vec{r}^s((i+1)\cdot\Delta\tau_b) - \vec{r}^s(i\cdot\Delta\tau_b)$ of the i-th Brownian timestep with a velocity and use the definition of an effective swimming velocity that immediately relates to a projection of $\vec{o}^s$ on a resulting particle velocity in the spirit of the Langevin-equation. This suggests the following definition of a running time average for the effective swiming velocity given by

$$v^s_{BD} = \frac{1}{\Delta\tau_b}\sum_i \Big\langle \Delta\vec{r}^s(i\cdot\Delta\tau_b)\cdot\vec{o}^s(i\cdot\Delta\tau_b)\Big\rangle, \tag{4.3.4}$$

where the brackets denote an average over all simulations. The comparison between the MCT-ITT predictions and the simulations results is depicted in the main figure of 4.3.13 in a range of densities at fixed $D^s_r = 1$. After adjusting the density for the MCT results according to the density-mapping for the SISFs from figure 4.3.4, the results for the effective swimming velocity are well in line with those predicted by the simulations in the density-regime where the mapping of the passive SISFs has provided an accurate match. The slight overprediction of v^s by BD might relate to the fact that the Green-Kubo equation for v^s is also entered by the ISF of the passive bath which is known from previous passive MCT studies to obey a slightly different density-mapping [51]. In view of further differences between MCT and BD represented by the influence of polydispersity effects and the general approximate nature of the MCT-ITT approach, the agreement can be regarded as very satisfactory, concluding that ABP-MCT feasibly accounts for the renormalization of a ϕ-independent v^s_0 to a ϕ dependent v^s from first-principle only by entering the equilibrium features of the system.

The inset of figure 4.3.13 v^s in a full density range without prior adjustment of the density. The simulation results reveal a linear decrease with the density in a low and medium density range, as reported active particles with a soft particle-type of interaction in [76]. This is, however, not seen for the MCT-ITT results, even after adjusting the density according to the mapping of the main figure. These discrepancies point to a wrong prediction of the density correlation functions for low-density systems, but not to a failure of the MCT-ITT approach itself. It has been shown that there exists a mapping of densities in the low and intermediate-density range which includes quadratic terms and provides consistent results for the density correlation functions. Adjusting the densities according to this mapping, the v^s between BD and MCT do even agree for low and intermediate densities [110].

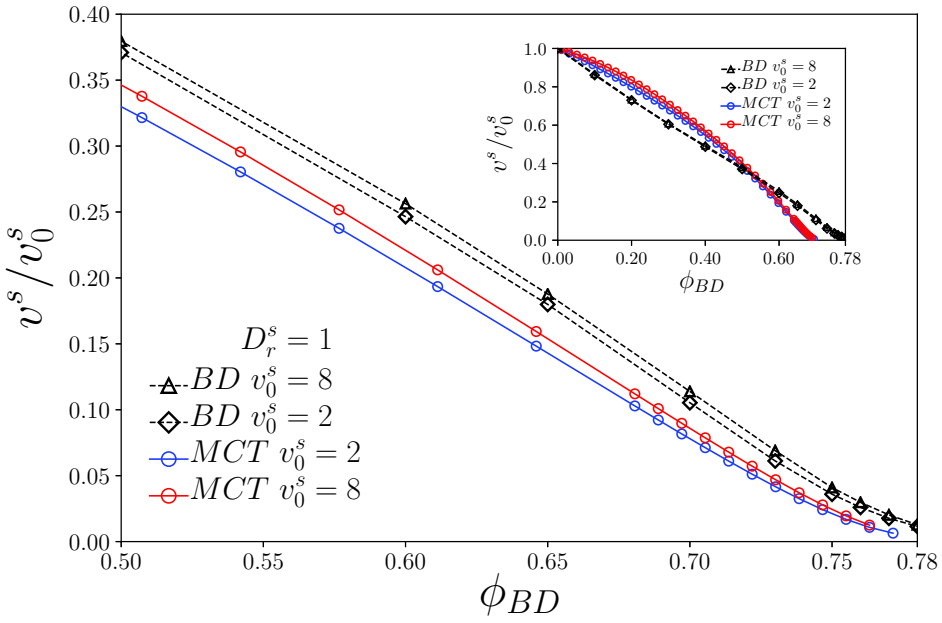

Figure 4.3.13.: *Normalized effective swimming velocity v^s/v_0^s of an active tracer particle in the passive hard-disk environment for different v_0^s in a range of densities and fixed $D_r^s = 1$. Coloured circles with solid lines are MCT-ITT predictions, black symbols with dashed lines are BD results from [110]. The main figure shows the comparison in a range of high densities with a prior density-adjustment for the MCT-ITT results from 4.2.1 (a). The inset compares the results without a density adjustment in the whole range of densities.*

4.4 Passive Tracer in the Active Bath

The scenario addressed in the following is that of a passive tracer particle immersed in an environment of identical active particles. Simulation results were obtained from stationary averaging over trajectories of a single passive tracer particle, whose diameter corresponds to the mean diameter of the active bath particles. Note that whereas the particles were assumed to follow the Stokes-Einstein relationship for the translational diffusion coefficient according to their individual particle size, the rotational diffusion coefficient was kept the same for all particles as otherwise this would distort the comparison with the results from the monodisperse ABP-MCT too much.

4.4.1 Self-Intermediate Scattering Function

A comparison for the SISFs of the passive tracer particle in the active bath, in which as in the previous section only the densities from MCT were adjusted according to the passive density-matching, is shown for the density $\phi_{BD} = 0.77$ in the figures 4.4.1 **(a)**-**(d)** and in 4.4.3 **(a)**-**(d)** each for $D_r = 1$ and $D_r = 0.05$ and different wavenumbers and self-propulsion velocities, where the ABP-MCT results related to this comparison are drawn as solid lines in the figures. In order to assess the effects of activity, the passive SISFs are additionally shown as a reference.

It can be seen that the structural relaxation of the bath particles is much more pronounced when increasing activity than in the case of a single active tracer. This is expected since the ability of cage breaking in the collective active system proceeds much more efficiently compared to the case of a single active particle. Moreover, the impact of the density differs in the present scenario as cageing effects associated with a densification of the system can be compensated with the concomitant enhanced coupling to the active forces of the bath particles, whereas in the former case of a single active tracer increasing the density would always lead to a slower dynamics.

Even though these qualitative features are reproduced both by ABP-MCT and simulations, a comparison that only accounts for a density mapping reveals systematic deviations which amplify with increasing self-propulsion velocities. It is seen that MCT consistently underestimates the influence of the activity on fluidizing the system compared to the predictions of the simulations. Similar to the density matching of the passive systems, it constitutes a reasonable approach to check for a mapping of self-propulsion velocities between MCT and BD for which the results for the SISFs optimally coincide. In the last section within the discussion of the active tracer, its dynamics at high densities was found to be strongly coupled to the properties of the passive environment, which was well matched by the density adjustment between the respective passive systems of MCT and BD. But in the scenario that is discussed here, it is not necessarily to be expected from first-principle that the properties of the active environment are equally captured in the mode-coupling approximation as in the simulations, which is why the quantitative outcomes for the dynamics of the tracer particle can be expected to differ such that the procedure of a velocity adjustment is well justified. By following the approach of a least-square method, the SISFs from MCT have therefore been fitted to those predicted from BD in a range of self-propulsion velocities at a fixed wavenumber $q = 7.5$. These SISFs for the optimally found self-propulsion velocities are additionally presented in the figures as dashed lines. Notably, one finds that a simple rescaling given by $v_0^{MCT} \approx 1.5 v_0^{BD}$ provides near quantitative agreements between MCT and BD results in a wide range of wavevectors and self-propulsion velocities. This agreement has also been verified for further densities and delivers consistent results for the α-relaxation times $\tau_\alpha^s(q)$ of the passive tracer particle in a wide range of wavenumbers and different densities as demonstrated in the figures 4.4.2 and 4.4.4 each for $D_r = 1$ and $D_r = 0.05$ and the same v_0 as for the presented SISFs. There, the effect of a pronounced coupling of the tracer particle to the active bath is best seen in the comparison with the relaxation times for $\phi_{BD} = 0.5$ that show a far weaker variation with activity and it is seen that this coupling amplifies when increasing the persistence time of the bath particles by comparing the results for $D_r = 1$ and $D_r = 0.05$.

Qualitative differences in the comparison between simulation and theory become striking for the SISFs with wavenumber $q = 2.5$ for $v_0 = 6$ and $D_r = 0.05$, where the MCT predicts pronounced undershoots for the correlation functions, that are not seen in the simulations. As with the free particle, these undershoots are an indicator of the ballistic motion of the passive tracer particle that is induced by the coupling to the active bath in the present theory. This suggests that there might arise qualitative differences in the description of the MSD in this parameter range, as will also be confirmed later.

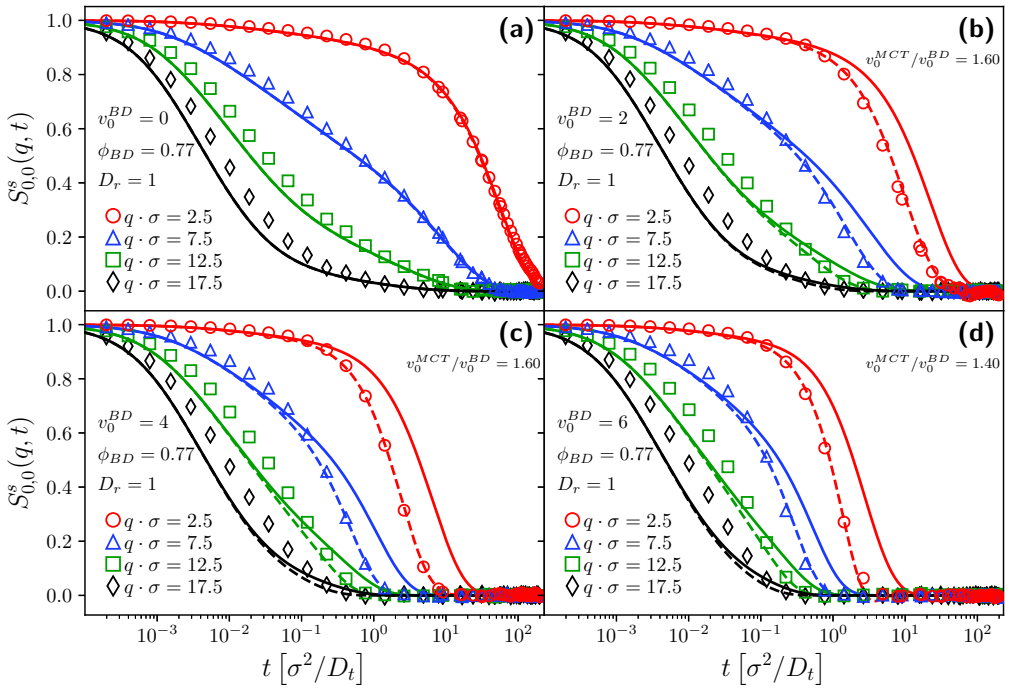

Figure 4.4.1.: ***(a)-(d)*** *$S^s_{0,0}(\vec{q},t)$ of a passive tracer particle in an active hard-disk environment for different wavenumbers q and self-propulsion velocities v_0 of the active bath at fixed $D_r = 1$ and $\phi_{BD} = 0.77$. Symbols show BD simulation results, solid lines are MCT fits where only ϕ_{MCT} was adjusted, dashed lines show additonal adjustments to v_0 (with v_0^{MCT} as indicated).*

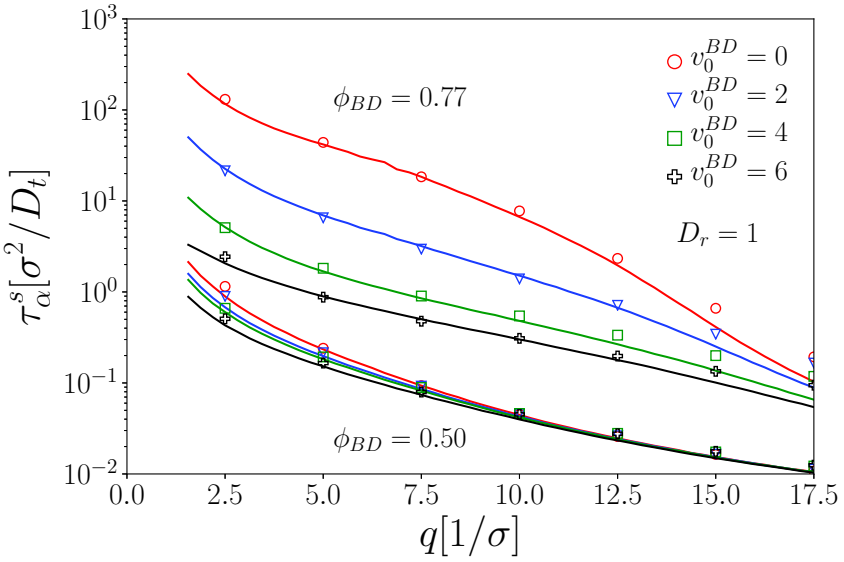

Figure 4.4.2.: *Relaxation times $\tau^s_\alpha(q)$ of a passive tracer particle in an active hard-disk environment as a function of the wavenumber q for different self-propulsion velocities v_0 of the active bath at fixed $D_r = 1$ for $\phi_{BD} = 0.77$ and $\phi_{BD} = 0.50$. Symbols show BD simulation results, solid lines are MCT fits with adjusted ϕ_{MCT} and adjusted v_0 (with v_0^{MCT} chosen as for the SISFs).*

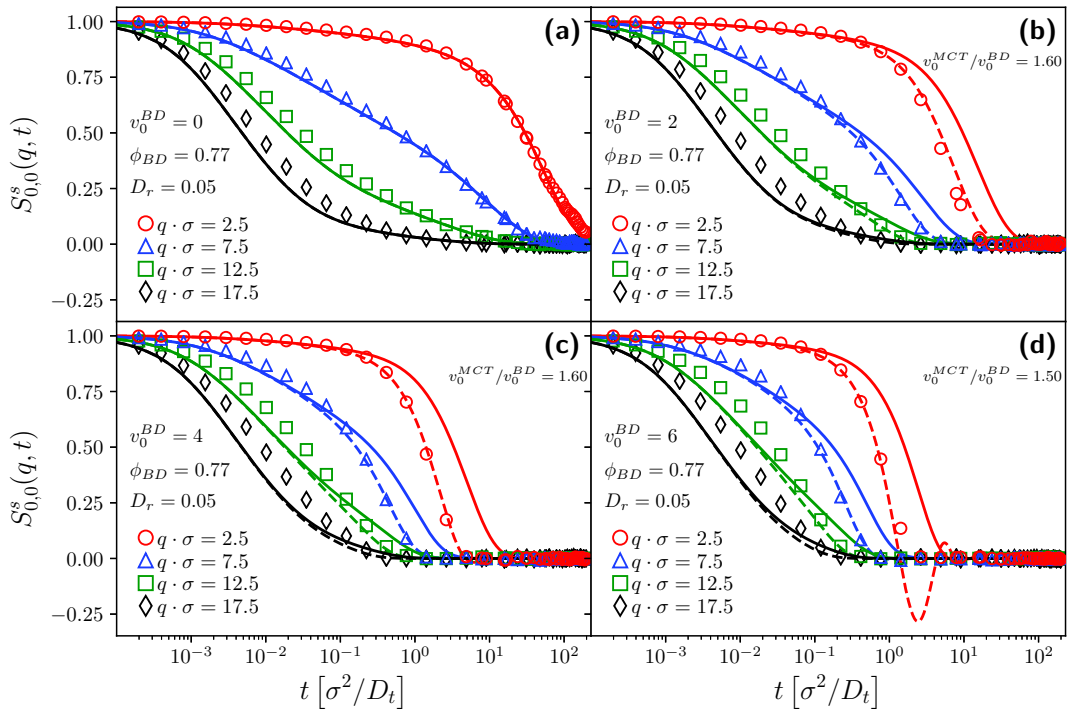

Figure 4.4.3.: ***(a)-(d)*** *$S^s_{0,0}(\vec{q},t)$ of a passive tracer particle in an active hard-disk environment for different wavenumbers q and self-propulsion velocities v_0 of the active bath at fixed $D_r = 0.05$ and $\phi_{BD} = 0.77$. Symbols show BD simulation results, solid lines are MCT fits where only ϕ_{MCT} was adjusted, dashed lines show additonal adjustments to v_0 (with v_0^{MCT} as indicated).*

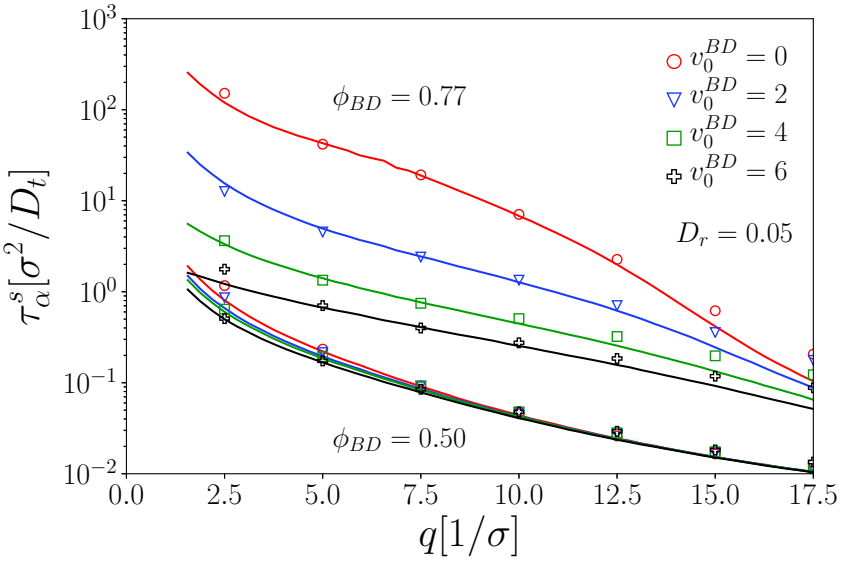

Figure 4.4.4.: *Relaxation times $\tau^s_\alpha(q)$ of a passive tracer particle in an active hard-disk environment as a function of the wavenumber q for different self-propulsion velocities v_0 of the active bath at fixed $D_r = 0.05$ for $\phi_{BD} = 0.77$ and $\phi_{BD} = 0.50$. Symbols show BD simulation results, solid lines are MCT fits with adjusted ϕ_{MCT} and adjusted v_0 (with v_0^{MCT} chosen as for the SISFs).*

When approaching the regime of low persistence lengths it is observed that the empirical velocity rescaling to match the correlation functions from ABP-MCT and BD fails. Instead, a direct mapping of $v_0^{MCT} = v_0^{BD}$ allows for a quantitative description of the simulation data. This is exemplified in figure 4.4.5 (a)-(d) for $D_r = 200$ at fixed density $\phi = 0.77$ for the same v_0 where clearly the direct mapping delivers the better results.

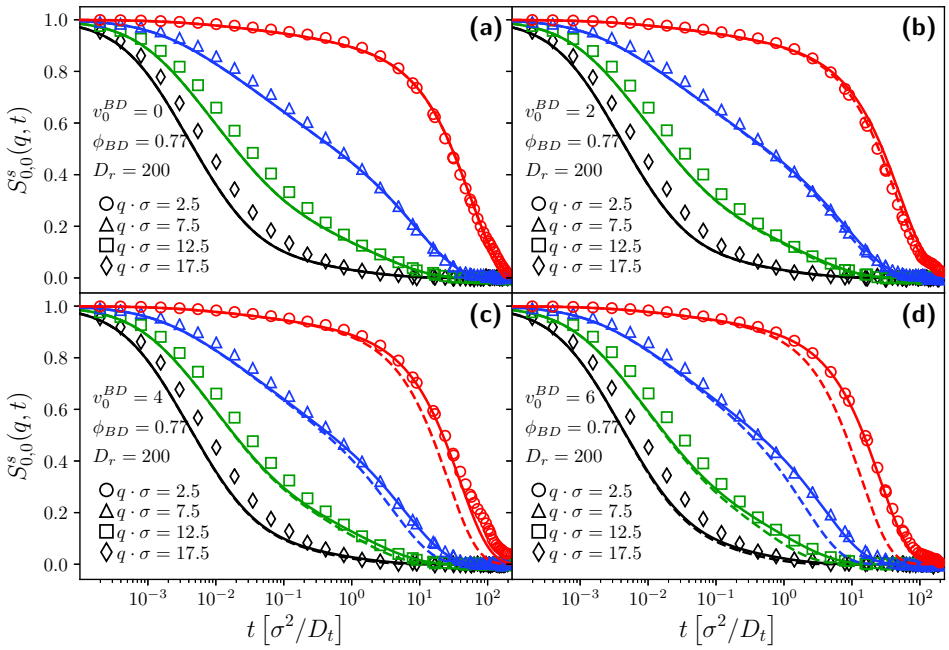

Figure 4.4.5.: ***(a)-(d)*** *$S^s_{0,0}(\vec{q},t)$ of a passive tracer particle in an active hard-disk environment for different wavenumbers q, self-propulsion velocities v_0 of the active bath and fixed $D_r = 200$, $\phi_{BD} = 0.77$. Symbols show BD simulation results, solid lines are MCT fits where only ϕ^{MCT} was adjusted, dashed lines show results for $v_0^{MCT} = 1.5 v_0^{BD}$.*

A much simpler MCT approach to address the regime $D_r \to \infty$ has been proposed by Farage et al in terms of an effective diffusion approximation [44]. It is achieved by the introduction of an effective Smoluchowski operator given by

$$\mathbf{\Omega}_{\text{eff}}(\Gamma) = \sum_{i=1}^{N} D_t \vec{\nabla}_i \left(\alpha \vec{\nabla}_i - \beta \vec{F}_i \right) + D_r \partial^2_{\theta_i}, \tag{4.4.1}$$

where the factor $\alpha := 1 + Pe$ accounts for an effectively enhanced temperature (but violates the FDT). This delivers the same outcome as for the passive MCT, but with a q-dependent prefactor in the memory-kernel that is obtained by replacing $\omega_{0,0}(q) \to D_t q^2 (1 + S(q)\, Pe)$ which is speeding up the dynamics when increasing Pe. But even for a large $D_r = 200$ this approach arguably fails to reproduce the simulation results as shown in figure 4.4.6. This failure points to the fact that even for a small persistence length as $l_p = 0.02\sigma$, given for $D_r = 200\sigma^2/D_t$ and $v_0 = 4D_t/\sigma$, the relevant length scale that describes the ballistic regime and under which the passive tracer feels the persistent motion of the active bath is $l_l = 2D_t/v_0 + l_p = 0.145\sigma$ which is in the order of the cage size formed by the active particles.

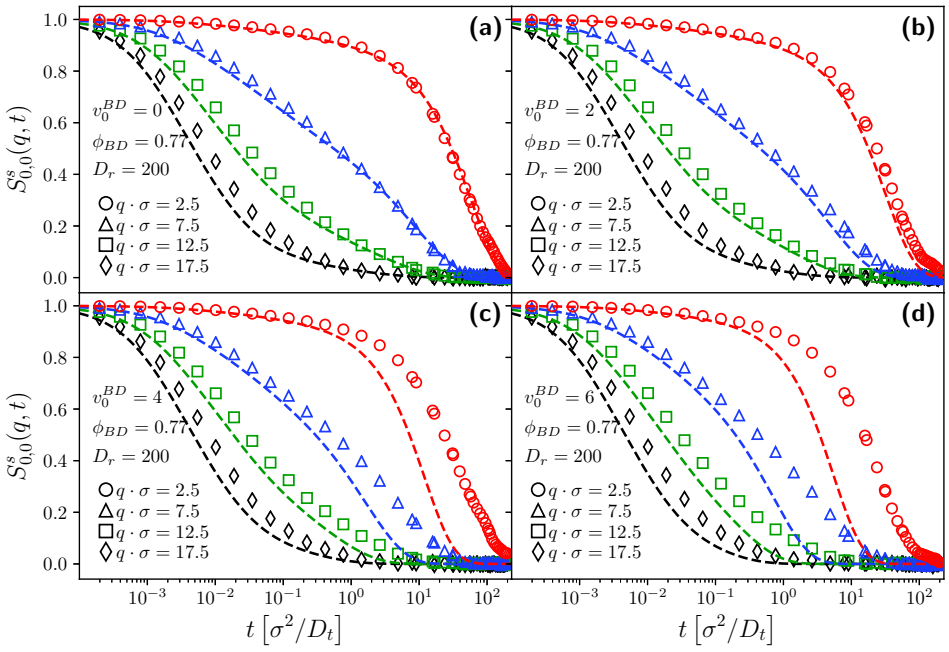

Figure 4.4.6.: ***(a)-(d)*** *$S^s_{0,0}(\vec{q},t)$ of a passive tracer particle in an active hard-disk environment for different wavenumbers q, self-propulsion velocities v_0 of the active bath and fixed $D_r = 200$, $\Phi_{BD} = 0.77$. Symbols show BD simulation results, dashed lines show results from the effective diffusion approach according to equation* (4.4.1).

4.4.2 Mean-Squared Displacement

Comparing the ABP-MCT predictions for the MSD according to equation (3.4.15) with the simulations results only with a mapping that adjusts the density confirms the observation made for the SISFs, that also here the MCT underestimates the influence of activity on fluidizing the system. With the same strategy as before, the MSDs predicted by MCT were adjusted to an optimal self-propulsion velocity to match the simulation results as shown in figure 4.4.7 (a) as well as for the resulting diffusion exponents in (b)-(e) for different densities and self-propulsion velocities at fixed $D_r = 1$. These optimally selected self-propulsion velocities from the least-square fit confirm the same empirical relation for the velocity mapping that has previously been found for the SISFs and provide a near quantitative agreement with the simulation results.

The passive tracer in the active bath exhibits the same characteristic transport regimes as the active tracer in the passive bath with phases of both sub- and superdiffusive behaviour. Nevertheless, the mechanisms of how activity influences these transport regimes differ from the previous scenario because the activity is no longer an intrinsic feature of the tracer particle, but arises through a coupling with an active bath. Since a collective activity is arguably way more efficient to fluidize the system leads to the observation that increasing activity has now a more pronounced effect on the relaxation time of the tracer particle. Moreover, the variation of the MSD from increasing v_0 becomes stronger when increasing the density, as the coupling to the bath is enhanced, whereas the opposite trend is seen in the scenario of an active tracer in a

passive bath. In the latter scenario, superdiffusion emerges because it is as an intrinsic feature of the active tagged particle. The superdiffusive behaviour for the passive tracer only occurs through its coupling to the active bath. ABP-MCT is capable to account for this transmission of superdiffusivity through the active environment which is only achieved by the correct resolution of the coupling of the passive tracer's translational degrees of freedom with the rotational degrees of freedom of the active bath described by the $S_{\pm 1,0}(\vec{q},t)$ correlation functions that enter the memory-kernel to determine the MSD. Theories that coarse-grain the rotational degrees of freedom like those in the spirit of an effective diffusion approach are not capable to account for such explicit coupling terms, meaning that these approaches will produce positive decaying correlation functions that can only assess an enhanced long-time diffusive behaviour concomitant with activity, but no superdiffusivity.

When approaching the regime of large Pe, it is observed from the ABP-MCT predictions that even though the underestimation to account for the influence of the activity to fluidize was demonstrated can be corrected by a simple velocity rescaling, this rescaling does not reproduce the enhancement of superdiffusion with activity quantitatively according to the simulation results. This means that this approach is limited to parameter regimes where superdiffusive behaviour does not occur or is only weakly indicated. This failure to correctly resolve the superdiffusion in the parameter range of large Pe is indicated in 4.4.7 (e), where MCT still delivers consistent results with the simulations but starts to overestimate $\alpha(t)$ in the superdiffusive regime. This effect is more pronounced for higher Pe as shown here, meaning that it was therefore not possible to achieve reasonable agreements between BD and MCT in the regime $Pe \gtrsim 10$ where superdiffusion was observed to be the dominant transport mechanism of the tracer particle. Addressing the MSDs for low Pe on the other hand, reveals the same picture as for the SISFs, that a quantitative agreement between MSDs from simulations and the ABP-MCT can be found without a prior velocity rescaling, exemplified for $D_r = 200$ in figure 4.4.8. Even though there emerges no superdiffusive behaviour of the tracer particle, an MCT approach to calculate the MSD in the spirit of an effective-diffusion approach by inserting the MCT-approximated correlation functions stemming from an effective Smoluchowski equation into the equation of motion for the MSD of a passive tracer in a passive bath fails to describe the simulation results, exemplified in figure 4.4.8 for $v_0 = 6$ where on the other hand ABP-MCT delivers quantitatively according to the predictions from the simulations.

The long-time diffusion coefficients extracted from the simulation results are depicted in figure 4.4.9 and compared with the prediction from ABP-MCT in a parameter range where a velocity rescaling approach was successful to assess the simulation results. The failure of ABP-MCT in the regime $Pe \approx 10$ is indicated as an excesively stronger increase of D_t^L at $Pe = 10$ which is due to its overprediction of superdiffusive behaviour compared to the BD results. The simulation results at large Pe reveal a striking observation in terms of a non-monotonic behaviour of the long-time diffusion constant as a function of density at fixed Pe. This suggests that the cageing of the tracer particle which is associated with an increase of the density can be overcompensated by the increased coupling to the activity of the bath particles. Even at very high densities, this can lead to long-time diffusion coefficients that exceed those of the free passive particle.

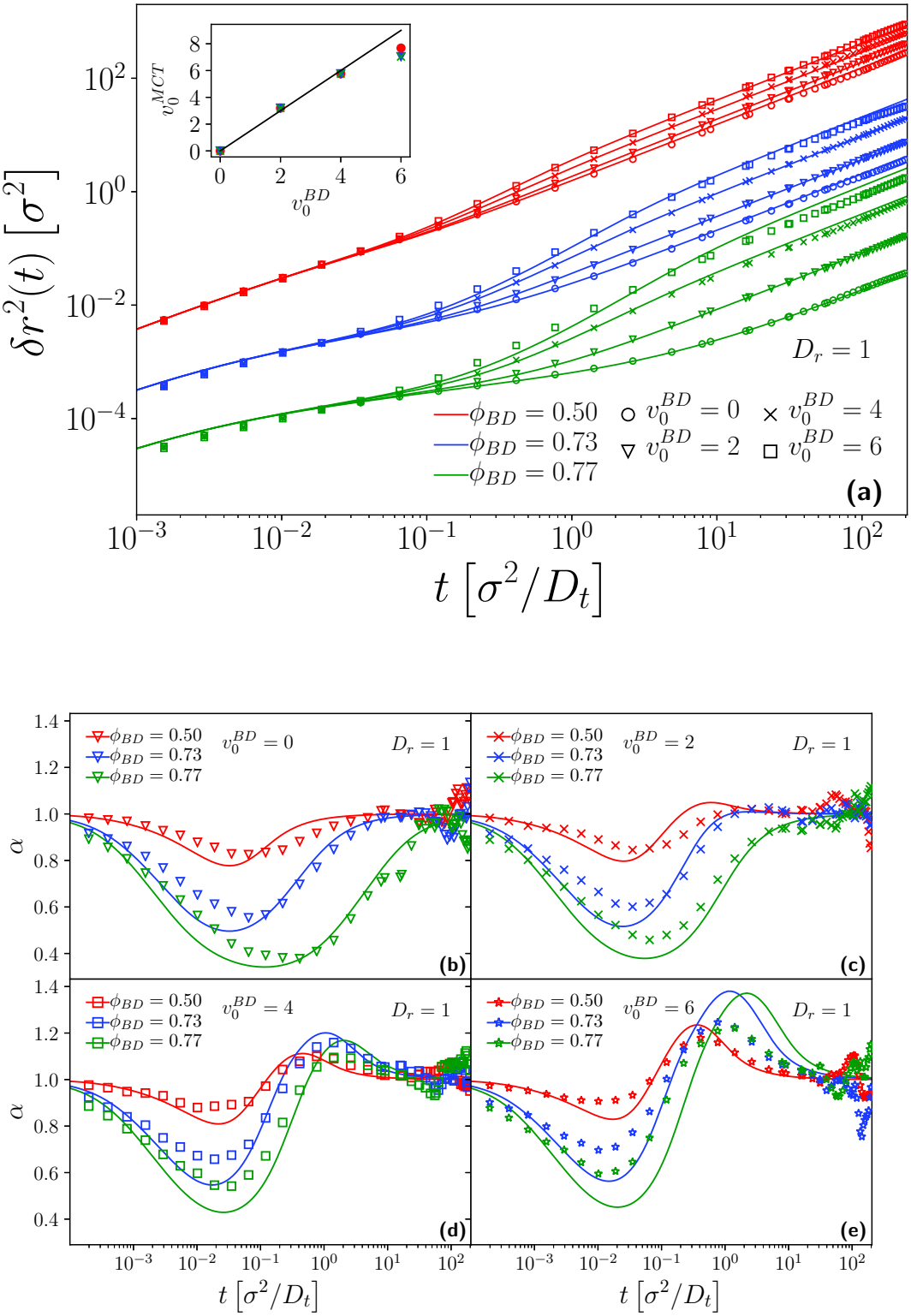

Figure 4.4.7.: ***(a)*** *MSDs of a passive tracer particle in an active hard-disk environment for different self-propulsion velocites v_0 and packing fractions ϕ_{BD} at fixed rotational diffusion coefficient $D_r = 1$. Symbols are simulation results, lines are MCT results with adjusted densities ϕ_{MCT} and adjusted v_0 (see inset). For clarity the curves with $\phi_{BD} = 0.73$ and $\phi_{BD} = 0.77$ have been shifted down by a factor 10 and 100 respectively. The inset shows the velocity mapping between MCT and BD that has provided the best agreement, where the black line is a fit $v_0^{MCT} = 1.5 v_0^{BD}$.* ***(b)-(e)*** *Local diffusion exponents $\alpha(t)$.*

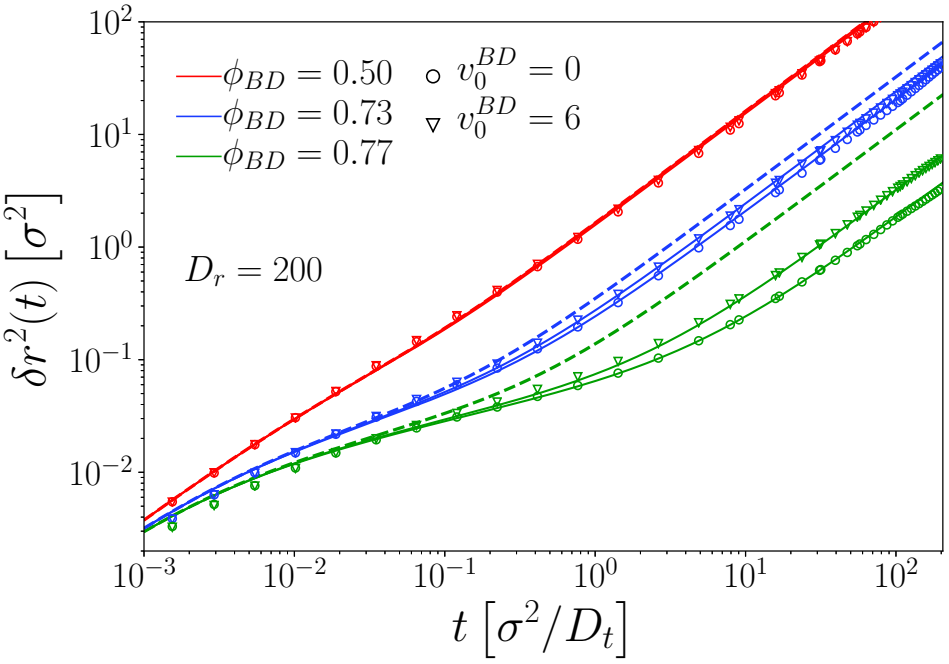

Figure 4.4.8.: *MSDs of a passive tracer particle in an active hard-disk environment for different self-propulsion velocites v_0 and packing fractions ϕ_{BD} at fixed rotational diffusion coefficient $D_r = 200$. Symbols are simulation results, solid lines are ABP-MCT predictions with adjusted densities ϕ_{MCT}, but with $v_0^{MCT} = v_0^{BD}$. The dashed lines shows the predictions of the effective-diffusion approach.*

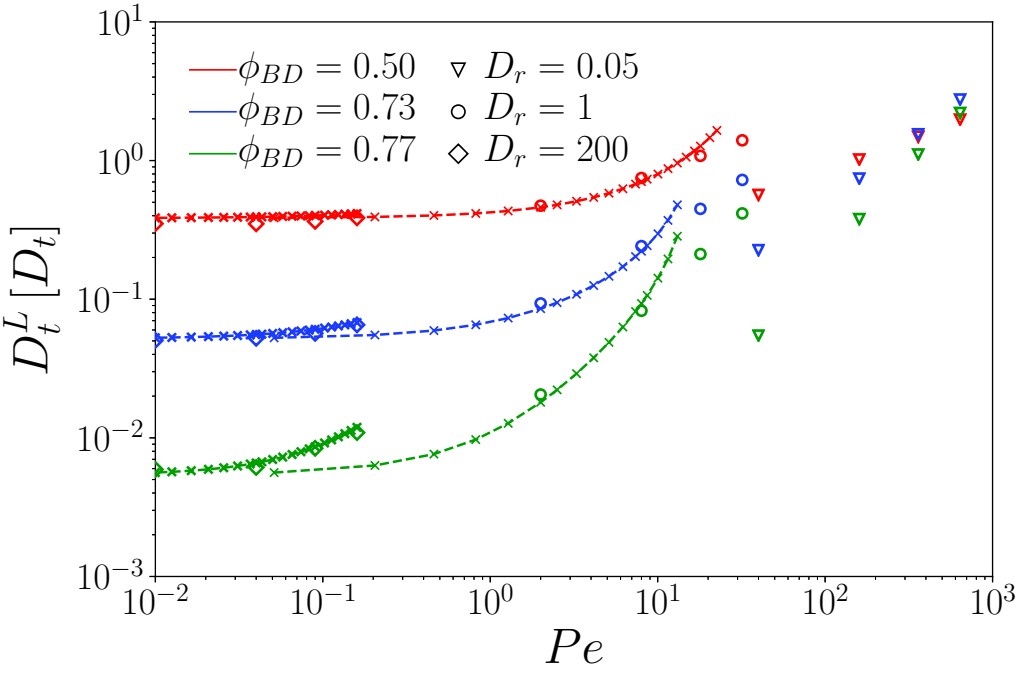

Figure 4.4.9.: *Long-time diffusion constants of a passive tracer in an active hard-disk environment as a function of the bath Péclet number Pe for different ϕ_{BD} and rotational diffusion coefficients D_r. Symbols are simulation results, crosses with dashed lines are ABP-MCT predictions with adjusted ϕ_{MCT} and $v_0^{MCT} = v_0^{BD}$ for $D_r = 200$, $v_0^{MCT} = 1.5 v_0^{BD}$ for $D_r = 1$.*

4.4.3 Active Microrheology

Transport coefficients of tracer particles can be purposefully exploited to probe the rheological properties of the surrounding medium. This constitutes a versatile method to explore the characteristics of complex fluids in the framework of so-called microrheology [111]. The most common example is the connection between the experienced friction of colloidal probe particles and the viscosity of the much smaller solvent particles in terms of a Stokes-Einstein relation. Passive MCT makes such a prediction even for solvents that consist of particles of similar size as the tracer particle and states that the product $D_t^L \cdot \eta$, with D_t^L denoting the long-time diffusion constant of the tracer and η the viscosity of the host particles, remains asymptotically constant when approaching dynamical arrest. This is because close to the glass transition, MCT predicts equal power laws for both D_t^L and η, but with exponents of opposite signs. So-called active microrheology approaches check if similar predictions can be made for systems far from equilibrium beyond the framework of linear response theory, in common to the active systems that are investigated here. In this sense, it is instructive to investigate how the long-time diffusion constant of a passive tracer in an active bath relates to the viscosity of the bath particles and if there still exists a regime that maintains the predictions from passive MCT. To check for such a fundamental relationship, the ABP-MCT predictions for the zero-shear viscosity of the active bath according to equation (3.6.7) and for the long-time diffusion coefficient D_t^L of the passive tracer, as well as the product of both are presented in figure 4.4.11 for different D_r as a function of Pe at fixed density $\phi_{BD} = 0.77$. It is seen that the relation $D_t^L \cdot \eta = const$ is well fulfilled in the regime of low and medium Péclet numbers, but that for large Pe, there emerges an excessively stronger increase in long-time diffusion compared to the simultaneous reduction in viscosity caused by the superdiffusive transport mediated by the active bath. This was also verified by local diffusion exponent that fulfilled $\alpha > 1$ in this regime.

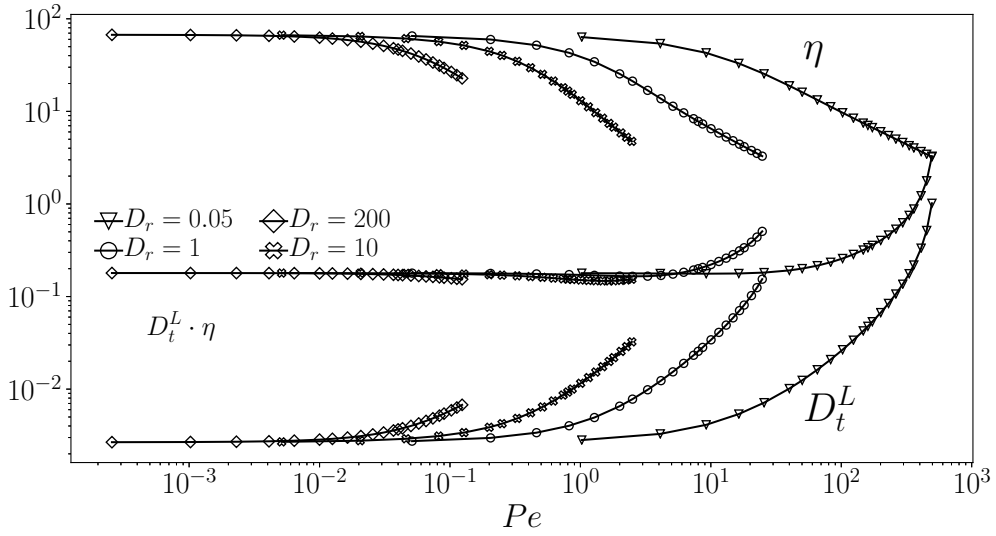

Figure 4.4.10.: *ABP-MCT predictions for the zero-shear viscosity η of an active bath, the long-time diffusion constants D_t^L of an immsersed passive tracer and the product $\eta \cdot D_t^L$ of both for different D_r at fixed $\phi_{BD} = 0.77$ as a function of Pe.*

Noting that the viscosity close to the glass transition point is, up to a prefactor, well-determined by the structural relaxation time allows comparing the ABP-MCT predictions with the simulation results. It is therefore sufficient to consider the product of $\tau_\alpha(q) \cdot D_t^L$ at fixed q, with $\tau_\alpha(q)$ denoting the relaxation time of the active bath, and to compare the result with a rescaling of $\eta \cdot D_t^L$ from the ABP-MCT predictions with a constant factor. This comparison shows that the deviations from $\tau_\alpha(q) \cdot D_t^L = const$ are consistently seen in the simulations as presented in 4.4.11 and suggests that the decoupling between structural relaxation of the active bath and the mediated transport properties of the tracer are not due to the overestimation of superdiffusion by ABP-MCT, but represent a generic phenomenon in the microrheology of active particles.

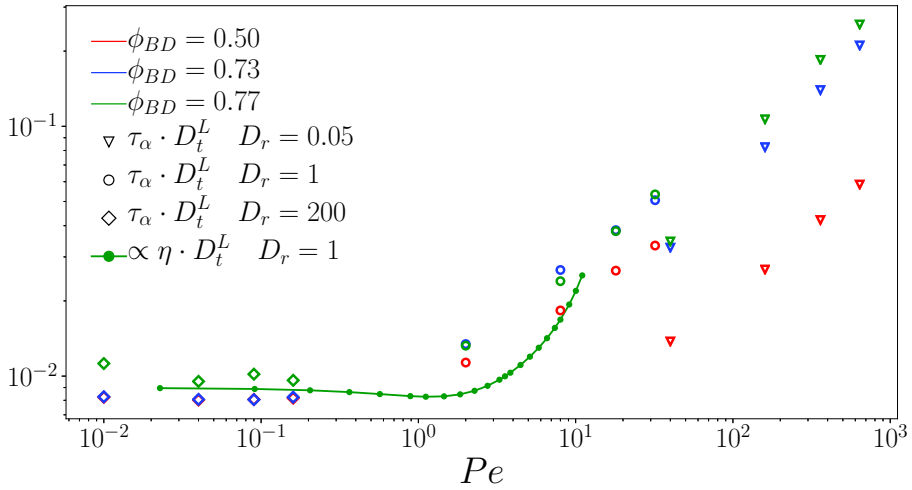

Figure 4.4.11.: *Product of $\tau_\alpha \cdot D_t^L$ for a passive tracer in an active hard-disk environment as a function of the bath Péclet number Pe, where τ_α is the α-relaxation time of the active bath particles at fixed $q = 7.5$ and D_t^L denotes the long-time diffusion constant of the passive tracer. Open symbols are simulation results. The solid green line shows the ABP-MCT prediction for $D_t^L \cdot \eta$ at fixed $D_r = 1$, shifted by a constant factor to match the simulation results for $Pe \to 0$ and with a velocity rescaling $v_0^{MCT} = 1.5 v_0^{BD}$.*

4.5 Active Tracer in the Active Bath

The following section discusses the tagged particle motion in a bath of identical active particles which allows the necessary averages in the simulations to be taken over all particles and thus makes it feasible to study quantities that have not easily been accessible in the study of single tracer particles so far, like transient-types of averages that are exclusively performed over the equilibrated initial state and form the theoretical basis for the ABP-MCT predictions. This allows to assess quantitative differences compared to a stationary-type statistics and to address the question if there can even arise qualitative differences in the comparison between both. With a better capability to sample the statistics of the system further allows for an exploration of a wider regime of parameters which will be exploited to compare the behaviour close to the glass transition point between the ABP-MCT predictions and the simulation results.

4.5.1 Self-Intermediate Scattering Function

Transient correlation functions were determined from the simulation results by exclusive averaging over the initially equilibrated state, in line with the definition of the ABP-MCT-predicted correlation functions, and compared to the stationary-type of correlation functions that exploit the Markovian properties of the steady-state to sample the statistics. For $S^s_{0,0}(\vec{q},t)$, qualitative differences between both types of averages could not be observed for the parameter range studied here, as presented in the figures 4.5.1 (a)-(d), which shows a comparison between both types of correlation function for fixed D_r and and different v_0 and q with the transient ABP-MCT predictions. Except for statistical errors, the equivalence between transient and steady-state correlation functions in the equilibrium system is very well confirmed. For the active system, the steady-state correlation functions show a slightly faster relaxation but do not reveal any qualitative differences. This observation is consistently confirmed by comparing the $\tau^s_\alpha(q)$ for the respective kind of averages as shown in figure 4.5.2, where also here the simple rescaling $v_0^{MCT} = 1.5 v_0^{BD}$ provides a near quantitative agreement between ABP-MCT predictions and stationary simulation results. One further notes that the slightly slower decay of the transient simulation results is most pronounced in the regime of intermediate wavenumbers wherein the regime of low wavenumbers transient and stationary types of averages deliver near-identical $\tau^s_\alpha(q)$. As for passive MCT, this low-q regime reflects the existence of a finite long-time diffusion constant seen in form of an asymptotic behaviour with $\tau^s_\alpha \sim 1/q^2$, indicated as a black dotted line and consistent with both ABP-MCT and simulation results.

Recall that as a consequence of the underlying non-equilibrium time evolution of ABPs, a symmetric relation between the non-diagonal SISFs $S^s_{1,0}(\vec{q},t)$ and $S^s_{0,1}(\vec{q},t)$ is not expected, as discussed in section 3.1.3. This is a manifestation of the transient nature of the ABP-MCT averages and the presence of different relaxation channels in the system which implies that $S^s_{1,0}(\vec{q},t)$ will always decay at least after the persistence time contrary to what is expected for $S^s_{0,1}(\vec{q},t)$. This striking ABP-MCT prediction is tested in the simulation by comparing with transient types of averages int the simulations, as presented in figure 4.5.3 (a). For this comparison, it is instructive to choose parameters that maximize the difference between the persistence time and the structural relaxation time, which is well achieved by choosing $D_r = 200$ and $\phi_{BD} = 0.77$. Also note that to obtain a better statistics, averages for non-isotropic correlation functions have been obtained by including both correlation functions with $\vec{q} = q\vec{e}_y$ and $\vec{q} = q\vec{e}_x$ transformed to $\vec{q} = q\vec{e}_y$ by using the unitary transformation for rotations of $\vec{q}$. Indeed, the ABP-MCT predictions and simulation results predict non-symmetric correlation functions with the $S^s_{1,0}(\vec{q},t)$ decaying after τ_r and the $S^s_{0,1}(\vec{q},t)$ showing the slow structural dynamics. The difference towards stationary averages is shown in subfigure (b), revealing that both non-diagonal components approach each other after $t \approx \tau_r$ and both decay on the time scale of structural relaxation time. This allows for the conclusion that both components will become non-ergodic above the glass transition, contrary to what is predicted by the ABP-MCT in the transient case. It further indicates that the qualitative differences between transient and steady-state averages might become important if the persistence time and the structural relaxation time become increasingly different, while at the same time the persistence length remains large, and thus the coupling of the non-diagonal elements to $S^s_{0,0}(q,t)$ presumably becomes more pronounced.

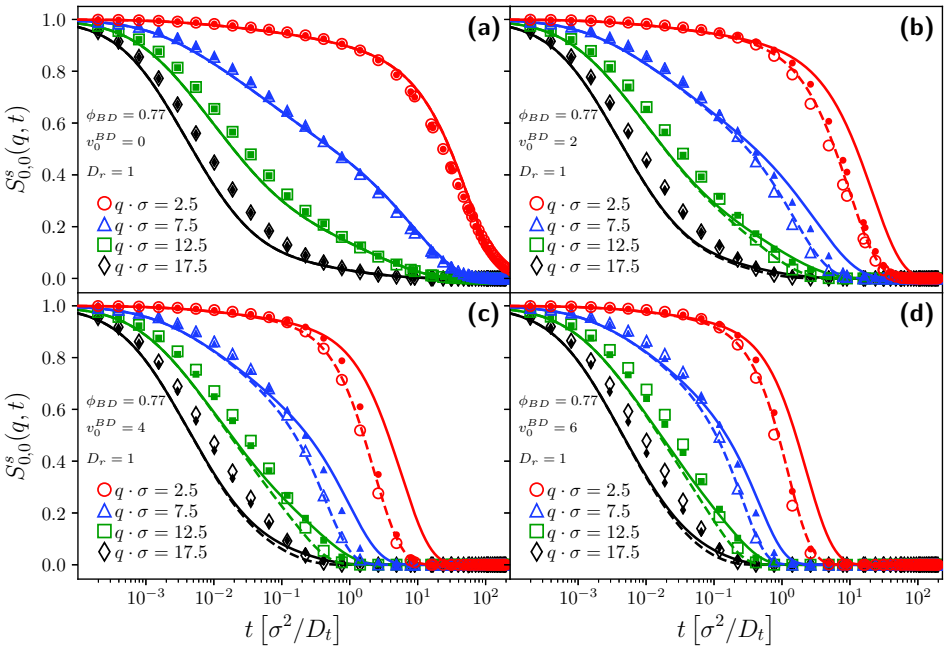

Figure 4.5.1.: ***(a)-(d)*** *$S^s_{0,0}(\vec{q},t)$ of an active tracer in an identical active hard-disk environment for different wavenumbers q, self-propulsion velocities v_0 and fixed $D_r = 1$ and $\phi_{BD} = 0.77$. Filled symbols are transient simulation results, empty symbols are stationary simulation results, solid lines are ABP-MCT results where only ϕ^{MCT} was adjusted, dashed lines are ABP-MCT results for an additonal adjustment of $v_0^{MCT} = 1.5 v_0^{BD}$.*

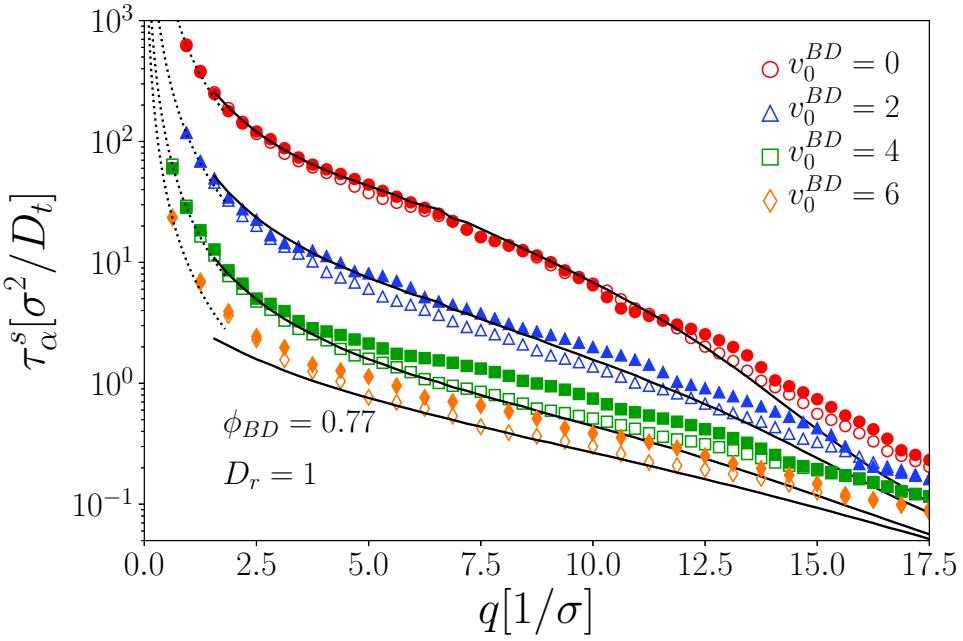

Figure 4.5.2.: *$\tau^s_\alpha(q)$ of an active tracer particle in an identical active hard-disk environment for a range of wavenumbers q and different self-propulsion velocities at fixed $D_r = 1$ and $\phi_{BD} = 0.77$. Filled symbols are transient simulation results, open symbols are stationary simulation results and black solid lines are MCT results with adjusted $\phi_{MCT} = 0.77$ and $v_0^{MCT} = 1.5 v_0^{BD}$. Black dotted lines are fits to the low-q asymptote $\tau^s \sim 1/q^2$.*

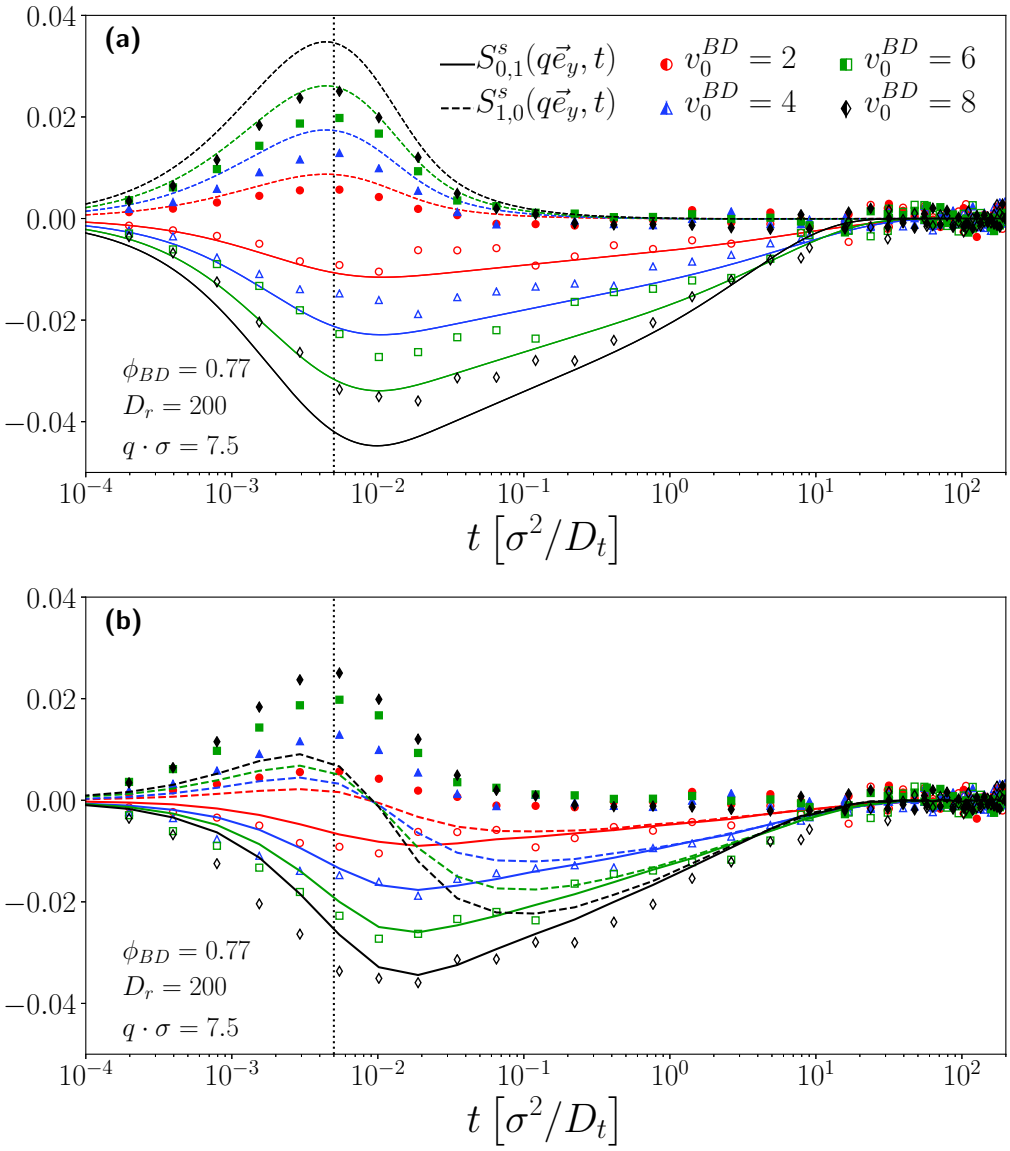

Figure 4.5.3.: *Non-diagonal elements $S^s_{1,0}(\vec{q},t)$ and $S^s_{0,1}(\vec{q},t)$ of an active tracer in an identical active hard-disk environment at fixed wavevector $\vec{q}=7.5e_y$, $D_r=200$, $\Phi_{BD}=0.77$ and different self-propulsion velocities. In each figure the dotted vertical line indicates the persistence time τ_r. **(a)** compares transient averages from BD (filled symbols for $S^s_{1,0}(\vec{q},t)$, open symbols for $S^s_{0,1}(\vec{q},t)$) with ABP-MCT predictions. **(b)** compares transient averages from BD, with same symbols as in (a), with stationary averages from BD (dashed lines for $S^s_{1,0}(\vec{q},t)$ and solid lines for $S^s_{0,1}(\vec{q},t)$)*

Justified by the good agreement between ABP-MCT predictions and stationary averages from simulations, the following discussion will restrict back to a comparison with a stationary type of statistics from the simulations. To address a further range of parameters, the extracted $\tau^s_\alpha(q)$ from both methods are examined in a wide range of densities for a fixed wavenumber $q=7.5$ as depicted in 4.5.4. This comparison delivers quantitative agreements in a wide range of densities for different v_0 that is also convincingly seen for the SISFs as shown in figure 4.5.5.

MCT predicts a divergent behaviour of the relaxation time when approaching the glass transition point according to

$$\tau_\alpha^s \sim (\phi_c - \phi)^{-\gamma}, \tag{4.5.1}$$

with both γ and ϕ_c depending on v_0 and D_r. This asymptotic power-law behaviour is only confirmed in the simulations for densities that are not too close to the glass transition point whereas for $\phi_{BD} > 0.77$ and low activities, the simulation results are subject to ergodicity restoring effects that are not captured by MCT.

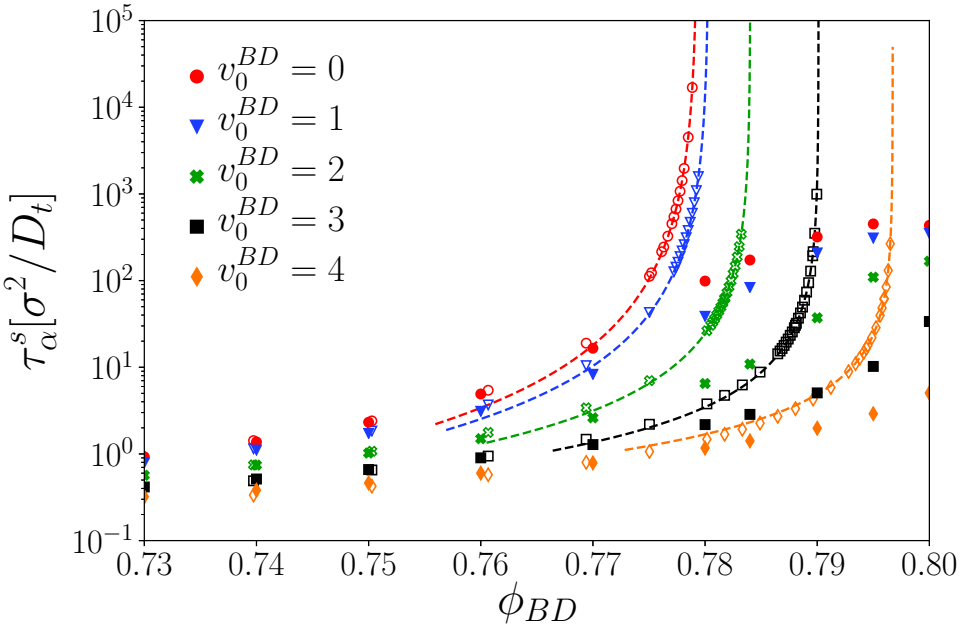

Figure 4.5.4.: $\tau_\alpha^s(q)$ *of an active tracer particle in an identical active hard-disk environment in a range of densities and different self-propulsion velocities at fixed* $D_r = 1$ *and fixed wavenumber* $q = 7.5$. *Filled symbols are simulation results, empty symbols are MCT predictions with adjusted* ϕ_{MCT} *and* $v_0^{MCT} = 1.5 v_0^{BD}$. *Dashed lines are power-law fits to the MCT results according to equation* (4.5.1). *For the resulting fit parameters see the table below.*

v_0^{BD}	0	1	2	3	4
ϕ_c^{BD}	0.779	0.780	0.784	0.790	0.797
γ	2.28	2.08	1.65	1.36	1.17

Resulting parameters for the power-law fits depicted in in figure 4.5.4.

A question that arises within the asymptotic regime of the ABP-MCT is how activity influences the parameters ϕ_c and γ that govern the power-law divergence of the relaxation time. While it is rather descriptive that particles undergoing a persistent motion are more likely to escape the neighbouring cages with the consequence of increasing ϕ_c with increasing v_0 and τ_r, there exists no illustrative picture to assess to influence on the exponent γ that quantifies the strength of the divergence. MCT, however, provides a quantitative description for γ through the determination of the exponent parameter λ from equation (3.2.10) by determining the left- and right eigenvectors h and $\hat{h}$ of the linear mapping of $C[h]$ in equation (3.2.6) in the case

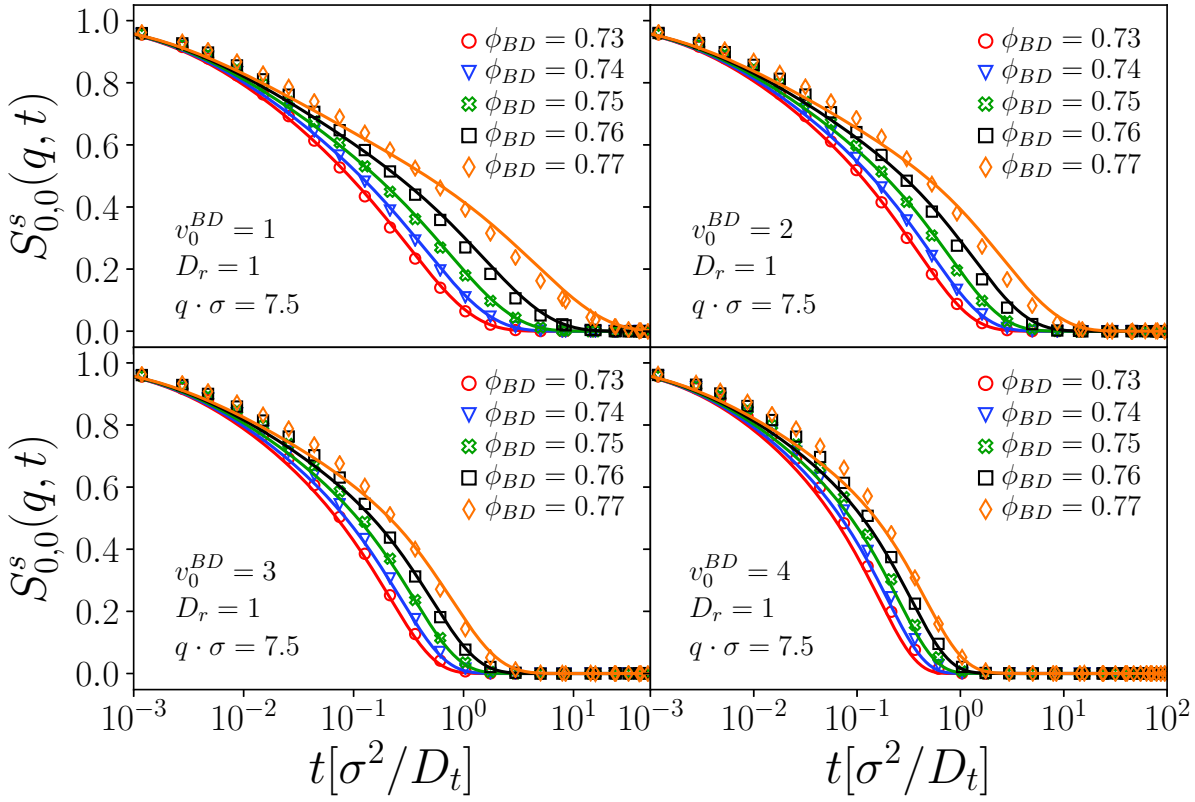

Figure 4.5.5.: *$S^s_{0,0}(\vec{q},t)$ of an active tracer in an identical active hard-disk environment for different self-propulsion velocities v_0 each for different ϕ_{BD} at fixed wavenumber $q = 7.5$, $D_r = 1$. Symbols are simulation results, solid lines are ABP-MCT predictions with adjusted ϕ^{MCT} and adjusted $v_0^{MCT} = 1.5 v_0^{BD}$.*

$D_r = 0$. The resulting exponents γ are depicted in figure 4.5.6 (a) in a wide range of v_0 and compared to the resulting fit parameters from figure 4.5.4 for $D_r = 1$. Both cases $D_r = 1$ and $D_r = 0$ consistently reveal an identical exponent $\gamma \approx 2.29$ in the passive case and are well in line with the passive MCT study by Bayer et al [107] for 2D hard-disks which has found $\gamma \approx 2.38$. Some exponents that were determined for the active system for $D_r = 0$ have additionally been verified by plotting the $\tau_\alpha(q)$ at fixed q, that were extracted from the ISF, against the relative distance from the glass transition point $\epsilon = (\phi - \phi_c)/\phi_c$, as depicted in figure 4.5.6 (b) and very well in line with the predicted power-law exponents. For increasing v_0, both cases $D_r = 0$ and $D_r = 1$ show a decrease of γ, as previously reported by Ni et al. for simulations of event-driven active Brownian hard-spheres in 3D [81]. The case $D_r = 0$ that is studied here shows that γ approaches a plateau of $\gamma \approx 1.76$ with increasing v_0 and an even steeper decrease is seen for $D_r = 1$. The interpretation of these results must be taken with care and do not necessarily indicate a non-monotonic behaviour with D_r as one might expect, because the case $D_r = 0$ always relates to the regime $\tau_r \gg \tau_\alpha(q)$, where the asmyptotic power-laws depicted in figure 4.5.4 fall into the regime $\tau_r < \tau_\alpha(q)$ for which different asymptotic laws are expected to arise, as seen by the more subtle structure of equation (3.2.1) with its hopping integral in the time domain that determines the non-ergodicity parameters.

The decrease of γ with increasing v_0 and the resulting divergence behaviour of the relaxation time translates into a notable behaviour of the viscosity of active fluids close to dynamical arrest. A striking consequence is that dense active suspensions in the fluid state with equal separations from the glass transition point can have viscosities that differ by an order of magnitude, as seen in 4.5.6 (c). This is even though that an active fluid with equal distance to the glass transition point compared to a less active fluid exists a higher density.

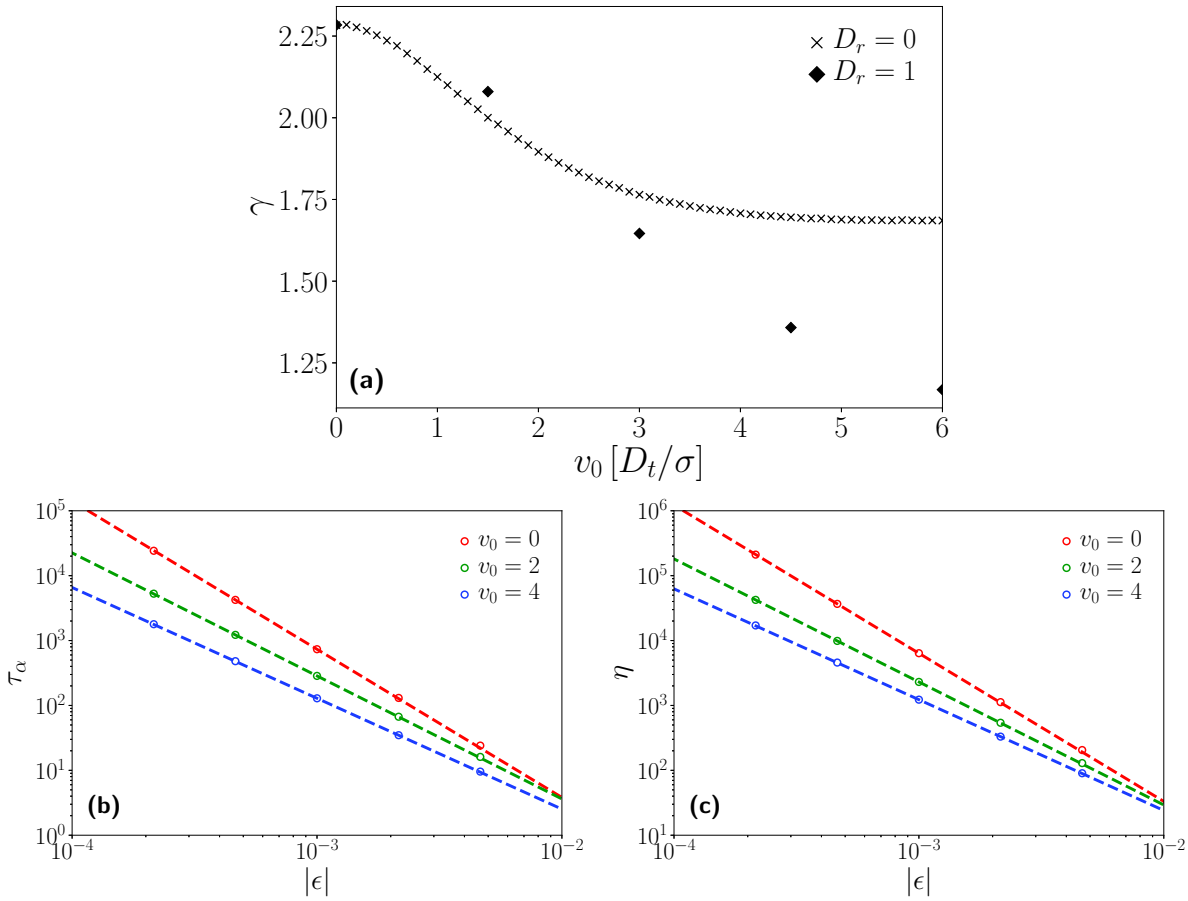

Figure 4.5.6.: ***(a)*** *ABP-MCT predicted divergence exponents γ for an active bath of ABPs as a function of the self-propulsion velocity v_0. Crosses are results from the asymptotic MCT equations for $D_r = 0$, rectangles are results from the power-law fits of figure 4.5.4.* ***(b)*** *shows the dependence of $\tau_\alpha(q)$ at fixed $q = 7.5$,* ***(c)*** *of the viscosity η as a function of the separation from the glass transition point for $D_r = 0$, where the dashed lines are power-laws with the γ from (a).*

4.5.2 Mean-Squared Displacement

Figure 4.5.7 displays MSDs of an active tracer in an identical active bath obtained both from ABP-MCT and simulations. To assess the influence of the activity of the tracer particle, it is instructive to compare the simulation results with the reference case of a passive tracer particle in the same active host system, indicated as black symbols. This further allows addressing polydispersity effects by noting that coloured and black symbols do not coincide even in the case $v_0 = 0$ as the latter stem from a collective average over a polydisperse passive bath where

black symbols are results obtained by taking averages over a single passive tracer particle with the same diameter as the mean diameter as the passive host environment. In case of an active bath, the active tracer exhibits both mechanisms of enhanced transport in terms of intrinsic activity and the persistent driving of the surrounding host particles. The direct comparison with the scenario of a passive tracer particle where only the second contribution arises allows assessing the dominant mechanism, depending on the considered density regime. The results for $\phi_{BD} = 0.73$ and $\phi_{BD} = 0.77$ indicate that the influence of the active bath is the way more dominant contribution as there emerge no notable differences when comparing the scenarios of passive and active tracers which is explained by the superior influence of the cageing effect of the active bath particles. On the other hand, the results for $\phi_{BD} = 0.50$ reveal that the dominant transport mechanism originates from the intrinsic activity of the tracer in the regime of low and moderate densities. This is a consequence of the weak coupling to the bath particles that are less effective in transmitting superdiffusivity to the tracer. Instead, superdiffusive motion comes from the intrinsic activity of the tracer particle as it is not suppressed by the bath particles because cageing effects are less pronounced and not capable to hinder the ballistic motion of the tracer.

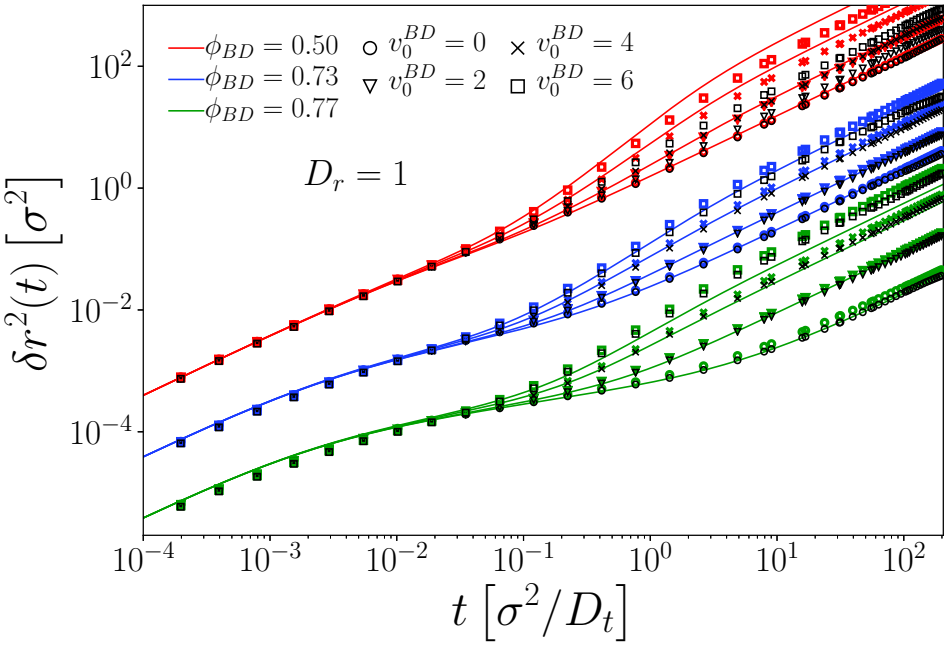

Figure 4.5.7.: *Comparison between MSDs of an active tracer in an identical active hard-disk environment and the MSDs of a passive tracer in the same environment for varying densities and self-propulsion velocities and fixed $D_r = 1$. Coloured symbols are BD results for the active tracer, black symbols are BD results for the passive tracer in an active hard-disk system repeated from figure 4.4.7. Lines are ABP-MCT predictions for an active tracer in an active hard-disk system with adjusted ϕ_{MCT} and adjusted $v_0^{MCT} = 1.5 v_0^{BD}$.*

4.5.3 Mean Effective Swimming Velocity

To conclude the discussion, the MCT-ITT predictions for the collective swimming velocity according to equation equation (3.5.10) are compared with respective simulation results as shown

in figure 4.5.8. Having established a rescaling of the density to match the dynamical correlation functions reveals consistent results in both theory and simulation in a density regime close to dynamical arrest, with v going to zero when approaching the (shifted) glass transition point. On the other hand, the agreement in the medium density is not as good as for the swimming velocity of an active tracer in a passive bath v^s, presented before in figure 4.3.13. The inset compares the same results without prior adjustment of the densities and as same as for the passive tracer, the large discrepancies that arise in the low- density regime are due to an erroneous prediction of the relaxation time, that can be corrected by including quadratic terms in the density mapping, rather than a general failure of the ABP-MCT approach to predict the effective swimming velocity.

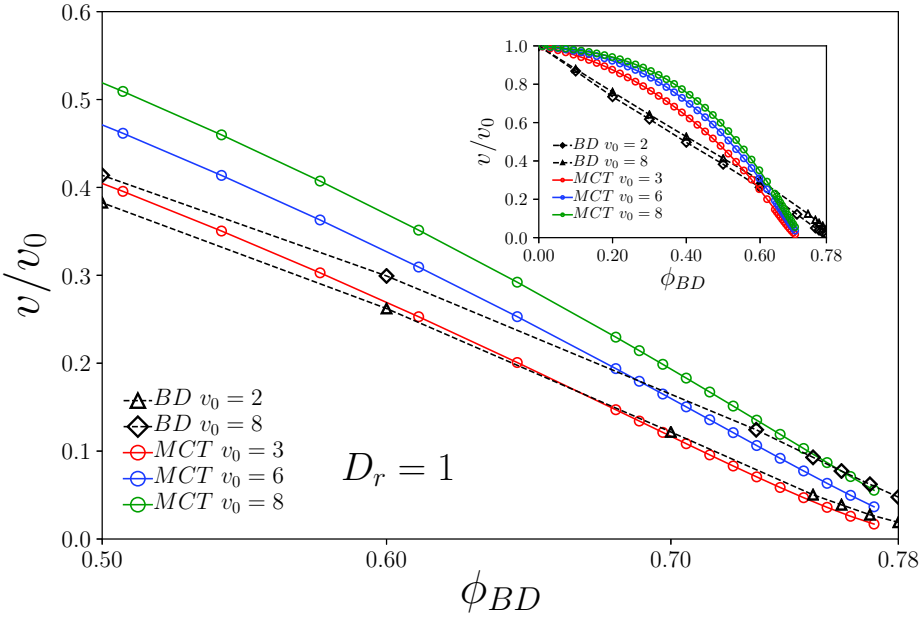

Figure 4.5.8.: *Normalized mean effective swimming velocity v/v_0 in an active hard-disk system at fixed $D_r = 1$. Red circles are MCT-ITT predictions, black symbols are BD results. The main figure shows the comparison after a prior density adjustment of the MCT-ITT results. The inset shows the comparison without such a density adjustment. BD results were obtained and provided by L. Granz [110].*

5. Comparison with Experiments

This chapter refers to recent experimental results from a setup with laser-driven diffusiophoretic Janus particles immersed in a binary colloidal suspension, reflecting the scenario of an active tracer in a bath of passive particles discussed in section 4.3. The experiments were conducted by Lozano et al. and the results have been published in [112]. First, the described experimental setup is briefly explained, allowing for an assessment of emerging deviations in the subsequent comparison with both the results for passive and active particles in active hard-disk environments according to the methods of this work.

5.1 Experimental Setup

The experiments were performed with a 50 : 50 mixture of binary colloids with diameters of $\sigma_s = 4.6\,\mu\text{m}$ and $\sigma_l = 6.3\,\mu\text{m}$ immersed in a water-lutidine mixture at a temperature of $T = 26\,^\circ\text{C}$. With the selected composition, the colloidal suspension did not show signs of crystalization in the whole range of investigated densities. The dimension of the sample cell was chosen that the particles were confined in a way that translational and rotational motion can be regarded as quasi-two-dimensional. Lozano et al. added few Janus particles with a diameter of σ_l to the suspension. These Janus particles were half-capped with light-absorbing patches, which heat up when illuminated with a laser. This heating triggers a critical demixing of the local surrounding water-lutidine mixture upon reaching a critical temperature of $T_c = 34\,^\circ\text{C}$. The phoretic effects that are associated with the emerging concentration gradient of the surrounding fluid subsequently result in a self-propelled motion of the tracer particle. This mechanism has been exploited in a various number of experimental realizations of active particles and offers a clean method to control activity on a single particle level. With the same surface power density of the laser, which was kept constant in all experiments considered here to compare with, a persistent motion of the Janus particle with a velocity of around $1\,\mu\text{m/s}$ was achieved in the diluted system. By tracking the particles' trajectories and the orientation of the caps, $r^2(t)$ and $\theta^2(t)$ were determined each for passive and active tracer Janus particles at several densities and averages were taken over varying number of Janus particles in the system.

In the experiment, a glass transition point indicated by a constant plateau value of the MSD was found near $\phi_{c,exp} = 0.784$. One of the central observation was that if the density was increased

up to just below the glass transition density, the measured rotational diffusion coefficients of the active particles revealed an increase by around a factor of 27 compared to the rotational diffusion coefficient of a tracer particle in a diluted suspension. On the other hand, if the density was further increased above the critical density, the rotational diffusion coefficient was observed to approach the same magnitude as for the free particle again. Such a variation of the rotational dynamics could not be detected for passive tracer particles and was explained by the viscoelastic response of the colloidal suspension to the active driving of the tracer, resulting in a torque that acts on tracer particles. This explanation was supported by fitting the experimental results to a viscoelastic-fluid Jeffreys liquid model [113] in [112].

5.2 Passive Tracer in the Passive Bath

Due to the different experimental and MCT glass transition points, the densities of the passive systems must first be adjusted for a comparison with the active experimental data as it was similarly done in the comparison with the simulation results. This further allows assessing possible sources of error, that might not be related to the activity of the particles. An important issue in that context is the dominant influence of hydrodynamic interactions between the colloids, which are entirely neglected in the ABP model but must be taken properly into account with regard to the high-density regime studied here, as it is well known that hydrodynamic interactions lead to a strong density dependence of the short-time diffusion coefficients as reported in [114,115]. This effect is not directly assessable from the experimentally reported MSDs, as these only allow the determination of the short-time diffusion coefficient of the free particle, but for higher densities, the short-time diffusive regime was not measured. Due to the lack of distinctive theories and the fact that the influence of hydrodynamic interactions is rather specific to the experimental details, assessing the slow down of short-time diffusion at high densities requires a more subtle approach. It can be achieved by noting that that the MCT predictions are rather insensitive on the short-time dynamics and that a change of the short-time diffusion coefficient only affects the MCT prediction through a simple rescaling in time. Therefore, the density dependence of the diffusive time scale can be extracted by allowing physically reasonable shifts of the time-axis of the MCT predictions when fitting to the experimental data by treating such shifts as an additional density-dependent fit parameter.

A further observation that needed to be taken into account for such a fit was that the MCT predicted plateau value of the MSD closely above the glass transition significantly differs from the plateau value reported from the experiment. It turns out that the associated localization length reported by Lozano et al. is underestimated by a factor of about seven in comparison to the expectation for hard-spheres of $l_c \approx 0.1\sigma$, that is in turn well fulfilled by MCT. The exact reasons for these discrepancies are not completely clear, but might be related to the deviations from an idealized hard-core potential in form of additional electrostatic forces or interactions with the surface of the sample cell. Deviations between experimental and MCT predicted localization lengths of a similar order of magnitude have also been observed in [107] in connection with a quasi-two-dimensional system with magnetic dipole interaction [116]. Bayer et al. corrected these deviations by introducing an effective diameter, that was accordingly chosen

to match the plateaus between experimental and MCT-predicted MSDs. Following the same strategy, the experimental data can also here be convincingly adapted to the MCT predictions by treating the system as effectively monodisperse with an effective diameter of $\sigma^{\text{eff}} \approx (1/7) \cdot \bar{\sigma}$ with $\bar{\sigma} = (\sigma_l + \sigma_s)/2$ despite the presence of a binary mixture in the experiments. The resulting MCT fits to the experimental data are depicted in figure 5.2.2 and are given in terms of the same physical units as reported in [112]. These fits reveal a nearly linear relationship between densities in the experiment and MCT as shown in the inset and as previously seen in the comparison between passive MCT and simulations. Figure 5.2.1 shows the resulting hydrodynamic factors $D(\phi)/D_0$ to match MCT-predicted and experimental MSD in an error minimizing way, where D_0 relates to the translational diffusion coefficient of a free particle with diameter σ^{eff} and $D(\phi)$ to the short time diffusion coefficient of the dense system. The fit reveals that the diffusive time scale in the case of the highest investigated density of $\phi_{exp} = 0.814$ is increased by a factor of four compared to the time scale of the diluted system, underlining the necessity to take hydrodynamic interactions seriously into account. The results of the fits are also supported by comparing them with former experimental works with colloidal suspensions in quasi-2D [117] or 3D [118] that reported consistent hydrodynamic factors with those found here.

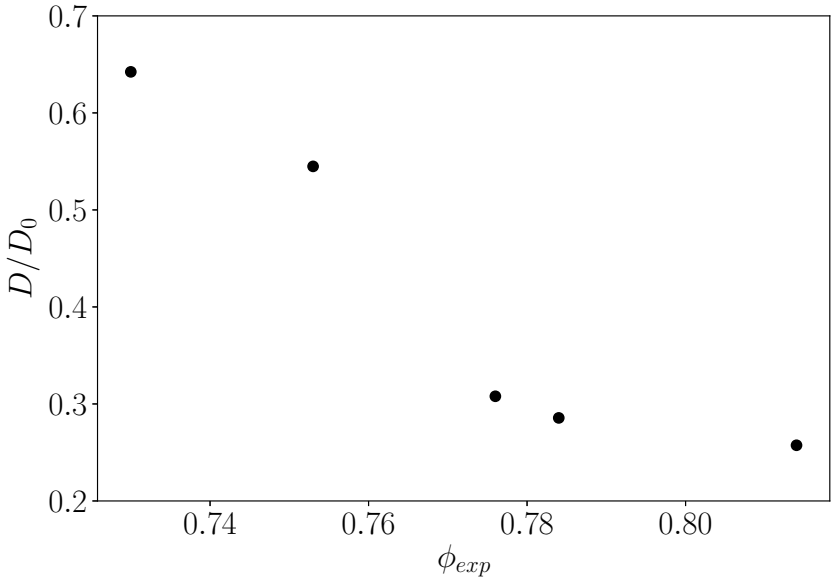

Figure 5.2.1.: *Hydrodynamic factors $D(\phi)/D_0$ of the translational short-time diffusion of a passive Janus particle immersed in a binary colloidal suspension for different ϕ_{exp} predicted from least-square fits of the experimental MSDs to the monodisperse passive MCT.*

By using the density mapping between MSDs predicted from MCT and simulations in figure 4.2.2, the experimental results can also be compared with the simulation results as presented in 5.2.2. The resulting MSDs from simulations describe the experimental data rather satisfactory, even though experimental and simulational densities slightly differ. This can mainly be retraced to the mixing effects that have been neglected in both MCT and simulations. Such mixing effects can be assessed by a comparison with the predictions of the MCT for binary mixtures in 2D which reveals a relative reduction of the glass transition point compared to a monodisperse system in the order of 1% [119] for the size composition in the experiment. This is rather

consistent with the observed deviations between the estimated experimental density of the glass transition point and the density estimated from the simulation. For the two densities in the glassy state, it is, however, observed that the simulation data show deviations in the intermediate time regime towards the plateau and that within the last time decade, there emerges a delocalization transition. The fact that this delocalization is not observed in the experiment, even though it is subject to similar ergodicity restoring effects, demonstrates a possible influence of ageing effects in the simulations due to an insufficient equilibration, that is easier to realize in the experiment. Despite these discrepancies, the simulation data describes the localization of the passive tracer particle consistent with the experiment in form of corresponding plateau values over several decades in time.

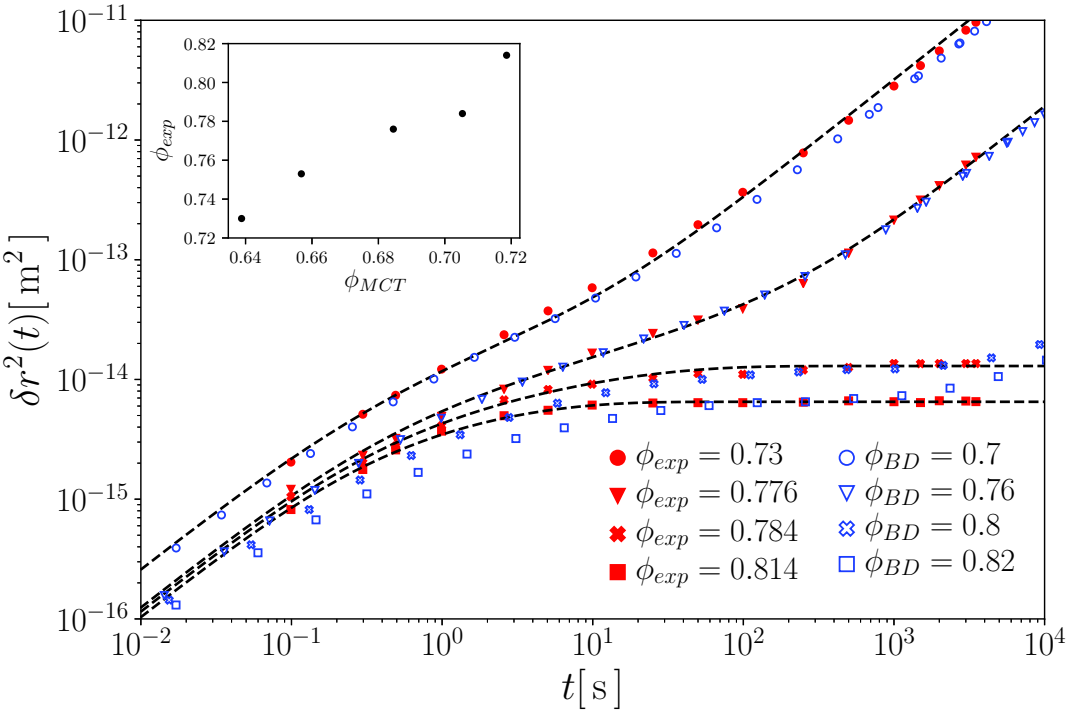

Figure 5.2.2.: *Comparison between the experimentally reported MSDs of a passive Janus particle in a binary colloidal suspension with simulation results and MCT predictions for the MSD of a passive tracer particle in a passive hard-disk environment. Red symbols are experimental results from [112]. Dashed back lines are MCT fits with adjusted densities as shown in the inset, blue symbols are simulations results with adjusted densities according to the inset of figure 4.2.2.*

5.3 Active Tracer in the Passive Bath

Having performed the necessary density adjustments for the passive bath, the experimental results of the active system are now to be compared with the methods of this work. Arguably, the rather simplified nature of a model of hard-core repulsive ABP might hamper the comparison to the far more complex experimental system as the ABP model is not feasible to account for the complex diffusiophoretic mechanisms upon the critical demixing and the hydrodynamic interactions triggered by the resulting persistent motion of the Janus particle. Still, such a

comparison might serve as an instructive test of the model.

To perform an adaption the ABP model, the rotational diffusion coefficients were extracted from the experimental data by determining the slope of $\langle\theta^2(t)\rangle$. For the free passive particle, a relative error of 50% of the resulting D_r compared to the prediction from the Stokes-Einstein relation between rotational and translational diffusion coefficients was found. These discrepancies demonstrate that solely measuring D_r would not provide a method to precisely quantify the slowdown of short-term diffusion, which underlines the necessity of the fitting procedure performed in the previous section. For the active Janus particles, $\delta\theta^2(t)/(2t)$ was subject to fluctuations in the order of magnitude of 20% at long times. These fluctuations might be explained by the force-dipole characteristic of self-propelled particles, which is known to cause torques triggered by the hydrodynamic interactions with the surface of the sample cell. This means that the rotational dynamics cannot be regarded as completely diffusive in contradiction with a model of spherical ABP with a purely diffusive rotational dynamics. Further, the reported effect of an increase of D_r close to the glass transition is not described by the ABP model and can only be contained by adjusting $D_r(\phi)$ by hand as it was done for the comparison.

The experimentally reported results for the MSDs of the active Janus particle are depicted in figure 5.3.1 for different densities. Within the extracted D_r, the MSD of a free Janus particle can be accordingly fitted to the analytic solution of the free ABP as shown as a dotted line. This fit yields a self-propulsion velocity of 1.07 µm/s, in line with the reported value from the experiment of 1 µm/s. In terms of the used ABP model units this is equivalent to $v_0 = 109\, D_{0,l}/\sigma_l^{\text{eff}}$, with $D_{0,l} = 0.0087\,\mu\text{m}^2/\text{s}$ denoting the experimentally reported diffusion coefficient of the free particle and $\sigma_l^{\text{eff}} = \sigma_l/7$ its effective diameter.

An estimation for the order of magnitude of the required v_0 to adapt the data to the ABP model is provided by a comparison with figure 4.3.9, where the MSDs for $\phi_{BD} = 0.77$ reveal a significant reduction of the relaxation time caused by activity. A similar effect is also seen for the MSDs reported in the experiment, concluding that they fall into a similar parameter range where necessary v_0 to adjust the data to the ABP-MCT are unfortunately far beyond the stability range of the numerical scheme that is limited to $v_0 \approx 8D_t/\sigma$.

Even though an adaption to the ABP-MCT was not possible, it is still instructive to fit simulations results to the experimental data. This has been achieved by adjusting v_0 with fixed D_r as reported in the experiment for each density. Thereby it was assumed that the influence of the laser-induced temperature increase of ΔT=8 °C on the short-time diffusion coefficients is negligible and that these do also not show a significant dependence on the activity, meaning that they are given by those determined in the last section from the passive systems. The simulation results which have provided the best qualitative agreement under these assumptions are additionally shown as blue symbols in figure 5.3.1 and provide a rather well agreement for all densities.

Nevertheless, this comparison reveals several puzzling observations, e.g. when comparing the MSDs for the densities $\phi_{exp} = 0.73$ and $\phi_{exp} = 0.776$. According to what has been reported in this thesis so far, the mobility of an active tracer particle shows a monotonically decreasing behaviour with both the rotational diffusion coefficient and the density, but the experimental

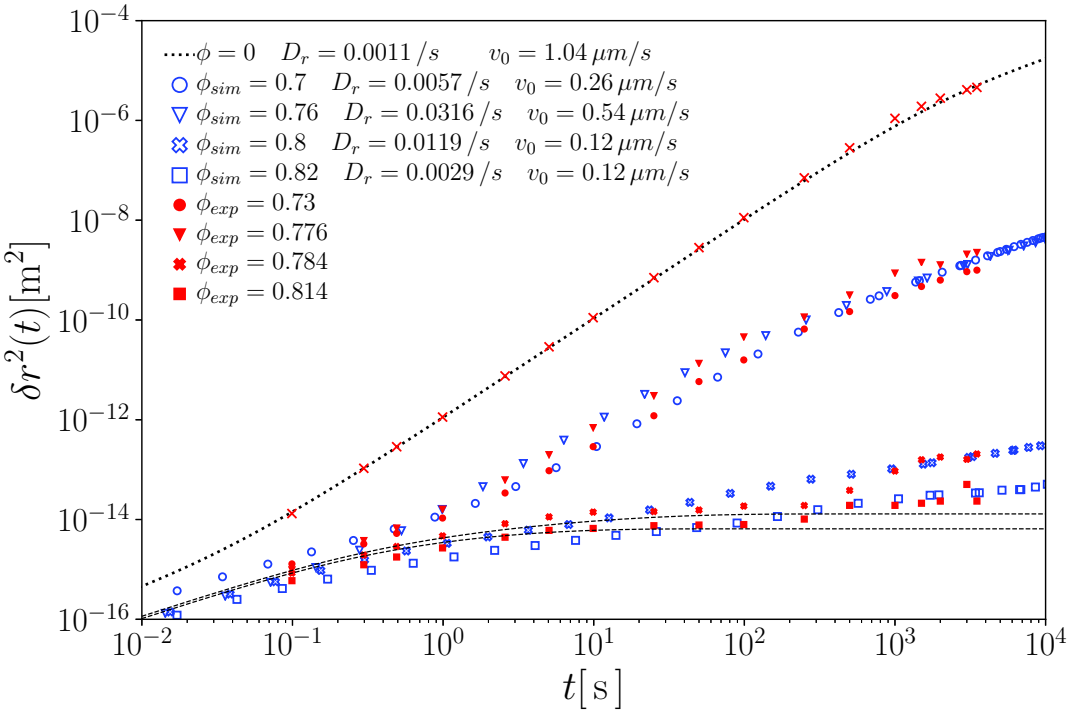

Figure 5.3.1.: *Comparison between the experimentally reported MSDs of an active Janus particle in a binary colloidal suspension with simulation results for the MSD of an ABP in a passive hard-disk environment. Red symbols are experimental results from [112], blue symbols are simulations results with resulting ABP parameters in terms of experimental units and adjusted densities as indicated. Black dotted lines correspond to the passive plateau values. The black dotted line shows a fit to the analytical solution of the free ABP, with fixed D_r as reported from the experiment.*

results contradict this observation. Despite an increase in density and even a concomitant increase of the rotational diffusion coefficient approximately by a factor of five, the MSD does not reveal an expected weaker transport for $\phi_{exp} = 0.776$ compared to $\phi_{exp} = 0.73$. Resolving this striking non-monotonic behaviour within the adaption to the simulation could only be achieved by a non-monotonic variation of the self-propulsion velocities, which had to be chosen twice as large for $\phi_{exp} = 0.776$ as for $\phi_{exp} = 0.73$ to match the experimental results. This seems questionable given the decreasing effectiveness of the laser-induced self-propulsion mechanism when increasing the density in the experiment, accordingly seen for $\phi_{exp} = 0.784$ and $\phi_{exp} = 0.814$ and therefore leaves some open questions.

A striking observation for the densities $\phi_{exp} = 0.784$ and $\phi_{exp} = 0.814$ above the glass transition is an increase of the MSD from the plateau value of the corresponding passive systems both in the simulations and in the experiment. In the simulations, this increase emerges at least one decade before the rise from the plateau caused by the deviations from an ideal glass as seen for the passive system and can therefore be attributed to the influence of the tracer's activity. For $\phi_{exp} = 0.784$ it is not possible to judge from the experimental data, whether these changes represent a delocalization transition in form of a finite long time-diffusion constant or a jump to another plateau value. Results reported from active microrheology for a tracer

particle pulled with a constant force suggest that the localization length before reaching the localization transition caused by a critical force increases to about one particle diameter [83] which corresponds to an increase of the plateau value by a factor of about 100 compared to the passive system as it is fulfilled here. It becomes also apparent that the crossover time scale that induces the change of the plateau in the experimental data does not match the rotational correlation time suggesting that this crossover could indeed be related to a delocalization of the tracer particle. On the other hand for $\phi_{exp} = 0.814$ the increase of the plateau value takes place on the same time scale as rotational correlation time in both experimental and simulation results which indicates a changeover to a new plateau value as it is similarly observed for the correlation functions with finite D_r [47]. Together with the observation that the change in the plateau value is only of factor 10 suggests that the tracer particle is still in a localized state in this case.

Even though passive MCT has proven to be a useful tool to assess the effects of hydrodynamic interactions, it was not possible to compare the experimental results of the active system with the ABP-MCT predictions due to its numerical limitations. Nonetheless, one can address the question if ABP-MCT predicts such a delocalization transition in the parameter range that is accessible. To check this, localization lengths l_c for an active tracer in the passive hard-disk system according to equation (3.4.20) have been calculated very closely above the critical glass transition density for the solvable case $D_r^s = 0$ as depicted in figure 5.3.2 in the range of accessible v_0^s. The results were obtained by calculating the critical non-ergodicity parameters $\boldsymbol{f}_c(\vec{q})$ and $\boldsymbol{f}_c^s(\vec{q})$ from the respective self-consistent iteratively solvable equations. Here $\boldsymbol{f}_c^s(\vec{q})$ converged up $v_0^s \approx 9$ and a better convergence in a regime of larger v_0^s could also not be achieved by increasing Λ_L. The critical localization length reveals an expected monotonically increasing behaviour with v_0^s, but a delocalization transition is not seen in the presented parameter range, but might be expected to occur at higher v_0^s when l_c approaches the magnitude of one particle diameter.

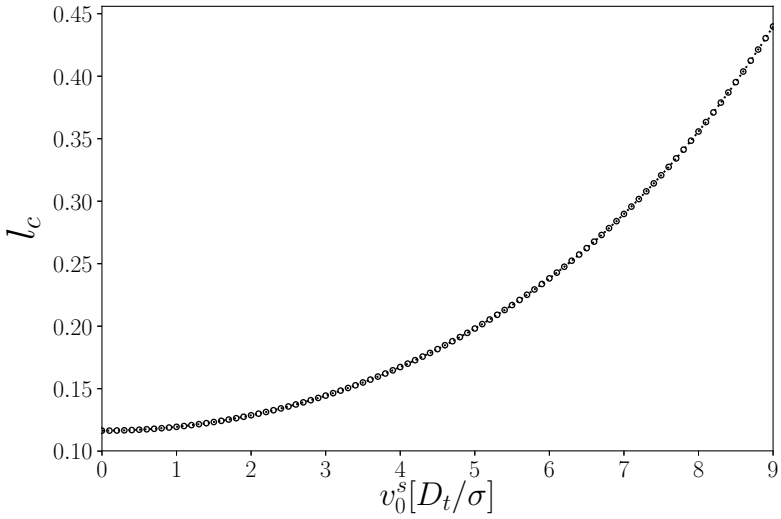

Figure 5.3.2.: *ABP-MCT predictions for the critical localization length of an active tracer particle in the passive hard-disk environment at the glass transition density in a range of v_0^s at fixed $D_r^s = 0$*

6. Mixtures of Active and Passive Particles

The numerical solutions of the ABP-MCT equations for mixtures of active and passive particles addressed so far have been restricted to compositions in which the concentration of a second particle type was only present in a highly diluted form, meaning that it had no influence on the dynamics of the bulk component in the thermodynamic limit. Since this work has constituted the framework to investigate arbitrary mixtures of active mixtures, this chapter aims to present first predictions of the ABP-MCT for the simplest conceivable composition of active and passive particles, that of a monodisperse binary mixture with varying concentration c of an active particle component. There are several reasons why the investigation of such a system might be of interest. First, there might arise technical difficulties to keep a global activity level in an experimental realization of active particles. Further, a controllable increase of the active components in the system allows to selectively modify the rheological properties of a sample, as it was already demonstrated in figure 4.5.6 that the viscosity of an active fluid can be manipulated to a great extent by making the system active and this effect could equivalently be achieved by adding small amounts of active particles. Moreover, the ABP-MCT for mixtures can be used to assess presumably non-linear influences of a composition change in order to modify the properties of samples in an efficient way.

6.1 Glass transition

Since the present theory lacks a strict method to determine the glass transition point in the case of non-vanishing rotational diffusion coefficients, as discussed in section 3.2, the case $D_r = 0$ is considered in this section. This allows to calculate the glass transition points in the same way as in passive MCT by using the iterative solutions of equation (3.2.5) in combination with a bisection method that searches for a root of the non-ergodicity parameter as a function of the density. The resulting fluid-glass transition diagram for the monodisperse mixture of passive particles and ABPs with an infinite persistence time is presented in figure 6.1.1 in the three-dimensional parameter space of (ϕ, c, v_0). The critical glass transition density shows to be monotonically increasing with both the concentration and activity of the active species, as already seen for the single component active system. By increasing the fraction of active particles of the system leads to a higher chance to escape cages formed by neighbouring particles with

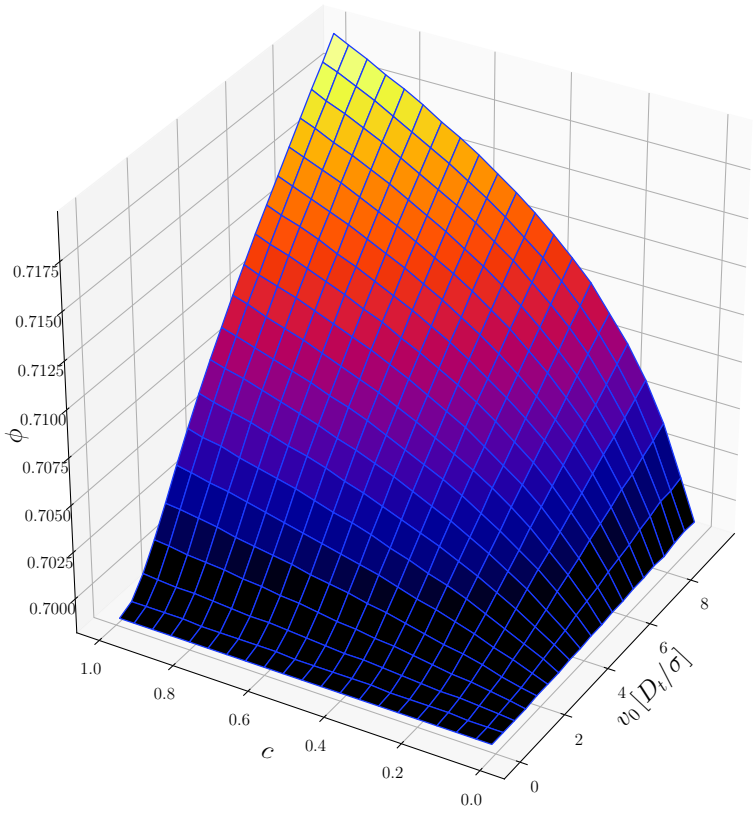

Figure 6.1.1.: *ABP-MCT-predicted fluid-glass transition diagram of the monodisperse binary mixture of active and passive particles with $D_r = 0$ in the three-dimensional parameter space of (ϕ, c, v_0). The colours indicate the magnitude of the critical density ϕ_c.*

the consequence of a shift of dynamical arrest to higher densities. A striking observation is, that the resulting transition diagram shows that this effect is not in general linearly related to the increase in the concentration of the active component. This is highlighted in figure 6.1.2 (a) which shows the intersecting lines of the transition diagram with the planes of constant activity. While an increase in the concentration of the active component is accompanied by a linear increase in the critical density at low activities, a non-linear dependence is observed for higher activities. In that case, the shift of the glass transition point is most efficiently achieved by only adding a small number of active components. This observation is in line with the glass transition diagrams reported for the MCT approach for mixtures of active Ornstein-Uhlenbeck particles in [120], where transition lines of similar shapes have been reported. This non-linear dependence can be explained by the cage picture. If several active particles form such a cage, some part of active forces will be compensated by means of opposite orientation vectors, which weakens the effects of an enhanced structural rearrangement. On the other hand, when considering such a cage in a system with a diluted active component, compensation effects of neighbouring active particles do only occur very rarely and the shift of the glass transition proceeds more efficiently.

Intersecting lines of the transition diagram with the planes of a constant concentration of the active component are shown in figure 6.1.2 (a). For the varying concentrations, it is observed that at low activities, the increase in v_0 is only slowly accompanied by an increase of ϕ_c with a quadratic dependence on v_0. This is an expected observation since the transition lines are symmetric under changing $v_0 \to -v_0$, meaning that their first-order expansion must be quadratic in leading order of v_0. Besides this effect, there do not emerge novel qualitative features compared to the homogeneous active case with $c = 1$. For this case, the resulting transition lines are presented with an additonal instructive test of cutoff dependencies on Λ_L by calculating the transition for $\Lambda_L = 2$ instead for $\Lambda_L = 1$. This comparison does not reveal strong quantitative differences for both cases and serves as further justification to restrict to $\Lambda_L = 1$ in the calculations in the presented parameter regime.

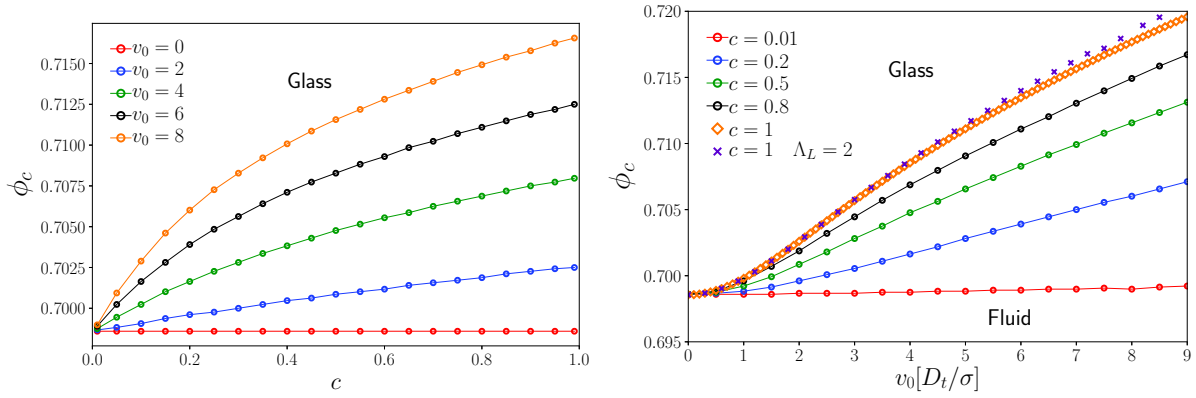

Figure 6.1.2.: *MCT-predicted fluid-glass transition lines of the monodisperse binary mixture of active and passive particles at fixed $D_r = 0$. **(a)** shows the intersecting lines of figure 6.1.1 with the planes of constant self-propulsion velocities v_0 of the active particle type. **(b)** shows the insersecting lines with the planes of constant concentration c of the active particle type. Orange and purple symbols are results for $c = 1$ each for a rotational cutoff number of $\Lambda_L = 1$ (orange) and $\Lambda_L = 2$ (purple).*

The resulting structure factor normalized critical non-ergodicity parameters

$$\hat{f}^{\alpha,\alpha}_{c\,0,0}(q) := f^{\alpha,\alpha}_{c\,0,0}(q)/S^{\alpha,\alpha}(q) \tag{6.1.1}$$

of active and passive types according to the transition lines for $v_0 = 4$ are presented in figure 6.1.3 for the same concentrations as shown in figure 6.1.2 (b). In the diluted cases of each active and passive particle type, the non-ergodicity parameters converge to those of the tagged particle dynamics, seen in form of a weaker modulation with the structure factor. This means that the red curve for the $\hat{f}^{a,a}_{c\,0,0}(q)$ approaches the non-ergodicity parameter of an active tracer in a passive bath, where the orange curve for $\hat{f}^{p,p}_{c\,0,0}(q)$ that of a passive tracer in an active bath. Since the critical density of active glasses is increased compared to passive glasses explains why in the latter case, the non-ergodicity parameters are larger. It is seen that the passive tracer in the active glass close is subject to stronger localization effects than an active tracer in a passive glass, which is due to the higher critical density in the former case.

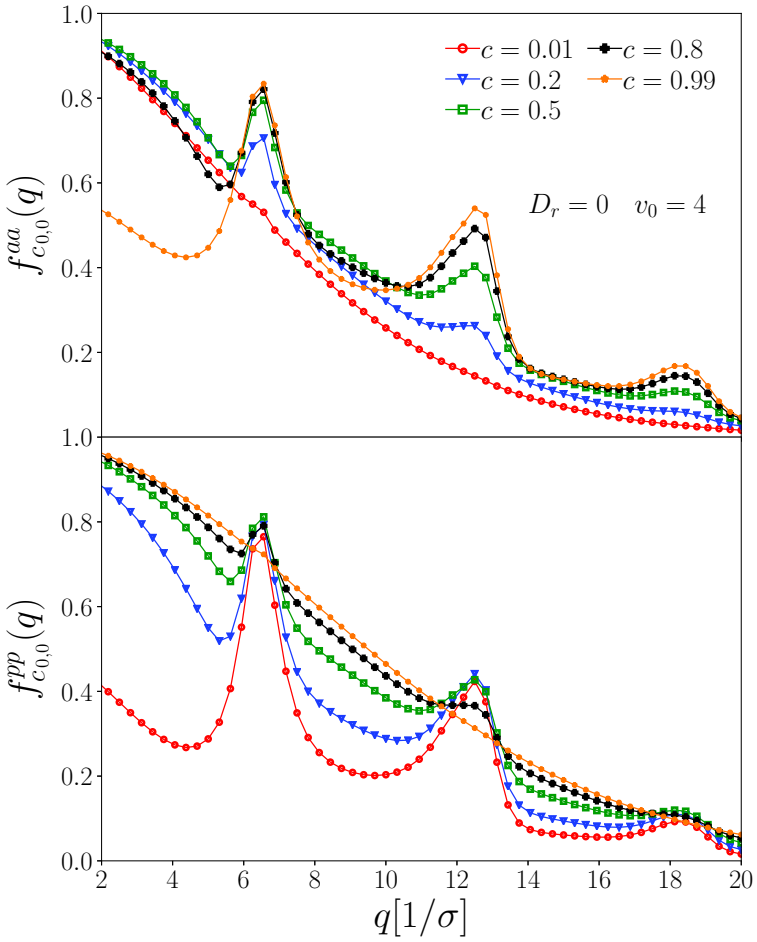

Figure 6.1.3.: *Structure-factor normalized critical nonergodicity parameters of the monodisperse mixture of active and passive particles for active (top) and passive (bottom) components for different concentrations c of the active species, fixed $D_r = 0$ and fixed $v_0 = 4$.*

6.2 Dynamics

The effects of a composition change can be observed equivalently on the fluid side of the glass transition. For this purpose, a monodisperse passive system just above the critical density $\phi_c \approx 0.6986$ is considered in the following and the dynamical properties are to be investigated by increasing the fraction of the active component in the system. The resulting structure factor normalized ISFs

$$\hat{S}^{\alpha,\alpha}_{0,0}(q) = S^{\alpha,\alpha}_{0,0}(q,t)/S^{\alpha,\alpha}(q) \tag{6.2.1}$$

of both active and passive particle types for a varying concentration of the active particle type are shown in figure 6.2.1. For a passive system closely above a dynamical arrested state, a low amount of active particles is sufficient to bring the system into the fluid state, as demonstrated by the red curve for $c = 0.07$. This happens for active and passive components alike and is expected by the MCT prediction of a coupling of all density fluctuations in the system, seen by the fact that the relaxation times $\tau_\alpha(q)$ at fixed q are almost identical for active and passive particle types. The further increase of the active particle concentration leads to a continuing

reduction of the relaxation time and a less pronounced β-relaxation phase, as the system is further driven from the glass transition point. A quantitative picture to describe the influence of the concentration on the relaxation time of the active component is provided by the inset in the lower picture, which illustrates the divergent behaviour for $c \to 0$. It is further important to note that the intersections of the ISFs of the passive component for different c is due to the transition from a collective to a self-dynamics concomitant with an increase of c and only arises due to the properties of the normalization, but not due to generic mixing effects between active and passive particles.

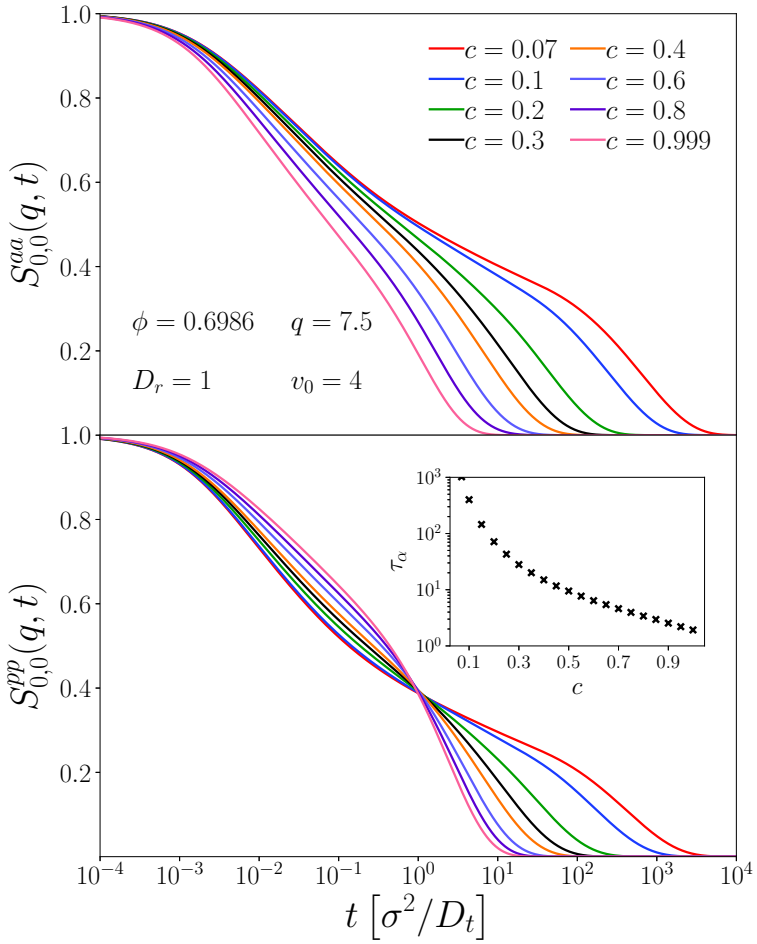

Figure 6.2.1.: *Structure-factor normalized ISFs of the monodisperse mixture of active and passive particles for the active (top) and passive (bottom) components for different concentrations c of the active species, fixed $D_r = 0$, fixed $v_0 = 4$ and fixed density $\phi = 0.6986$. The inset of the bottom figure shows the dependence of $\tau_\alpha(q)$ at fixed $q = 7.5$ in a wide range of c.*

7. Conclusion

The development of novel theoretical concepts for systems far from equilibrium constitutes an ongoing challenge in the field of statistical physics. This work has provided a variety of contributions to this endeavour by extending the mode-coupling theory for active Brownian particles (ABP-MCT) for the calculation of non-equilibrium transport coefficients in dense active suspensions. The predictions of the theory have further been tested against simulation results and the agreement has been found to be overall well. This chapter aims to summarize and recapitulate the main achievements of this work and concludes by providing some ideas on prospective research topics that have arisen within the results of this work.

In chapter 2, the integration-through-transients (ITT) formalism has provided a suitable theoretical framework to describe a non-equilibrium dynamics by stating exact relations for transient correlation functions in terms of equilibrium averages. Such transient correlation functions form the cornerstone of the ABP-MCT. Chapter 3 has started from an exact description of both translational and rotational microscopic degrees of freedom of the system. With the time evolution of the phase space distribution being exactly described by the Smoluchowski-equation, the Mori-Zwanzig projection operator formalism has subsequently been applied to obtain an exact rewriting for the equation of motion for the transient correlation function of two microscopic angle-resolved densities, designated as intermediate scattering-function (ISF). Formal solutions for the ISF of non-interacting ABPs have been provided in section 3.1.2 and generalized to correlation functions that include the rotational degrees of freedom. This has been achieved by deriving matrices that describe the basis change from spherical harmonics expanded density-fluctuations to the basis of Mathieu functions by following the work of Kurzthaler et al. [86]. The ABP-MCT to describe the collective dynamics of identical ABPs [47] has subsequently been generalized to describe the dynamics of arbitrary mixtures with both active and passive constituents. One key principle, represented by the presence of separate relaxation channels in the system, has conserved the features of a diffusive relaxational dynamics of the rotational degrees of freedom, in line with the definition of spherical ABPs with a purely diffusive rotational dynamics. The approximation of the memory-kernel, that determines the time evolution of the ISF in dense active systems has been generalized to mixtures within the framework of the mode-coupling approximation. These generalized ABP-MCT equations have further been exploited to describe compositions of active and passive particles, in which one component only exists in a highly diluted form, resulting in MCT equations to describe the self-intermediate

scattering function (SISF) of active or passive tracer particle both in active or passive dense host environments. This theory was further investigated in the limit of low wavenumbers, which has resulted in a novel approach to calculate the mean-squared displacement (MSD) of tracer particles in dense active or passive suspensions beyond any preliminary coarse-graining of the rotational degrees of freedom. This makes the theory capable to resolve the various regimes of anomalous diffusion for both active and passive tracer particles in terms of activity-induced superdiffusive motion and sub-diffusive motion due to cageing which has been achieved by the correct inclusion of the competing time scales of persistent motion and structural relaxation. Expressions for further transport coefficients given by the zero-shear viscosity and the effective swimming velocity have been derived within the ITT formalism and have been approximated with the MCT-predicted dynamical correlation functions by using a projection operator technique.

A further main achievement of this work was to demonstrate that the ABP-MCT is indeed capable to make accurate predictions in comparison with results from an event-driven simulation of active Brownian hard-disks. This was demonstrated by an in-depth analysis of each conceivable scenario of both active and passive tagged particle motion in an active or passive hard-disk environment, that is recapitulated for each scenario in the following:

- The motion of a **passive tracer** in a **passive bath** has formed the basis for a quantitative comparison between ABP-MCT predictions and simulation results for active systems by providing a calibration for the density, that was performed in section 4.2. This gauging is necessary to correct a well-known error of MCT to quantitatively overpredict the tendency for the glass-formation, though it was demonstrated that this error can be corrected by a linear mapping between MCT and BD densities. This has provided near quantitatively agreeing results for both the tagged particle dynamics and the MSD in the passive system in a wide range of densities.

  Within chapter 5, such a system was also investigated in form of experimental results for the MSD of tracer particles in a binary colloidal suspension near the glass transition point. Although such systems have already been studied in detail and compared with the predictions of passive MCT, it was emphasized that it can make accurate predictions for dense colloidal suspensions and is an effective method to quantify the influence of hydrodynamic interactions on the reduction of the short-time diffusion coefficient.

- The scenario of an **active tracer** particle in a **passive bath** was presented in section 4.3. It turned out, that the tagged particle correlation functions predicted by ABP-MCT show only little variation compared to the passive self-dynamics in a range of self-propulsion velocities at least up to eight diameters per diffusive time unit. This is explained by the dominant influence of the cage effect of the surrounding passive bath in this parameter regime, where the impacts of the tracer's activity on the dynamics and the structural relaxation time is only felt on large length scales. A much stronger variation with the ABP parameters of the tracer has been observed for the tagged particle MSD, which has revealed all phases of anomalous diffusion which have been resolved almost quantitatively identically within both ABP-MCT predictions and the simulation results. The condition

for the occurrence of a superdiffusive behaviour has been argued by the competition of the structural relaxation time due to the volume exclusion and the persistence time of the active tracer. The corresponding length scales, given by the cageing length and the crossover length scales of the free active particle derived in section 2.2 have provided a simple condition for the occurrence of a superdiffusive motion before the cageing. Moreover, it was shown that an MCT-ITT approach is feasible to account for the renormalization of the swimming velocity of the active tracer due to its interaction with the passive host environment.

Further simulations have revealed that there is indeed a stimulating influence on the structural relaxation of the active tagged particle if its activity is chosen sufficiently high. In this parameter regime, the localisation effects of the passive bath are attenuated, so that the motion of the tracer particle has revealed the characteristics of free active motion with an effective swimming velocity. It has, however, turned out that this represents a parameter regime which has not been accessible by ABP-MCT within the numerical efforts of this work due to occurring numerical instabilities at high self-propulsion velocities. Their presumed origins will be discussed separately at the end of this section.

Laser-driven diffusiophoretic Janus particles in binary colloidal suspensions comprise the simplest experimental approach to study the active motion of tracer particles in dense environments as presented in chapter 5. The conducted experiments by Lozano et al. have revealed an unexpected viscoelastic response of active motion, that led to a strong amplification of the rotational diffusion close to the dynamical arrested state. If this effect is correctly included in the respective ABP model parameter, the experimentally measured MSDs of such a system can be reproduced within the methods of BD simulations. Moreover, the experiments by Lozano et al. have revealed a delocalisation transition of the active Janus particle in a glass-like environment, which has also been observed in the simulations if the activity of the tracer was chosen sufficiently high.

- The motion of a **passive tracer** particle in an **active bath** was investigated in section 4.4. Here the activity of the bath has led to a significantly faster relaxation of the passive tagged particle dynamics. It has turned out that ABP-MCT underestimates the influence of the active perturbation to fluidize the system, but this effect has been successfully corrected by an empirical rescaling of the self-propulsion velocities, which has delivered very satisfactory agreements between ABP-MCT predictions and simulations results for both the tagged particle dynamics and the MSD in a wide range of parameters. A remarkable achievement of ABP-MCT is its capability to account for the transmission of superdiffusivity from an active bath to a passive tracer particle, that is only possible by the inclusion of correlation functions between rotational and translational degrees of freedom. More common approaches proceed by integrating out the rotational degrees of freedom in terms of an effective Smoluchowski operator and it is not clear if such approximation are capable to account for a superdiffusive motion of passive particles.

- The behaviour of a **active tracer** in an **active bath** at high densities has shown great similarities with that of a passive tracer particle in the same active bath, through the neg-

ligible influence of the tracer's activity on the cage structure in the investigated parameter range. It was demonstrated that within the same empirical rescaling of the self-propulsion velocity as for a passive tracer in the active bath, ABP-MCT can make accurate predictions for the tagged particle dynamics in a wide range of densities that are not too close to the glass transition. A consistent observation from both MCT and BD is that activity leads to a decrease of the exponent that characterizes the divergence behaviour of the relaxation time. This effect has been studied in more detail by investigating the asymptotic ABP-MCT equations in the case of a vanishing rotational diffusion coefficient. Moreover, the peculiar feature of non-symmetric correlation functions that arises within the non-equilibrium time evolution and the transient nature of the ABP-MCT averages has been successfully confirmed within the simulations.

An existing problem in connection with the time-decimation algorithm [47] to numerically solve the ABP-MCT equations are instabilities associated with high self-propulsion velocities. Their origin can presumably be seen in the matrix structure of the theory with the necessary cutoff of the rotational modes. The degree of justification of performing such a cutoff decreases with increasing activities, where couplings of higher modes might have a non-negligible influence on the dynamics. An impression of this is effect has been provided by the analytical expression for the inverse of the translation frequency matrix of an active tracer particle in figure 3.3.2, which has emphasized, that inversion and performing a cutoff at high activities are highly non-commutative. This has shown to lead to systematic errors in the range of low wavenumbers and at sufficiently high activities this error range has extended up to a relevant wave number regime for the integration of the memory-kernel. Even though these effects can be corrected for the inverse of the frequency matrix by employing the correct inversion formula, similar cutoff-dependencies are expected to occur for the ISF, since its inverse explicitly enters the time-decimation scheme to solve the MCT-approximated equation of motion. Numerical analyses show that both the complexity and the memory demand of the time decimation procedure increases in the third power with the size of the considered matrices [84] which implies enormous limitations to explore parameter regimes that require the inclusion of larger matrices.

The ABP-MCT predictions regarding mixtures of active and passive particles have been investigated in chapter 6 and have revealed a non-linear impact of the compositional change of the active species on the shift of the glass transition point. The presented study of mixing effects which are associated with the increase of the amount of an active component in a monodisperse system has provided a first preliminary step to address the effects that are associated with the change of the size of the constituents. The influence of the size composition on the dynamics and the glass transition of passive systems is well-studied [38,119] and shows peculiar non-monotonic dependencies on the size disparity. It is, however, unclear how activity interplays with such a size disparity change. Addressing this question constitutes a promising prospective research topic, for which this work has established the necessary theoretical framework to deal with. However, when investigating active mixtures within the ABP-MCT, there arise further numerical limitations, emphasized by the observation that the increase of numerical complexity to investigate an active binary mixture with the same wavenumber discretization as a single component system

has been observed to be increased by a factor of around eight. At the same time, the investigation of mixing effects due to changes in the size composition requires a better discretization of the wavenumber grid, which additionally increases computational times and requires future work to optimize the used integration schemes. One promising approach in that context is given by a recent study on non-uniform wavenumber grids and their impact on the complexity of the MCT numerics [121], which can be significantly reduced by using more sophisticated discretization schemes. More elaborated wavenumber grids would also allow for an investigation of the ABP-MCT on a logarithmic wavenumber grid which can be exploited to explore the long-time tails of the velocity autocorrelation function by suitable analysis of the long-wavelength dynamics as previously done for dense systems of passive Brownian hard-spheres [122]. Performing an analogous study in high-density systems of ABPs constitutes a further interesting project to which the ABP-MCT might deliver a valuable contribution.

Appendix

MCT Calculations

A.1 ABP mixtures

The necessary steps to arrive at the expressions for the vertex functions, equation (3.1.48) and (3.1.49), to describe the mode-coupling approximated memory-kernel are carried out in detail in the following. For clarity the necessary quantities and approximations are again summarized below:

The MCT approximation of the memory-kernel after performing the second projection step is given by

$$\begin{aligned} m_{l,l'}^{\alpha,\beta}\left(\vec{q},t\right) &\approx \left\langle \rho_l^\alpha(\vec{q})^* \boldsymbol{\Omega}^\dagger \boldsymbol{\mathcal{Q}} \boldsymbol{\mathcal{P}}_2 \mathrm{e}^{\boldsymbol{\Omega}_{\mathrm{irr}}^\dagger t} \boldsymbol{\mathcal{P}}_2 \boldsymbol{\mathcal{Q}} \boldsymbol{\Omega}^\dagger \rho_{l'}^\beta(\vec{q}) \right\rangle \\ &= \sum_{\substack{1,2,3,4 \\ 1'2'3'4'}} \left\langle \rho_l^\alpha(\vec{q})^* \boldsymbol{\Omega}^\dagger \boldsymbol{\mathcal{Q}} \rho_1 \rho_2 \right\rangle g_{1,2,3,4} \left\langle \rho_3^* \rho_4^* e^{\boldsymbol{\Omega}_{\mathrm{irr}}^\dagger t'} \rho_{1'} \rho_{2'} \right\rangle g_{1',2',3',4'} \left\langle \rho_{3'}^* \rho_{4'}^* \boldsymbol{\mathcal{Q}} \boldsymbol{\Omega}^\dagger \rho_{l'}^\beta(\vec{q}) \right\rangle, \end{aligned}$$

with the normalization tensor

$$g_{1,2,3,4} = \frac{1}{2} \left(S^{-1}\right)_{l_1,l_1}^{\gamma_1,\gamma_3}(q_1) \left(S^{-1}\right)_{l_2,l_2}^{\gamma_2,\gamma_4}(q_2)\ \delta_{\vec{q}_1,\vec{q}_3} \delta_{\vec{q}_2,\vec{q}_4} \delta_{l_1,l_3} \delta_{l_2,l_4}. \tag{A.1.1}$$

Moreover, there applies the mode-coupling approximation that reads

$$\left\langle \rho_3^* \rho_4^* \mathrm{e}^{\boldsymbol{\Omega}_{\mathrm{irr}}^{\dagger,} t} \rho_{1'} \rho_{2'} \right\rangle \approx S_{3,1'}(t)\, S_{4,2'}(t)\, \delta_{\vec{q}_3,\vec{q}_{1'}} \delta_{\vec{q}_4,\vec{q}_{2'}} + 1' \leftrightarrow 2'. \tag{A.1.2}$$

The action of the adjoint Smoluchowski operator is splitted into equilibrium and non-equilibrium contributions, i.e., $\boldsymbol{\Omega}^\dagger = \boldsymbol{\Omega}_{\mathrm{eq}}^\dagger + \delta\boldsymbol{\Omega}^\dagger$ with

$$\boldsymbol{\Omega}_{\mathrm{eq}}^\dagger = \sum_{(j,\alpha)} \left(\vec{\nabla}_j^\alpha + \beta \vec{F}_j^\alpha\right) \vec{\nabla}_j^\alpha + D_r \partial_{\varphi_j}^{\alpha^2}, \qquad \delta\boldsymbol{\Omega}^\dagger = \sum_{(j,\alpha)} v_0^\alpha \vec{\nabla}_j^\alpha \cdot \vec{o}_j^\alpha.$$

It is further convenient to use the following identity for a representation of a vector in polar

coordinates $\vec{q} = (q, \varphi_q)$, that is

$$\vec{q} \cdot \boldsymbol{T} \cdot \left(\delta_{l,l'+1}, \delta_{l,l'-1}\right)^T = q e^{-i(l-l')\varphi_q} \delta_{|l-l'|,1} \quad \text{with} \quad \boldsymbol{T} := \begin{pmatrix} 1 & 1 \\ -i & i \end{pmatrix}. \tag{A.1.3}$$

This allows to express the action of $\delta\boldsymbol{\Omega}^\dagger$ on a density $\rho_i := \rho_{l_i}^{\gamma_i}(\vec{q}_i)$ in a compact notation as

$$\delta\boldsymbol{\Omega}^\dagger \rho_i = \sum_{n=1}^{N_{\gamma_i}} i\frac{v_0^{\gamma_i}}{2}\vec{q}_i \cdot \begin{pmatrix} e^{i\theta_n^{\gamma_i}} + e^{-i\theta_n^{\gamma_i}} \\ -ie^{i\theta_n^{\gamma_i}} + ie^{-i\theta_n^{\gamma_i}} \end{pmatrix} e^{i\vec{q}_i \cdot \vec{r}_n^{\gamma_i}} e^{il_i\theta_n^{\gamma_i}} = i\frac{v_0^{\gamma_i}}{2}\vec{q}_2 \cdot \boldsymbol{T} \cdot \begin{pmatrix} \rho_{i^+} \\ \rho_{i^-} \end{pmatrix}, \tag{A.1.4}$$

with the short-hand notation $\rho_{i^\pm} = \rho_{l_i \pm 1}^{\gamma_i}(\vec{q}_i)$. Moreover, the following approximations for the appearing static correlation functions which involve 3 densities will be used

$$\left\langle \rho_1^* \rho_2^* \rho_3 \right\rangle \approx \frac{1}{\sqrt{N}} \sum_\epsilon \frac{1}{x_\epsilon^2} S_{l_1,l_1}^{\gamma_1,\epsilon}(q_1) S_{l_2,l_2}^{\gamma_2,\epsilon}(q_2) S_{l_3,l_3}^{\gamma_3,\epsilon}(q_3) \delta_{\vec{q}_1+\vec{q}_2,\vec{q}_3} \delta_{l_1+l_2,l_3}, \tag{A.1.5}$$

$$\left\langle \rho_1^* \rho_2 \rho_3 \right\rangle \approx \frac{1}{\sqrt{N}} \sum_\epsilon \frac{1}{x_\epsilon^2} S_{l_1,l_1}^{\gamma_1,\epsilon}(q_1) S_{l_2,l_2}^{\gamma_2,\epsilon}(q_2) S_{l_3,l_3}^{\gamma_3,\epsilon}(q_3) \delta_{\vec{q}_1,\vec{q}_2+\vec{q}_3} \delta_{l_1,l_2+l_3}. \tag{A.1.6}$$

To calculate the static vertex functions the following identity is further needed. Two scalar observables A and B fulfill

$$\left\langle A(\vec{\nabla}_i + \beta\vec{F}_i)\vec{\nabla}_i B \right\rangle = -\left\langle \vec{\nabla}_i A \vec{\nabla}_i B \right\rangle. \tag{A.1.7}$$

This is seen by showing that $\langle A\beta\vec{F}_i B\rangle = -\langle\vec{\nabla}_i(AB)\rangle$ through integration by parts.

With these relations at hand, the calculation of the vertex functions proceeds straightforward. Starting with the right part of the vertex and using the orthogonal projector of $\boldsymbol{\mathcal{Q}}$ brings

$$\left\langle \rho_{3'}^* \rho_{4'}^* \boldsymbol{\mathcal{Q}}\boldsymbol{\Omega}^\dagger \rho_{l'}^\beta(\vec{q}) \right\rangle = \left\langle \rho_{3'}^* \rho_{4'}^* \boldsymbol{\Omega}^\dagger \rho_{l'}^\beta(\vec{q}) \right\rangle - \left\langle \rho_{3'}^* \rho_{4'}^* \boldsymbol{\mathcal{P}}\boldsymbol{\Omega}^\dagger \rho_{l'}^\beta(\vec{q}) \right\rangle. \tag{A.1.8}$$

Inserting the projector brings for the second term

$$\begin{aligned}
\left\langle \rho_{3'}^* \rho_{4'}^* \boldsymbol{\mathcal{P}}\boldsymbol{\Omega}^\dagger \rho_{l'}^\beta(\vec{q}) \right\rangle &= \sum_{3'',4''} \left\langle \rho_{3'}^* \rho_{4'}^* \rho_{3''} \right\rangle \left(S^{-1}\right)_{l_{3''},l_{4''}}^{\gamma_{3''},\gamma_{4''}}(q_{3''}) \left\langle \rho_{4''}^* \boldsymbol{\Omega}^\dagger \rho_{l'}^\beta(\vec{q}) \right\rangle \\
&= -\frac{1}{\sqrt{N}} \sum_{3'',4'',\epsilon} \frac{1}{x_\epsilon^2} S_{l_{3'},l_{3'}}^{\gamma_{3'},\epsilon}(q_{3'}) S_{l_{4'},l_{4'}}^{\gamma_{4'},\epsilon}(q_{4'}) S_{l_{3''},l_{3''}}^{\epsilon,\gamma_{3''}} \left(S^{-1}\right)_{l_{3''},l_{4''}}^{\gamma_{3''},\gamma_{4''}}(q_{3''}) \omega_{l_{4''},l'}^{\gamma_{4''},\beta}(q) \\
&\qquad \times \delta_{\vec{q}_{3'}+\vec{q}_{4'},\vec{q}}\, \delta_{\vec{q}_{3''},\vec{q}}\, \delta_{\vec{q}_{4''},\vec{q}}\, \delta_{l_{3'}+l_{4'},l_{4''}} \\
&= -\frac{1}{\sqrt{N}} \sum_{l_{4''},\epsilon} \frac{1}{x_\epsilon^2} S_{l_{3'},l_{3'}}^{\gamma_{3'},\epsilon}(q_{3'}) S_{l_{4'},l_{4'}}^{\gamma_{4'},\epsilon}(q_{4'}) \omega_{l_{4''},l'}^{\epsilon,\beta}(q) \delta_{\vec{q}_{3'}+\vec{q}_{4'},\vec{q}}\, \delta_{l_{3'}+l_{4'},l'} \\
&= -\frac{1}{\sqrt{N}x_\beta} \left(D_t^\beta q^2 + D_r^\beta l'^2\right) S_{l_{3'},l_{3'}}^{\gamma_{3'},\beta}(q_{3'}) S_{l_{4'},l_{4'}}^{\gamma_{4'},\beta}(q_{4'}) \delta_{\vec{q}_{3'}+\vec{q}_{4'},\vec{q}}\, \delta_{l_{3'}+l_{4'},l'} \\
&\quad + \frac{iv_0^\beta q}{2\sqrt{N}} e^{i(l'-l'_3-l_{4'})\varphi_q} \sum_\epsilon \frac{1}{x_\epsilon^2} S_{l_{3'},l_{3'}}^{\gamma_{3'},\epsilon}(q_{3'}) S_{l_{4'},l_{4'}}^{\gamma_{4'},\epsilon}(q_{4'}) S_{l_{3'}+l_{4'},l_{3'}+l_{4'}}^{\epsilon,\beta}(q)
\end{aligned}$$

$$\times\, \delta_{\vec{q}_{3'}+\vec{q}_{4'},\vec{q}}\; \delta_{|l'-l_{3'}-l_{4'}|,1}$$

Terms which arise from equilibrium and non-equilibrium contributions in the first term of (A.1.8) are calculated separately. Starting with the equilibrium contribution reveals

$$\begin{aligned}\left\langle \rho^*_{3'}\rho^*_{4'}\boldsymbol{\Omega}^\dagger_{\mathrm{eq}}\rho^\beta_{l'}\left(\vec{q}\right)\right\rangle =& -\frac{D^\beta_t}{\sqrt{N}}\vec{q}\cdot\left[\vec{q}_{3'}S^{\beta,\gamma_{4'}}_{l_{4'},l_{4'}}(q_{4'})\delta_{\beta,\gamma_{3'}}+\vec{q}_{4'}S^{\beta,\gamma_{3'}}_{l_{3'},l_{3'}}(q_{3'})\delta_{\beta,\gamma_{4'}}\right]\delta_{\vec{q}_{3'}+\vec{q}_{4'},\vec{q}}\;\delta_{l_{3'}+l_{4'},l'}\\ &-\frac{D^\beta_r}{\sqrt{N}}l'^2S^{\gamma_{3'},\beta}_{l_{3'},l_{3'}}(q_{3'})S^{\gamma_{4'},\beta}_{l_{4'},l_{4'}}(q_{4'})\;\delta_{\vec{q}_{3'}+\vec{q}_{4'},\vec{q}}\;\delta_{l_{3'}+l_{4'},l'},\end{aligned}$$

and for the non-equilibrium part

$$\begin{aligned}\left\langle \rho^*_{3'}\rho^*_{4'}\delta\boldsymbol{\Omega}^\dagger\rho^\beta_{l'}\left(\vec{q}\right)\right\rangle &= \frac{iv^\beta_0}{2}\vec{q}\cdot\boldsymbol{T}\cdot\begin{pmatrix}\langle\rho^*_{3'}\rho^*_{4'}\rho^\beta_{l'+1}\rangle\\ \langle\rho^*_{3'}\rho^*_{4'}\rho^\beta_{l'-1}\rangle\end{pmatrix}\\ &= \frac{iv^\beta_0}{2\sqrt{N}}\vec{q}\cdot\boldsymbol{T}\cdot\begin{pmatrix}\delta_{l_{3'}+l_{4'},l'+1}\\ \delta_{l_{3'}+l_{4'},l'-1}\end{pmatrix}\sum_\epsilon\frac{1}{x^2_\epsilon}S^{\gamma_{3'},\epsilon}_{l_{3'},l_{3'}}(q_{3'})S^{\gamma_{4'},\epsilon}_{l_{4'},l_{4'}}(q_{4'})S^{\epsilon,\beta}_{l_{3'}+l_{4'},l_{3'}+l_{4'}}(q)\\ &\qquad\times\,\delta_{\vec{q}_{3'}+\vec{q}_{4'},\vec{q}}\;\delta_{|l'-l_{3'}-l_{4'}|,1}\\ &= \frac{iv^\beta_0 q}{2\sqrt{N}}e^{i(l'-l_{3'}-l_{4'})\varphi_q}\sum_\epsilon\frac{1}{x^2_\epsilon}S^{\gamma_{3'},\epsilon}_{l_{3'},l_{3'}}(q_{3'})S^{\gamma_{4'},\epsilon}_{l_{4'},l_{4'}}(q_{4'})S^{\epsilon,\beta}_{l_{3'}+l_{4'},l_{3'}+l_{4'}}(q)\\ &\qquad\times\,\delta_{|l'-l_{3'}-l_{4'}|,1}\;\delta_{\vec{q}_{3'}+\vec{q}_{4'},\vec{q}}.\end{aligned}$$

Apparently the active parts from the first and second term of equation (A.1.8) cancel out and one arrives at

$$\begin{aligned}&\left\langle \rho^*_{3'}\rho^*_{4'}\boldsymbol{\mathcal{Q}}\boldsymbol{\Omega}^\dagger\rho^\beta_{l'}\left(\vec{q}\right)\right\rangle\\ &\quad=-\frac{D^\beta_t}{\sqrt{N}}\vec{q}\cdot\left[\vec{q}_{3'}S^{\beta,\gamma_{4'}}_{l_{4'},l_{4'}}(q_{4'})\delta_{\beta,\gamma_{3'}}+\vec{q}_{4'}S^{\beta,\gamma_{3'}}_{l_{3'},l_{3'}}(q_{3'})\delta_{\beta,\gamma_{4'}}-\frac{1}{x_\beta}\vec{q}\,S^{\gamma_{3'},\beta}_{l_{3'},l_{3'}}(q_{3'})S^{\gamma_{4'},\beta}_{l_{4'},l_{4'}}(q_{4'})\right]\\ &\qquad\times\,\delta_{\vec{q}_{3'}+\vec{q}_{4'},\vec{q}}\;\delta_{l_{3'}+l_{4'},l'}.\end{aligned}$$

After taking the sub-sum over the normalization tensor yields

$$\begin{aligned}&\sum_{3',4'}g_{1',2',3',4'}\left\langle \rho^*_{3'}\rho^*_{4'}\boldsymbol{\mathcal{Q}}\Omega^\dagger\rho^\beta_{l'}\left(\vec{q}\right)\right\rangle\\ &\quad=-\frac{D^\beta_t}{2\sqrt{N}}\vec{q}\cdot\left[\vec{q}_{1'}\left(\,S^{-1}\right)^{\gamma_{1'},\beta}_{l_{1'},l_{1'}}(q_{1'})\delta_{\gamma_{2'},\beta}+\vec{q}_{2'}\left(S^{-1}\right)^{\gamma_{2'},\beta}_{l_{2'},l_{2'}}(q_{2'})\delta_{\gamma_{1'},\beta}-\frac{1}{x_\beta}\vec{q}\;\delta_{\gamma_{1'},\beta}\delta_{\gamma_{2'},\beta}\right]\\ &\qquad\times\,\delta_{l_{1'}+l_{2'},l'}\delta_{\vec{q}_{1'}+\vec{q}_{2'},\vec{q}}.\end{aligned}$$

This expression can be further simplified by using the Ornstein-Zernicke relation given by equation (3.1.6) which results in

$$\begin{aligned}&\sum_{3',4'}g_{1',2',3',4'}\left\langle \rho^*_{3'}\rho^*_{4'}\boldsymbol{\mathcal{Q}}\Omega^\dagger\rho^\beta_{l'}\left(\vec{q}\right)\right\rangle\\ &\quad=\frac{\rho D^\beta_t}{2\sqrt{N}}\left[\left(\vec{q}\cdot\vec{q}_{1'}\right)c^{\gamma_{1'},\beta}(q_{1'})\delta_{l_{1'},0}\delta_{\gamma_{2'},\beta}+\left(\vec{q}\cdot\vec{q}_{2'}\right)c^{\gamma_{2'},\beta}(q_{2'})\delta_{l_{2'},0}\delta_{\gamma_{1'},\beta}\right]\end{aligned}$$

$$
\begin{aligned}
&\times \delta_{l_{1'}+l_{2'},l'}\,\delta_{\vec{q}_{1'}+\vec{q}_{2'},\vec{q}} \\
&= \frac{\rho}{2\sqrt{N}}\mathcal{V}^{\beta,\gamma_{1'},\gamma_{2'}}_{l',l_{1'},l_{2'}}\left(\vec{q},\vec{q}_{1'},\vec{q}_{2'}\right)\delta_{\vec{q}_{1'}+\vec{q}_{2'},\vec{q}},
\end{aligned}
$$

with $\mathcal{V}^{\beta,\gamma_{1'},\gamma_{2'}}_{l',l_{1'},l_{2'}}\left(\vec{q},\vec{q}_{1'},\vec{q}_{2'}\right)$ as given in the main text.

The calculation of the left vertex proceeds in a similar fashion. Writing again

$$
\left\langle \rho^{\alpha}_{l}(\vec{q})^{*}\boldsymbol{\Omega}^{\dagger}\boldsymbol{\mathcal{Q}}\rho_1\rho_2\right\rangle = \left\langle \rho^{\alpha}_{l}(\vec{q})^{*}\boldsymbol{\Omega}^{\dagger}\rho_1\rho_2\right\rangle - \left\langle \rho^{\alpha}_{l}(\vec{q})^{*}\boldsymbol{\Omega}^{\dagger}\boldsymbol{\mathcal{P}}\rho_1\rho_2\right\rangle \tag{A.1.9}
$$

reveals for the first term

$$
\begin{aligned}
\left\langle \rho^{\alpha}_{l}(\vec{q})^{*}\boldsymbol{\Omega}^{\dagger}\boldsymbol{\mathcal{P}}\rho_1\rho_2\right\rangle = &-\frac{1}{\sqrt{N}x_\alpha}\left(D^{\alpha}_{t}q^2 + D^{\alpha}_{r}l^2\right)S^{\alpha,\gamma_1}_{l_1,l_1}(q_1)S^{\alpha,\gamma_2}_{l_2,l_2}(q_2)\delta_{l,l_1+l_2}\delta_{\vec{q},\vec{q}_1+\vec{q}_2} \\
&+ \frac{iq}{2\sqrt{N}}e^{i(l_1+l_2-l)\varphi_q}\sum_{\epsilon}\frac{v^{\epsilon}_{0}}{x^2_{\epsilon}}S^{\alpha,\epsilon}_{l,l}(q)S^{\epsilon,\gamma_1}_{l_1,l_1}(q_1)S^{\epsilon,\gamma_2}_{l_2,l_2}(q_2)\;\delta_{|l_1+l_2-l|,1}\delta_{\vec{q},\vec{q}_1+\vec{q}_2}.
\end{aligned}
$$

The equilibrium contributions of the second term are given by

$$
\begin{aligned}
\left\langle \rho^{\alpha}_{l}(\vec{q})^{*}\boldsymbol{\Omega}^{\dagger}_{\mathrm{eq}}\rho_1\rho_2\right\rangle = &-\frac{D^{\alpha}_{t}}{\sqrt{N}}\vec{q}\cdot\left[\vec{q}_1 S^{\alpha,\gamma_2}_{l_2,l_2}(q_2)\delta_{\alpha,\gamma_1} + \vec{q}_2 S^{\alpha,\gamma_1}_{l_1,l_1}(q_1)\delta_{\alpha,\gamma_2}\right]\delta_{\vec{q},\vec{q}_1+\vec{q}_2}\delta_{l,l_1+l_2} \\
&- \frac{D^{\alpha}_{r}}{\sqrt{N}}l^2 S^{\alpha,\gamma_1}_{l_1,l_1}(q_1)S^{\alpha,\gamma_2}_{l_2,l_2}(q_2)\;\delta_{\vec{q},\vec{q}_1+\vec{q}_2}\delta_{l,l_1+l_2},
\end{aligned}
$$

and the respective active contributions are

$$
\begin{aligned}
\left\langle \rho^{\alpha}_{l}(\vec{q})^{*}\delta\boldsymbol{\Omega}^{\dagger}\rho_1\rho_2\right\rangle &= \frac{iv^{\gamma_1}_{0}}{2}\vec{q}_1\cdot\boldsymbol{T}\cdot\begin{pmatrix}\langle\rho^{\alpha^*}_{l'}\rho_2\rho_{1^+}\rangle\\ \langle\rho^{\alpha^*}_{l'}\rho_2\rho_{1^-}\rangle\end{pmatrix} + 1\leftrightarrow 2 \\
&= \frac{iq_1}{2\sqrt{N}}e^{i(l_1+l_2-l)\alpha_{q_1}}\sum_{\epsilon}\frac{v^{\gamma_1}_{0}}{x^2_{\epsilon}}S^{\alpha,\epsilon}_{l,l}(q)S^{\epsilon,\gamma_1}_{l-l_2,l-l_2}(q_1)S^{\epsilon,\gamma_2}_{l_2,l_2}(q_2)\delta_{\vec{q},\vec{q}_1+\vec{q}_2}\delta_{|l-l_1-l_2|,1} \\
&\quad + 1\leftrightarrow 2.
\end{aligned}
$$

Alltogether this yields

$$
\begin{aligned}
&\left\langle \rho^{\alpha}_{l}(\vec{q})^{*}\boldsymbol{\Omega}^{\dagger}\boldsymbol{\mathcal{Q}}\rho_1\rho_2\right\rangle \\
&= -\frac{D^{\alpha}_{t}}{\sqrt{N}}\vec{q}\cdot\left[\vec{q}_1 S^{\alpha,\gamma_2}_{l_2,l_2}(q_2)\delta_{\alpha,\gamma_1} + \vec{q}_2 S^{\alpha,\gamma_1}_{l_1,l_1}(q_1)\delta_{\alpha,\gamma_2} - \frac{1}{x_\alpha}\vec{q}\,S^{\alpha,\gamma_1}_{l_1,l_1}(q_1)S^{\alpha,\gamma_2}_{l_2,l_2}(q_2)\right]\delta_{\vec{q},\vec{q}_1+\vec{q}_2}\delta_{l,l_1+l_2} \\
&\quad + \frac{i}{2\sqrt{N}}\sum_{\epsilon}\left[\frac{1}{x^2_{\epsilon}}v^{\gamma_1}_{0}q_1 e^{i(l_1+l_2-l)\alpha_{q_1}}S^{\alpha,\epsilon}_{l,l}(q)S^{\epsilon,\gamma_1}_{l-l_2,l-l_2}(q_1)S^{\epsilon,\gamma_2}_{l_2,l_2}(q_2)\right. \\
&\qquad\quad + \frac{1}{x^2_{\epsilon}}v^{\gamma_2}_{0}q_2 e^{i(l_1+l_2-l)\alpha_{q_2}}S^{\alpha,\epsilon}_{l,l}(q)S^{\epsilon,\gamma_1}_{l_1,l_1}(q_1)S^{\epsilon,\gamma_2}_{l-l_1,l-l_1}(q_2) \\
&\qquad\quad \left. - \frac{1}{x^2_{\epsilon}}v^{\epsilon}_{0}q e^{i(l_1+l_2-l)\varphi_q}S^{\alpha,\epsilon}_{l,l}(q)S^{\epsilon,\gamma_1}_{l_1,l_1}(q_1)S^{\epsilon,\gamma_2}_{l_2,l_2}(q_2)\right]\delta_{\vec{q},\vec{q}_1+\vec{q}_2}\;\delta_{|l-l_1-l_2|,1}.
\end{aligned}
$$

Taking again the sub-sum over the normalization tensor and exploiting the Ornstein-Zernike

relation results in

$$\begin{aligned}
&\sum_{1,2}\Big\langle \rho_l^\alpha(\vec{q})^* \boldsymbol{\Omega}^\dagger \boldsymbol{\mathcal{Q}} \rho_1 \rho_2 \Big\rangle g_{1,2,3,4} \\
&\quad = \frac{\rho D_t^\alpha}{2\sqrt{N}} \Big[(\vec{q}\cdot\vec{q}_3) c^{\alpha,\gamma_3}(q_3)\delta_{l_3,0}\delta_{\alpha,\gamma_4} + (\vec{q}\cdot\vec{q}_4) c^{\alpha,\gamma_4}(q_4)\delta_{l_4,0}\delta_{\alpha,\gamma_3}\Big] \delta_{\vec{q},\vec{q}_3+\vec{q}_4}\ \delta_{l_3+l_4,l} \\
&\qquad + \frac{i}{4\sqrt{N}} \Bigg[\sum_{\gamma_1} \frac{1}{x_{\gamma_4}^2} v_0^{\gamma_1} q_3 e^{i(l_3+l_4-l)\alpha_{q_3}} S_{l,l}^{\alpha,\gamma_4}(q) S_{l-l_4,l-l_4}^{\gamma_4,\gamma_1}(q_3) \left(S^{-1}\right)_{l_3,l_3}^{\gamma_1,\gamma_3}(q_3) \\
&\qquad\qquad + \sum_{\gamma_2} \frac{1}{x_{\gamma_3}^2} v_0^{\gamma_2} q_4 e^{i(l_3+l_4-l)\alpha_{q_4}} S_{l,l}^{\alpha,\gamma_3}(q) S_{l-l_3,l-l_3}^{\gamma_3,\gamma_2}(q_4) \left(S^{-1}\right)_{l_4,l_4}^{\gamma_2,\gamma_4}(q_4) \\
&\qquad\qquad - \frac{1}{x_{\gamma_3}^2} v_0^{\gamma_3} q e^{i(l_3+l_4-l)\varphi_q} \delta_{\gamma_3,\gamma_4} S_{l,l}^{\alpha,\gamma_3}(q) \Bigg] \delta_{\vec{q},\vec{q}_3+\vec{q}_4} \delta_{|l-l_3-l_4|,1} \\
&\quad = \frac{\rho}{2\sqrt{N}} \mathcal{W}_{l,l_3,l_4}^{\alpha,\gamma_3,\gamma_4}(\vec{q},\vec{q}_3,\vec{q}_4)\, \delta_{\vec{q},\vec{q}_3+\vec{q}_4}.
\end{aligned}$$

After applying the mode-coupling approximation for $\left\langle \rho_3^* \rho_4^* \mathrm{e}^{\boldsymbol{\Omega}_{\mathrm{irr}}^\dagger t} \rho_{1'}\rho_{2'} \right\rangle$ and evaluating the wavevector delta functions, the single remaining wavevector sum is expressed in the thermodynamic limit as $\sum_{\vec{p}} = V/(2\pi)^2 \int d^2p$ finally results in equation (3.1.47).

A.2 Tagged Particle Dynamics

The memory-kernel $\boldsymbol{m}^s(\vec{q},t)$ is explicitly calculated from equation (3.1.47) by multiplying out the vertexfunctions, restricting to the only contributing terms of structure $S^s(\vec{q}_1,t)S^{\alpha,\beta}(\vec{q}_2,t)$ where $\alpha,\beta \neq s$. Abbreviating $\vec{k} = \vec{q}-\vec{p}$ and splitting the memory-kernel in $\boldsymbol{m}^s(\vec{q},t) = \boldsymbol{m}^s_{\mathrm{eq}}(\vec{q},t) + \delta\boldsymbol{m}^s(\vec{q},t)$ yields for the equilibrium part

$$\begin{aligned}
(m_{\mathrm{eq}})_{l,l'}^s(\vec{q},t) \approx\ & (D_t^s)^2 \frac{\rho}{2} \int \frac{d^2p}{(2\pi)^2} \sum_{\substack{l_1..l_4 \\ \gamma_1\neq s,\gamma_2\neq s}} \Big[\delta_{l_3,0}\delta_{l_1,0} (\vec{q}\cdot\vec{k})^2 c^{\gamma_1,s}(k) c^{\gamma_2,s}(k) S_{l_1,l_3}^{\gamma_1,\gamma_2}(\vec{k},t) S_{l_2,l_4}^s(\vec{p},t) \\
&\qquad + \delta_{l_4,0}\delta_{l_2,0} (\vec{q}\cdot\vec{p})^2 c^{\gamma_1,s}(p) c^{\gamma_2,s}(p) S_{l_1,l_3}^s(\vec{k},t) S_{l_2,l_4}^{\gamma_1,\gamma_2}(\vec{p},t) \Big] \delta_{l_1+l_2,l}\ \delta_{l_3+l_4,l'} \\
=\ & (D_t^s)^2 \rho \int \frac{d^2p}{(2\pi)^2} \sum_{\substack{l_1,l_2 \\ \gamma_1\neq s,\gamma_2\neq s}} c^{\gamma_1,s}(k) c^{\gamma_2,s}(k) \left(\vec{q}\cdot\vec{k}\right)^2 \delta_{l,l_2}\delta_{l_1,0} S_{l_2,l'}^s(\vec{p},t)\ S_{l_1,0}^{\gamma_1,\gamma_2}(\vec{k},t) \\
=\ & \rho \int \frac{d^2p}{(2\pi)^2} \sum_{\substack{l_1,l_2 \\ \gamma_1\neq s,\gamma_2\neq s}} (\mathcal{V}_{\mathrm{eq}})_{l,l_1,l_2}^{s,\gamma_1,\gamma_2}(\vec{q},\vec{k},\vec{p}) S_{l_2,l'}^s(\vec{p},t)\ S_{l_1,0}^{\gamma_1,\gamma_2}(\vec{k},t).
\end{aligned}$$

Here a factor 2 was obtained by changing $\vec{p} \leftrightarrow \vec{k}$, $l_1 \leftrightarrow l_2$ and $l_3 \leftrightarrow l_4$ in the second line and the vertex $(\mathcal{V}_{\mathrm{eq}})_{l,l_1,l_2}^{s,\gamma_1,\gamma_2}(\vec{q},\vec{k},\vec{p})$ coincides with the definition of the main text. The contributing terms of the active part of the memory-kernel are given by

$$\delta m_{l,l'}^s(\vec{q},t) \approx \frac{D_t^s}{4} \int \frac{d^2p}{(2\pi)^2} \sum_{\substack{l_1..l_4 \\ \gamma_1\neq s,\gamma_2\neq s}} (\vec{q}\cdot\vec{k}) c^{\gamma_2,s}(k) S_{l_1,l_3}^{\gamma_1,\gamma_2}(\vec{k},t) S_{l_2,l_4}^s(\vec{p},t) \delta_{l_3,0}\delta_{l_3+l_4,l'}\delta_{|l-l_1-l_2|,1}$$

$$
\begin{aligned}
&\times \Bigg[\frac{1}{x_s^2} i v_0^s k e^{i(l_1+l_2-l)\alpha_k} S^{s,s}_{l,l}(q) S^{s,s}_{l-l_2,l-l_2}(k) \big(S^{-1}\big)^{s,\gamma_1}_{l_1,l_1}(k) \\
&\quad + \frac{1}{x_s^2} \sum_{\epsilon \neq s} i v_0^\epsilon k e^{i(l_1+l_2-l)\alpha_k} S^{s,s}_{l,l}(q) S^{s,\epsilon}_{l-l_2,l-l_2}(k) \big(S^{-1}\big)^{\epsilon,\gamma_1}_{l_1,l_1}(k) \\
&\quad + \frac{1}{x_{\gamma_1}^2} i v_0^s p e^{i(l_1+l_2-l)\alpha_p} S^{s,\gamma_1}_{l,l}(q) S^{\gamma_1,s}_{l-l_1,l-l_1}(p) \big(S^{-1}\big)^{s,s}_{l_2,l_2}(p) \\
&\quad + \frac{1}{x_{\gamma_1}^2} \sum_{\epsilon \neq s} i v_0^\epsilon p e^{i(l_1+l_2-l)\alpha_p} S^{s,\gamma_1}_{l,l}(q) S^{\gamma_1,\epsilon}_{l-l_1,l-l_1}(p) \big(S^{-1}\big)^{\epsilon,s}_{l_2,l_2}(p) \Bigg] \\
&+ \frac{D_t^s}{4} \int \frac{d^2p}{(2\pi)^2} \sum_{\substack{l_1..l_4 \\ \gamma_1 \neq s, \gamma_2 \neq s}} (\vec{q}\cdot\vec{p}) c^{\gamma_2,s}(p) S^s_{l_1,l_3}(\vec{k},t) S^{\gamma_1,\gamma_2}_{l_2,l_4}(\vec{p},t) \delta_{l_4,0} \delta_{l_3+l_4,l'} \delta_{|l-l_1-l_2|,1} \\
&\times \Bigg[\frac{1}{x_s^2} i v_0^s p e^{i(l_1+l_2-l)\alpha_p} S^{s,s}_{l,l}(q) S^{s,s}_{l-l_1,l-l_1}(p) \big(S^{-1}\big)^{s,\gamma_1}_{l_2,l_2}(p) \\
&\quad + \frac{1}{x_s^2} \sum_{\epsilon \neq s} i v_0^\epsilon p e^{i(l_1+l_2-l)\alpha_p} S^{s,s}_{l,l}(q) S^{s,\epsilon}_{l-l_1,l-l_1}(p) \big(S^{-1}\big)^{\epsilon,\gamma_1}_{l_2,l_2}(p) \\
&\quad + \frac{1}{x_{\gamma_1}^2} i v_0^s k e^{i(l_1+l_2-l)\alpha_k} S^{s,\gamma_1}_{l,l}(q) S^{\gamma_1,s}_{l-l_2,l-l_2}(k) \big(S^{-1}\big)^{s,s}_{l_1,l_1}(k) \\
&\quad + \frac{1}{x_{\gamma_1}^2} \sum_{\epsilon \neq s} i v_0^\epsilon k e^{i(l_1+l_2-l)\alpha_k} S^{s,\gamma_1}_{l,l}(q) S^{\gamma_1,\epsilon}_{l-l_2,l-l_2}(k) \big(S^{-1}\big)^{\epsilon,s}_{l_1,l_1}(k) \Bigg].
\end{aligned}
$$

The appearing terms can be simplified by using $S^{s,s}_{l,l'} = x_s \delta_{l,l'}$, $S^{s,\gamma}_{l,l'} \propto x^s \delta_{l,l'}$ as shown in the main text. Further, the Ornstein-Zernike equation for the inverse structure factors is applied. Inserting these relations and evaluating the delta functions in the rotational indices reveals that the last two terms after both integrations vanish in the limit $x_s \to 0$. Again a factor 2 with the same variable transformation as for the passive vertex and the result reads

$$
\begin{aligned}
\delta m^s_{l,l'}(\vec{q},t) \approx \rho \int \frac{d^2p}{(2\pi)^2} \sum_{\substack{l_1,l_2 \\ \gamma_1 \neq s, \gamma_2 \neq s}} & i D_t^s \frac{(\vec{q}\cdot\vec{k})}{2} k e^{i(l_1+l_2-l)\alpha_k} c^{\gamma_2,s}(k) \Bigg[v_0^{\gamma_1} \frac{S^{s,\gamma_1}(k)}{\rho x_s x_{\gamma_1}} \delta_{l,l_2} - v_0^s c^{\gamma_1,s}(k) \delta_{l_1,0} \Bigg] \\
&\times S^{\gamma_1,\gamma_2}_{l_1,0}(\vec{k},t) S^s_{l_2,l'}(\vec{p},t) \delta_{|l-l_1-l_2|,1}.
\end{aligned}
$$

Finally write $S^{s,\gamma_1}(k)/x_s = \sum_{\epsilon \neq s} \rho S^{\gamma_1,\epsilon}(k) c^{\epsilon,s}(k)$ for $\gamma_1 \neq s$ to get the form of the non-equilibrium vertex as given in the main text.

A.3 Equations of Motion for the MSD

The resulting equations of motion for the tagged particle MSD as given in the main text are derived in detail. For clarity, the fundamental equations are repeated again:

$$\partial_t \delta r^2(t) + \lim_{\vec{q}\to 0} \underbrace{\int_0^t dt' \sum_l \Big(m^s_{0,l}(\vec{q}, t-t') \omega^{s^{-1}}_{T_{l,0}}(\vec{q}) \Big) \partial_{t'} \delta r^2(t')}_{\mathrm{I}} = 4D^s_t + \lim_{\vec{q}\to 0} \frac{4}{q^2} \Big[\sum_{\pm} \omega^s_{0,\pm 1} S^s_{\pm 1,0}(\vec{q}, t) \Big]$$
$$+ \lim_{\vec{q}\to 0} \underbrace{\int_0^t dt' \frac{4}{q^2} \sum_{\substack{l \\ l'\neq 0}} \Big[m^s_{0,l}(\vec{q}, t-t') \omega^{s^{-1}}_{T_{l,l'}}(\vec{q}) (\partial_{t'} S^s_{l',0}(\vec{q}, t') + l'^2 D^s_r S^s_{l',0}(\vec{q}, t')) \Big]}_{\mathrm{II}},$$

$$\partial_t S^s_{l,0}(\vec{q}, t) + \sum_{l'} \omega_{l,l'} S^s_{l',0}(\vec{q}, t) =$$
$$- \int_0^t dt' \sum_{l',l''} m^s_{l,l'}(\vec{q}, t-t') \omega^{s^{-1}}_{T_{l',l''}}(\vec{q}) \Big[\partial_{t'} S^s_{l'',0}(\vec{q}, t') + l''^2 D^s_r S^s_{l'',0}(\vec{q}, t') \Big].$$

Also recall that the leading order in $\vec{q}$ for $m^s_{l,l'}(\vec{q}, t)$ is $\mathcal{O}(\vec{q})$ for $|l - l'| = 1$, and $\mathcal{O}(\vec{q}^2)$ else.

A.3.1 Passive Tracer

For the passive tracer recall that $\omega^s_{l,l'}(\vec{q}) = (D^s_t q^2 + D^s_r l^2)\delta_{l,l'}$ and $\omega^{s^{-1}}_{T_{l,l'}}(\vec{q}) = 1/(D^s_t q^2)\delta_{l,l'}$, meaning that

$$\lim_{\vec{q}\to 0} \mathrm{I} = \lim_{\vec{q}\to 0} \int_0^t dt' \frac{m^s_{0,0}(q, t-t')}{D^s_t q^2} \delta r^2(t') = D^s_t \int_0^t dt' \hat{m}^s(t-t') \delta r^2(t'),$$

with $\hat{m}^s(t)$ defined as in (3.4.15). The MSD further couples to $S^s_{l,0}(\vec{q}, t)$ SISFs with $l \neq 0$ whose equation of motion read

$$\partial_t S_{l,0}(\vec{q}, t) = -\omega^s_{l,l} S^s_{l,0}(\vec{q}, t) - \int_0^t dt' \sum_{l'} m^s_{l,l'} \omega^{s^{-1}}_{T_{l',l'}}(\vec{q}) \Big[\partial_{t'} S_{l',0}(\vec{q}, t) + D_r l'^2 S^s_{l',0}(\vec{q}, t) \Big],$$

where the diagonlity of both $\boldsymbol{\omega}^s(\vec{q})$ and $\boldsymbol{\omega}^{s^{-1}}_T(\vec{q})$ has been exploited. Inspecting the expression for the tagged particle memory-kernel, equation (3.3.13), one sees that $m^s_{l,l'}(\vec{q}, t)$ only couples to the $S^s_{l,l'}(\vec{q}, t)$ component of the tagged particle correlator. This means that $\boldsymbol{m}^s(\vec{q}, t)$ must be diagonal because $S^s_{l,l'}(\vec{q}, t)$ has a vanishing initial value for $l \neq l'$. But this also means that for $l \neq 0$ the only trivial solution to equation (A.3.1) is $S^s_{l,0}(\vec{q}, t) = 0$ because the equation of motion only couples to other $S^s_{l',0}(\vec{q}, t)$ with $l' \neq 0$.

A.3.2 Active Tracer

Recall that the terms for both the frequency matrix and the inverse of its translational part for $v_0^s \neq 0$ are

$$\omega^s_{l,l'}(\vec{q}) = (D_t^s q^2 + D_r^s l^2)\delta_{l,l'} - i\frac{v_0^s q}{2}e^{-i(l-l')\varphi_q}, \quad \omega^{s^{-1}}_{T_{l,l'}}(\vec{q}) = e^{-i(l-l')\varphi_q} i^{|l-l'|}\left(\frac{1}{v_0^s q} - \frac{|l-l'|D_t^s}{(v_0^s)^2}\right) + \mathcal{O}(q)$$

This means that the only contributing terms in I are for $\delta_{|l|,1}$ because only then $m_{0,l}$ is of order $\mathcal{O}(q)$. One keeps

$$\lim_{\vec{q}\to 0} \mathrm{I} = \lim_{\vec{q}\to 0} \int_0^t dt' \sum_{\pm} m^s_{0,\pm 1}(\vec{q}, t-t') e^{\mp i\varphi_q} \frac{i}{v_0^s q} \partial_{t'} \delta r^2(t') = \frac{i}{v_0^s} \int_0^t dt' \sum_{\pm} \hat{m}^s_{\pm 1,0}(t-t') \partial_{t'} \delta r^2(t'),$$

as in the main text.

Potentially contributing terms that arise in leading order of q in II are for

$$\begin{aligned}\mathrm{II} = \frac{4}{q^2} \int_0^t dt' \sum_{\substack{l \\ l'\neq 0}} m^s_{0,l}(\vec{q}, t-t') \omega^{s^{-1}}_{T_{l,l'}}(\vec{q}) \Big[\partial_{t'} S^s_{l',0}(\vec{q}, t') + D_r l'^2 S^s_{l',0}(\vec{q}, t')\Big] \\ \times \Big(\delta_{l,0}\delta_{|l'|,1} + \delta_{|l|,1}\delta_{|l'|,1} + \delta_{|l|,2}\delta_{|l'|,1} + \delta_{|l|,1}\delta_{|l'|,2}\Big) + \mathcal{O}(q).\end{aligned}$$

The $\delta_{|l|,2}\delta_{|l'|,1}$ terms do not contribute as exemplified:

$$\begin{aligned}&\frac{4}{q^2} \int_0^t dt' \sum_{\substack{l \\ l'\neq 0}} m^s_{0,l}(\vec{q}, t-t') \omega^{s^{-1}}_{T_{l,l'}}(\vec{q}) \Big[\partial_{t'} S^s_{l',0}(\vec{q}, t') + D_r l'^2 S^s_{l',0}(\vec{q}, t')\Big] \delta_{|l|,2}\delta_{|l'|,1} \\ &= \frac{4}{q^2} \int_0^t dt' \sum_{|l|=2} \sum_{\pm} m^s_{0,l}(\vec{q}, t-t') e^{-il\varphi_q} e^{\pm i\varphi_q} \frac{i^{|l\mp 1|}}{v_0^s q} \Big[\partial_{t'} S^s_{\pm 1,0}(\vec{q}, t') + D_r S^s_{\pm 1,0}(\vec{q}, t')\Big],\end{aligned}$$

which vanishes by using the symmetry $e^{i\varphi_q} S^s_{1,0}(\vec{q}, t) = e^{-i\varphi_q} S^s_{-1,0}(\vec{q}, t)$. For the same reasons of symmetry, also the $\delta_{|l|,1}\delta_{|l'|,2}$ terms do not contribute. It seem that the overall order of the $\delta_{|l|,1}\delta_{|l'|,1}$ terms is of $\mathcal{O}(q^{-1})$ which means taht and one also has to take into account the next leading order of $\omega^{s^{-1}}_{T_{l,l'}}(\vec{q})$:

$$\begin{aligned}&\frac{4}{q^2} \int_0^t dt' \sum_{\substack{l \\ l'\neq 0}} m^s_{0,l}(\vec{q}, t-t') \omega^{s^{-1}}_{T_{l,l'}}(\vec{q}) \Big[\partial_{t'} S^s_{l',0}(\vec{q}, t') + D_r l'^2 S^s_{l',0}(\vec{q}, t')\Big] \delta_{|l|,1}\delta_{|l'|,1} \\ &= \frac{4}{q^2} \int_0^t dt' \sum_{\substack{l=\pm 1 \\ l'=\pm 1}} m^s_{0,l}(\vec{q}, t-t') e^{-i(l-l')\varphi_q} i^{|l-l'|} \frac{1}{v_0^s q} \Big[\partial_{t'} S^s_{l',0}(\vec{q}, t') + D_r l'^2 S^s_{l',0}(\vec{q}, t')\Big] \\ &\quad - \frac{4}{q^2} \int_0^t dt' \sum_{\substack{l=\pm 1 \\ l'=\pm 1}} m^s_{0,l}(\vec{q}, t-t') e^{-i(l-l')\varphi_q} i^{|l-l'|} |l-l'| \frac{D_t^s}{(v_0^s)^2} \Big[\partial_{t'} S^s_{l',0}(\vec{q}, t') + D_r l'^2 S^s_{l',0}(\vec{q}, t')\Big],\end{aligned}$$

where the potentially dangerous terms in the second line vanishes for the same symmetry reasons

as before. In the last line there remain contributions for l and l' with opposite signs. Alltogether with the $\delta_{l,0}\delta_{|l'|,1}$ contribution one gets

$$\begin{aligned}\lim_{\vec{q}\to 0}\mathrm{II} &= \lim_{\vec{q}\to 0}\frac{4}{q^2}\int_0^t dt' m^s_{0,0}(q,t-t')\frac{ie^{\pm i\varphi_q}}{v_0^s q}\sum_{\pm}\Big[\partial_{t'}S^s_{\pm1,0}(\vec{q},t')+D_r^s S^s_{\pm1,0}(\vec{q},t')\Big]\\ &\quad+\lim_{\vec{q}\to 0}\frac{8}{q^2}\int_0^t dt'\sum_{\pm}e^{\mp i\varphi_q}m^s_{0,\pm1}(\vec{q},t-t')\frac{D_t^s}{(v_0^s)^2}e^{\pm i\varphi_q}\Big[\partial_{t'}S^s_{\pm1,0}(\vec{q},t')+D_r S^s_{\pm1,0}(\vec{q},t')\Big]\\ &= \frac{4i}{v_0^s}\int_0^t dt'\hat{m}^s_{0,0}(t-t')\sum_{\pm}\left[\partial_{t'}\hat{\phi}^s_{\pm1,0}(t')+D_r^s\hat{\phi}^s_{\pm1,0}(t')\right]\\ &\quad+\frac{4D_t^s}{(v_0^s)^2}\int_0^t dt'\sum_{\pm}\hat{m}^s_{0,\pm1}(t-t')\sum_{\pm}\left[\partial_{t'}\hat{\phi}^s_{\pm1,0}(t')+D_r^s\hat{\phi}^s_{\pm1,0}(t')\right],\end{aligned}$$

with the isotropic and q-independent quantities

$$\hat{\phi}_{\pm1,0}(t)=\lim_{\vec{q}\to 0}e^{\pm i\varphi_q}\frac{S^s_{\pm1,0}(\vec{q},t)}{q},\qquad \hat{m}^s_{l,l'}(t)=\lim_{\vec{q}\to 0}e^{i(l-l')\varphi_q}\frac{m^s_{l,l'}(\vec{q},t)q^{|l-l'|}}{q^2},$$

as defined as in the main text. Still an equation of motion for $\hat{\phi}_{\pm1,0}$ is needed. It reads

$$\begin{aligned}\partial_t\hat{\phi}_{\pm1,0}(t)-\frac{iv_0^s}{2}+D_r^s\hat{\phi}_{\pm1,0}(t) =&\\ -\lim_{\vec{q}\to 0}\frac{e^{\pm i\varphi_q}}{q}\int_0^t dt'\sum_{l,l'}m^s_{\pm1,l}(\vec{q},t-t')\omega^{s^{-1}}_{T_{l,l'}}(\vec{q})\left[\partial_t S^s_{l',0}(\vec{q},t)+D_r^s l'^2 S^s_{l',0}(\vec{q},t)\right]&\\ \times\delta_{|l'|1}\delta_{|\pm1-l|,1}.&\end{aligned}$$

By inserting the expression for $\omega^{s^{-1}}_{T_{l,l'}}(\vec{q})$ one easily checks that there only surive terms for $l=0$ which leads to

$$\partial_t\hat{\phi}^s_{\pm1,0}(t)=\frac{iv_0^s}{2}-D_r^s\hat{\phi}^s_{\pm1,0}(t)-\frac{i}{v_0^s}\int_0^t dt'\hat{m}^s_{\pm1,0}(t-t')\sum_{\pm}\left[\partial_{t'}\hat{\phi}^s_{\pm1,0}(t')+D_r^s\hat{\phi}^s_{\pm1,0}(t')\right].$$

as given in the main text.

A.4 ITT Effective Swimming Velocity

This section aims to derive the MCT approximated expression for the irredubible correlator $C^{\alpha,\gamma}_{\mathrm{irr}}(t)$ given by equation (3.5.9). Recall that

$$C^{\alpha,\gamma}_{\mathrm{irr}}(t)\approx\sum_{i=1}^{N_\alpha}\sum_{j=1}^{N_\gamma}\sum_{\substack{1,2,3,4\\1'2'3'4'}}\Big\langle\vec{F}_j^\gamma\cdot\vec{o}_j^\gamma\,\rho_1\rho_2\Big\rangle g_{1,2,3,4}\Big\langle\rho_3^*\rho_4^*e^{\mathbf{\Omega}^\dagger_{\mathrm{irr}}t'}\rho_{1'}\rho_{2'}\Big\rangle g_{1',2',3',4'}\Big\langle\rho^*_{3'}\rho^*_{4'}\vec{F}_i^\alpha\cdot\vec{o}_i^\alpha\Big\rangle.$$

Starting with the left vertex one gets

$$\begin{aligned}\sum_i \left\langle \vec{o}_i^{\,\gamma} \vec{F}_i^{\gamma} \rho_1 \rho_2 \right\rangle &= -\frac{1}{\beta} \sum_i \left\langle \vec{o}_i^{\,\gamma} \vec{\nabla}_i^{\gamma} (\rho_1 \rho_2) \right\rangle = -\frac{i}{2\beta} \delta_{\gamma,\gamma_1}\, \vec{q}_1 \cdot \boldsymbol{T} \cdot \begin{pmatrix} \langle \rho_2 \rho_{1^+} \rangle \\ \langle \rho_2 \rho_{1^-} \rangle \end{pmatrix} + 1 \leftrightarrow 2 \\ &= -\frac{i}{2\beta} \delta_{\gamma,\gamma_1} \vec{q}_1 \cdot \boldsymbol{T} \cdot \begin{pmatrix} \delta_{-l_2,l_1+1} \\ \delta_{-l_2,l_1-1} \end{pmatrix} S^{\gamma_1,\gamma_2}_{l_2,l_2}(q_1) \delta_{\vec{q}_1,-\vec{q}_2} + 1 \leftrightarrow 2 \\ &= -\frac{i}{2\beta} \delta_{\gamma,\gamma_1} q_1 e^{i(l_1+l_2)\varphi_{q_1}} S^{\gamma_1,\gamma_2}_{l_2,l_2}(q_1) \delta_{\vec{q}_1,-\vec{q}_2} \delta_{|l_1+l_2|,1} + 1 \leftrightarrow 2\end{aligned}$$

And after summation over $(1,2)$.

$$\begin{aligned}\sum_i \sum_{1,2} \left\langle \rho_1 \rho_2 \vec{F}_i^{\gamma} \cdot \vec{o}_i^{\,\gamma} \right\rangle g_{1,2,3,4} &= \frac{i\rho}{4\beta} \delta_{|l_3+l_4|,1} \delta_{\vec{q}_3,-\vec{q}_4} c^{\gamma_3,\gamma_4}(q_3) q_3 \Big(e^{il_4\varphi_{q_3}} \delta_{l_3,0} \delta_{\gamma,\gamma_4} - e^{il_3\varphi_{q_3}} \delta_{l_4,0} \delta_{\gamma,\gamma_3} \Big) \\ &:= \mathcal{Y}^{\gamma,\gamma_3,\gamma_4}_{l_3,l_4}(\vec{q}_3) \delta_{\vec{q}_3,-\vec{q}_4}.\end{aligned}$$

The result of the right vertex can be directed concluded by exploiting that the projected force is a real function. This means that $\sum_i \sum_{3',4'} \left\langle \rho^*_{3'} \rho^*_{4'} \vec{F}_i^{\alpha} \cdot \vec{o}_i^{\,\alpha} \right\rangle g_{1',2',3',4'} = \left(\mathcal{Y}^{\alpha,\gamma_{1'},\gamma_{2'}}_{l_{1'},l_{2'}}(\vec{q}_{1'}) \right)^* \delta_{\vec{q}_{1'},-\vec{q}_{2'}}$. After applying the mode-coupling approximation of the propagator and evaluation of the wavevector delta functions there remains a single wavenumber integral that is carried out in polar coordinates by with the use of isotropic correlation functions $S^{\gamma_1,\gamma_2}_{l,l'}(\vec{q},t) = e^{-i(l-l')\varphi_q} \hat{S}^{\gamma_1,\gamma_2}_{l,l'}(q,t)$ as follows:

$$\begin{aligned}\frac{D_t^{\alpha}\beta^2}{N_{\alpha}} C^{\alpha,\gamma}_{\mathrm{irr}}(t) &= \frac{D_t^{\alpha} V}{2\pi^2 N_{\alpha}} \int d^2p \sum_{\substack{l_1..l_4 \\ \gamma_1..\gamma_4}} \mathcal{Y}^{\gamma,\gamma_1\gamma_2}_{l_1,l_2}(\vec{p}) S^{\gamma_1,\gamma_3}_{l_2,l_4}(\vec{p},t) S^{\gamma_2,\gamma_4}_{l_1,l_3}(-\vec{p},t) \mathcal{Y}^{\alpha,\gamma_3,\gamma_4}_{l_3,l_4}(\vec{p}) \\ &= \frac{D_t^{\alpha}\rho}{32\pi^2 x_{\alpha}} \int_0^{2\pi} d\varphi \int_0^{\infty} dp \sum_{\substack{l_1..l_4 \\ \gamma_1..\gamma_4}} p^3 c^{\gamma_1,\gamma_2}(p) c^{\gamma_3,\gamma_4}(p) \delta_{|l_1+l_2|,1} \delta_{|l_3+l_4|,1} \\ &\qquad \times \Big[\big(e^{il_2\varphi} \delta_{l_1,0} \delta_{\gamma,\gamma_2} - e^{il_1\varphi} \delta_{l_2,0} \delta_{\gamma,\gamma_1} \big) \big(e^{-il_4\varphi} \delta_{l_3,0} \delta_{\alpha,\gamma_4} - e^{-il_3\varphi} \delta_{l_4,0} \delta_{\alpha,\gamma_3} \big) \Big] \\ &\qquad \times e^{-i(l_1-l_3)\varphi} \hat{S}^{\gamma_1,\gamma_3}_{l_1,l_3}(p,t) e^{-i(l_2-l_4)(\varphi+\pi)} \hat{S}^{\gamma_2,\gamma_4}_{l_2,l_4}(p,t) \\ &= \frac{D_t^{\alpha}\rho}{8\pi x_{\alpha}} \sum_{\substack{\gamma_1..\gamma_4 \\ l=\pm1, l'=\pm1}} \int_0^{\infty} dp\, p^3 c^{\gamma_1,\gamma_2}(p) c^{\gamma_3,\gamma_4}(p) \delta_{\gamma,\gamma_2} \\ &\qquad \times \Big(\hat{S}^{\gamma_1,\gamma_3}_{0,0}(p,t) \hat{S}^{\gamma_2,\gamma_4}_{l,l'}(p,t) \delta_{\alpha,\gamma_4} + \hat{S}^{\gamma_1,\gamma_3}_{0,l}(p,t) \hat{S}^{\gamma_2,\gamma_4}_{l',0}(p,t) \delta_{\alpha,\gamma_3} \Big),\end{aligned}$$

as given in the main text.

A.5 ITT Zero-Shear Viscosity

In the main text it was shown that by following the ITT formalism, there arise two stress contributions $\left\langle \hat{\sigma}^{x,y} \right\rangle^{v_0}$ and $\left\langle \hat{\sigma}^{x,y} \right\rangle^{\dot{\gamma}}$ in equation (3.6.7) which respective mode-coupling approximations

are derived in the following. The active contribution is

$$\begin{aligned}\Big\langle \hat{\sigma}^{x,y}\Big\rangle^{v_0} &\approx -\int_0^\infty dt\, \sum_{(i,\alpha)} v_0^\alpha \Big\langle \vec{o}_i^\alpha \beta \vec{F}_i^\alpha \boldsymbol{\mathcal{P}}_2 e^{\boldsymbol{\Omega}^\dagger t} \boldsymbol{\mathcal{P}}_2 \hat{\sigma}^{x,y}\Big\rangle \\ &= -\int_0^\infty dt \sum_{(i,\alpha)} \sum_{\substack{1,2,3,4\\1'2'3'4'}} v_0^\alpha \Big\langle \vec{o}_{i,\alpha}\beta\vec{F}_{i,\alpha}\rho_1\rho_2\Big\rangle g_{1,2,3,4}\Big\langle \rho_3^*\rho_4^* \mathrm{e}^{\boldsymbol{\Omega}^\dagger t}\rho_{1'}\rho_{2'}\Big\rangle g_{1',2',3',4'}\Big\langle \rho_{3'}^*\rho_{4'}^*\hat{\sigma}^{x,y}\Big\rangle.\end{aligned}$$

From the last section one can conclude

$$\begin{aligned}-\sum_{\substack{(i,\alpha)\\1,2}} v_0^\alpha \Big\langle \vec{o}_i^\alpha\beta\vec{F}_i^\alpha\rho_1\rho_2\Big\rangle g_{1,2,3,4} &= -\sum_\alpha \frac{i\rho}{4} v_0^\alpha \delta_{|l_3+l_4|,1}\delta_{\vec{q}_3,-\vec{q}_4} c^{\gamma_3,\gamma_4}(q_3) q_3 \\ &\qquad \times (e^{il_4\varphi_{q_3}}\delta_{l_3,0}\delta_{\alpha,\gamma_4} - e^{il_3\varphi_{q_3}}\delta_{l_4,0}\delta_{\alpha,\gamma_3}) \\ &= -\sum_\alpha v_0^\alpha \mathcal{Y}_{l_3,l_4}^{\alpha,\gamma_3,\gamma_4}(\vec{q}_3)\delta_{\vec{q}_3,-\vec{q}_4}\end{aligned}$$

and the calculation of the right vertex is conducted as follows:

$$\begin{aligned}\Big\langle \rho_{3'}^*\rho_{4'}^*\hat{\sigma}^{x,y}\Big\rangle &= -\frac{1}{NV}\sum_{\substack{i,i_{3'},i_{4'}\\ \gamma,\gamma_{3'},\gamma_{4'}}} \Big\langle F_{i,x}^\gamma r_{i,y}^\gamma e^{-i\vec{q}_{3'}\left(\vec{r}_{i_{3'}}^{\gamma_{3'}} - \vec{r}_{i_{4'}}^{\gamma_{4'}}\right)} e^{-il_{3'}\theta_{i_{3'}}^{\gamma_{3'}}} e^{-il_{4'}\theta_{i_{4'}}^{\gamma_{4'}}}\Big\rangle \delta_{\vec{q}_{3'},-\vec{q}_{4'}} \\ &= \frac{1}{N\beta V}\sum_{\substack{i,i_{3'},i_{4'}\\ \gamma,\gamma_{3'},\gamma_{4'}}} \Big\langle r_{i,y}^\gamma e^{-il_{3'}\theta_{i_{3'}}^{\gamma_{3'}}} e^{-il_{4'}\theta_{i_{4'}}^{\gamma_{4'}}} \partial_{i,x}^\gamma e^{-i\vec{q}_{3'}\left(\vec{r}_{i_{3'}}^{\gamma_{3'}} - \vec{r}_{i_{4'}}^{\gamma_{4'}}\right)}\Big\rangle \delta_{\vec{q}_{3'},-\vec{q}_{4'}} \\ &= \frac{1}{N\beta V}\sum_{\substack{i,i_{3'},i_{4'}\\ \gamma,\gamma_{3'},\gamma_{4'}}} \Big\langle e^{-il_{3'}\theta_{i_{3'}}^{\gamma_{3'}}} e^{-il_{4'}\theta_{i_{4'}}^{\gamma_{4'}}} iq_{3',x}(\delta_{i,i_{4'}}\delta_{\gamma,\gamma_{4'}} - \delta_{i,i_{3'}}\delta_{\gamma,\gamma_{3'}}) \\ &\qquad \times r_{i,y}^\gamma e^{-i\vec{q}_{3'}\left(\vec{r}_{i_{3'}}^{\gamma_{3'}} - \vec{r}_{i_{4'}}^{\gamma_{4'}}\right)}\Big\rangle \delta_{\vec{q}_{3'},-\vec{q}_{4'}} \\ &= \frac{1}{\beta V}\frac{q_{3',x}q_{3',y}}{q_{3'}}\partial_{q_{3'}} S_{0,0}^{\gamma_{3'},\gamma_{4'}}(q_{3'})\delta_{l_{3'},0}\delta_{l_{4'},0}\delta_{\vec{q}_{3'},-\vec{q}_{4'}},\end{aligned}$$

where in the last line the transformation rule for polar coordinates $\partial_{q_{3',y}} = (q_{3',y}/q_{3'})\partial_{q_{3'}}$ was exploited. Taking the sub-sum over $g_{1',2',3',4'}$ shows

$$\begin{aligned}\sum_{3',4'} g_{1',2',3',4'}\Big\langle \rho_{3'}^*\rho_{4'}^*\hat{\sigma}^{x,y}\Big\rangle &= \frac{1}{2\beta V}\frac{q_{1'}^x q_{1'}^y}{q_{1'}}\sum_{\gamma_{3'},\gamma_{4'}} (S^{-1})_{0,0}^{\gamma_{2'},\gamma_{4'}}(q_{1'})(S^{-1})_{0,0}^{\gamma_{1'},\gamma_{3'}}(q_{1'})\partial_{q_{1'}} S_{0,0}^{\gamma_{3'},\gamma_{4'}}(q_{1'}) \\ &\qquad \times \delta_{l_{1'},0}\delta_{l_{2'},0}\delta_{\vec{q}_{1'},-\vec{q}_{2'}} \\ &= \frac{\rho}{2\beta V}\frac{q_{1'}^x q_{1'}^y}{q_{1'}}\partial_{q_{1'}} c^{\gamma_{1'},\gamma_{2'}}(q_{1'})\delta_{l_{1'},0}\delta_{l_{2'},0}\delta_{\vec{q}_{1'},-\vec{q}_{2'}} := \mathcal{X}_{l_{1'},l_{2'}}^{\gamma_{1'},\gamma_{2'}}(\vec{q}_{1'})\delta_{\vec{q}_{1'},-\vec{q}_{2'}},\end{aligned}$$

which follows by using the product rule and the Ornstein-Zernike equation in the first line:

$$\sum_{\gamma_{3'}} (S^{-1})_{0,0}^{\gamma_{1'},\gamma_{3'}}\partial_{q_{1'}} S_{0,0}^{\gamma_{3'},\gamma_{4'}} = -\sum_{\gamma_{3'}} S_{0,0}^{\gamma_{3'},\gamma_{4'}}\partial_{q_{1'}}(S^{-1})_{0,0}^{\gamma_{1'},\gamma_{3'}} = \rho\sum_{\gamma_{3'}} S_{0,0}^{\gamma_{3'},\gamma_{4'}}\partial_{q_{1'}} c^{\gamma_{1'},\gamma_{3'}}.$$

Having determined the static vertex functions one can write

$$\begin{aligned}\left\langle\hat{\sigma}^{x,y}\right\rangle^{v_0} &= -\frac{V}{2\pi^2}\int_0^\infty dt\int d^2p\sum_{\substack{l_1..l_4\\ \gamma_1..\gamma_4}}\sum_\alpha v_0^\alpha \mathcal{X}^{\gamma_1,\gamma_2}_{l_1,l_2}(\vec{p})S^{\gamma_1,\gamma_3}_{l_1,l_3}(\vec{p},t)S^{\gamma_2,\gamma_4}_{l_1,l_3}(-\vec{p},t)\mathcal{Y}^{\alpha,\gamma_3,\gamma_4}_{l_3,l_4}(\vec{p})\\ &= \frac{\rho^2}{16i\pi^2\beta}\int_0^\infty dt\int_0^\infty dp\sum_{\substack{l_1..l_4\\ \gamma_1..\gamma_4}} p^3\partial_q c^{\gamma_1,\gamma_2}(q)c^{\gamma_3,\gamma_4}(q)\hat{S}^{\gamma_2,\gamma_4}_{l_2,l_4}(p,t)\hat{S}^{\gamma_1,\gamma_3}_{l_1,l_3}(p,t)\\ &\times\int_0^{2\pi}d\varphi\cos\varphi\sin\varphi\sum_\alpha v_0^\alpha\Big(e^{il_4\theta}\delta_{l_3,0}\delta_{\alpha,\gamma_4}-v_0^{\gamma_3}e^{il_3\theta}\delta_{l_4,0}\delta_{\alpha,\gamma_3}\Big)e^{-i(l_1-l_3)\varphi}e^{-i(l_2-l_4)(\varphi+\pi)}\\ &\qquad\times\delta_{|l_3+l_4|,1}\delta_{l_1,0}\delta_{l_2,0},\end{aligned}$$

which vanishes after carrying out the φ integration.

The shear-induced contribution to the viscosity after inserting two-point projectors reads

$$\begin{aligned}\left\langle\hat{\sigma}^{x,y}\right\rangle^{\dot\gamma} &\approx \int_0^\infty dt\,\dot\gamma\beta V\left\langle\hat{\sigma}^{x,y}\boldsymbol{\mathcal{P}}_2 e^{\boldsymbol{\Omega}^\dagger t}\boldsymbol{\mathcal{P}}_2\hat{\sigma}^{x,y}\right\rangle\\ &= \sum_{\substack{1,2,3,4\\ 1'2'3'4'}}\dot\gamma\beta V\left\langle\hat{\sigma}^{x,y}\rho_1\rho_2\right\rangle g_{1,2,3,4}\left\langle\rho^*_3\rho^*_4\mathrm{e}^{\boldsymbol{\Omega}^\dagger t}\rho_{1'}\rho_{2'}\right\rangle g_{1',2',3',4'}\left\langle\rho^*_{3'}\rho^*_{4'}\hat{\sigma}^{x,y}\right\rangle\end{aligned}$$

And because $\hat{\sigma}^{x,y}$ is a real function allows to conclude

$$\begin{aligned}\left\langle\hat{\sigma}^{x,y}\right\rangle^{\dot\gamma} &\approx \frac{\dot\gamma\beta V}{2\pi^2}\int_0^\infty dt\int d^2p\sum_{\substack{l_1..l_4\\ \gamma_1..\gamma_4}}\mathcal{X}^{\gamma_1,\gamma_2}_{l_1,l_2}(\vec{p})S^{\gamma_1,\gamma_3}_{l_1,l_3}(\vec{p},t)S^{\gamma_2,\gamma_4}_{l_1,l_3}(-\vec{p},t)\mathcal{X}^{\gamma_3,\gamma_4}_{l_3,l_4}(\vec{p})\\ &= \dot\gamma\frac{\rho^2}{8\pi^2\beta}\int_0^\infty dt\int d^2p\,\frac{p_x^2p_y^2}{p^2}\sum_{\gamma_1,\gamma_2\gamma_3\gamma_4}S^{\gamma_1,\gamma_3}_{0,0}(p,t)\partial_p c^{\gamma_1,\gamma_2}(p)S^{\gamma_2,\gamma_4}_{0,0}(p,t)\partial_p c^{\gamma_3,\gamma_4}(p)\\ &= \dot\gamma\frac{\rho^2}{32\pi\beta}\int_0^\infty dt\int_0^\infty dp\,p^3\ \mathrm{tr}\left[\Big(\boldsymbol{S}_{0,0}(p,t)\partial_p\boldsymbol{c}(p)\Big)^2\right].\end{aligned}$$

Bibliography

[1] Kenneth Locey and Jay Lennon. Scaling laws predict global microbial diversity. January 2015.

[2] J. Elgeti, R. G. Winkler, and G. Gompper. Physics of microswimmers–single particle motion and collective behavior: a review. *Reports on Progress in Physics*, 78(5):056601, April 2015.

[3] E. M. Purcell. Life at low reynolds number. *American Journal of Physics*, 45(2):3–11, January 1977.

[4] Tian Qiu, Tung-Chun Lee, Andrew G. Mark, Konstantin I. Morozov, Raphael Münster, Otto Mierka, Stefan Turek, Alexander M. Leshansky, and Peer Fischer. Swimming by reciprocal motion at low reynolds number. *Nature Communications*, 5(1):5119, November 2014.

[5] C. J. BROKAW. Non-sinusoidal bending waves of sperm flagella. *J. Exp. Biol.*, 43(1):155, August 1965.

[6] Linda Turner, William S. Ryu, and Howard C. Berg. Real-time imaging of fluorescent flagellar filaments. *J. Bacteriol.*, 182(10):2793, May 2000.

[7] M. C. Marchetti, J. F. Joanny, S. Ramaswamy, T. B. Liverpool, J. Prost, Madan Rao, and R. Aditi Simha. Hydrodynamics of soft active matter. *Rev. Mod. Phys.*, 85:1143–1189, Jul 2013.

[8] Allison P. Berke, Linda Turner, Howard C. Berg, and Eric Lauga. Hydrodynamic attraction of swimming microorganisms by surfaces. *Phys. Rev. Lett.*, 101:038102, Jul 2008.

[9] Jinglei Hu, Mingcheng Yang, Gerhard Gompper, and Roland G. Winkler. Modelling the mechanics and hydrodynamics of swimming e. coli. *Soft Matter*, 11(40):7867–7876, 2015.

[10] Ivo Buttinoni, Julian Bialké, Felix Kümmel, Hartmut Löwen, Clemens Bechinger, and Thomas Speck. Dynamical clustering and phase separation in suspensions of self-propelled colloidal particles. *Phys. Rev. Lett.*, 110:238301, Jun 2013.

[11] Walter F. Paxton, Kevin C. Kistler, Christine C. Olmeda, Ayusman Sen, Sarah K. St. Angelo, Yanyan Cao, Thomas E. Mallouk, Paul E. Lammert, and Vincent H. Crespi. Catalytic nanomotors:- autonomous movement of striped nanorods. *J. Am. Chem. Soc.*, 126(41):13424–13431, October 2004.

[12] Jonathan R. Howse, Richard A. L. Jones, Anthony J. Ryan, Tim Gough, Reza Vafabakhsh, and Ramin Golestanian. Self-motile colloidal particles: From directed propulsion to random walk. *Phys. Rev. Lett.*, 99:048102, Jul 2007.

[13] Thomas Bickel, Arghya Majee, and Alois Würger. Flow pattern in the vicinity of self-propelling hot janus particles. *Phys. Rev. E*, 88:012301, Jul 2013.

[14] Alexander M. Maier, Cornelius Weig, Peter Oswald, Erwin Frey, Peer Fischer, and Tim Liedl. Magnetic propulsion of microswimmers with dna-based flagellar bundles. *Nano Lett.*, 16(2):906–910, February 2016.

[15] Clemens Bechinger, Roberto Di Leonardo, Hartmut Löwen, Charles Reichhardt, Giorgio Volpe, and Giovanni Volpe. Active particles in complex and crowded environments. *Rev. Mod. Phys.*, 88(4):045006, November 2016.

[16] Rachel R. Bennett and Ramin Golestanian. A steering mechanism for phototaxis in chlamydomonas. *Journal of The Royal Society Interface*, 12(104):20141164, March 2015.

[17] Benjamin M. Friedrich and Frank Jülicher. Chemotaxis of sperm cells. *Proc Natl Acad Sci USA*, 104(33):13256, August 2007.

[18] George H. Wadhams and Judith P. Armitage. Making sense of it all: bacterial chemotaxis. *Nature Reviews Molecular Cell Biology*, 5(12):1024–1037, December 2004.

[19] Gáspár Jékely. Evolution of phototaxis. *Philosophical transactions of the Royal Society of London. Series B, Biological sciences*, 364(1531):2795–2808, October 2009.

[20] A. Roberts. Mechanisms of gravitaxis in chlamydomonas. *The Biological bulletin*, 210:78–80, May 2006.

[21] Deasung Jang, Jinwon Jeong, Hyeonseok Song, and Sang Kug Chung. Targeted drug delivery technology using untethered microrobots: a review. *Journal of Micromechanics and Microengineering*, 29(5):053002, March 2019.

[22] Shuailong Zhang, Erica Y. Scott, Jastaranpreet Singh, Yujie Chen, Yanfeng Zhang, Mohamed Elsayed, M. Dean Chamberlain, Nika Shakiba, Kelsey Adams, Siyuan Yu, Cindi M. Morshead, Peter W. Zandstra, and Aaron R. Wheeler. The optoelectronic microrobot: A versatile toolbox for micromanipulation. *Proc Natl Acad Sci USA*, 116(30):14823, July 2019.

[23] Yaouen Fily and M. Cristina Marchetti. Athermal phase separation of self-propelled particles with no alignment. *Phys. Rev. Lett.*, 108:235702, Jun 2012.

[24] Gabriel S. Redner, Aparna Baskaran, and Michael F. Hagan. Reentrant phase behavior in active colloids with attraction. *Phys. Rev. E*, 88:012305, Jul 2013.

[25] Gabriel S. Redner, Michael F. Hagan, and Aparna Baskaran. Structure and dynamics of a phase-separating active colloidal fluid. *Phys. Rev. Lett.*, 110:055701, Jan 2013.

[26] Joakim Stenhammar, Adriano Tiribocchi, Rosalind J. Allen, Davide Marenduzzo, and Michael E. Cates. Continuum theory of phase separation kinetics for active brownian particles. *Phys. Rev. Lett.*, 111:145702, Oct 2013.

[27] Alexandre P. Solon, Joakim Stenhammar, Raphael Wittkowski, Mehran Kardar, Yariv Kafri, Michael E. Cates, and Julien Tailleur. Pressure and phase equilibria in interacting active brownian spheres. *Phys. Rev. Lett.*, 114:198301, May 2015.

[28] A. P. Solon, Y. Fily, A. Baskaran, M. E. Cates, Y. Kafri, M. Kardar, and J. Tailleur. Pressure is not a state function for generic active fluids. *Nature Physics*, 11(8):673–678, August 2015.

[29] Aitor Martín-Gómez, Demian Levis, Albert Díaz-Guilera, and Ignacio Pagonabarraga. Collective motion of active brownian particles with polar alignment. *Soft Matter*, 14(14):2610–2618, 2018.

[30] Andreas Fischer, Friederike Schmid, and Thomas Speck. Quorum-sensing active particles with discontinuous motility. *Phys. Rev. E*, 101(1):012601, January 2020.

[31] Ben Fabry, Geoffrey N. Maksym, James P. Butler, Michael Glogauer, Daniel Navajas, and Jeffrey J. Fredberg. Scaling the microrheology of living cells. *Phys. Rev. Lett.*, 87(14):148102, September 2001.

[32] M. Poujade, E. Grasland-Mongrain, A. Hertzog, J. Jouanneau, P. Chavrier, B. Ladoux, A. Buguin, and P. Silberzan. Collective migration of an epithelial monolayer in response to a model wound. *Proc Natl Acad Sci USA*, 104(41):15988, October 2007.

[33] Xavier Trepat, Michael R. Wasserman, Thomas E. Angelini, Emil Millet, David A. Weitz, James P. Butler, and Jeffrey J. Fredberg. Physical forces during collective cell migration. *Nature Physics*, 5(6):426–430, June 2009.

[34] Thomas E. Angelini, Edouard Hannezo, Xavier Trepat, Jeffrey J. Fredberg, and David A. Weitz. Cell migration driven by cooperative substrate deformation patterns. *Phys. Rev. Lett.*, 104(16):168104, April 2010.

[35] Andy Aman and Tatjana Piotrowski. Cell migration during morphogenesis. *Special Section: Morphogenesis*, 341(1):20–33, May 2010.

[36] Thomas E. Angelini, Edouard Hannezo, Xavier Trepat, Manuel Marquez, Jeffrey J. Fredberg, and David A. Weitz. Glass-like dynamics of collective cell migration. *Proc Natl Acad Sci USA*, 108(12):4714, March 2011.

[37] Wolfgang Götze. *Complex Dynamics of Glass-Forming Liquids: A Mode-Coupling Theory*. 2009.

[38] Thomas Voigtmann. *Mode Coupling Theory of the Glass Transition in Binary Mixtures*. PhD thesis, 2002.

[39] W. Till Kranz, Matthias Sperl, and Annette Zippelius. Glass transition for driven granular fluids. *Phys. Rev. Lett.*, 104(22):225701, June 2010.

[40] V. Krakoviack. Liquid-glass transition of confined fluids: insights from a mode-coupling theory. *Journal of Physics: Condensed Matter*, 17(45):S3565–S3570, October 2005.

[41] Lukas Schrack and Thomas Franosch. Mode-coupling theory of the glass transition for colloidal liquids in slit geometry. *Philosophical Magazine*, 100(8):1032–1057, April 2020.

[42] M. Fuchs and M. E. Cates. A mode coupling theory for brownian particles in homogeneous steady shear flow. *Journal of Rheology*, 53(4):957–1000, July 2009.

[43] Ludovic Berthier, Elijah Flenner, and Grzegorz Szamel. Glassy dynamics in dense systems of active particles. *J. Chem. Phys.*, 150(20):200901, May 2019.

[44] T. F. F. Farage and J. M. Brader. Dynamics and rheology of active glasses, 2014.

[45] Grzegorz Szamel, Elijah Flenner, and Ludovic Berthier. Glassy dynamics of athermal self-propelled particles: Computer simulations and a nonequilibrium microscopic theory. *Phys. Rev. E*, 91(6):062304, June 2015.

[46] Grzegorz Szamel. Theory for the dynamics of dense systems of athermal self-propelled particles. *Phys. Rev. E*, 93(1):012603, January 2016.

[47] Alexander Liluashvili, Jonathan Ónody, and Thomas Voigtmann. Mode-coupling theory for active brownian particles. *Phys. Rev. E*, 96:062608, Dec 2017.

[48] Matthias Fuchs and Michael E. Cates. Theory of nonlinear rheology and yielding of dense colloidal suspensions. *Phys. Rev. Lett.*, 89(24):248304, November 2002.

[49] Walter Kob and Hans C. Andersen. Scaling behavior in the β-relaxation regime of a supercooled lennard-jones mixture. *Phys. Rev. Lett.*, 73(10):1376–1379, September 1994.

[50] Th. Voigtmann, A. M. Puertas, and M. Fuchs. Tagged-particle dynamics in a hard-sphere system: Mode-coupling theory analysis. *Phys. Rev. E*, 70(6):061506, December 2004.

[51] F. Weysser, A. M. Puertas, M. Fuchs, and Th. Voigtmann. Structural relaxation of polydisperse hard spheres: Comparison of the mode-coupling theory to a langevin dynamics simulation. *Phys. Rev. E*, 82(1):011504, July 2010.

[52] Fabian Weysser and David Hajnal. Tests of mode-coupling theory in two dimensions. *Phys. Rev. E*, 83(4):041503, April 2011.

[53] G. Li, W. M. Du, X. K. Chen, H. Z. Cummins, and N. J. Tao. Testing mode-coupling predictions for α and β relaxation in $ca_{0.4}k_{0.6}(no_3)_{1.4}$ near the liquid-glass transition by light scattering. *Phys. Rev. A*, 45(6):3867–3879, March 1992.

[54] W. van Megen and S. M. Underwood. Glass transition in colloidal hard spheres: Mode-coupling theory analysis. *Phys. Rev. Lett.*, 70(18):2766–2769, May 1993.

[55] W. Götze and Th. Voigtmann. Universal and nonuniversal features of glassy relaxation in propylene carbonate. *Phys. Rev. E*, 61(4):4133–4147, April 2000.

[56] G. G. Stokes. On the effect of the internal friction of fluids on the motion of pendulums. *Trans. Camb. Phil. Soc. 9, 8–106.*

[57] Nicholas C. Darnton, Linda Turner, Svetlana Rojevsky, and Howard C. Berg. On torque and tumbling in swimming escherichia coli. *J. Bacteriol.*, 189(5):1756, March 2007.

[58] Jens Elgeti and Gerhard Gompper. Wall accumulation of self-propelled spheres. *EPL (Europhysics Letters)*, 101(4):48003, February 2013.

[59] Thomas Speck. Collective behavior of active brownian particles: From microscopic clustering to macroscopic phase separation. *The European Physical Journal Special Topics*, 225(11):2287–2299, November 2016.

[60] Nicole Meyer-Vernet and Jean-Pierre Rospars. How fast do living organisms move: Maximum speeds from bacteria to elephants and whales. *American Journal of Physics*, 83(8):719–722, August 2015.

[61] Julian Reichert. Druck selbstangetriebener teilchen: Brownsche- und multi-particle collision dynamik. Master's thesis, Universität des Saarlandes, 2017.

[62] Tamás Vicsek, András Czirók, Eshel Ben-Jacob, Inon Cohen, and Ofer Shochet. Novel type of phase transition in a system of self-driven particles. *Phys. Rev. Lett.*, 75(6):1226–1229, August 1995.

[63] M. E. Cates and J. Tailleur. When are active brownian particles and run-and-tumble particles equivalent? consequences for motility-induced phase separation. *EPL (Europhysics Letters)*, 101(2):20010, January 2013.

[64] Étienne Fodor, Cesare Nardini, Michael E. Cates, Julien Tailleur, Paolo Visco, and Frédéric van Wijland. How far from equilibrium is active matter? *Phys. Rev. Lett.*, 117(3):038103, July 2016.

[65] K. Kruse, J. F. Joanny, F. Jülicher, J. Prost, and K. Sekimoto. Asters, vortices, and rotating spirals in active gels of polar filaments. *Phys. Rev. Lett.*, 92(7):078101, February 2004.

[66] Stefan Klumpp, Reinhard Lipowsky, and David R. Nelson. Cooperative cargo transport by several molecular motors. *Proceedings of the National Academy of Sciences of the United States of America*, 102(48):17284–17289, 2005.

[67] Dapeng Bi, Xingbo Yang, M. Cristina Marchetti, and M. Lisa Manning. Motility-driven glass and jamming transitions in biological tissues. *Phys. Rev. X*, 6(2):021011, April 2016.

[68] Dirk Drasdo and Stefan Höhme. A single-cell-based model of tumor growthin vitro: monolayers and spheroids. *Physical Biology*, 2(3):133–147, July 2005.

[69] M. Reza Shaebani, Adam Wysocki, Roland G. Winkler, Gerhard Gompper, and Heiko Rieger. Computational models for active matter. *Nature Reviews Physics*, 2(4):181–199, April 2020.

[70] *A Modern Course in Statistical Physics, 4th revised and updated edition*. Linda E. Reichl., 2016.

[71] Borge Hagen, Sven van Teeffelen, and Hartmut Löwen. Non-gaussian behaviour of a self-propelled particle on a substrate. *Condensed Matter Physics*, 12, June 2009.

[72] Jérémie Palacci, Cécile Cottin-Bizonne, Christophe Ybert, and Lydéric Bocquet. Sedimentation and effective temperature of active colloidal suspensions. *Phys. Rev. Lett.*, 105(8):088304, August 2010.

[73] J. J. Hermans and R. Ullman. The statistics of stiff chains, with applications to light scattering. *Physica*, 18:951–971, November 1952.

[74] Amir Shee, Abhishek Dhar, and Debasish Chaudhuri. Active brownian particles: mapping to equilibrium polymers and exact computation of moments. *Soft Matter*, 16(20):4776–4787, 2020.

[75] S. Papenkort and Th. Voigtmann. Multi-scale lattice boltzmann and mode-coupling theory calculations of the flow of a glass-forming liquid. *J. Chem. Phys.*, 143(20):204502, November 2015.

[76] A. Sharma and J. M. Brader. Communication: Green-kubo approach to the average swim speed in active brownian systems. *J. Chem. Phys.*, 145(16):161101, October 2016.

[77] Sara Dal Cengio, Demian Levis, and Ignacio Pagonabarraga. Linear response theory and green-kubo relations for active matter. *Phys. Rev. Lett.*, 123(23):238003, December 2019.

[78] T. Franosch, M. Fuchs, W. Götze, M. R. Mayr, and A. P. Singh. Asymptotic laws and preasymptotic correction formulas for the relaxation near glass-transition singularities. *Phys. Rev. E*, 55(6):7153–7176, June 1997.

[79] M. Fuchs, W. Götze, and M. R. Mayr. Asymptotic laws for tagged-particle motion in glassy systems. *Phys. Rev. E*, 58(3):3384–3399, September 1998.

[80] W. Till Kranz, Fabian Frahsa, Annette Zippelius, Matthias Fuchs, and Matthias Sperl. Integration through transients for inelastic hard sphere fluids. *Phys. Rev. Fluids*, 5(2):024305, February 2020.

[81] Ran Ni, Martien A. Cohen Stuart, and Marjolein Dijkstra. Pushing the glass transition towards random close packing using self-propelled hard spheres. *Nature Communications*, 4(1):2704, October 2013.

[82] Jean-Pierre Hansen I.R. McDonald. *Theory of Simple Liquids, 4th Edition*. 2013.

[83] M. Gruber, G. C. Abade, A. M. Puertas, and M. Fuchs. Active microrheology in a colloidal glass. *Phys. Rev. E*, 94(4):042602, October 2016.

[84] A. Liluashvili. *Mode-Coupling Theory of Active Brownian Hard Disks*. PhD thesis, 2017.

[85] Robert Zwanzig. *Nonequilibrium Statistical Mechanics*. 2004.

[86] Christina Kurzthaler, Clémence Devailly, Jochen Arlt, Thomas Franosch, Wilson C. K. Poon, Vincent A. Martinez, and Aidan T. Brown. Probing the spatiotemporal dynamics of catalytic janus particles with single-particle tracking and differential dynamic microscopy. *Phys. Rev. Lett.*, 121:078001, Aug 2018.

[87] C. H. Ziener, M. Rückl, T. Kampf, W. R. Bauer, and H. P. Schlemmer. Mathieu functions for purely imaginary parameters. *Journal of Computational and Applied Mathematics*, 236(17):4513–4524, November 2012.

[88] T. Franosch and Th. Voigtmann. Completely monotone solutions of the mode-coupling theory for mixtures. *Journal of Statistical Physics*, 109(1):237–259, October 2002.

[89] Gerhard Jung, Thomas Voigtmann, and Thomas Franosch. *Scaling equations for mode-coupling theories with multiple decay channels*. May 2020.

[90] Kyozi Kawasaki. Correlation-function approach to the transport coefficients near the critical point. i. *Phys. Rev.*, 150(1):291–306, October 1966.

[91] Setsuo Ichimaru. Strongly coupled plasmas: high-density classical plasmas and degenerate electron liquids. *Rev. Mod. Phys.*, 54(4):1017–1059, October 1982.

[92] Rolf Schilling and Thomas Scheidsteger. Mode coupling approach to the ideal glass transition of molecular liquids: Linear molecules. *Phys. Rev. E*, 56(3):2932–2949, September 1997.

[93] Yaakov Rosenfeld and N. W. Ashcroft. Theory of simple classical fluids: Universality in the short-range structure. *Phys. Rev. A*, 20(3):1208–1235, September 1979.

[94] M. Baus and J. L. Colot. Theoretical structure factors for hard-core fluids. *Journal of Physics C: Solid State Physics*, 19(28):L643–L648, October 1986.

[95] Alice Thorneywork, Simon Schnyder, Dirk Aarts, Jürgen Horbach, Roland Roth, and Roel Dullens. Structure factors in a two-dimensional binary colloidal hard sphere system. *Molecular Physics*, 116:1–13, July 2018.

[96] J. Ónody. *Dense Microswimmer Systems in Model Porous Media*. PhD thesis, 2020.

[97] Y. Huang and W. F. McColl. Analytical inversion of general tridiagonal matrices. *Journal of Physics A: Mathematical and General*, 30(22):7919–7933, November 1997.

[98] Michael E. Cates and Julien Tailleur. Motility-induced phase separation. *Annu. Rev. Condens. Matter Phys.*, 6(1):219–244, March 2015.

[99] Roberto Alonso-Matilla, Barath Ezhilan, and David Saintillan. Microfluidic rheology of active particle suspensions: Kinetic theory. *Biomicrofluidics*, 10(4):043505–043505, June 2016.

[100] S. C. Takatori and J. F. Brady. Superfluid behavior of active suspensions from diffusive stretching. *Phys. Rev. Lett.*, 118(1):018003, January 2017.

[101] David Saintillan. Rheology of active fluids. *Annu. Rev. Fluid Mech.*, 50(1):563–592, January 2018.

[102] G. Foffi, C. De Michele, F. Sciortino, and P. Tartaglia. Scaling of dynamics with the range of interaction in short-range attractive colloids. *Phys. Rev. Lett.*, 94(7):078301, February 2005.

[103] A. Scala, Th. Voigtmann, and C. De Michele. Event-driven brownian dynamics for hard spheres. *The Journal of Chemical Physics*, 126(13):134109, Apr 2007.

[104] Suvendu Mandal, Christina Kurzthaler, Thomas Franosch, and Hartmut Löwen. Crowding-enhanced diffusion: An exact theory for highly entangled self-propelled stiff filaments. *Phys. Rev. Lett.*, 125(13):138002, September 2020.

[105] Werner Krauth. *Statistical Mechanics: Algorithms and Computations*. Oxford University Press, 2006.

[106] Boris D. Lubachevsky and Frank H. Stillinger. Geometric properties of random disk packings. *Journal of Statistical Physics*, 60(5):561–583, September 1990.

[107] M. Bayer, J. M. Brader, F. Ebert, M. Fuchs, E. Lange, G. Maret, R. Schilling, M. Sperl, and J. P. Wittmer. Dynamic glass transition in two dimensions. *Phys. Rev. E*, 76(1):011508, July 2007.

[108] Parisi G Zamponi F. Charbonneau P, Jin Y. Hopping and the stokes– einstein relation breakdown in simple glass formers. *Proc Natl Acad Sci USA. 111:15025. doi: 10.1073/pnas.1417182111*, 2014.

[109] Jean-Philippe Bouchaud Luca Cipelletti Ludovic Berthier, Giulio Biroli and Wim van Saarloos. *Dynamical Heterogeneities in Glasses, Colloids, and Granular Media*. Oxford Science Publications, 2011.

[110] Leon Granz. Event-driven molecular dynamics simulations of dense two-dimensional active brownian systems. Master's thesis, 2020.

[111] T. G. Mason and D. A. Weitz. Optical measurements of frequency-dependent linear viscoelastic moduli of complex fluids. *Phys. Rev. Lett.*, 74(7):1250–1253, February 1995.

[112] Celia Lozano, Juan Ruben Gomez-Solano, and Clemens Bechinger. Active particles sense micromechanical properties of glasses. *Nature Materials*, 18(10):1118–1123, October 2019.

[113] Yuriy L. Raikher, Victor V. Rusakov, and Régine Perzynski. Brownian motion in a viscoelastic medium modelled by a jeffreys fluid. *Soft Matter*, 9(45):10857–10865, 2013.

[114] Jesús Santana-Solano, Angeles Ramírez-Saito, and José Luis Arauz-Lara. Short-time dynamics in quasi-two-dimensional colloidal suspensions. *Phys. Rev. Lett.*, 95(19):198301, October 2005.

[115] Chen W. Fischer-T. Weitz D. & Tong P. Peng, Y. Short-time self-diffusion of nearly hard spheres at an oil-water interface. *Journal of Fluid Mechanics*, 618:243–261, 2009.

[116] H. König, R. Hund, K. Zahn, and G. Maret. Experimental realization of a model glass former in 2d. *Eur. Phys. J. E*, 18(3):287–293, November 2005.

[117] Alice Thorneywork, Roberto E. Rozas, Roel Dullens, and Jürgen Horbach. Effect of hydrodynamic interactions on self-diffusion of quasi-two-dimensional colloidal hard spheres. *Physical Review Letters*, 115, December 2015.

[118] W. van Megen, T. C. Mortensen, S. R. Williams, and J. Müller. Measurement of the self-intermediate scattering function of suspensions of hard spherical particles near the glass transition. *Phys. Rev. E*, 58(5):6073–6085, November 1998.

[119] David Hajnal, Joseph M. Brader, and Rolf Schilling. Effect of mixing and spatial dimension on the glass transition. *Phys. Rev. E*, 80(2):021503, August 2009.

[120] Meng-kai Feng and Zhong-huai Hou. Mode-coupling theory for glass transition of active-passive binary mixture. *Chinese Journal of Chemical Physics*, 31(4):584–594, August 2018.

[121] Michele Caraglio, Lukas Schrack, Gerhard Jung, and Thomas Franosch. An improved integration scheme for mode-coupling-theory equations, 2020.

[122] Suvendu Mandal, Lukas Schrack, Hartmut Löwen, Matthias Sperl, and Thomas Franosch. Persistent anti-correlations in brownian dynamics simulations of dense colloidal suspensions revealed by noise suppression. *Phys. Rev. Lett.*, 123:168001, Oct 2019.

Acknowledgements

This work should not end without having acknowledged all those who have supported me during its creation.

First and foremost, I would like to express my sincere thanks to my supervisor **Prof. Thomas Voigtmann**, not only for giving me the opportunity to continue my research in the field of active matter but in particular for his warm and supportive manner, which I have very much appreciated during the past years. He followed my work with great interest and was always available for questions. With his vast experience and optimistic approach to solving problems, he has been an extremely valuable support during my entire time as a doctoral student.

I gratefully acknowledged the funding of this work by the **SPP 1726** of the **German Research Foundation**.

Moreover, I would also like to thank the head of the Institute of Materials Physics in Space at DLR, **Prof. Andreas Meyer**, in particular for the excellent computational resources he has provided at the institute and for giving me the opportunity to complete my thesis at DLR beyond the funding through the SPP 1726.

I would like to express my special gratitude towards **Dr. Suvendu Mandal** for providing his implementation of the event-driven Brownian dynamics simulation, which was a tremendous help to finish this work in time.

Also, I want to extend my thanks to **Dr. Celia Lozano** for granting me access to her experimental data.

Further, I would like to acknowledge **Prof. Hartmut Löwen** for being available as a second reviewer and mentor of this work.

During my time at the DLR, I had the pleasure to meet many great colleagues. These include in particular **Dr. Alexander Liluashvili**, who I would like to thank in view of the helpful introduction he gave me into his work, my lunch partner **Dr. Sandro Szabó** for the numerous and exciting discussions beyond our scientific works, my former and new office colleagues **Jonathan Ónody** and **Sebastian Steinhäuser** for creating a pleasant working atmosphere in the pre-Corona office and many more. Moreover, I wish to thank **Leon Granz**, who was a great help in view of numerous scientific discussions we had and for providing some valuable simulation results.

Undoubtedly, the greatest thanks are due to my family and in particular to my parents, who have supported me unconditionally in every possible way during my life so far.